FULL-WAVEFORM INVERSION FOR IMAGING SPATIALLY VARYING SUBSOIL DENSITY

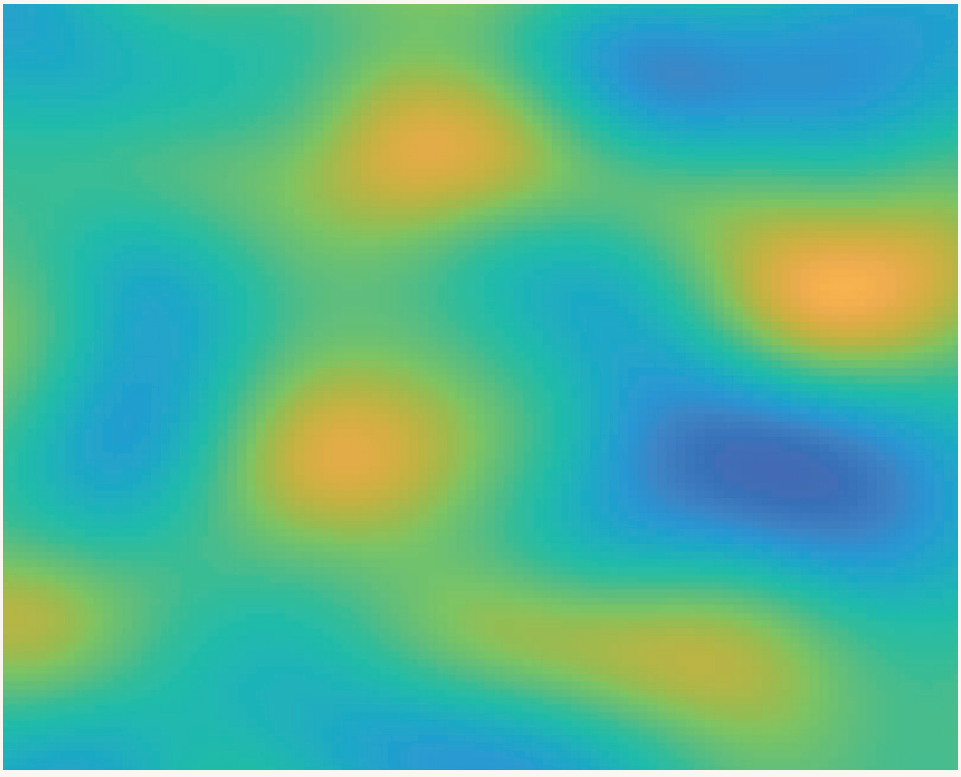

Yusuke Kawasaki

FULL-WAVEFORM INVERSION FOR IMAGING SPATIALLY VARYING SUBSOIL DENSITY

FULL-WAVEFORM INVERSION FOR IMAGING SPATIALLY VARYING SUBSOIL DENSITY

Dissertation

for the purpose of obtaining the degree of doctor
at Delft University of Technology
by the authority of the Rector Magnificus, Prof. dr. ir. H. Bijl,
chair of the Board for Doctorates,
to be defended publicly on
Tuesday, 31 March 2026 at 17:30

by

Yusuke KAWASAKI

This dissertation has been approved by the promotors.

Composition of the doctoral committee:

Rector Magnificus,	chairperson
Dr. R. Ghose,	Delft University of Technology, *promotor*
Dr. ir. D.S. Draganov,	Delft University of Technology, *promotor*
Independent members:	
Prof. dr. ir. E.C. Slob	Delft University of Technology
Prof. dr. M.A. Hicks	Delft University of Technology
Prof. dr. ir. L.V. Socco	Delft University of Technology
Prof. dr. T. Bohlen	Karlsruhe Institute of Technology, Germany
Dr. D. Rovetta,	Fugro, The Netherlands
Em. Prof. dr. W.A. Mulder	Delft University of Technology, reserve member

Keywords: Full-waveform inversion, subsoil density, horizontal-force seismic source

To my parents

Yusuke Kawasaki

Contents

Summary xi

Samenvatting xv

List of acronyms xix

1 Introduction 1
- 1.1 Conventional approaches for obtaining subsoil density . . . 2
- 1.2 Seismic full-waveform inversion (FWI) for subsoil density estimation: benefits and challenges . . . 3
- 1.3 Research goals . . . 6
- 1.4 Thesis outline . . . 6

2 Imaging subsoil density variability: specific considerations in 2D FWI 9
- 2.1 Introduction . . . 10
- 2.2 Methodology . . . 11
  - 2.2.1 2D SH FWI . . . 11
  - 2.2.2 Inversion workflow addressing parameter coupling . . . 13
  - 2.2.3 Initial model building strategy . . . 14
- 2.3 Field data application: data acquisition and preprocessing . . . 16
  - 2.3.1 Data acquisition . . . 17
  - 2.3.2 Data preprocessing for the FWI . . . 18
  - 2.3.3 Building of initial models for the FWI . . . 19
  - 2.3.4 Estimating optimum Q_S for the FWI . . . 20
  - 2.3.5 FWI parameter settings . . . 21
- 2.4 Field data application: investigating FWI strategies . . . 22
  - 2.4.1 Effect of the used inversion workflow . . . 23
  - 2.4.2 Effect of the used initial models . . . 23
- 2.5 Discussion . . . 28
  - 2.5.1 Spatially varying density structure estimated from FWI . . . 28
  - 2.5.2 Limitation of the analysis . . . 32
  - 2.5.3 Validating V_S estimates from FWI using SCPT data . . . 32
  - 2.5.4 Considerations for building the initial density model . . . 33
- 2.6 Conclusions . . . 34

3 2D FWI for subsoil density: building aliasing-free seismic data using seismic interferometry 35
- 3.1 Introduction . . . 36
- 3.2 Methodology . . . 38
  - 3.2.1 Building aliasing-free seismic data from SI . . . 38
  - 3.2.2 Designing a weighted misfit function for the merged data . . . 40

3.3 Field-data application . . . 41
3.3.1 Characterizing artifacts due to spatial aliasing . . . 41
3.3.2 Results: retrieved virtual Love wave data . . . 45
3.3.3 Results: FWI applied to the merged real+virtual seismic source data 47
3.4 Discussion . . . 52
3.4.1 Improved subsurface structure due to the use of virtual shot records . 52
3.4.2 Further investigation into the retrieved Love wave data . . . 54
3.5 Conclusions . . . 57

4 3D FWI for subsoil density: test on synthetic data for different force directions of the seismic source 59
4.1 Introduction . . . 60
4.2 Methodology . . . 62
4.2.1 3D FWI . . . 62
4.2.2 Approach to evaluate different force directions in 3D FWI for density 64
4.3 Results of 3D FWI for different force directions: noise, parameter coupling and resolution . . . 67
4.3.1 Noise robustness . . . 67
4.3.2 Parameter coupling . . . 68
4.3.3 Resolution . . . 70
4.4 Near-surface models: results of 3D FWI for different force directions . . . 71
4.4.1 FWI results for a spatially uncorrelated model . . . 72
4.4.2 FWI results for a realistic subsoil model . . . 75
4.5 Discussion . . . 85
4.5.1 Reason behind the superiority of a horizontal-force source for density reconstruction . . . 85
4.5.2 Limitation of the analyses . . . 86
4.5.3 Practical considerations for horizontal-force sources . . . 88
4.6 Conclusions . . . 88
4.7 Appendix . . . 89
4.7.1 Preconditioning filter based on diagonal Hessian . . . 89
4.7.2 Parameter-coupling analysis for V_S using a realistic subsoil model . . 90
4.7.3 Inversion results for V_S using a realistic subsoil model . . . 92
4.8 Supplementary Material . . . 93
4.8.1 FWI results using an f_x dataset for a realistic subsoil model . . . 93
4.8.2 In-depth evaluation of the estimated density . . . 94

5 3D FWI for subsoil density: considerations for the force direction of the seismic source 99
5.1 Introduction . . . 100
5.2 Methodology: 3D FWI using a single source component and the $f_x + f_y$ source combination . . . 101
5.3 Data acquisition and 3D FWI settings . . . 102
5.3.1 Seismic data acquisition . . . 102
5.3.2 3D FWI settings . . . 103

5.4 Challenges in 3D FWI with horizontal-force sources: influence of leaky waves . . . 105
5.4.1 Large initial misfits caused by leaky waves . . . 105
5.4.2 Choosing specific receiver components for the vertical- and horizontal-force datasets . . . 108
5.5 Results of 3D FWI . . . 111
5.5.1 FWI using single source component: vertical-force (f_z) and horizontal-force (f_x or f_y) sources . . . 112
5.5.2 3D FWI combining data from f_x and f_y seismic sources: potential benefits of joint inversion . . . 115
5.6 Discussion . . . 118
5.6.1 Reason behind superiority of horizontal-force sources for successful density reconstruction . . . 118
5.6.2 Further investigation into potential benefits of 3D FWI using $f_x + f_y$ source combination . . . 120
5.6.3 Limitations in the current 3D FWI results . . . 122
5.7 Conclusions . . . 125

6 Conclusions and recommendations **127**
6.1 Conclusions . . . 127
6.2 Recommendations for future work . . . 131

References **135**

Acknowledgements **149**

Curriculum Vitæ **151**

List of Publications **153**

Summary

Bulk density (ρ) of soil is an important parameter that reflects the ability of the soil to provide structural support, solute and water transport, and soil aeration. Subsoil density generally exhibits significant spatial variation, which is vital information to simulate water/solute movement in soils, to evaluate embankment stability, estimate groundwater effects for predicting crop productivity, and forecast the seismic site response, among others. Density of soil can also vary with time. With rapid climate change and growing use of the underground space, change of soil density at a given location can eventually increase soil vulnerability, eventually causing structural failure and ground collapse. There are several established approaches to measure density in the field or in the laboratory on soil samples. Those approaches cannot generally capture the spatial variability of density, and often the estimates do not represent the undisturbed soil condition. There are several surface geophysical methods that do capture the lateral variability of density in a noninvasive manner, but they either lack in resolution, or being indirectly linked to density, require empirical relations to derive density, or are essentially based on the assumption of an one-dimensional (1D) earth structure.

Seismic full-waveform inversion (FWI) is a nonlinear inversion method that estimates multiple seismic parameters simultaneously by fitting synthetic seismic waveforms to observed waveforms. FWI can provide spatially varying 2- or 3-dimensional (2D or 3D) seismic velocity and density images of the subsoil. So far, in near-surface geophysical applications, FWI has been used mostly to image the shear-wave velocity (V_S) field. Due to inherent difficulties, reliable estimation of the ρ variability in soils using FWI is a more challenging task compared to estimating the spatial variability of V_S. One major difficulty in estimating reliably ρ is due to the well-known parameter-coupling problem, wherein elastic parameters are not independently resolvable in FWI, and errors in V_S propagate into errors in ρ. Secondly, it is quite difficult to get a good background ρ model from FWI, which further aggravates the parameter-coupling problem. Thirdly, having many seismic sources and receivers at fine spacing is required to achieve high-resolution seismic imaging of the near-surface. However, it is expensive, especially to have a dense seismic source distribution in the field. A sparse source distribution causes spatial aliasing in data, which leads to artifacts and reduced resolution in the FWI results. Also, having independent ground truths is important in order to evaluate the FWI results and/or optimize the inversion for reliability and resolution.

We address these specific challenges of FWI in the context of ρ estimation. The overarching goal is to capture subsoil ρ variability in a more robust and economically advantageous way than it has so far been possible. First, we concentrate on 2D FWI and investigate the main difficulties that one faces when deriving the subsoil ρ image from the SH/Love-wave-dominated field data. In the second part, we focus on 3D FWI for ρ estimation, using both synthetic and field data. Ground truths gathered at our test site through independent field and laboratory tests are used to improve FWI for subsoil ρ estimation and

to validate the FWI results.

We first develop a sequential workflow for FWI that enables weakening the coupling effect between V_S and ρ. Our new workflow is made of two stages: in the first stage, a multi-parameter inversion reduces the errors in V_S, and then in the second stage the ρ is updated in the relatively correct direction by starting with a less erroneous V_S model. We test this workflow on a 2D SH/Love-wave dataset that we acquire at a soil site in the northern Netherlands. Compared to conventional simultaneous inversion, our workflow greatly improves the ρ estimates. The estimated values match well with the independent measurements of ρ obtained from density logging and from laboratory experiments on soil samples collected in boreholes. The sequential inversion, after the convergence, also results in a better fit between the observed and the synthetic seismograms. We also examine how good the initial model for V_S needs to be to further mitigate the parameter-coupling issue in FWI. Inversion tests are conducted to compare two different initial V_S models: an 1D V_S model derived from smoothing the V_S profile obtained from seismic cone penetration test (SCPT) data and a 2D V_S model derived from multichannel analysis of Love waves (MALW). Our results indicate that a smoothed version of the SCPT-derived V_S profile used for input in FWI results in a less erroneous ρ variability and a better waveform matching. The proposed workflow and the SCPT-derived initial V_S model are advantageous in order to minimize the risk of falling into local minima due to parameter coupling.

On the same 2D field dataset, we investigate the negative effects of spatial aliasing in data on the FWI result. We find that a sparse distribution of the seismic sources limits the lateral resolution in both V_S and ρ fields derived from FWI. Due to spatial aliasing caused by the sparse source distribution, artifacts showing up as striped pattern are created in the gradient of the FWI around the shot positions. The artifacts are due to insufficient suppression of the oscillatory side lobes that appear around each shot location. These artifacts are responsible for the limited lateral resolution in the obtained images. The absolute values of ρ also become less accurate due to spatial aliasing. To tackle this issue, we at first retrieve, using seismic interferometry (SI), the surface-wave records at each receiver position from the surface-wave-dominated field shot (common-source) gathers. The retrieved dataset is then combined with the original field dataset to create densely distributed shot gathers. FWI is performed on the merged data. To use the retrieved virtual records having a lower S/N than the original records, we correct the SI-related (amplitude and phase) errors using a matched filter, together with additional low-frequency correction. We introduce a weighted misfit function. We find that these data-correction approaches enable a stable performance of the FWI on the real+virtual merged dataset. Our proposed approach of FWI on merged real+virtual data reduces the striped-pattern artifacts, compared to FWI on field data only, thereby improving the lateral resolution in both the V_S and ρ models. The spatial distribution of ρ obtained from this new approach shows a better correlation with the distribution of CPT cone-tip resistance, compared to when using only the aliased real (field) data in the FWI.

Next, we examine on synthetic data the performance of 3D FWI for estimating subsoil ρ distribution depending on the force direction of the used seismic source. Focusing on the scattered wavefield and the shape of the misfit function (given by its gradient and Hessian), we evaluate three indicators for the FWI performance for each force-direction dataset: noise robustness, parameter coupling, and resolution. Given a point-localized perturbation model,

we evaluate, for all three indicators, the merits of using horizontal-force sources compared to vertical-force sources. FWI of the seismic data generated by a horizontal-force source is found to be relatively more robust to noise present in the data, less prone to parameter coupling, and more promising in reconstructing a high-resolution gradient. Inversion tests for two different subsoil models also confirm the superiority of the horizontal-force sources over the vertical-force source. FWI using horizontal-force source data can build a high-resolution gradient for ρ without severe parameter-coupling artifacts (i.e., artifacts due to error in V_S), allowing the update for ρ to occur in a relatively correct direction. The estimated ρ distribution from 3D FWI applied to horizontal-force data correlates well with the actual distribution in a layered, near-surface soil model.

Finally, we test the performance of 3D FWI on a 3D field dataset that we have acquired. We investigate how a selective use of the source component may influence V_S and ρ estimates from 3D FWI. We focus on three source components, viz. vertical force and two cross-polarized horizontal forces. FWI applied to inline horizontal-component source data fails to resolve a subsurface model with good waveform matching, even if the inversion starts with the lowest frequency available in the data. Thorough numerical investigations reveal that this issue is attributable to erroneously simulated leaky waves, which are pronounced in a specific source-receiver component dataset. Based on this finding, we propose excluding leaky-wave-contaminated components from being used in FWI. For the horizontal-force data, we use crossline horizontal-component receiver traces dominated by SH/Love waves, while vertical component traces are used only in FWI of vertical-force source data. The inversion tests show that FWI of SH/Love-wave dominated data generated by crossline horizontal-force sources offers better estimates of both V_S and ρ than FWI of vertical-force source data. Furthermore, for a greater accuracy of the V_S and ρ estimates, we recognize the benefit of using simultaneously data from two cross-polarized horizontal-force sources in FWI. This happens because, in case of such joint FWI, the misfit function takes a shape that leads to a better convergence than when a single-component horizontal-force source data are used.

Throughout this thesis, we have demonstrated that FWI using horizontal-force source data recorded by a receiver component where SH/Love-waves are dominant, is capable of mapping subsoil ρ distribution with good accuracy in both 2D and 3D. The data-selection strategy allows one to extract ρ from a seismic dataset at a relatively low cost through a gradient-based FWI. The obtained ρ variability in the soil can contribute to improved soil characterization, such as understanding the spatial distribution of soil types, soil compaction or hardness, and porosity/void ratio. Successful use of FWI will enable mapping ρ in a noninvasive manner over a wide area and also temporal monitoring.

There are several limitations that need to be addressed in the future. First, our understanding of the physical mechanisms behind the advantages of using horizontal-force source data in FWI is still incomplete. In particular, the contributions of the different wave modes observed in the field data need to be investigated in more detail. Second, the efficacy of the proposed strategies, especially the sequential inversion workflow and the use of virtual sources, may depend on the assumed subsurface model. Further synthetic studies using systematically different near-surface models with different degrees of heterogeneity would help establish more general guidelines for accurate ρ estimation using FWI. Finally, additional information contained in the field data has not been fully exploited in this research,

e.g., waveform amplitude information, higher-frequency components, and nine-component seismic data for 3D FWI. Incorporating this information into the inversion framework could improve further the achievable resolution and accuracy of the ρ estimates.

Samenvatting

De bulkdichtheid (ρ) van de bodem is een belangrijke parameter die de capaciteit van de bodem weerspiegelt om structurele ondersteuning te bieden, het transport van opgeloste stoffen en water te faciliteren, en de bodemdoorluchting te waarborgen. De dichtheid van de ondergrond vertoont doorgaans aanzienlijke ruimtelijke variatie, wat cruciale informatie is voor het simuleren van water- en opgeloste stofbeweging in de bodem, het evalueren van de stabiliteit van dijken, het schatten van de effecten op het grondwater voor het voorspellen van de gewasproductiviteit, en het voorspellen van onder andere de seismische respons van locaties. De dichtheid van de bodem kan ook in de tijd variëren. Door de snelle klimaatverandering en de toenemende benutting van de ondergrond kan de verandering van de bodemdichtheid op een bepaalde locatie uiteindelijk de kwetsbaarheid van de bodem vergroten, wat kan leiden tot structurele falen en grondverzakking. Er zijn verschillende gevestigde methoden om de dichtheid in het veld of in het laboratorium op bodemmonsters te meten. Deze methoden kunnen doorgaans de ruimtelijke variabiliteit van de dichtheid niet vastleggen, en vaak vertegenwoordigen de schattingen niet de ongestoorde bodemgesteldheid. Er zijn verschillende oppervlakte-geofysische methoden die de laterale variabiliteit van de dichtheid op een niet-invasieve manier vastleggen, maar deze hebben ofwel een gebrek aan resolutie, zijn indirect gekoppeld aan de dichtheid, vereisen empirische relaties om de dichtheid af te leiden, of zijn in wezen gebaseerd op de aanname van een eendimensionale (1D) aardstructuur.

Seismische full-waveform inversie (FWI) is een niet-lineaire inversiemethode die meerdere seismische parameters gelijktijdig schat door synthetische seismische golfvormen aan waargenomen golfvormen aan te passen. FWI kan ruimtelijk variërende twee- en driedimensionaal (2D en 3D) seismische snelheden en dichtheden van de ondergrond bieden afbeelden. Tot nu toe is FWI in near-surface geofysische toepassingen voornamelijk gebruikt om het shear-wave snelheidsveld (V_S) in beeld te brengen. Vanwege inherente moeilijkheden is een betrouwbare schatting van de ρ -variabiliteit in bodems met behulp van FWI een uitdagendere taak in vergelijking met het schatten van de ruimtelijke variabiliteit van V_S. Een uitdaging bij het betrouwbaar schatten van ρ is vanwege het welbekende parameter-koppelingsprobleem, waarbij elastische parameters niet onafhankelijk oplosbaar zijn in FWI, en fouten in V_S zich vertalen in fouten in ρ. Ten tweede is het vrij moeilijk om een goed achtergrond ρ-model uit FWI te verkrijgen, wat het parameter-koppelingsprobleem verder verergert. Ten derde is het nodig om veel seismische bronnen en ontvangers met fijne tussenruimten te hebben om hoge-resolutie seismische beeldvorming van de near-surface te Verkrijgen. Dit is echter kostbaar, vooral om een dichte seismische bronverdeling in het veld te hebben. Een spaarzame bronverdeling veroorzaakt ruimtelijke vouwvervorming in de gegevens, wat leidt tot artefacten en verminderde resolutie in de FWI-resultaten. Daarnaast is het hebben van onafhankelijke grondwaarheden belangrijk om de FWI-resultaten te evalueren en/of de inversie te optimaliseren voor betrouwbaarheid en resolutie.

We pakken deze specifieke uitdagingen van FWI aan in de context van ρ-schatting.

Het overkoepelende doel is om de variabiliteit van ρ in de ondergrond op een robuustere en economisch voordeligere manier vast te leggen dan tot nu toe mogelijk is geweest. Ten eerste concentreren we ons op 2D FWI en onderzoeken we de belangrijkste moeilijkheden waarmee men wordt geconfronteerd bij het afleiden van het ρ-beeld van de ondergrond uit de SH/Love-golf gedomineerde veldgegevens. In het tweede deel richten we ons op 3D FWI voor ρ-schatting, waarbij we zowel synthetische als veldgegevens gebruiken. Grondwaarheden verzameld op onze testlocatie door middel van onafhankelijke veld- en laboratoriumtests worden gebruikt om FWI te verbeteren voor de schatting van ρ in de ondergrond en om de FWI-resultaten te valideren.

We ontwikkelen eerst een sequentiële workflow voor FWI die het mogelijk maakt om het koppelingseffect tussen V_S en ρ te verzwakken. Onze nieuwe workflow bestaat uit twee fasen: in de eerste fase vermindert een multi-parameter inversie de fouten in V_S, en in de tweede fase wordt ρ bijgewerkt in de relatief juiste richting door te beginnen met een minder foutief V_S-model. We testen deze workflow op een 2D SH/Love-golf dataset die we hebben verkregen op een bodemlocatie in het noorden van Nederland. In vergelijking met conventionele gelijktijdige inversie verbetert onze workflow de ρ-schattingen aanzienlijk. De geschatte waarden komen goed overeen met de onafhankelijke metingen van ρ verkregen uit dichtheidslogging en uit laboratoriumexperimenten op bodemmonsters die uit boorgaten zijn verzameld. De sequentiële inversie resulteert, na de convergentie, ook in een betere overeenkomst tussen de waargenomen en de synthetische seismogrammen. We onderzoeken ook hoe goed het initiële model voor V_S moet zijn om het parameter-koppelingsprobleem in FWI verder te verlichten. Inversietests worden uitgevoerd om twee verschillende initiële V_S-modellen te vergelijken: een 1D V_S-model afgeleid van het gladstrijken van het V_S-profiel verkregen uit seismische cone penetratietests (SCPT) en een 2D V_S-model afgeleid van multichannel analyse van Love-golven (MALW). Onze resultaten geven aan dat een gladgestreken versie van het SCPT-afgeleide V_S-profiel dat als input voor FWI wordt gebruikt, resulteert in een minder foutieve ρ-variabiliteit en een betere golfvormmatching. De voorgestelde workflow en het SCPT-afgeleide initiële V_S-model zijn voordelig om het risico te minimaliseren om in lokale minima te vallen als gevolg van parameterkoppeling.

Op dezelfde 2D velddataset onderzoeken we de negatieve effecten van ruimtelijke aliasing in de gegevens op het FWI-resultaat. We ontdekken dat een spaarzame verdeling van de seismische bronnen de laterale resolutie in zowel de V_S- als de ρ-velden, die uit FWI zijn afgeleid, beperkt. Door de ruimtelijke aliasing veroorzaakt door de spaarzame bronverdeling ontstaan er artefacten die verschijnen als een gestreept patroon in de gradient van de FWI rond de schotposities. De artefacten zijn het gevolg van onvoldoende onderdrukking van de oscillatorende zijlobben die rond elke schotlocatie verschijnen. Deze artefacten zijn verantwoordelijk voor de beperkte laterale resolutie in de verkregen beelden. De absolute waarden van ρ worden ook minder nauwkeurig door ruimtelijke aliasing. Om dit probleem aan te pakken, halen we eerst, met behulp van seismische interferometrie (SI), de oppervlaktegolfrecords op bij elke ontvangers positie uit het oppervlaktegolf gedomineerde veldschot (gemeenschappelijke bron) verzamelingen. De opgehaalde dataset wordt vervolgens gecombineerd met de oorspronkelijke velddataset om dicht verspreide schotverzamelingen te creëren. FWI wordt uitgevoerd op de samengevoegde gegevens. Om de opgehaalde virtuele opnamens met een lagere S/N dan de oorspronkelijke opnamens te gebruiken, corrigeren we de SI-gerelateerde (amplitude- en fase) fouten met behulp van een

gematcht filter, samen met een aanvullende lage-frequentiecorrectie. We introduceren een gewogen misfitfunctie. We ontdekken dat deze gegevenscorrectiebenaderingen een stabiele prestatie van de FWI op de samengevoegde echte+virtuele dataset mogelijk maken. Onze voorgestelde benadering van FWI op samengevoegde echte+virtuele gegevens vermindert de gestreepte patroonartefacten in vergelijking met FWI op alleen veldgegevens, waardoor de laterale resolutie in zowel de V_S- als de ρ-modellen verbetert. De ruimtelijke verdeling van ρ die uit deze nieuwe benadering is verkregen, vertoont een betere correlatie met de verdeling van de CPT-conetipweerstand in vergelijking met wanneer alleen de gealiaseerde echte (veld)gegevens in de FWI worden gebruikt.

Vervolgens onderzoeken we op synthetische gegevens de prestaties van 3D FWI voor het schatten van de ρ-verdeling in de ondergrond, afhankelijk van de krachtrichting van de gebruikte seismische bron. Door ons te concentreren op het verspreide golfveld en de vorm van de misfitfunctie (gegeven door de gradient en Hessiaan), evalueren we drie indicatoren voor de FWI-prestaties voor elke kracht-richting dataset: ruisrobustheid, parameterkoppeling en resolutie. Gegeven een punt-gelocaliseerd verstoringsmodel, evalueren we voor alle drie de indicatoren de voordelen van het gebruik van horizontale-krachtbronnen in vergelijking met verticale-krachtbronnen. FWI van de seismische gegevens die door een horizontale-krachtbron zijn gegenereerd, blijkt relatief robuuster te zijn tegen ruis in de gegevens, minder gevoelig voor parameterkoppeling en veelbelovender in het reconstrueren van een hoge-resolutie gradient. Inversietests voor twee verschillende ondergrondmodellen bevestigen ook de superioriteit van de horizontale-krachtbronnen ten opzichte van de verticale-krachtbron. FWI met behulp van gegevens van horizontale-krachtbronnen kan een hoge-resolutie gradient voor ρ opbouwen zonder ernstige parameter-koppelingsartefacten (d.w.z. artefacten als gevolg van fouten in V_S), waardoor de update voor ρ in een relatief juiste richting kan plaatsvinden. De geschatte ρ-verdeling van 3D FWI toegepast op horizontale-krachtgegevens correleert goed met de werkelijke verdeling in een gelaagd, near-surface bodemmodel.

Ten slotte testen we de prestaties van 3D FWI op een 3D velddataset die we hebben verworven. We onderzoeken hoe een selectief gebruik van de broncomponent de V_S- en ρ-schattingen uit 3D FWI kan beïnvloeden. We concentreren ons op drie broncomponenten, namelijk verticale kracht en twee kruisgepolariseerde horizontale krachten. FWI toegepast op inline horizontale-component brongegevens slaagt er niet in om een ondergronds model met goede golfvormmatching op te lossen, zelfs niet als de inversie begint met de laagste frequentie die in de gegevens beschikbaar is. Grondige numerieke onderzoeken onthullen dat dit probleem te wijten is aan onjuist gesimuleerde lekkende golven, die uitgesproken zijn in een dataset van specifieke bron-ontvangercomponenten. Op basis van deze bevinding stellen we voor om lekkende-golf-gecontamineerde componenten uit te sluiten van gebruik in FWI. Voor de horizontale-krachtgegevens gebruiken we kruislijn horizontale-component ontvangertracés die gedomineerd worden door SH/Love-golven, terwijl verticale componenttracés alleen worden gebruikt in de FWI van verticale-krachtbrongegevens. De inversietests tonen aan dat FWI van SH/Love-golf gedomineerde gegevens die zijn gegenereerd door kruislijn horizontale-krachtbronnen betere schattingen van zowel V_S als ρ biedt dan FWI van verticale-krachtbrongegevens. Bovendien erkennen we, voor een grotere nauwkeurigheid van de V_S- en ρ-schattingen, het voordeel van het gelijktijdig gebruiken van gegevens van twee kruisgepolariseerde horizontale-krachtbronnen in FWI. Dit gebeurt omdat, in het ge-

val van een dergelijke gezamenlijke FWI, de misfitfunctie een vorm aanneemt die leidt tot een betere convergentie dan wanneer gegevens van een enkele-component horizontale-krachtbron worden gebruikt.

Gedurende deze thesis hebben we aangetoond dat FWI met behulp van horizontale-kracht brongegevens die zijn geregistreerd door een ontvangercomponent waar SH/Love-golven dominant zijn, in staat is om de ρ-verdeling in de ondergrond met goede nauwkeurigheid in zowel 2D als 3D in kaart te brengen. De gegevensselectiestrategie stelt men in staat om ρ uit een seismische dataset te extraheren tegen relatief lage kosten via een op gradienten gebaseerde FWI. De verkregen ρ-variabiliteit in de bodem kan bijdragen aan een verbeterde bodemkarakterisering, zoals het begrijpen van de ruimtelijke verdeling van bodemtypes, bodemverdichting of hardheid, en porositeit/lege verhouding. Succesvol gebruik van FWI zal het mogelijk maken om ρ op een niet-invasieve manier over een groot gebied in kaart te brengen en ook temporele monitoring mogelijk te maken.

Er zijn echter enkele beperkingen die in toekomstig onderzoek moeten worden aangepakt. Ten eerste is ons begrip van de fysische mechanismen achter de voordelen van het gebruik van horizontale-krachtbronnen nog onvolledig. Met name moet de bijdrage van de verschillende golfmodi die in de veldgegevens worden waargenomen nader worden onderzocht. Ten tweede kan de effectiviteit van de voorgestelde strategieën, met name de sequentiële inversieworkflow en het gebruik van virtuele bronnen, afhankelijk zijn van het aangenomen ondergrondmodel. Verdere systematische synthetische studies met verschillende near-surface modellen met uiteenlopende mate van heterogeniteit kunnen helpen om meer algemene richtlijnen vast te stellen voor een nauwkeurige schatting van de ρ-verdeling met behulp van FWI. Ten slotte is er aanvullende informatie in de veldgegevens die in dit onderzoek niet volledig is benut, zoals amplitude-informatie van golfvormen, hogere frequentiecomponenten en negencomponent seismische gegevens voor 3D FWI. Het integreren van deze gegevens in toekomstige inversies kan de haalbare resolutie en nauwkeurigheid van de geschatte ρ-verdeling verder verbeteren.

List of acronyms

Acronyms	Full names
FWI	Full-waveform inversion
GCN	Global correlation norm
FDTD	Finite-difference time-domain
SD	Steepest descent
NCG	Nonlinear conjugate gradient
l-BFGS	limited-memory Broyden-Fletcher-Goldfarb-Shanno
CPT	Cone penetration test
SCPT	Seismic cone penetration test
LMS	Linear-motor-system
MASW	Multichannel analysis of surface waves
MALW	Multichannel analysis of Love waves
SI	Seismic interferometry
S/N	Signal-to-noise ratio
CMP	Common midpoint
CMPCC	Common-midpoint cross-correlation
PTF	Pedotransfer function
OMC	Organic matter content
MCMC	Markov Chain Monte-Carlo
TRM	Time reverse mirror
ED	Experimental design
DAS	Distributed acoustic sensing

1

Introduction

Bulk density (ρ) of soil, defined as the dry mass of soil in a given volume, is an important soil-physical parameter that reflects soil's ability to provide structural support, solute and water movement, and soil aeration. Bulk density is used in physical, chemical and biological assessments of soil quality. It is an indicator of soil compaction. Soil density is controlled by soil texture, porosity, fluid saturation, and the density of the constituents - sand, silt, clay, organic matter, and the fluids in the pores. Bulk density, ρ, is a fundamental property in soil mechanics, as it plays a crucial role in determining the soil behaviour under various loads. It is essential in geotechnical engineering – ρ affects the bearing capacity, stability, and settlement of structures constructed on soil. A good estimation of ρ is important not only to assess soil's structural supportability, but also to understand the hydrological processes and to conduct agricultural investigations, e.g., in forecasting crop productivity in a given field. Density is, therefore, a key parameter to consider for effective utilization of the shallow subsurface in civil, environmental and agricultural engineering projects.

Bulk density of soil is generally quite variable in space, depending on varying mineral/soil types, soil structure/texture, soil moisture content, and presence of organic matter. The variability of ρ is directly or indirectly related to the distribution of porosity and hydraulic conductivity, which – in turn – is controlled by volume and continuity of the pore spaces in the soil structure. These properties are essential to simulate the movement of water/solute in soils and to evaluate the stability of the embankment and the effects of groundwater. Void ratio or relative density also represents the pore-space characteristics, and is commonly used to assess the potential for soil liquefaction due to strong seismic vibrations. The seismic response of the ground is largely influenced by the spatial distribution of the small-strain shear modulus, which is a function of both density and seismic shear-wave velocity.

Bulk density of soil can change significantly also with time. With the growing effects of extreme weather events, this issue has lately become more important. Not only the effects of accelerating climate change, but also those of intensifying human activities triggered by increasing demand for underground space utilization, lead to increased soil vulnerability, such as progressive weakening of soil compaction and soil hardness over time. These result

in destabilization of water-retaining and hydraulic structures including dikes and levees, and formation of voids in the subsurface, eventually causing subsidence and ground collapse. In order to prevent such calamities, temporal monitoring of subsoil density is important.

Although spatial and temporal changes in soil bulk density are widely recognized and known to differ at different scales, capturing such density variability in soil remains still quite challenging.

1.1. Conventional approaches for obtaining subsoil density

There are age-old, established approaches in geotechnical engineering to estimate ρ experimentally. The core and clod methods (VanRemortel & Shields, 1993) are commonly used in civil engineering and agricultural sciences. In the core method, soil samples of a certain volume are collected in the field, which are then dried and weighed, followed by estimation of ρ. In the clod method, a natural soil clod/lump is coated with a water-repellent wax. The volume of the waxed clod and the weighed mass of the dried clod are used to estimate ρ. The main drawback of these methods is that they are generally labor- and time-intensive because of the need to collect undisturbed samples. The characteristics of soils in the field, such as soil types and soil condition, largely determine the reliability of such ρ measurements on soil samples. It is especially challenging to collect undisturbed samples in loose, granular soils such as coarse sand or gravel. Also, it is hard to collect samples in very stiff clays. These difficulties translate to near-impossibility of measuring ρ in many locations at multiple depths, and/or at the same location at different times. It is practically not feasible to infer the spatial or temporal variability of ρ from direct measurement on samples.

There are also indirect methods to measure ρ, e.g., radiation and regression methods. The radiation method makes use of the relationship between ρ and the degree of gamma-ray decay (Lobsey & Viscarra Rossel, 2016). This is a useful technique for continuous measurements of ρ with depth at a given location. The gamma-gamma density logging, which has traditionally been used for oil & gas exploration purpose, is performed along a pre-drilled borehole to obtain the continuous vertical distribution of ρ (Tittman & Wahl, 1965). For unconsolidated soft soils, a nuclear density cone penetrometer can be used to obtain vertically varying ρ without a priori drilling (Tjelta et al., 1985; Shibata et al., 1992; Karthikeyan et al., 2007). The regression method or the so-called pedotransfer functions (PTFs) approach provides ρ estimates from other measured soil properties in a given field, such as soil types, soil structure, pH, and organic-matter content or OMC (Brahim et al., 2012). Both these indirect measurement approaches are time-consuming and costly, while the regression method ideally require site-specific calibration. It is also impractical to obtain the spatial variability of ρ over a wide area in the field by performing such one-dimensional profiling at many locations.

In contrast to these approaches, surface geophysical methods have a distinct advantage as they attempt to capture the spatial variability of ρ and that under in-situ conditions. Since geophysical methods are generally non-invasive and cost-effective, they can be used to cover a relatively large area; they can also be used for temporal monitoring. The microgravity method is particularly suitable for estimating subsurface ρ; by measuring minute changes in the gravitational field of the Earth, one can estimate the subsurface density variations. This

method has long been used to detect low-ρ anomalies indicative of subsurface voids (Yule et al., 1998; Tuckwell et al., 2008), to delineate sharp boundaries between basement rock and overlying soil deposits, and to characterize soil layering (Hayashi et al., 2005; Arisona et al., 2018). While microgravity allows efficient mapping of the distribution of ρ over wide areas, its spatial resolution is inherently limited (Hayashi et al., 2005). Also, microgravity surveys are very sensitive to noise, including microseismic accelerations and lower-frequency noise sources. Electrical resistivity/conductivity measurements also provide insight into ρ at very shallow depths (2–3 m), which are particularly relevant for agricultural and hydrogeological applications (Weihnacht & Börner, 2007; Allred et al., 2008; Franko & Grote, 2013). Seismic velocities (V_P and V_S), which are generally positively correlated with ρ, are also used to indirectly image the ρ structure (Ludwig, 1970; Donohue et al., 2012; Anbazhagan et al., 2016; Romero-Ruiz et al., 2021). However, such empirical approaches result in limited resolution and limited accuracy. Moreover, the relationships among soil properties are generally highly site-specific, calling for availability of a priori site-specific database for a reliable interpretation. Also, recently, muography has emerged as an alternative method for imaging the distribution of ρ in soils (e.g., Baccani et al., 2021). Muons, produced by cosmic ray interactions in the upper atmosphere, experience attenuation depending on the ρ of materials along their path. Although this method offers the possibility of wide-area surveying, its application remains limited due to the requirement of data acquisition in transmission geometry and long acquisition times (Baccani et al., 2021).

In this dissertation, we explore the possibility of extracting lateral variability of ρ from active-source surface-seismic data through special adaptation of the full-waveform inversion approach. We identify several challenges that must be addressed to fully exploit the information contained in the seismic data for accurate estimation of ρ variability.

1.2. Seismic full-waveform inversion (FWI) for subsoil density estimation: benefits and challenges

Surface waves generally constitute the most energetic phase in the seismic data. At greater source-receiver distances the surface wave energy gets significantly attenuated. Near-surface seismic data that are acquired especially in the near-field region are, therefore, dominated by surface waves, viz. Rayleigh or Love waves. The dispersive nature of these surface waves is sensitive mainly to the vertical distribution of the shear-wave velocity (V_S). As a result, various approaches of inversion of the geometrical dispersion curves of surface waves, that aim to interpret the 1D or locally 1D V_S structure, such as multichannel analysis of surface waves (MASW) or multichannel analysis of Love waves (MALW) (Park et al., 1999; Xia et al., 1999, 2012), have so far been widely used. A guideline for practical use of surface wave analyses is presented in Foti et al. (2018).

Non-destructive, near-surface imaging using surface waves has a few distinct advantages. First, the field data acquisition is relatively simple and inexpensive compared to, for instance, the seismic reflection method. This practical reason has contributed to a wider user-acceptance of this method. Also, given the energetic presence of surface waves in the near-surface seismic data, the signal-to-noise ratio is generally high for the surface waves. Secondly, unlike the seismic refraction method, the inversion of phase velocity of dispersive surface waves does not require the seismic wave velocities in the subsurface to increase with

depth, allowing detection of low velocity layers/zones. Thirdly, incorporating the higher modes of the surface waves can improve the resolution, accuracy and stability of the derived near-surface velocity model. Recently, it has been shown that transdimensional Markov Chain Monte-Carlo (MCMC) inversion of surface waves can determine the optimal number of layers, leading to more accurate results (e.g., Aleardi et al., 2020; Rahimi Dalkhani, 2024). It has also been found that if the target depth is less than 1/2 the dominant shear-wave wavelength, the surface-wave imaging using time reverse mirrors (TRMs) migration can theoretically produce even higher resolution (Fu et al., 2018). Last but not least, the surface-wave inversion approach is quite versatile, as it can be applied to various scales.

However, there are also limitations of the surface-wave-dispersion-based approaches. First, the conventional surface-wave imaging methods are mainly sensitive to the V_S structure (depth distribution) in the subsurface, and the sensitivity to V_P and ρ is intrinsically limited. Therefore, if the goal is to obtain the lateral variability of ρ, as it is the case in this research, the inversion of surface-wave dispersion curves alone fails to provide reliable results (Xia et al., 1999; Foti & Strobbia, 2002; L. Pan et al., 2019). Secondly, MASW or MALW usually relies on the assumption of an 1D subsurface model made of a stack of homogeneous elastic layers. When there is strong lateral variability in the subsurface, these methods generally do not give acceptable results. Third, inversion of surface waves is a strongly mixed-determined problem (Foti et al., 2018). This is because near the top surface a detailed and accurate reconstruction of thin layers may be obtained, as typically dense information is available in the high-frequency band (especially if active-source data are used) and the sensitivity of the dispersion curve to model parameters is high. However, the resolution and accuracy drop markedly with increasing depth. Finally, if higher modes are not recognized and accounted for in the inversion, large errors may occur in the estimated velocity profile, especially at greater depths. Higher modes are not always clear in the data, and unambiguous mode interpretation, particularly at lower frequencies, is generally difficult (e.g., Yan et al., 2022).

In the recent decades, there has been a growing interest to use full-waveform inversion (FWI) to capture in detail the lateral variability in the shallow subsoil. FWI is a nonlinear inversion method that estimates multiple seismic parameters simultaneously by fitting synthetic seismic waveforms to the observed waveforms (e.g., Tarantola, 1986; Pratt et al., 1998; Virieux & Operto, 2009). The multiple seismic parameters are V_P, V_S, ρ, Q_P, and Q_S. Q_P and Q_S are P-wave and S-wave quality factor, respectively, which represent the inverse of energy attenuation as the waves propagate in the subsurface. The goals of FWI applied to near-surface seismic data include detailed soil characterization (Tran & McVay, 2012; Kallivokas et al., 2013; Groos et al., 2017), localization of voids and areas of possible subsidence (Tran et al., 2013; Tran & Sperry, 2018; Wang et al., 2019), and archaeological investigations (Köhn et al., 2019; Mecking et al., 2021; J. Liu, Ghose, & Draganov, 2022). There are many examples of successful FWI performed on 2D seismic datasets. More recently, 3D FWI has also become feasible primarily due to the availability of sufficient computational power (Smith et al., 2019; Tran et al., 2019; Teodor et al., 2021; Irnaka et al., 2022; Mirzanejad et al., 2022).

FWI can, in principle, redress the above-mentioned shortcomings of the surface-wave-dispersion-based approaches. It can be used to invert, in addition to V_S, also the ρ distribution, which is the target in the present research. Since FWI uses the complete information contained in seismic wavefields (both phase and amplitude), it enables extracting material

properties at high resolutions. FWI of SH- and Love-waves has recently gained attention due to its sensitivity to both V_S and ρ and the computing advantage over Rayleigh-wave inversion (e.g., Chen & Tran, 2021). Also, unlike surface-wave-dispersion-based approaches, FWI does not assume a 1D subsurface. With proper care, the detailed lateral variability in the subsoil can be imaged through FWI. Finally, supplementing the seismic body-wave reflection information to the full waveform data of the dispersive surface waves helps improving the low wavenumber contents (e.g., Masoni et al., 2014; Zhou et al., 2015; Nuber et al., 2015; Eppinger et al., 2024) and, thereby, achieving improved imaging at greater depths, where use of MASW alone fails to offer sufficient accuracy and resolution.

There are, however, several well-known technical challenges that one needs to overcome, in addition to computational challenges, in order to achieve high-resolution, reliable near-surface imaging using FWI. The main difficulties are the convergence of the misfit function towards local minima because of the limited accuracy of the starting model, the lack of low frequencies causing cycle-skipping problem, the presence of noise, the limited source-receiver offset curtailing the sensitivity of seismic imaging to intermediate depths, uneven sensitivity distribution to different depths due to uneven body- and surface-wave amplitudes, the approximate modelling of the wave-physics complexity, etc. These issues have been subjects of considerable research in the recent decades, many useful references of which can be found in Virieux and Operto (2009), Nuber et al. (2017), Y. Pan et al. (2019), Wang et al. (2025), among others.

In near-surface applications, FWI has mostly been used to image the V_S field. There are relatively few reports on the estimation of the ρ distribution in soils using FWI. This is mainly due to some inherent difficulties in ρ inversion. Several important reasons why capturing the ρ variability in the subsurface using FWI is difficult are as follows:

(1) *Limited sensitivity of the seismic wavefield to ρ and the parameter-coupling problem:* One major difficulty in estimating reliably ρ from near-surface seismic data is due to the relatively low sensitivity of the seismic wavefield to ρ compared to seismic velocities. This is also linked to the well-known parameter-coupling issue, wherein elastic parameters are not independently resolvable, and errors in one parameter (e.g., V_S) propagate into the inversion result of another parameter (e.g., ρ) (Virieux & Operto, 2009). In the context of the nonlinear inverse problem, parameter coupling is related to the shape of the misfit function, characterized by its gradient and Hessian. Numerous studies have investigated the parameter coupling through theoretical analyses of scattering patterns based on the Born approximation (Virieux & Operto, 2009; W. Pan, Geng, & Innanen, 2018; W. Pan et al., 2019), numerical examination of the shape of a misfit function (W. Pan, Geng, & Innanen, 2018; W. Pan et al., 2019), and synthetic inversion tests (Dokter et al., 2017; W. Pan, Geng, & Innanen, 2018; W. Pan et al., 2019; Gao et al., 2021). These works consistently demonstrate that parameter coupling between V_S and ρ can be severe, making it difficult to obtain accurate ρ estimates. Inversion schemes incorporating accurately the inverse of the Hessian (unlike the gradient-based approaches) have lately shown promise in estimating ρ through FWI (Métivier et al., 2013, 2015; Sun et al., 2017; Gao et al., 2021, 2023), but these advanced optimization techniques are generally computationally quite demanding and, as a result, they do not often fit into the budgetary constraints of near-surface geophysical, geoenvironmental and geotechnical site investigations.

(2) *Difficulty in estimating the background density field:* Compared to the distribution

of seismic velocities, the background distribution of ρ is especially difficult to recover using FWI. This is a significant problem in ρ estimation because both body waves and surface waves produce only weak scattering in response to perturbations in ρ over wide apertures (Virieux & Operto, 2009; Operto et al., 2013; W. Pan, Geng, & Innanen, 2018; W. Pan et al., 2019; Gao et al., 2021), leading to poor recovery of the low-wavenumber component, and hence poor background ρ field. A poor model for the background ρ also aggravates the above-mentioned parameter-coupling problem.

(3) *Need of dense source and receiver coupling:* High-resolution V_S and ρ field reconstruction through FWI requires a dense distribution of seismic sources and receivers to avoid spatial aliasing, which otherwise degrades the inversion results. However, deployment of numerous seismic sources leads to logistical challenges, increasing acquisition time and cost.

(4) *Difficulty in obtaining the ground truth:* Independent measurements of the target property is necessary not only to check directly the goodness of the inversion and if necessary to improve it, but also they are useful to build a starting model which can then be used in FWI to capture the lateral variability in the subsurface. For ρ estimation, it has been difficult to obtain the ground truth at multiple depths and locations in the shallow subsoil and validate the FWI result.

1.3. Research goals

In light of the key challenges listed above, the specific goals of the present research are:

(1) to investigate the possibility of mitigation of the parameter coupling through enabling updating of ρ in a preferred direction in the parameter-space, and incorporating a more accurate background ρ model;

(2) to explore if aliasing-free seismic data, reconstructed through enhanced spatial sampling in the source domain via seismic interferometry, can help extracting more accurate and higher-resolution ρ field through FWI;

(3) to examine systematically how choosing correctly the force direction of the seismic source can contribute to reduction of parameter coupling and increase of ρ-sensitivity, and thereby leading to greater accuracy, resolution and robustness to noise of ρ estimation through FWI;

(4) to inquire into the possibility of obtaining through FWI more reliable and finer ρ-variability in 3D by choosing proper combination of the force directions for the seismic source; and

(5) to test the FWI results using ground truth, i.e., independent measurements of V_S and ρ, and their variability in the near-surface soil.

The overarching goal is to improve on the technical and economic feasibility and the reliability of estimation of in-situ ρ and its variability in soil through judicious application of FWI.

1.4. Thesis outline

In Chapters 2 and 3 of this thesis, we address, in the context of 2D FWI, the above-mentioned research goals (1) and (2), respectively. The results of our research on goals (3) and (4) are presented in Chapters 4 and 5, respectively, where 3D FWI is tested. Independent

ground-truthing data are rigorously used in the research presented in Chapters 2, 3 and 5. Following is a brief outline of the contents of each chapter.

In Chapter 2, we look into 2D FWI of Love-wave-dominated field data at a soft-soil site to image spatial variability of ρ. This chapter primarily focuses on addressing the parameter-coupling issue. We develop a sequential inversion workflow for FWI based on how the parameter-coupling occurs in theory. The goal is to reduce the parameter coupling and, thereby, to improve the accuracy of the ρ estimates. The proposed workflow is validated by comparing with a conventional simultaneous inversion. The results are checked using independent field measurements of ρ. We also explore how different initial V_S models affect the degree of parameter coupling.

Chapter 3 addresses the issue of limited seismic source density, which negatively affects the resolution and accuracy of the estimated ρ distribution through FWI. While a dense seismic source spacing improves the performance, it dramatically increases the acquisition cost. We develop in this research a new approach that integrates seismic interferometry (SI) with FWI. This enables performing FWI without severe spatial aliasing effects. In this method, SI retrieves surface waves at each receiver position from active surface-wave records, and then these two datasets are combined to be used as input data in FWI. To avoid the deterioration of the FWI result due to erroneous full waveforms of the virtual shot data, a matched filter is used to correct the amplitude/phase error in the retrieved data, and a weighted misfit function is introduced. We apply our proposed method to 2D field data dominated by Love waves.

In Chapter 4, we shift our focus to 3D FWI, and investigate how the choice of the force-direction of a seismic source can contribute to successful FWI for ρ imaging. We evaluate three indicators for FWI performance: noise robustness, parameter coupling, and resolution. Given a typical near-surface model, we numerically examine the scattered wavefield and the shape of the misfit function (its gradient and Hessian) for the different force-direction sources.

Chapter 5 presents results of FWI performed on 3 different source components - vertical force and two cross-polarized horizontal force sources. The FWI-derived V_S and ρ models are validated against independent ground-truthing data from the field. We discover a critical issue with inline horizontal-force source data: the waveform misfit remains high even when starting the inversion with the lowest frequency band available in the field data. We perform in-depth numerical investigations and come up with a data-selection strategy that leads to reliable FWI results. In this chapter, we also discuss the potential benefits of simultaneous use of two cross-polarized horizontal-force datasets in 3D FWI.

In Chapter 6, we summarize the key findings of this dissertation and provide recommendations for future work.

2

Imaging subsoil density variability: specific considerations in 2D FWI

Bulk density (ρ) of soil is controlled by soil type, stiffness, and the degree of water saturation. The spatially heterogeneous distribution of the subsoil ρ is of great importance in hydrology, geotechnical engineering, and agriculture. Seismic FWI is a promising method to obtain a high-resolution ρ image without conducting geotechnical measurements at many points. However, accurate ρ estimates are difficult to obtain by FWI mainly due to the well-known parameter-coupling issue: an error in a certain parameter class (e.g., V_S) is mapped into the other parameter class (e.g., ρ). Additionally, the background ρ distribution cannot be easily reconstructed because of the specific pattern of the scattered wavefield due to a ρ perturbation. In this chapter, we explore an FWI strategy to solve these issues in practice using a 2D SH/Love seismic dataset acquired in the field. To mitigate the severe parameter coupling, we build a sequential inversion workflow to update ρ in the relatively correct direction. The comparison with the conventional simultaneous inversion shows that the estimated ρ is dramatically improved by employing our inversion workflow. The proposed workflow also improves the waveform fitting. Another remedy to the parameter-coupling problem is to reduce the error in the initial V_S, which is a source of parameter coupling. To achieve that, we build an 1D V_S model from SCPT and a 2D V_S model obtained from MALW, and then investigate how the different initial V_S models affect the ρ estimates. The approach is tested at a field location. In this specific site, SCPT provides much more accurate V_S distribution than MALW, resulting in a relatively accurate ρ structure from FWI. In order to incorporate the background ρ distribution into the inversion, we derive a reliable initial ρ model from the density logging performed on the seismic line. A comparison with the case of using homogeneous ρ for the initial model shows that the density-log-derived initial ρ greatly contributes to the accurate reconstruction of ρ up to 15 m depth. The variability obtained

A part of this chapter is published in conference proceedings (Kawasaki et al. (2025)).

in the distribution of ρ is consistent with that obtained from independent geotechnical measurements, including ρ and V_S, soil type, and cone penetration tests (CPT). Our results demonstrate that FWI applied to SH/Love-wave seismic data, in combination with a density log at only one calibration point, can capture with reasonable accuracy the spatial variability of subsoil density, without the need of geotechnical tests at multiple locations.

2.1. Introduction

The subsoil ρ generally exhibits variability in both vertical and lateral directions. The spatially variable density distribution is of great importance in assessing the structural support, understanding the hydrological processes, and for natural hazard assessments. Density value is beneficial for soil characterization like obtaining the distribution of soil type, soil hardness, and the degree of water saturation. Subsoil density is also closely related to other crucial soil properties in geotechnical engineering, agriculture, and hydrogeology: porosity/void ratio, hydraulic conductivity and small-strain shear modulus.

The subsoil density is conventionally measured by laboratory experiments performed on an undisturbed soil sample collected from a given point, or by radiation and regression methods using the gamma-ray, for example from a density logging performed in a borehole. Both of these approaches are time-consuming and expensive. Also, it is generally not easy to collect undisturbed soil sample from multiple depths for accurate measurement of the density changes. From an economic point of view, the existing approaches are often not feasible for application at multiple locations in a given field. Consequently, inferring the spatial variability of density in soil remains quite challenging.

In recent years, the distribution of subsoil density has been obtained from FWI applied to SH/Love wave seismic data that are independent of the compressional-wave velocity (V_P) (Dokter et al., 2017; Wittkamp et al., 2018; Chen et al., 2021; Chen & Tran, 2021; Mecking et al., 2021). SH FWI is capable of simultaneously reconstructing multiple parameters, namely the shear-wave velocity (V_S), density (ρ), and seismic attenuation (Q_S), by fitting the synthetic seismic data with the observed seismic data. The estimation of accurate ρ from FWI, however, remains a daunting task. The main difficulty in estimating ρ is attributed to the well-known parameter-coupling issue: error contained in a certain parameter class is mapped into the other parameter class. Previous research involving numerical studies has demonstrated that strong parameter coupling occurs especially between V_S and ρ (W. Pan, Geng, & Innanen, 2018), resulting in erroneous ρ estimates.

Several approaches of FWI have been proposed to mitigate the parameter-coupling effect and to simultaneously retrieve multiple parameters with high accuracy. For example, the optimization approach that incorporates the accurate Hessian inverse into the inversion (e.g., truncated-Newton method) is a powerful tool to obtain high-resolution subsurface images without suffering from the severe coupling issue (Métivier et al., 2015; Yang et al., 2016; Sun et al., 2017; Gao et al., 2021, 2023). However, this sophisticated optimization method requires huge computation resources to solve iteratively Newton's equation using the second-order adjoint-state method (Métivier et al., 2013). This is computationally prohibitive for the typical near-surface applications with limited available funding. Another idea is to avoid the severe parameter-coupling effect by adopting a sequential inversion workflow that is specially designed for the multi-parameter inversion. Earlier research has demonstrated, on both synthetic and field data, that this approach is superior over the

conventional simultaneous inversion in terms of accurate ρ estimation (Jeong et al., 2012; Prieux et al., 2013; Ren & Liu, 2016); however, these studies have mostly been focused on body-wave-dominated wavefields. How the sequential inversion workflow can be effective on the surface-wave-dominated near-surface seismic data still needs to be investigated.

In FWI, compared to the background distribution of seismic velocities (V_P and V_S), the background distribution of ρ is generally difficult to be recovered satisfactorily. This problem is attributed to the fact that due to a ρ perturbation the seismic wavefields are not scattered with a wide aperture, making it difficult to resolve the large wavelengths of the ρ structure (Virieux & Operto, 2009). Sun et al. (2017) applied a truncated Newton method to a synthetic dataset in order to mitigate the parameter-coupling effect for accurate ρ estimation. However, such an approach has not helped to reconstruct well the background ρ distribution. To overcome this difficulty in practice, either the low-wavenumber content of ρ should be sufficiently present in the initial model, or a joint inversion scheme utilizing additional independent data (e.g., gravity data) should be used (Sun et al., 2017).

In this chapter, we apply FWI to 2D SH/Love seismic data acquired in the field, in order to investigate what is necessary for improving the accuracy of the ρ estimates. To tackle the parameter-coupling problem, we construct a new sequential inversion workflow based on how the parameter coupling occurs in theory (e.g., W. Pan, Geng, & Innanen, 2018; W. Pan et al., 2019; Kawasaki et al., 2024). The effectiveness of our workflow is verified through a comparison with the conventional simultaneous inversion workflow, in terms of the accuracy of ρ estimates and the finally obtained misfit value. We also investigate how an initial V_S model needs to be accurate in order to mitigate further the parameter-coupling effect, by comparing between the use of the initial V_S models derived from SCPT data and initial V_S models obtained from the inversion of Love-wave dispersion (MALW). To incorporate the background ρ distribution into FWI, we use a good initial ρ model obtained from density logging performed in a borehole. We examine the need of a good initial model by comparing with the case when a constant ρ value is assumed initially for the whole model. An in-depth evaluation of the FWI results is carried out based on independently measured V_S from SCPTs and ρ from density logs and laboratory experiments conducted at multiple locations along the seismic line. This research aims to demonstrate on field data that the spatial variability of the ρ distribution in soil can indeed be obtained through a dedicated FWI of the seismic SH/Love wave data, and that performing expensive soil-physical measurements in boreholes at many locations in the field is not necessary to capture the density variability.

2.2. METHODOLOGY

We first review briefly the theory of 2D SH FWI which is adapted in this research. Then, we provide the details on investigating the FWI strategy to address the two major issues introduced in Section 2.1, namely the parameter-coupling effect and the background ρ distribution.

2.2.1. 2D SH FWI

FWI is a nonlinear inversion process to obtain an optimum subsurface model by minimizing the misfit function E which measures the difference between the synthetic and observed seismic waveforms. In this study, we use the global correlation norm (GCN) for the misfit

function defined as follows (Choi & Alkhalifah, 2012):

$$E = -\sum_{i=1}^{ns}\sum_{j=1}^{nr}\left[\frac{u_{ij}^{\text{syn}}\, u_{ij}^{\text{obs}}}{\left\|u_{ij}^{\text{syn}}\right\|\left\|u_{ij}^{\text{obs}}\right\|}\right], \tag{2.1}$$

where u^{syn} is the synthetic seismic (displacement) data calculated for a given model m (V_S and ρ, in this study) and u^{obs} is the observed seismic data. ns and nr represent the number of shots and receivers, respectively. Note that the misfit function does not include explicit regularization terms. Instead, the inversion stability is ensured by applying several preconditioning filters to the gradient of the misfit function, as often done in FWI studies (e.g., Dokter et al., 2017; Köhn et al., 2019). These include wavefield-energy-based preconditioning to compensate for uneven illumination, circular tapers around source locations, and Gaussian smoothing to suppress small-scale artifacts below the resolution limit. These filters provide implicit regularization and help stabilize the inversion. The details of the adopted filters are given in Section 2.3.5. Here we consider the visco-elastic SH/Love wavefield to simulate u^{syn} through a finite-difference time-domain (FDTD) method (Virieux, 1984). Viscoelatic damping is implemented considering a generalized standard linear solid with one relaxation mechanism (e.g., Bohlen, 2002).

The GCN focuses on phase matching (rather than amplitude matching) by maximizing the cross-correlation of the normalized synthetic and observed waveforms (see eq. 2.1). This may reduce the sensitivity to ρ variations, as the subsurface ρ primarily influences seismic amplitudes (Płonka et al., 2016). Nevertheless, we choose the GCN here, instead of the conventional square of l_2 norm, to address the strong anelastic attenuation in soil that is observed in field data ($Q_S \sim 5$, see Section 2.3.4). The amplitude of the seismic waveform propagating in such a highly attenuating medium drops rapidly with the increase of the source-receiver offset, making it difficult to use effectively the small-amplitude, far-offset data in the inversion. The GCN allows both near- and far-offset data to contribute to the inversion regardless of their amplitudes, thereby improving the robustness of the inversion. This phase-focused misfit function also weakens the distortion of the FWI result due to insufficient 3D to 2D correction of the geometrical spreading effects (Forbriger et al., 2014; Schäfer et al., 2014; J. Liu, Ghose, & Draganov, 2022; J. Liu, Draganov, & Ghose, 2022), and the receiver coupling effect varying at receiver positions (Dokter et al., 2017; Köhn et al., 2019). Although the use of the square of the l_2 norm could potentially improve the accuracy of ρ estimation by incorporating amplitude information, it would require more accurate attenuation modelling and/or incorporation of attenuation parameters into the FWI.

Since FWI is a nonlinear large-scale optimization problem, the misfit function E is typically minimized by iteratively updating the model m through a local optimization approach based on the following equation:

$$m_{n+1} = m_n + \alpha_n \Delta m_n, \tag{2.2}$$

where m_n is the model parameter at the nth iteration, Δm_n is the descent direction of the misfit function E, and α_n is the step-length which is estimated by a line-search method (Nocedal & Wright, 2006). In a line-search method, each iteration computes the search direction Δm_n and then decides how far to move along that direction. In this study, to calculate Δm_n we employ a gradient-based approach such as steepest descent (SD),

or nonlinear conjugate gradient (NCG), or limited-memory Broyden-Fletcher-Goldfarb-Shanno (l-BFGS). The simplest of these approaches, SD, is based on the following formula:

$$\Delta m_n = -P \nabla_m E_n, \tag{2.3}$$

where $\nabla_m E_n$ is the gradient of the misfit function with respect to a given model parameter m, and P is a preconditioning filter. NCG and l-BFGS also use the same formula at the first iteration, but after that Δm_n is calculated using the gradient at the current iteration and the previous history of $\nabla_m E_n$. In this research, we adopt the NCG method (Nocedal & Wright, 2006) to calculate Δm_n in the time domain to make the convergence speed faster. Δm_n is normalized by the maximum value of each parameter class, and then scaled by the representative value of each model parameter. This allows using the same step-length α_n for all parameter classes to simultaneously update multiple parameters.

We do not use a Newton-based method, which incorporates the accurate Hessian inverse into the inversion (e.g., truncated-Newton method), although it is a powerful tool to significantly reduce the parameter coupling. This choice is made apprehending a high computational cost for a Newton-based method. In the approach implemented here, two forward simulations are required per nonlinear iteration to compute the gradient. In contrast, the truncated-Newton method requires solving Newton's equation iteratively using the second-order adjoint method. In total, this involves $2 + 2N_{\text{iter}}$ forward simulations per nonlinear iteration, where N_{iter} is the number of inner iterations required by the second-order adjoint method (Métivier et al., 2013). Assuming an averaged value of $N_{\text{iter}} = 5$ as in Métivier et al. (2013), the truncated-Newton method would require approximately twelve forward simulations per nonlinear iteration. This corresponds to roughly six times more forward simulations per iteration compared to the gradient-based method. We, therefore, adopt the conventional NCG approach to keep the computational time for FWI manageable.

2.2.2. INVERSION WORKFLOW ADDRESSING PARAMETER COUPLING

The conventional multi-parameter FWI inverts for several model parameters simultaneously. The simultaneous inversion generally suffers from the coupling among different parameters. To mitigate the severe parameter coupling in multi-parameter FWI, we build the inversion workflow based on how the parameter coupling occurs in theory. Parameter coupling originates from parameter ambiguity inherent in multi-parameter inversion problems, reflecting similar radiation patterns of the scattered wavefields for different model parameters (e.g., Virieux & Operto, 2009; Operto et al., 2013; W. Pan, Geng, & Innanen, 2018). This makes it difficult to determine uniquely which parameter perturbation is responsible for the misfit between the observed and the simulated waveforms. In the gradient-based simultaneous inversion, this ambiguity manifests itself as the transfer of imaging errors between different parameters. In the case of SH FWI, for example, errors in V_S contaminates the gradient for ρ, resulting in erroneous updates of ρ.

When the misfit function is assumed to be a quadratic function of m (i.e., the model m is sufficiently close to an optimum solution m^{opt}), the gradient $\nabla_m E$ with respect to each model parameter class (m: V_S and ρ, in this study) is written based on the Newton's equation in the matrix form:

$$-\begin{bmatrix} \nabla_{V_S} E \\ \nabla_{\rho} E \end{bmatrix} = \begin{bmatrix} H_{V_S V_S} & H_{V_S \rho} \\ H_{\rho V_S} & H_{\rho\rho} \end{bmatrix} \begin{bmatrix} \Delta {V_S}^N \\ \Delta \rho^N \end{bmatrix}, \tag{2.4}$$

where $H_{m_i m_j}$ is the multi-parameter Hessian of the misfit function E (m_i, m_j: V_S and ρ), and Δm^N is the model-update direction toward an optimum solution (i.e., Newton step). In eq. 2.4, the diagonal elements of the Hessian matrix (i.e., $H_{V_S V_S}$ and $H_{\rho\rho}$) are the coefficients for the Newton step, while its off-diagonal elements (i.e., $H_{V_S\rho}$ and $H_{\rho V_S}$) represent the coefficients for the inter-parameter trade-off. Here, we focus on the gradient with respect to ρ as follows:

$$-\nabla_\rho E = H_{\rho V_S} \Delta {V_S}^N + H_{\rho\rho} \Delta \rho^N. \tag{2.5}$$

The second term on the right-hand side of eq. 2.5 is required to update ρ in the correct direction, while the first term on the right-hand side of eq. 2.5 controls how errors in V_S (i.e., $\Delta {V_S}^N$) is mapped into $-\nabla_\rho E$. Since the model is updated along $-\nabla_\rho E$ in the framework of the gradient-based inversion, ρ can be updated in the incorrect direction due to $\Delta {V_S}^N$; this is indeed the parameter-coupling effect considered in this study. In order to avoid the parameter coupling, one needs the less contaminated gradient for ρ by minimizing the V_S error, $\Delta {V_S}^N$.

Similar to the gradient for ρ, $-\nabla_{V_S} E$ is also contaminated by error in ρ (i.e., $\Delta \rho^N$). However, this contamination is not significant as demonstrated in previous synthetic studies, in case the initial V_S and ρ models are not too far off the truth (Dokter et al., 2017; W. Pan, Geng, & Innanen, 2018; Kawasaki et al., 2024). Based on this observation, we build a new sequential inversion workflow that makes use of the difference in the degree of the parameter-coupling effect on V_S and ρ (Fig. 2.1). The workflow first inverts for V_S and ρ simultaneously as in a typical multi-parameter inversion. This results in a relatively accurate V_S model without severe parameter coupling, but in an erroneous ρ owing to the error contained in the initial V_S model. The updated V_S model is kept for the subsequent stage, and the erroneous ρ after the first stage is dropped. In the second stage, we perform the simultaneous inversion again starting with the updated V_S in the first stage and the very initial ρ. This two-step strategy is expected to reduce the dominance of the coupling term (i.e., the first term on the right-hand side of eq. 2.5) in $\nabla_\rho E$ by increasing the accuracy of the initial V_S model for the second stage, thereby enabling the update of ρ in a relatively more correct direction than in the first stage.

There are earlier-proposed sequential workflows that are built on similar concepts as ours (e.g., Jeong et al., 2012; Prieux et al., 2013; Ren & Liu, 2016). However, they mostly focus on seismic body waves and are tested in oil and gas exploration scale. Near-surface seismic data, on the other hand, are typically dominated by the surface waves. Therefore, in this research, we examine how the adaptation of a sequential inversion workflow can contribute to the success of ρ estimation in the scale of near-surface seismic studies to image the unconsolidated soils up to ~15 m depth. The efficacy of our workflow is evaluated in Subsection 2.4.1 by investigating the accuracy of ρ estimates and the finally obtained misfit value compared to conventional simultaneous inversion workflows (i.e., only the first stage of our workflow).

2.2.3. Initial model building strategy

In FWI, a good initial model is needed to avoid falling into the local minima due to the well-known cycle-skipping issue. In this subsection, we discuss briefly the reasons why good initial V_S and ρ models are required for estimating an accurate ρ model in the end.

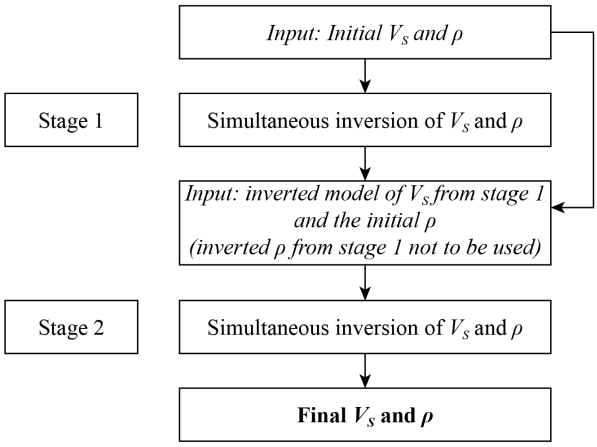

Figure 2.1: Sequential inversion workflow.

As explained in Subsection 2.2.2, starting the inversion with a good initial V_S model is important to mitigate the strong parameter-coupling effect on ρ estimates due to errors in V_S ($\Delta {V_S}^N$ in eq. 2.5). Our sequential inversion workflow (see Section 2.2.2) is expected to reduce the risk of an inferior estimation of ρ due to the parameter-coupling problem. However, to reduce further the parameter-coupling effect, the initial V_S model needs to be good, such that $\Delta {V_S}^N$ is small.

The need of a good initial model for ρ is to be considered also from a different perspective: the initial model of ρ should contain sufficient background ρ information for the success of the FWI. Earlier research on synthetic data has shown that the scattered wavefields due to a ρ perturbation propagate mainly in the backward direction (with a small aperture and hence little back-scattered energy at larger angles), leading to a lack of the low-wavenumber contents of ρ in the wavefields (Virieux & Operto, 2009; W. Pan, Geng, & Innanen, 2018; Kawasaki et al., 2024). This makes it difficult to retrieve the background ρ model through FWI.

In Subsection 2.4.2, we investigate on field data how different initial V_S and ρ models having different accuracies affect the estimated ρ model. We first focus on how the ρ estimates differ due to two different initial V_S models: an 1D initial V_S model derived from an SCPT conducted on the seismic line, and a 2D initial V_S model obtained by MALW (e.g., Xia et al., 2012) applied to the observed Love wave data. Next, as a good initial ρ model, we use the 1D ρ model derived from a highly smoothed version of the density log obtained in a borehole located on the seismic line; we assume that this model contains sufficient information on the low-wavenumber component of the ρ distribution. We discuss why the density log is needed to build the initial model for a reasonably accurate reconstruction of the ρ field through FWI, by comparing with the results of FWI performed with a starting homogeneous ρ model. The performance of FWI with different initial V_S and ρ models is evaluated through examination of both the ρ estimates and the final misfit values.

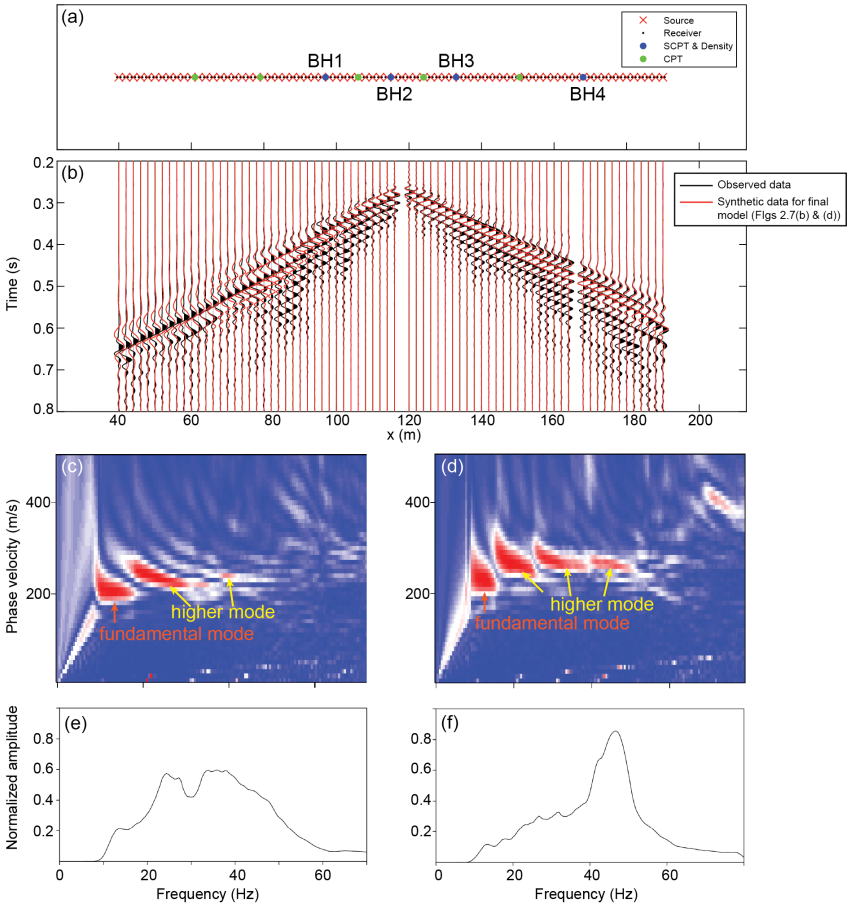

Figure 2.2: (a) Acquisition geometry for 2D seismic survey and geotechnical (SCPT and density) measurements. (b) An example of a filtered (10–80 Hz) shot gather with source at $x = 118$ m. For visualization, each trace is normalized individually by the maximum amplitude in that trace. (c) Love-wave dispersion image calculated from this shot gather for $x < 118$ m in (b), and (d) for $x > 118$ m in (b). (e) Amplitude spectrum of the shot gather for $x < 118$ m in (b), and (f) same as (e) but for $x > 118$ m

2.3. Field data application: data acquisition and preprocessing

We acquire a 2D SH/Love seismic dataset at a soft soil site in the northern part of the Netherlands to investigate how FWI captures the spatially varying ρ using different FWI strategies. At this site, for an independent evaluation of the FWI results, V_S and ρ are also measured by SCPT, density logging and laboratory tests carried out on soil samples collected in boreholes located on the seismic line. This section presents a detailed description of the seismic and geotechnical data acquisition, and data preprocessing for FWI.

2.3.1. Data acquisition

2D SH/Love seismic data are acquired along a 600-m-long line. Since we need to perform FWI multiple times for a good comparison of different FWI strategies (see Section 2.2), to keep the computation time short, we restrict our analysis to a seismic line length of 150 m only (Fig. 2.2(a)) and up to a depth of 15 m. The locations of the independent geotechnical measurements are shown in Fig. 2.2(a). Geotechnical laboratory and field tests are performed by the company Fugro. In the seismic survey, to generate SH-waves we use an electrical linear-motor-driven shear-wave vibrator which was developed by the company Seismic Mechatronics in collaboration with TU Delft (Noorlandt et al., 2015; Brodic et al., 2021). The frequency band for the linear sweep is 8–250 Hz, the sweep length is 20 s. The vertical (source) stack count is 4. The fixed receiver array consists of 152 3-component geophone nodes with a natural frequency of 5 Hz, planted at 1 m spacing along the seismic line. The source is moved along the seismic line at 2 m spacing. We cross-correlate the raw vibrograms for each shot with a pilot (reference) trace. 76 common-source (shot) gathers are used in our research. The maximum frequency used in FWI is restricted to 80 Hz, to keep the computation time manageable.

Fig. 2.2(b) shows a typical shot gather. The dispersive Love waves dominate the observed wavefield, while the body waves (i.e., direct wave, refracted wave, and reflected wave) are not distinct in the band-limited data between 10 and 80 Hz. To further characterize the dispersive Love waves, we calculate the dispersion images of Love waves. This is illustrated for a shot gather (Fig. 2.2(b)) with the source located at $x = 118$ m, separately for the left-side ($x < 118$ m) and the right-side ($x > 118$ m) of the shot gather (Figs 2.2(c) and (d), respectively). The higher modes are visible in the dispersion images at frequencies exceeding 15 Hz. The left and right sides of the shot gather exhibit different dispersion patterns for the higher modes, suggesting lateral heterogeneity in the subsurface. Note that the fundamental mode is primarily present at the low frequencies (< 15 Hz), and the amplitude at this frequency range is much smaller than that of the higher-frequency higher modes (see Figs 2.2(e) and(f)). This makes it difficult to identify the fundamental mode clearly in the time domain. Most of the events observed in Fig. 2.2(b) are, therefore, dominated by the higher modes rather than the fundamental mode. The fundamental mode is more clearly identified in the dispersion images (Figs 2.2(c) and (d)). The remaining differences (see on the left side of the shot gather in Fig. 2.2(b)) between the observed data and the synthetic data for the final FWI model is due to the remaining discrepancy in reconstructing a part of the higher modes. This can be noticed in Figs 2.2(c) and (d), and will be explained further in Fig. 2.14

In Fig. 2.3 we show an example of the results of geotechnical tests performed on the 2D seismic line (in this case, at the centre of the line, i.e., in borehole BH2 as shown in Fig. 2.2(a)). Fugro's geotechnical tests consist of CPTs, SCPTs to estimate V_S as a function of depth, and the ρ measurements from both density logging performed in boreholes and laboratory experiments on soil samples collected in the same boreholes (see Fig. 2.2(a)). The density logging is carried out in boreholes BH1 and BH2, while laboratory tests are done on soil samples collected at certain depths in all 4 boreholes shown in Fig. 2.2(a) — BH1–BH4. It has been possible to collect undisturbed soil samples at these depths in the boreholes.

In Figs 2.3(b) and (c) we illustrate also the initial models that are built for the FWI

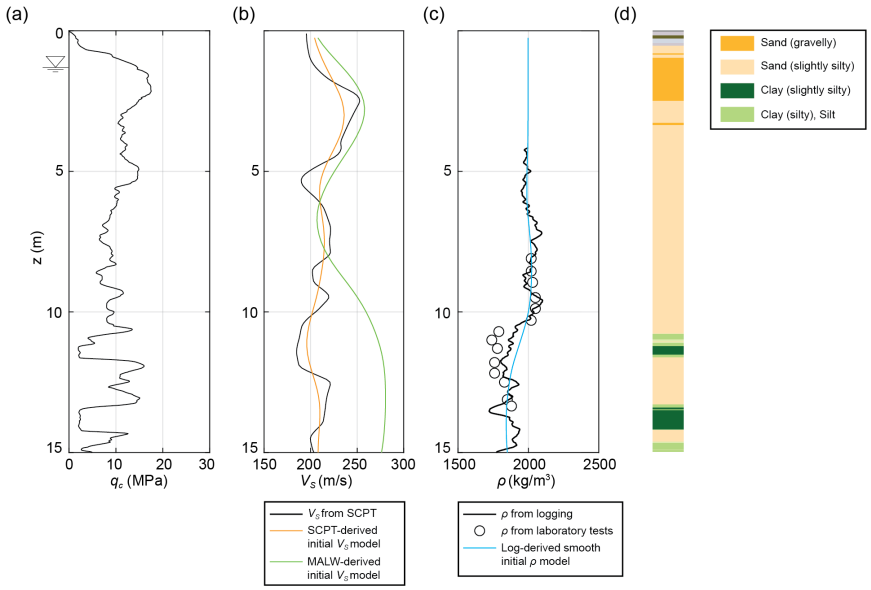

Figure 2.3: Independent geotechnical measurements done in borehole BH2 (see 2.2(a)). (a) Cone-tip resistance q_c from CPT. (b) V_S derived from SCPT, and two different initial models of V_S for the FWI. (c) ρ from density logging and from the laboratory tests on soil samples, and the initial model of ρ for the FWI. (d) Soil type estimated from CPT (Robertson, 1990).

(see Section 2.3.3 for details). The shallowest part of the soil column is composed of sand with high V_S and ρ, while below ~ 10 m depth, there are alternating layers of clay and sand having generally low V_S and ρ. Based on laboratory soil tests, the difference in V_S and ρ between the shallow and the deep sand layers is due to the difference in grain size – relatively coarse-grained sand is present at the very shallow part, while at greater depths the sand is relatively fine. The specific soil structure at this site, particularly the high-velocity layer at the shallow depth excites significant higher-mode surface waves that are visible in the dispersion images (Figs 2.2(c)-(d)). The groundwater table at this site, as known from multiple boreholes, is located at ~ 1.3 m depth, allowing us to assume full water saturation in soils below 1.3 m. Therefore, the observed variability of ρ, as illustrated in Fig. 2.3(c), mainly reflects changes in porosity in different soil types. The goal of the FWI here is to capture the spatially variable ρ structure which, in turn, should offer information on the distribution of the soil type and the porosity.

2.3.2. Data preprocessing for the FWI

It is necessary to preprocess the raw field-seismic data before FWI can be successfully performed. The acquired point-source data contain the effect of geometrical spreading in 3D, while the forward simulation in 2D FWI assumes line-source data with 2D geometrical spreading. Therefore, the observed 3D effects need to be transformed into 2D wavefields. We first apply the 3D to 2D point-to-line source correction by convolving the observed records with $\sqrt{t^{-1}}$, where t is the recording time (Forbriger et al., 2014; Schäfer et al.,

2014). To transform 3D to 2D geometrical spreading, we follow the hybrid transformation proposed by Forbriger et al. (2014) and Schäfer et al. (2014), and tested by many others more recently (e.g., J. Liu, Ghose, & Draganov, 2022; J. Liu, Draganov, & Ghose, 2022). The traces at relatively small offsets (< 5 m in our case) are scaled by $\sqrt{2r v_{ph}}$, where r is the source-receiver offset and v_{ph} is the phase velocity. This scaling factor is gradually shifted by applying a $\sqrt{t^{-1}}$ time-domain taper, and is finally replaced by $r\sqrt{2}$ at the large offsets (> 10 m in our case). We assume v_{ph} = 200 m/s based on the dispersion image (see Figs 2.2(c)-(d)). Also, the traces from receivers which are located within 1 m distance from the source are killed because signals in such near-offsets are generally clipped (Y. Pan et al., 2019). We additionally kill the traces with low signal-to-noise ratio (S/N) to make the inversion stable. Finally, we apply a time delay (0.25 s) to the data so that the estimated source-time function is not leaked to the acausal part.

2.3.3. Building of initial models for the FWI

As explained in Section 2.2.3, we construct two different initial models for V_S and ρ, and investigate their impact on the FWI results. A depth-dependent (1D) V_S model is obtained by smoothing the SCPT-derived V_S profile at the centre of the seismic line (BH2) (orange line in Fig. 2.3(b) and 2D image in Fig. 2.4(a)). This serves as one of the two tested initial V_S models for FWI. A second initial V_S model is built by applying MALW to the dispersive Love waves present in the observed data (see Fig. 2.3(b) and Fig. 2.4(b)). We adopt the CMPCC (common-midpoint cross-correlation) method to calculate the dispersion image, avoiding strong distortions due to lateral heterogeneity (Hayashi & Suzuki, 2004). This is followed by picking the dispersion curves at common midpoints (CMPs) at an interval of 2 m. To build the initial model for MALW, we apply the empirical 1/3 wavelength transformation to the dispersion curves (Hayashi, 2008). In the inversion, the multimodal dispersions in the observed data are used, following the approach of Hayashi (2012); the inversion minimizes the difference between observed and synthetic phase velocities that have the maximum relative amplitude among all modes at each frequency. Finally, we obtain the 2D V_S model by applying spatial smoothing to the pseudo-2D V_S models obtained from MALW (Fig. 2.4(b)). This model serves as the second initial model for FWI. The MALW-derived V_S model at BH2 matches well with the SCPT-derived V_S till ~ 8 m depth (see green and orange lines in Fig. 2.3(b)). These two initial V_S models have different spatial distribution of accuracy; the SCPT-derived initial V_S is 1D and hence does not contain any lateral variations, while the MALW-derived initial V_S model is laterally varying and it differs from the SCPT-derived V_S model below ~ 8 m depth. We focus on the difference in the derived ρ distribution due to the two different initial V_S models.

Next, to construct a good initial model of ρ for FWI, we apply smoothing to the density log from a borehole located at the center of the seismic line (BH2). Since the density log could not measure well the ρ values at the very shallow (shallower than 4 m) depths due to the local soil condition, we assume ρ = 2000 kg/m^3 as a realistic value for the shallowest depths, considering also the fact that the sand layer just below 4 m depth is known to have a density value of 2000 kg/m^3 (see Fig. 2.3(c)). This is justified also because a thick sand layer with high q_c and V_S is known to be present here from 1 to 5 m depth (see Figs 2.3(a)-(b)). The density-log-derived initial ρ is shown in Fig. 2.3(c) (light blue line) and Fig. 2.4(c) (2D image). Additionally, we use a homogeneous ρ model with a constant ρ

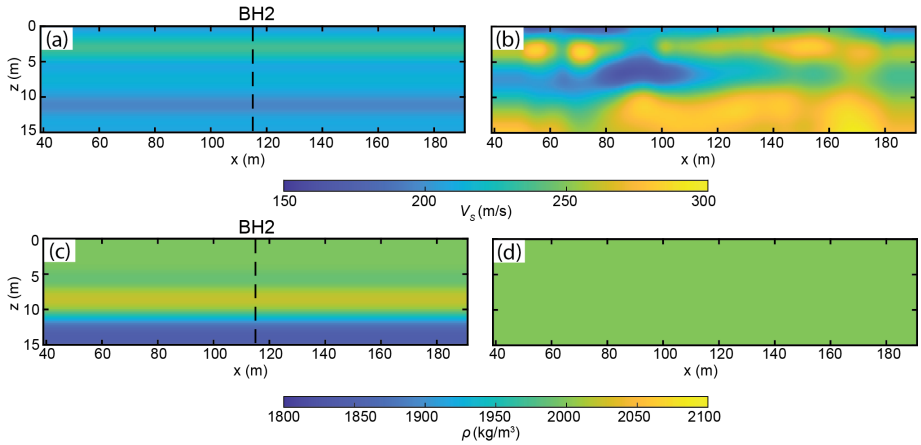

Figure 2.4: Initial models of V_S and ρ for FWI for ρ inversion. (a) Initial 1D V_S model derived by smoothing the V_S profile from the SCPT at BH2. (b) Initial V_S model derived from MALW applied to field seismic (Love wave) data. (c) Initial ρ model from the density log at BH2. (d) Initial homogeneous ρ model.

value of 2000 kg/m^3 as the second initial model for ρ for FWI (see Fig. 2.4(d)).

2.3.4. Estimating optimum Q_S for the FWI

Anelastic attenuation in soil must be carefully taken into consideration in order to obtain reliable FWI results (Groos et al., 2014). Gao et al. (2020) demonstrated on synthetic data that use of an inaccurate attenuation value produces much more artifacts in the inverted ρ image than in the inverted V_S image. In this research, we assume a constant Q_S value for the entire model space. An optimum value for Q_S is derived following two different approaches.

First, we use the approach of Groos et al. (2014), where the Q_S value that offers the minimum misfit between the observed and the synthetic data is derived through a grid search. To do this, we use the highly smoothed version of the SCPT-derived V_S (Fig. 2.4(a)) and the density log-derived ρ (Fig. 2.4(c)) as the initial models. The source-time function is estimated by a stabilized deconvolution, considering an initial model (Groos et al., 2014). Since the anelastic attenuation mainly affects the waveform amplitude rather than the phase information, the square of the l_2 norm misfit function is used for Q_S estimation. The traces within a source-receiver offset range of 40 m are used in the grid search, assuming their amplitudes are less influenced by the 3D structure, compared to traces at greater offsets. The grid search finally provides an optimum Q_S value of 5 that corresponds to the minimum misfit value (Fig. 2.5(a)).

In order to validate the estimated Q_S from the grid search, we roughly calculate a constant value for Q_S by making use of the amplitude information of Love waves (e.g., Xia et al., 2013). Assuming the observed Love wave to be a plane wave propagating in a homogeneous medium, the quality factor of Love wave Q_L is determined based on the following equation (Johnston & Toksöz, 1981):

$$Q_L = \frac{\pi f}{\alpha_L v_L}, \tag{2.6}$$

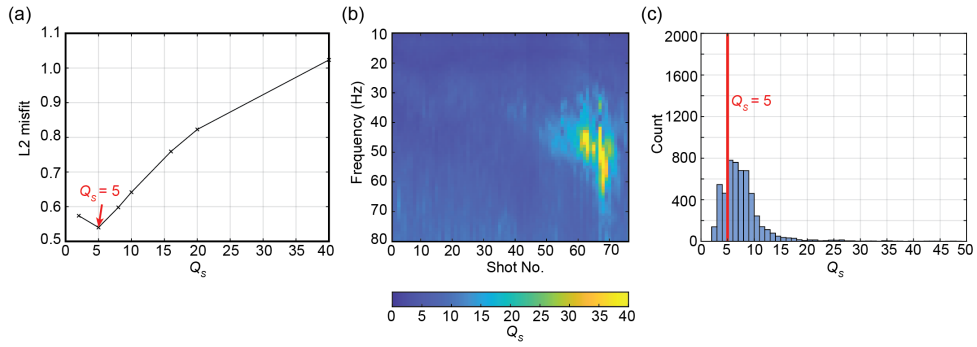

Figure 2.5: Estimation of an optimum value for Q_S. (a) Grid search. (b) Estimated Q_S from a linear fit for each shot and each frequency. (c) Histogram of the estimated Q_S shown in (b).

where α_L represents the attenuation coefficient of Love wave, v_L is the Love wave velocity, and f is the frequency. α_L is calculated using $U(x+dx) = U(x)e^{-\alpha dx}$, where U is Love wave amplitude, x is the nearest source-receiver offset, and dx is the receiver interval (Kudo & Shima, 1970). The offset for the calculation of α_L is restricted to 40 m, similar to the grid search. v_L is assumed to be 200 m/s based on the dispersion images (Figs 2.2(c)-(d)). We assume that the Q_L value calculated from eq. 2.6 roughly represents the Q_S value in a homogeneous medium. The estimated Q_S value for each shot record and frequency generally varies between 3 and 10 (Fig. 2.5(b)) with a peak at Q_S = 5–6 (see Fig. 2.5(c)), which is consistent with the estimated Q_S value from the grid search (Fig. 2.5(a)). Accordingly, we consider Q_S = 5 as an optimum value for the attenuation parameter to be used in FWI.

To examine further the goodness of the chosen Q_S value, we compare the synthetic waveforms with the observed waveforms, without any amplitude scaling (Fig 2.6). The observed seismic amplitudes decay rapidly with increasing source–receiver offset, which is reproduced in the synthetic data for Q_S = 5 (compare between Figs 2.6(a) and (c)).

2.3.5. FWI PARAMETER SETTINGS

In FWI, we perform multi-parameter inversion to obtain both V_S and ρ, while Q_S is considered fixed (same value for the entire model space). The inversion starts with the low-frequency band of 10–15 Hz to avoid falling into the local minima due to cycle-skipping. The maximum frequency for the inversion is then gradually increased to 25 Hz, 40 Hz, 50 Hz, 60 Hz, 70 Hz, and 80 Hz in the framework of the multi-scale inversion (Bunks et al., 1995). In order to further reduce the nonlinearity, we start the inversion with data at short source-receiver offset (< 40 m) for the first frequency stage (10–15 Hz) only, and then the maximum offset is increased to 90 m for the subsequent inversion. The new workflow of sequential inversion designed to reduce the parameter-coupling effect, as discussed in Section 2.2 (Fig. 2.1), is applied to each frequency stage. The iteration at each frequency stage is stopped when the relative change between the misfit of the current iteration step and that of the second to the last iteration step is less than 1%. We estimate the source-time function using the near-offset data (< 6.5 m) at the first iteration of each frequency stage, and then it is fixed during the same frequency stage. For the preconditioning, we apply circular tapers

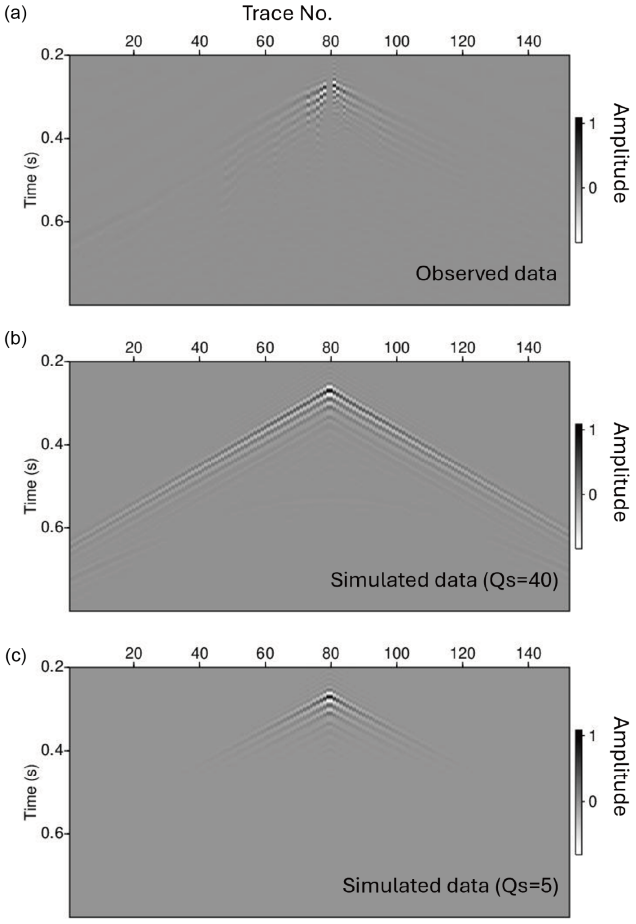

Figure 2.6: Validating the chosen Q_S value. (a) Observed data. (b) Synthetic data with Q_S=40. (c) Synthetic data with Q_S=5.

to the gradient around the source locations. A preconditioning filter based on the wavefield energy (Zhang et al., 2012) is also applied to the gradient in order to make the convergence faster. Finally, a Gaussian filter with the length of half the dominant wavelength is applied for damping small-scale artifacts below the FWI resolution limit (Ravaut et al., 2004).

2.4. Field data application: investigating FWI strategies

We investigate the impact of the adopted FWI strategy (i.e., inversion workflow and initial model) on the estimated ρ distribution. The accuracy of the ρ estimates obtained by FWI is evaluated based on an in-depth comparison with the measured ρ by density logging and the laboratory estimates of ρ on soil samples from boreholes BH1–BH4 (Fig. 2.2(a)).

2.4.1. Effect of the used inversion workflow

In this subsection, we discuss results regarding how the new sequential inversion workflow (Fig. 2.1) contributes to the accuracy of the estimated ρ compared to the conventional simultaneous inversion workflow of FWI. In both workflows, we use the same initial models, that is the smoothed version of the SCPT-derived V_S profile and the smoothed version of the log-derived ρ (Figs 2.4(a) and (c), respectively). This allows us to concentrate on the sole impact of the two different workflows on the FWI result.

After the convergence, both workflows result in similar V_S images (see Figs 2.7(a) and (b)), with only slight difference in the resolution. The V_S values in the vertical direction approximately corresponds to the results of geotechnical (SCPT) measurements; high V_S for sand at the shallow part and low V_S for the alternating layer of clay and sand at the deeper part (see Fig. 2.3). However, unlike V_S, the inverted ρ models differ dramatically depending on the employed FWI workflow, as shown in Figs 2.7(c) and (d). The colour scale is same for Figs 2.7(c) and (d). The conventional simultaneous inversion workflow produces unrealistic ρ values ($\rho_{\text{min}} \sim 800$ kg/m^3, $\rho_{\text{max}} \sim 2500$ kg/m^3, see Fig. 2.7(e)). Given the fact that the soil at this site (made of sand and clay) below ~ 1.3 m depth is fully water-saturated (Fig. 2.3(a)), the inverted ρ values are indeed unrealistic. Furthermore, these inverted ρ values are very different from the measured ρ values in the laboratory on soil samples (sand: $\sim$ 2000 kg/m^3, clay: $\sim$ 1800 kg/m^3, see Fig. 2.3(c) and Fig. 2.7(e)). Our proposed sequential inversion workflow (Fig. 2.1), however, provides much better ρ estimates (Fig. 2.7(d)); the ρ estimates ($\rho_{\text{min}} \sim 1750$ kg/m^3, $\rho_{\text{max}} \sim 2100$ kg/m^3) are within the range of the measured ρ values in the field (logging) and in the laboratory (see Fig. 2.7(f)).

We compare the data misfit, after the convergence in FWI, to investigate how the synthetic waveforms fit with the observed waveforms (Fig. 2.8). The proposed sequential inversion reaches a lower misfit (-0.69) value compared to the conventional simultaneous inversion (-0.67). The new sequential inversion possibly prevents the distortion of the ρ estimates that occur due to the severe parameter coupling, as discussed in Subsection 2.2.2.

Our results demonstrate that it is important to minimize the parameter-coupling effect for the success of the ρ reconstruction through FWI, and that, for this purpose, the proposed sequential inversion workflow is beneficial.

2.4.2. Effect of the used initial models

We investigate the impact of the different initial V_S and ρ models on the inverted ρ. We first compare the estimated ρ from FWI between the MALW-derived 2D V_S as the initial model (Fig. 2.4(b)) and the smoothed version of the SCPT-derived 1D V_S as the initial model (Fig. 2.4(a)). The smoothed version of the density log-derived 1D ρ (Fig. 2.4(c)) is used as the initial ρ model in both these cases. The workflow for this investigation is shown in Fig. 2.9. The results are shown in Figs 2.7 and 2.10. The overall characteristics and resolution of inverted V_S and ρ are similar between FWI with the MALW-derived initial V_S (Figs 2.10(a) and (b)) and FWI with SCPT-derived initial V_S (Figs 2.7(b) and (d)). However, we notice in both inverted V_S and ρ images blocky structures (see black circles in Figs 2.10(a) and (b)) when the MALW-derived 2D V_S field is used as the initial model. Such blocky structures are not anticipated in our test site based on independent information. These structures do not appear when the smoothed version of the SCPT-derived velocity profile is used as the initial V_S model. The laterally varying accuracy in the 2D V_S field derived from MALW

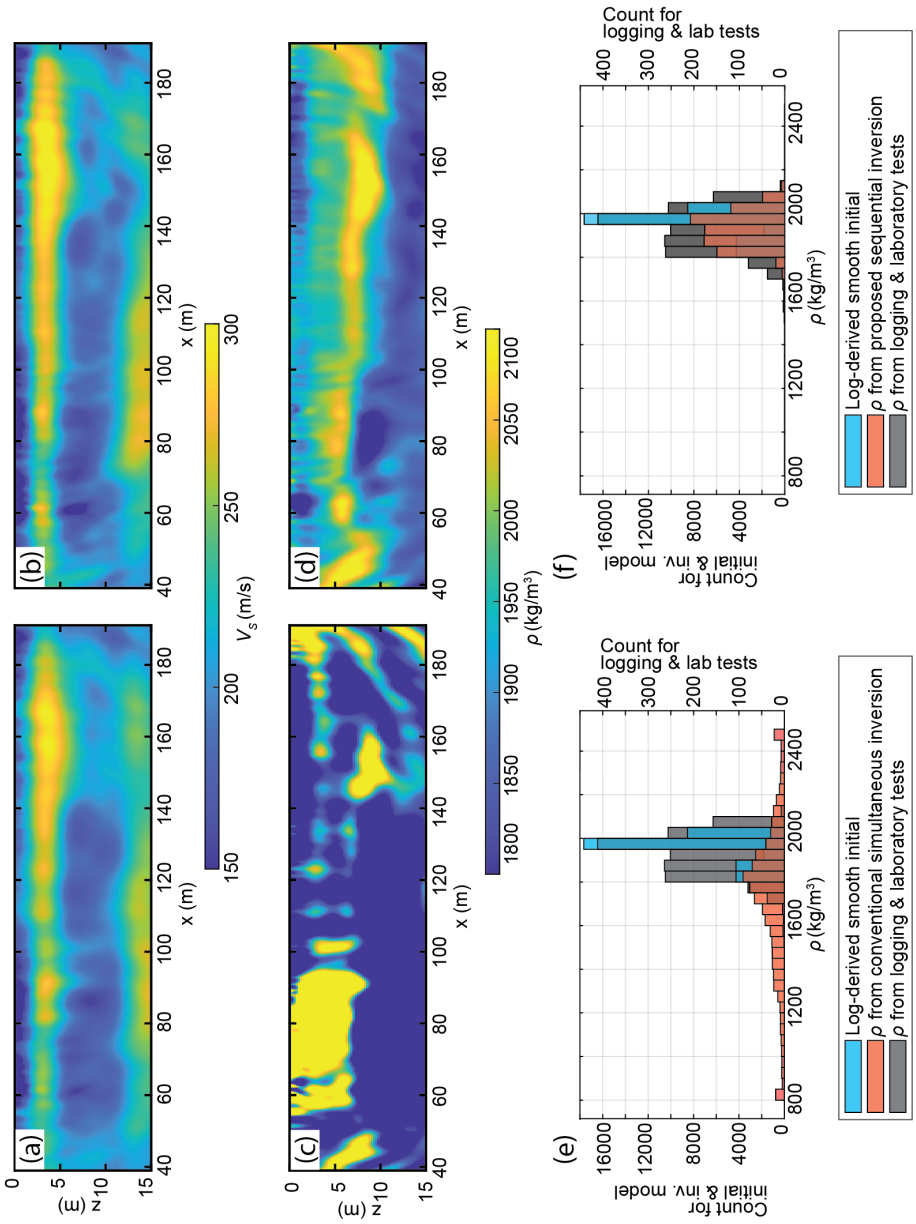

Figure 2.7: Comparison of results for two different FWI workflows. (a) Inverted V_S from the conventional simultaneous inversion workflow. (b) Inverted V_S from the new sequential inversion workflow proposed in this research (Fig. 2.1). (c) Inverted ρ from the conventional simultaneous inversion workflow. (d) Inverted ρ from the new sequential inversion workflow. (e) Comparison of the histogram of ρ estimates from the conventional simultaneous inversion workflow with the histogram of the initial ρ model derived from smoothing density logging at BH2, and the histogram of the ρ values from logging and laboratory tests. (f) Same comparison as (e), but for the proposed sequential inversion workflow.

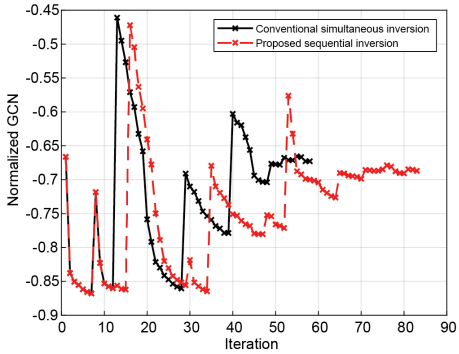

Figure 2.8: Comparison of the data misfit evolution for the two FWI workflows (the conventional simultaneous inversion and the new sequential inversion) . Normalized GCN = -0.67 for the conventional simultaneous inversion, while normalized GCN = -0.69 for the proposed sequential inversion after the convergence. Note that the misfit increases as higher-frequency data are incorporated into the inversion, because the model is still not sufficiently accurate to reproduce the corresponding shorter-wavelength seismic waveforms.

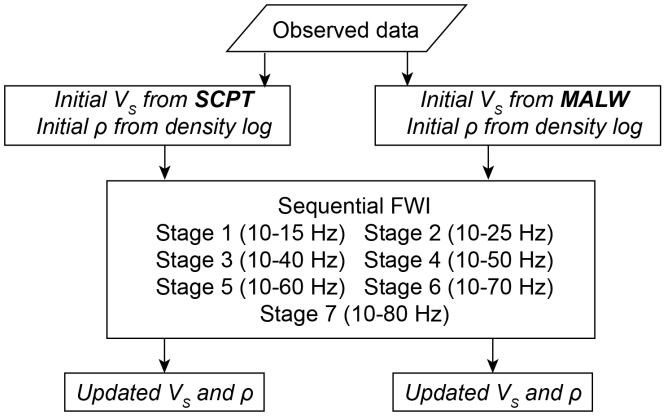

Figure 2.9: Workflow for investigating the effect of the used initial V_S on FWI.

might produce such structures: it is likely that MALW has provided relatively inaccurate V_S models at locations where blocky structures appear in the inversion result. The blocky structures are not present in the MALW-derived initial V_S, but are produced during FWI. This could happen as FWI attempts to reduce the waveform differences that are caused by errors in the initial V_S.

To evaluate more critically the accuracy of the ρ estimates from FWI for different initial models, we use independent measurements made at different locations on our seismic line. In Figs 2.10(c)-(f) the estimated value of density from the laboratory tests made on collected soil samples are plotted at 4 borehole locations — BH1–BH4. Also, the density logs at BH1 and BH2 are shown. Note that, at BH1, the density logging did not succeed to measure continuously the density values due to the influence of the borehole casing joints: these disturbed data points are removed from the log (see Fig. 2.10(c)). The density logs

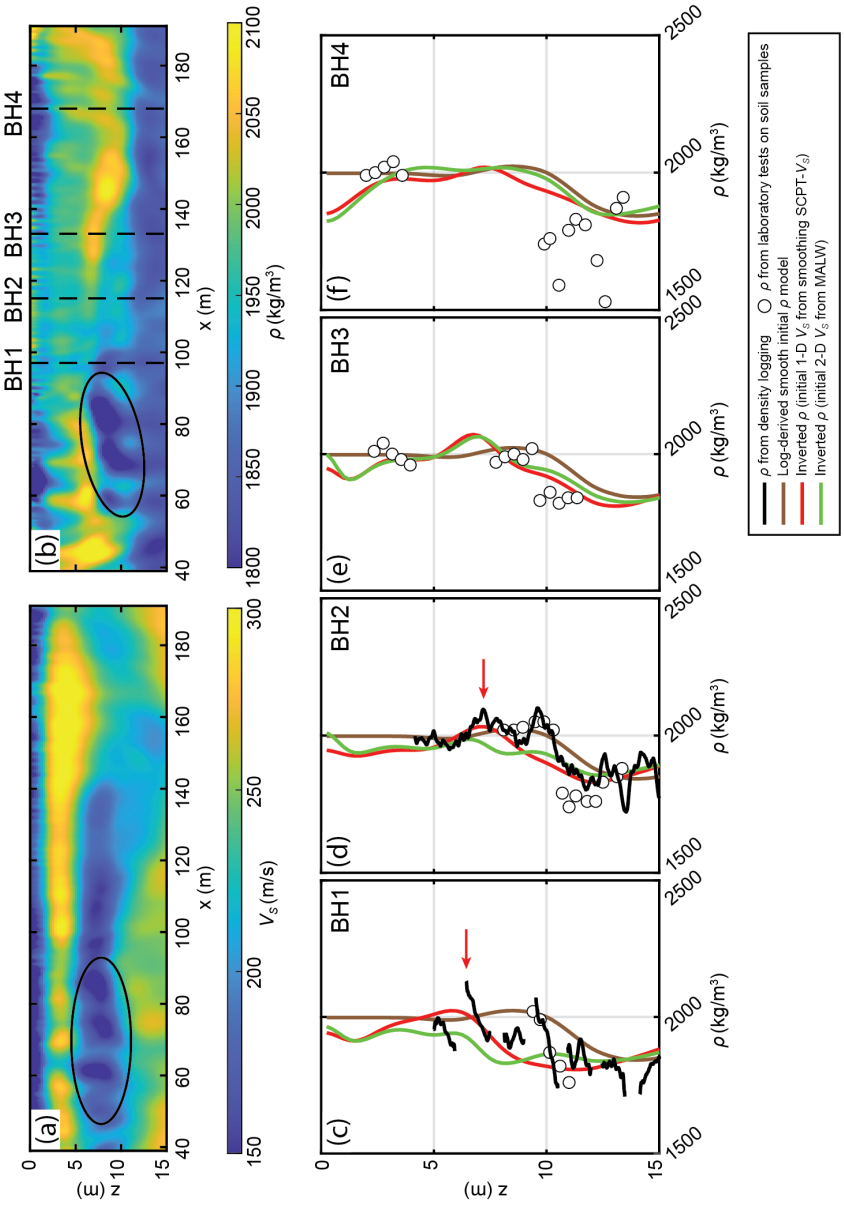

Figure 2.10: FWI results using the smoothed version of the MALW-derived 2D V_S field as the initial model. (a) Inverted V_S. (b) Inverted ρ. (c)-(f) Checking the ρ estimates from FWI using independent density measurements (density logging and laboratory estimates made on soil samples). Note that, at BH1, the density logging could not continuously measure accurate density values due to the influence of the casing joints; removal of these disturbed data points is responsible for the discontinuous nature seen here.

clearly show the existence of a thin layer with high ρ value at around 7–8 m depth (see red arrows in Figs 2.10(c) and (d)). This is correctly captured by FWI only when the smoothed version of the SCPT-derived V_S is used for the initial model (red lines in Figs 2.10(c) and (d)). Assuming that the SCPT-V_S represents the true distribution of V_S, MALW has not constrained the low V_S existing at depths greater than 10 m depth (see green line in Fig. 2.3(b)), which is consistently observed at other SCPT points too (BH1, BH3, BH4). Thus, for this test site, SCPT provides a more accurate and useful initial V_S model than MALW. This SCPT-derived initial V_S allows us to minimize the parameter-coupling effect. This results in a less erroneous estimate of ρ through FWI, even though both inversions start with the same initial ρ. Since the accuracy of the MALW-V_S is site-specific, the SCPT-V_S may not always be necessary. However, in soft soil sites, one SCPT performed on the seismic line for building a good initial V_S model might be a good option in order to successfully estimate ρ by FWI.

Next, we examine the estimated ρ from FWI when the initial ρ value is either constant (Fig. 2.4(d)) or it is the smoothed version of the ρ profile obtained by density logging (Fig. 2.4(c)). For this experiment, the initial V_S model is fixed to the smoothed version of the SCPT-derived V_S profile (Fig. 2.4(a)). Fig. 2.11 shows the workflow for this investigation. The results are illustrated in Fig. 2.12. Clearly, the estimated ρ by FWI is more erroneous when a constant value of ρ is used for the initial ρ model. For the two different initial ρ models and the same initial V_S, we obtain almost identical image of the inverted V_S from FWI (see Fig. 2.7(b) and Fig. 2.12(a)). This indicates that the parameter-coupling effect due to errors in ρ is not severe, which has been also demonstrated in the past synthetic research (Dokter et al., 2017; W. Pan, Geng, & Innanen, 2018; Kawasaki et al., 2024). This effect is also much less than the parameter-coupling effect on the ρ estimates due to errors in V_S (see Fig. 2.10), which could be due to the greater sensitivity of the surface-wave dominated seismic data to V_S than to ρ (e.g., Kawasaki et al., 2022). The FWI starting with different initial ρ models resolves similar ρ structure at depths shallower than 10 m. For example, the anomaly with low ρ at $x \sim 80$ m and that with high ρ at $x \sim 150$ m is clear in both inversion results (see Fig. 2.7(d) and the black arrows in Fig. 2.12(b)). However, those soft soils having a low ρ occurring at depths greater than 10 m, which are clearly recognisable in the density logs and in the laboratory density-measurement results (see the low ρ values at depths of 10 m and deeper in Fig. 2.3(c)), is not reconstructed well by the FWI starting with a homogeneous initial ρ model (see the light blue lines and the red arrows in Figs 2.12(c)-(f)). Such depth-dependent differences in the accuracy of ρ estimates could be attributed to the spatially varying accuracy of the initial ρ model. The assumed constant ρ value (= 2000 kg/m^3) for the initial model represents the trend of the true ρ above 10 m depth, while it is too far from the mean ρ value ($\sim$ 1750 kg/m^3) below 10 m depth (see brown dashed line in Figs 2.12(c)-(f)). This suggests that the initial ρ model needs to contain sufficient background ρ information in order to estimate accurately ρ values from FWI. In this regard, a density log, as used here, is a promising tool to build such a good initial model.

Finally, we investigate the final data misfit in FWI for different initial V_S and ρ models (Fig. 2.13). We first examine the difference in the misfit due to the different initial V_S models (see red and green lines in Fig. 2.13). The FWI using the MALW-derived 2D initial V_S converges with a slightly higher misfit value (-0.68) compared to that using the

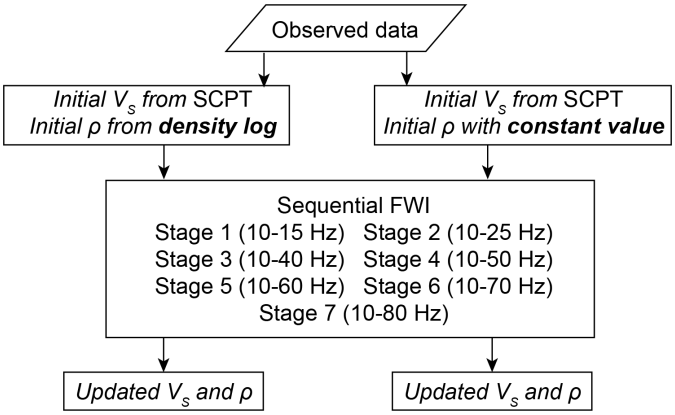

Figure 2.11: Workflow for investigating the effect of the used initial ρ on FWI.

smoothed version of the SCPT-derived 1D initial V_S (-0.69). Besides, the misfit value at the very first iteration for the MALW-derived initial V_S (-0.60) is much worse than that for the SCPT-derived initial V_S (-0.67): the SCPT-derived initial V_S provides synthetic data that are more in agreement with the measured data. This suggests that the SCPT-derived initial V_S does allow the inversion to start at a point which is much closer to the optimum solution, compared to the MALW-derived initial V_S. Starting the inversion at a point close to the optimum solution is obviously much more desirable in FWI. For two different initial ρ models, the density log-derived initial ρ produces much better waveform fitting between the observed and the synthetic data than the homogeneous (constant value) initial ρ model (compare the red and blue lines in Fig. 2.13). In Fig. 2.2(b), we have seen an example of the comparison of the observed waveforms with the synthetic waveforms for the best case, i.e., when using the smoothed version of the SCPT-derived initial V_S model and the density log-derived initial ρ model. To check how the dispersive Love waves match after the convergence, we calculate the dispersion image for the synthetic waveforms (Fig. 2.14). A comparison with the measured dispersion image (Figs 2.2(c)-(d)) shows that the fundamental mode (< 15 Hz) is well reconstructed. In contrast, there are remaining discrepancies in a part of the higher modes, corresponding to the unmatched waveforms at late time in Fig. 2.2(b).

The results in this section indicate that, compared to V_S, ρ being a much more difficult parameter to estimate, the initial models of V_S and ρ based on independent geotechnical measurements might be of great value in order to achieve acceptable accuracy in the spatially varying ρ image, with a good fit between the observed and the synthetic seismic waveforms.

2.5. Discussion

2.5.1. Spatially varying density structure estimated from FWI

In Section 2.4, the comparisons of different FWI workflows have demonstrated that, starting with smooth versions of the SCPT-derived 1D V_S model and density-log-derived 1D ρ model, our proposed scheme of sequential inversion applied to SH/Love-wave data can

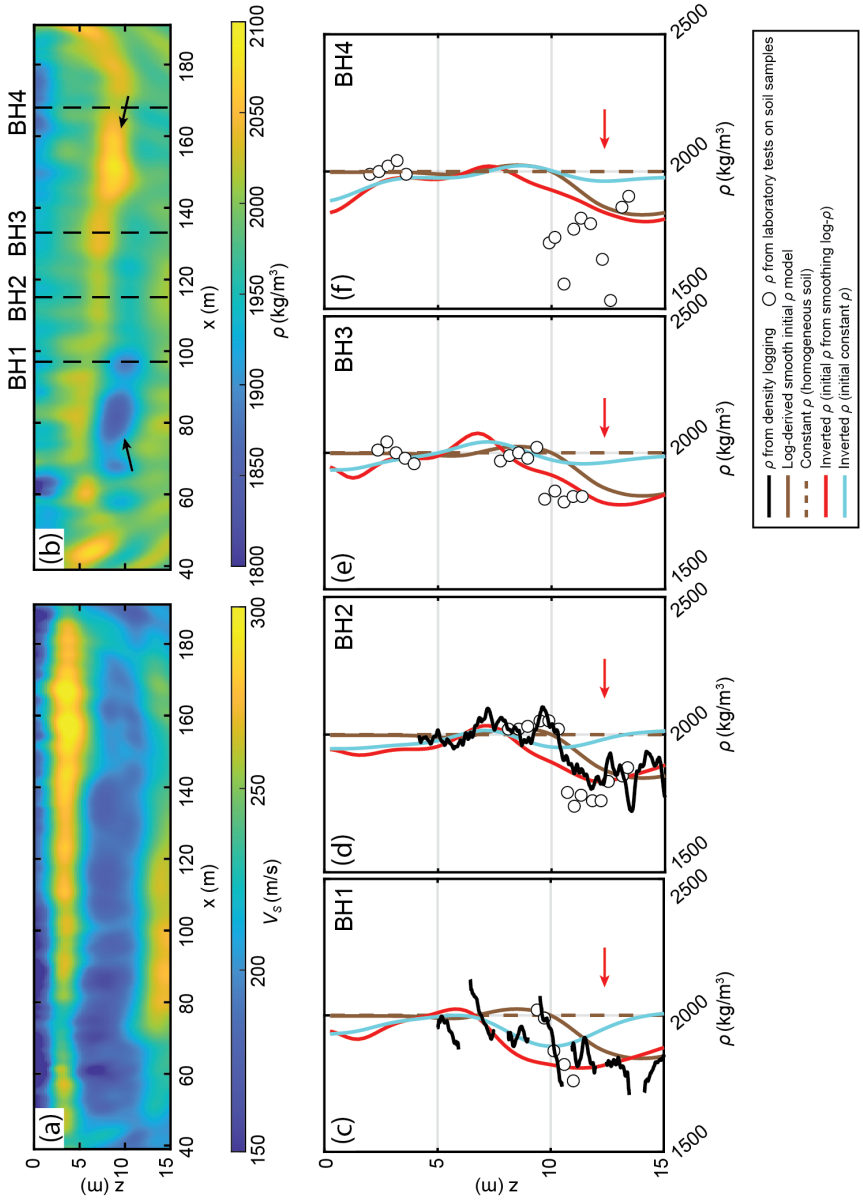

Figure 2.12: FWI results using a homogeneous initial ρ model. (a) Inverted V_S. (b) Inverted ρ. (c)-(f) Checking the ρ estimates from FWI using independent density measurements (density logging and laboratory estimates on soil samples). Note that, at BH1, the density logging could not continuously measure accurate density values due to the influence of the borehole casing joints: the data disturbed due to this problem are removed from the log.

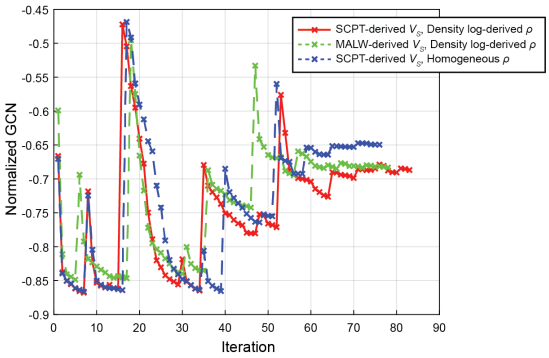

Figure 2.13: Comparison of data-misfit evolution for different initial model-building strategies. Note that the misfit increases as higher-frequency data are incorporated into the inversion, because the model is still not sufficiently accurate to reproduce the corresponding shorter-wavelength seismic waveforms.

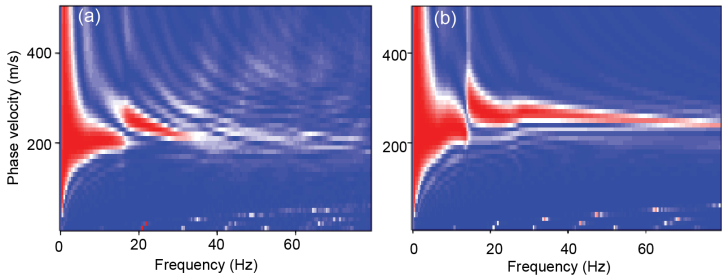

Figure 2.14: Love-wave dispersion images calculated from the synthetic data for the final model to compare the observed dispersion images shown in Figs 2.2(c)-(d).

capture the spatially varying distribution of the ρ in soils. In this subsection, we look again into the obtained ρ image from the FWI along with a closer check of the independent geotechnical data: the ρ measurements (Fig. 2.15(a)), the soil classification from the CPTs based on Robertson (1990) (Fig. 2.15(b)), the V_S from SCPTs and FWI (Fig. 2.15(c)), and the pseudo-2D section of the cone tip resistance q_c constructed by interpolating all CPTs performed on our seismic line as shown in Fig. 2.2(a) (see Fig. 2.15(d)).

The image of ρ in soil obtained from FWI is mainly characterized by a sharp transition from a high ρ to a low ρ at around 10 m depth — which is laterally continuous (Figs 2.15(a) and (b)). This sharp change in ρ corresponds to the boundary between sand and the alternating layers of clay and sand from the soil classification (see red arrows in Fig. 2.15(b)). This transition depth in the FWI result matches well with the ρ measurements in boreholes BH1–BH4 (see red arrows in Fig. 2.15(a)). Both FWI and geotechnical ρ measurements show low ρ values in the sand layer below $\sim$ 10 m depth (see Fig. 2.15(a)), reflecting a difference in grain size; sand at the deeper part is finer than that in the shallower part, which is confirmed in soil sampling made in the boreholes. This could indirectly result in a relatively larger porosity at the deeper part, which in turn offers lower ρ. In theory, porosity is not controlled by the grain size, as the inter-grain space is determined

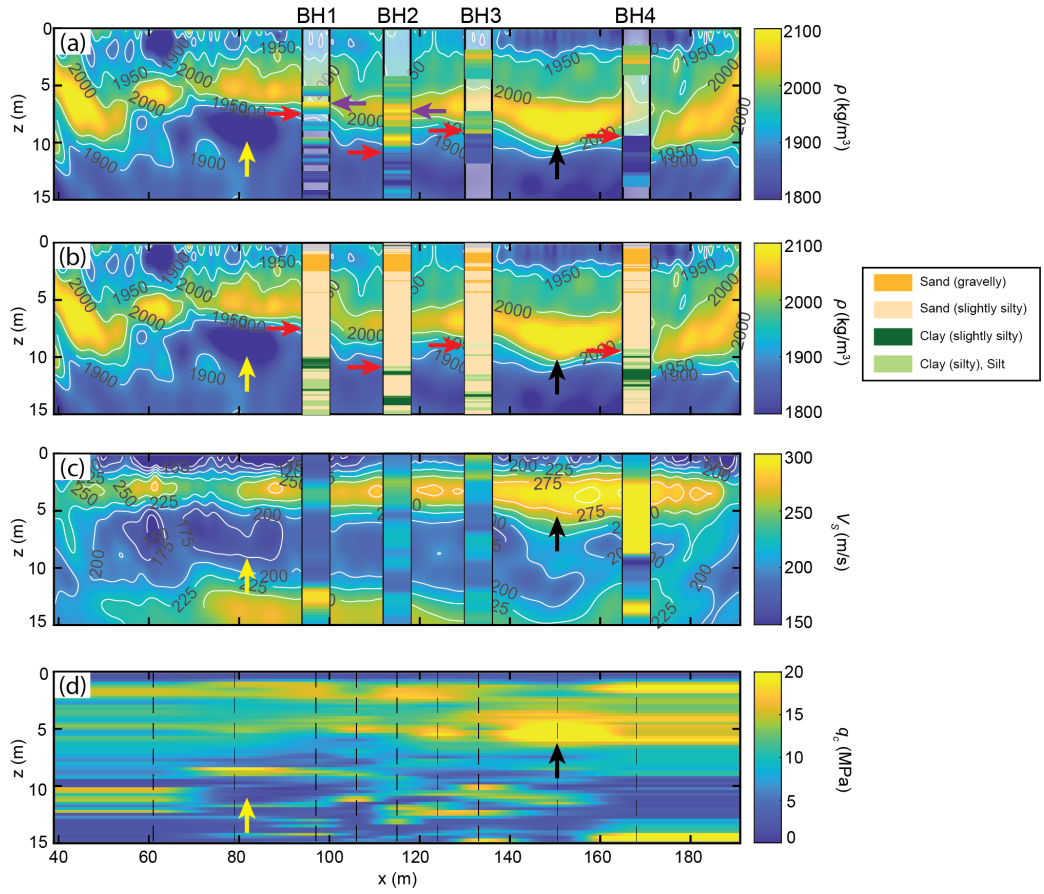

Figure 2.15: Validating ρ from FWI using independent (a) density measurements, (b) soil types obtained from CPT data (Robertson, 1990), (c) V_S from FWI and SCPT, and (d) CPT cone tip resistance (q_c).

by the grain packing which, in turn, is controlled by many factors like grain shape, grain sorting, cementation/diagenesis, etc. However, previous studies have shown a reduction of the sand-grain size correlating with an increase of the void ratio or porosity (Pryor, 1973; Al-Homadhi & Hamada, 2001; Patra et al., 2010; Ogolo et al., 2015; Bell, 2016; Atapour & Mortazavi, 2018). Rice-Birchall et al. (2022) showed that compaction by grain rearrangement, which is generally grain-size dependent, can be significant.

Another characteristic of our test site is a hard sand layer having high ρ (> 2000 kg/m^3) occurring at very shallow depths. This high-ρ sand layer is laterally continuous. This layer is observed also in the density logs (BH1 and BH2), almost at the same depths in the two boreholes (see purple arrows in Fig. 2.15(a)). The hard sand layer has a peak ρ value at around $x = 150$ m (see black arrows in Figs 2.15(a) and (b)). We mark the existence of the highest V_S and q_c at the same lateral distance (see black arrows in Figs 2.15(c) and (d)). The highest value of ρ appears at a relatively deep part compared to that of V_S and q_c.

The discrepancy in depth among the different parameters may represent the true subsurface structure, although the impact of limited resolution in the FWI results cannot be ruled out. Additional V_S and ρ measurements at that lateral distance ($x = 150$ m) might help unravelling this discrepancy. The low-ρ anomaly is also visible at around $x = 80$ m (see yellow arrows in Figs 2.15(a) and (b)) where the low V_S and q_c are observed too (see yellow arrows in Figs 2.15(c) and (d)), indicating the presence of the very soft clay. These observations suggest that the lateral variability in ρ that has been derived by FWI is meaningful, and this should be beneficial for soil characterization including finding soil type, stiffness, and porosity.

2.5.2. Limitation of the analysis

Our proposed sequential inversion workflow and the initial model-building strategy enabled reconstruction of ρ that matched well with the independent ρ measurements and CPT data. The proposed approach can facilitate ρ estimation from SH-wave FWI. The sequential inversion workflow has previously been shown to be effective in exploration-scale applications, mostly focusing on body waves (Jeong et al., 2012; Prieux et al., 2013; Ren & Liu, 2016). Our results suggest that this strategy is also effective in near-surface conditions, where surface waves dominate the recorded wavefield. However, our investigations have been focused primarily on field data. To evaluate the robustness of the sequential inversion to reduce parameter-coupling effects, synthetic tests using a spatially uncorrelated model as in Kawasaki et al. (2024) would be beneficial.

The efficacy of our initial model-building strategy may depend on the degree of lateral heterogeneity in the subsurface. In our field application, the use of an 1D initial V_S model derived from SCPT has given more accurate results than MALW-derived initial V_S model. This is possibly because the subsurface in this case does not have strong lateral variations. For more heterogeneous environments, MALW can capture 2D variations to some extent and, therefore, may be a more appropriate option for initial Vs model building for FWI. To substantiate this, one needs to perform systematic synthetic tests using models with varying degrees of heterogeneity. This would help establish more general guidelines for ρ reconstruction using SH-wave FWI.

2.5.3. Validating V_S estimates from FWI using SCPT data

We evaluate the accuracy of the V_S obtained from FWI using SCPT data. The overall spatial distribution of V_S from FWI is comparable with the SCPT-derived V_S as shown in Fig. 2.15(c) and Fig. 2.16. Note that while the initial 1D V_S model for FWI is derived here by smoothing the SCPT-derived V_S at BH2, the lateral variability in V_S, shown in Fig. 2.15(c) is captured by the FWI. In order to check the validity of the V_S estimates from the FWI, we calculate the first-arrival travel times by seismic ray tracing using the SCPT-derived V_S and the FWI-derived V_S. We then compare these first-arrival travel times with the arrival times observed in the SCPT data. The result is illustrated in Fig. 2.16. The first-arrival travel times for the FWI-derived V_S fit surprisingly well with the arrival times in the SCPT waveforms that are acquired independently of the SH/Love surface-seismic data. This is strongly indicative of the robustness of the estimated V_S from FWI. We notice only minor mismatches at some specific depth ranges between the first-arrival travel times for the SCPT-derived V_S and those for the FWI-derived V_S. For example, at depths of 7–10 m at BH4 (see Fig. 2.16(d)), the travel times for the FWI-derived V_S appear to fit better the travel times in

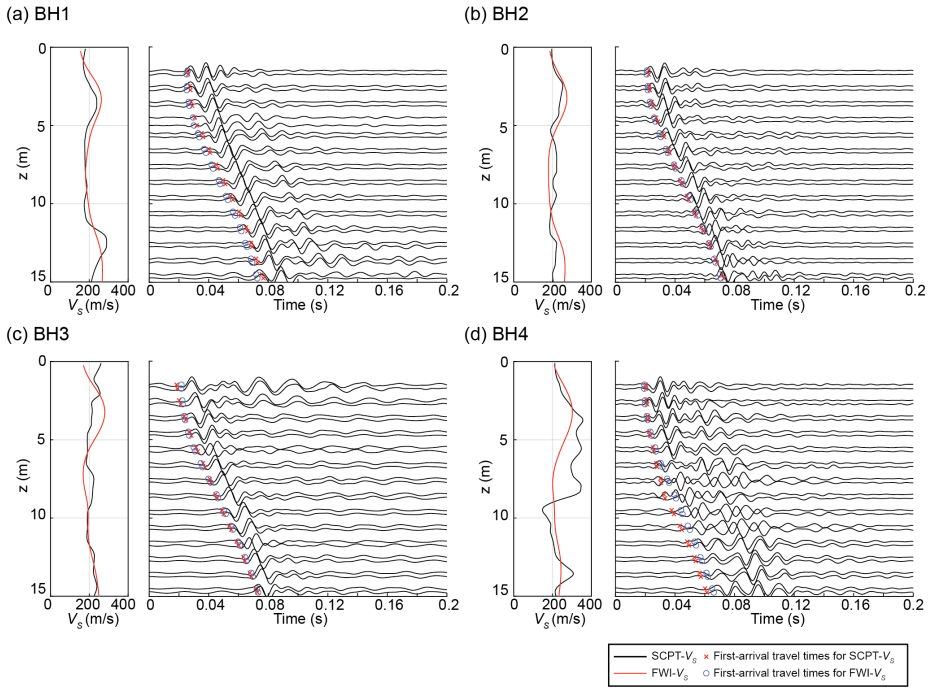

Figure 2.16: 1D validation of the FWI-derived V_S at four different boreholes. Notice the fit among the first-arrival travel times calculated for the FWI-derived V_S, that for the SCPT-derived V_S, and the arrival times seen directly in the SCPT waveforms. The first-arrival times for the 2D FWI-derived and 1D SCPT-derived V_S fields are computed by seismic ray tracing. On the left of each plot the SCPT-derived V_S and the FWI-derievd V_S are checked against each other at the same location.

the SCPT waveforms rather than those for the SCPT-derived V_S. This might, however, be due to an inaccuracy in the SCPT-derived V_S. The SCPT-derived V_S is estimated from the difference in the travel times at two consecutive depths calculated from the cross-correlation between the waveforms observed at those depths, thus providing a high-resolution 1D V_S profile (e.g., Campanella & Stewart, 1992). However, for the acquired SCPT data at BH4 in our test site, the observed waveforms at depths of 7–10 m have relatively low S/N as can be seen in Fig. 2.16(d). This might have resulted in an inaccurate V_S in this depth range from the SCPT.

2.5.4. Considerations for building the initial density model

Our results in Section 2.4.2 have shown that a good initial ρ model from the density log performed on the seismic line helps to obtain rather accurately the spatial variability of the ρ in soil. However, in some cases, the density log may not be available due to budgetary constraints. In such situations, one may avoid the use of the density log to build the initial ρ model for FWI. For example, our investigations have demonstrated that, starting with a homogeneous (constant) initial ρ model, FWI can still provide a meaningful spatial variability of ρ. Note in Figs 2.12(c)-(f) that reasonably good ρ values are obtained above

10 m depth where the assumed constant ρ value in the initial model is close to the true background ρ. Another typical approach for building an initial ρ model is to rely on a good empirical relationship between seismic velocities (V_P and V_S) and density (e.g., Ludwig, 1970; Gardner et al., 1974; Anbazhagan et al., 2016), or employing a linear gradient model as used in Dokter et al. (2017) and Gao et al. (2020). One may, however, encounter a difficulty in choosing an appropriate initial ρ model for the soil at a given site, and a site-specific calibration might be required. Also, to build a sufficiently accurate initial ρ model, one may consider using a nuclear-density cone penetrometer (Tjelta et al., 1985; Shibata et al., 1992; Karthikeyan et al., 2007) which is less expensive than performing density logging in an a-priori drilled borehole.

In this research, we could not evaluate quantitatively how or to what extent an initial ρ model needs to be accurate for the success of ρ reconstruction from the FWI. Addressing this problem might help to choose an appropriate initial model-building strategy at a specific site. Such evaluation could be achieved by investigating the differences in the accuracy of the ρ estimates due to different initial ρ models having different range of wavenumber contents, for several types of near-surface models.

2.6. Conclusions

In this chapter, in order to estimate the spatial distribution of the soil density, we investigated FWI applied to the SH/Love-wave seismic data acquired in the field. We explored practical strategies in order to address two major issues that arise when estimating density through FWI, namely the parameter-coupling effect and the building of the background (initial) density model.

We proposed a sequential inversion workflow to effectively suppress the severe parameter-coupling effect. Compared to the conventional simultaneous inversion workflow, the workflow proposed here improves greatly the accuracy of the estimated density field and the goodness of the seismic-waveform fitting. The derived, spatially varying density field by FWI is relatively accurate, which is validated by independent density measurements at our test site. Building a good 1D initial V_S model for FWI based on the SCPT data from one location in the field provided a less erroneous density structure, compared to a 2D initial model derived from the MALW. This is due to additional mitigation of the parameter-coupling effect due to small error in the SCPT-derived initial V_S model. To incorporate sufficient background density information into the inversion, we derived an initial density model from the data of density logging performed at one point on the seismic line. This 1D density field obtained from the logging data is beneficial for obtaining the well-resolved spatial variability of the soil density up to at least 15 m depth. Here, the 15 m depth restriction is imposed only to keep the computation time short. Our results illustrate on the field-seismic data that the spatial variability of the soil density can be captured reasonably accurately from SH-wave FWI in combination with SCPT and density log data collected at only one location in the test site for the initial model-building purpose. The subsoil density distribution obtained from the FWI offers useful information viz. the spatial variability of the soil type, soil stiffness, and porosity, without the need to perform expensive density measurements at many points in the field to derive finally a rather imperfect image of the density variability. This will open up important possibilities for practical applications in the field.

3

2D FWI FOR SUBSOIL DENSITY: BUILDING ALIASING-FREE SEISMIC DATA USING SEISMIC INTERFEROMETRY

Seismic FWI is capable of providing the spatial distribution of subsurface properties such as V_P, V_S, and ρ. To obtain a high-resolution subsurface image through FWI, we need to perform a seismic survey with many seismic sources and receivers positioned at sufficiently fine spacing (in the wavelength sense); otherwise, spatial aliasing limits the achievable resolution in an inverted image. However, having many sources is logistically and economically more challenging than having many receivers, due to the time-consuming process of generating seismic vibration at many points in the field. To tackle this issue, we propose to enhance the spatial sampling in the source domain by making use of surface waves retrieved by SI. This enables one to obtain aliasing-free seismic data by merging the virtual shot gathers with the field-observed shot gathers enriched in surface waves. This chapter demonstrates the applicability of our proposed concept through tests on actual field data. 2D SH-wave seismic data dominated by Love wave are used. In practice, SI cannot retrieve fully accurate amplitude and phase information of surface waves mainly due to the insufficient distribution of seismic sources used in SI. In this regard, we effectively use virtual shot records together with real shot records in FWI, through application of a matched filter and defining a new weighted misfit function. We find that, at our specific site, the spatial aliasing produces artifacts appearing as striped patterns in the gradient of the misfit function and in the inversion result, disturbing the lateral continuity of an underground structure. The reason for such artifacts is that a sparse distribution of seismic sources fails to suppress the oscillatory side lobes that occur around the source positions in the gradient of the misfit function. Also, spatial aliasing can cause a loss of accuracy in the estimated ρ value. The aliasing-free seismic data from our proposed approach help reducing the striped patterns,

leading to an improved resolution in both V_S and ρ images. Furthermore, an in-depth investigation made through a comparison with the CPT data also confirms the possibility of improvement of the accuracy of the ρ estimate in this way. Our data-driven approach allows us to avoid the time-consuming seismic acquisition in the field using many seismic sources in order to derive a high-resolution image of the subsurface via FWI.

3.1. INTRODUCTION

A high-resolution spatial distribution of seismic properties in soil, such as V_P, V_S, and ρ, is important for various near-surface applications in areas like geoengineering, urban planning, and disaster prevention. Field-acquired seismic data in the near-surface scale is generally dominated by the surface waves, which are sensitive to the V_S structure in the subsurface. Accordingly, soil characterization has been conventionally achieved using the distribution of V_S obtained from a dispersion-curve-based inversion using Rayleigh wave (MASW, Xia et al., 1999; Park et al., 1999) or Love wave (MALW, Xia et al., 2012). These methods have been successfully applied to solve many geotechnical engineering problems over the years; however, there is a difficulty in capturing the lateral variability in soil layers with a high resolution due to the made 1D assumption. Furthermore, the dispersion curves are not much influenced by the variation of other seismic properties like V_P and ρ (Xia et al., 1999; Foti & Strobbia, 2002), limiting the applicability of the above-mentioned surface-wave methods to the estimation of V_S only.

In the recent decade, seismic FWI has received the attention as a promising tool for simultaneously estimating multiple parameters (V_P, V_S, and ρ) at the near-surface scale (e.g., Tran et al., 2013; Köhn et al., 2019; J. Liu, Ghose, & Draganov, 2022; J. Liu, Draganov, & Ghose, 2022). More recently, synthetic and field studies have shown that FWI applied to SH/Love wavefields (thus independent of V_P) enables one to reconstruct in high-resolution the V_S and ρ images without suffering from the well-known inter-parameter coupling problem (Dokter et al., 2017; Wittkamp et al., 2018). In this regard, we have already shown on field data (Chapter 2 of this thesis) that 2D SH-wave FWI, following a specific workflow and utilizing a good initial model, can capture the spatial variability of V_S and ρ, as confirmed by independent geotechnical measurements (see Chapter 2).

For a successful seismic imaging, in general, a dense sampling of the seismic wavefield in both time and space is of great importance in order to achieve a high-resolution image without generating artifacts due to aliasing. To avoid aliasing in both time and space domains, we must acquire seismic data with a time sampling $\Delta t_{\text{samp}} \leq 1/2f_{\text{max}}$, and a spatial sampling $\Delta_{\text{samp}} \leq 1/2k_{\text{max}}$, where f_{max} is the maximum frequency considered in a specific application and k_{max} is the maximum horizontal wavenumber for the propagating plane wave. Here, k_{max} is defined as follows:

$$k_{\text{max}} = \frac{f_{\text{max}} \sin\theta}{v_{\text{min}}}, \tag{3.1}$$

where v_{min} is the minimum velocity of the seismic waves in the subsurface medium, and θ is the emergence angle of a propagating seismic wave. As k_{max} becomes maximum at $\theta = 90°$, one can perform completely aliasing-free seismic imaging with the following relationship

regarding spacing of seismic sources (Δs) and receivers (Δr):

$$(\Delta r, \Delta s) \leq \Delta_{\text{samp}} = \frac{\lambda_{\text{min}}}{2}, \tag{3.2}$$

where λ_{min} is the minimum wavelength. Spatial aliasing makes it difficult to map steeply dipping structures at the correct location using seismic migration, especially at high frequencies (Yilmaz, 2001). Such difficulties have been conventionally avoided, for example, by trace interpolation (e.g., Spitz, 1991; Gray, 1992).

In the context of waveform inversion, the computation of the gradient of a misfit function is equivalent to the conventional pre-stack migration operation (Mora, 1987). Hence, spatial aliasing can also distort the inverted subsurface image obtained from a gradient-based waveform inversion. Brenders and Pratt (2007) showed, through synthetic study at the lithospheric scale, that increasing either Δs or Δr ($> \Delta_{\text{samp}}$) produces spurious lateral artifacts in the velocity model derived from FWI. However, in their research, three times larger spacing for the seismic sources than the requirement given by eq. 3.2 (i.e., $\Delta_{\text{samp}} < \Delta s \leq 3\Delta_{\text{samp}}$) still provided an acceptable velocity model for a receiver spacing which is shorter than Δ_{samp}. At the near-surface scale, Romdhane et al. (2011) investigated the sensitivity of an inverted model to source spacing for a realistic synthetic landslide model. In contrast to the results of Brenders and Pratt (2007), the sparse distribution of seismic sources ($\Delta s = 4$ m $< 3\Delta_{\text{samp}} = 5.34$ m) in Romdhane et al. (2011) is found to produce many artifacts especially near the free surface and to cause a decrease in resolution of a deeper structure. These different observations at different scales reflect the difference in the horizontal-wavenumber components of the propagating seismic waves that dominate each observation. Brenders and Pratt (2007) stated that the wavefields that are mainly considered in their research possibly propagate with $\theta < 90^\circ$ (i.e., refracted/reflected waves), allowing $(\Delta r, \Delta s) > \Delta_{\text{samp}} = \lambda_{\text{min}}/2$ to provide a reasonably good inverted model (see eqs 3.1 and 3.2). On the contrary, the near-surface FWI can be relatively strongly influenced by the spatial aliasing resulting from the high horizontal-wavenumber components of the surface waves that propagate parallel to the free surface (i.e., $\theta \sim 90^\circ$ in eq. 3.1).

In a typical seismic survey, having many sources, thus respecting eq. 3.2, is much more difficult than planting receivers densely. This is because, in order to have many seismic sources, one needs to generate seismic vibration at many points in the field - with the source aligned in a specific direction - and multiple times at each source location to enhance the signal-to-noise ratio (S/N); this increases the costs of seismic acquisition. Optimizing the acquisition configurations for an arbitrary number of sources and receivers is possible, for example by employing the experimental design (ED) tools (Nuber et al., 2017). However, such technique needs a rough subsurface model in advance. A simple approach for mitigating the spatial aliasing effect is to precondition the gradient of a misfit function using a spatial smoothing filter in either space or wavenumber domain, unfortunately at a cost of decreasing the resolution of the inverted model (Mao et al., 2016).

In this research, we propose to retrieve the virtual surface-wave records at each receiver location by using SI, for building aliasing-free seismic data by combining such virtual seismic records with surface-wave dominated real records. Given the dense distribution of receivers ($\Delta r \leq \lambda_{\text{min}}/2$) in the field, one can generate virtual shot gathers with the same lateral spacing for the sources as the receivers in the field ($\Delta s \leq \lambda_{\text{min}}/2$), using data from

real sources that are sparsely distributed. Our approach does not need a priori information regarding subsurface (velocity and structure). However, amplitude and phase errors occur in the retrieved surface waves mainly due to the insufficient distribution of the sources used in SI (Wapenaar & Fokkema, 2006; D. Halliday & Curtis, 2008; Kimman & Trampert, 2010; van Dalen et al., 2013). We correct errors in the virtual records by means of a matched filter estimated using the shot record for the nearest source to the virtual source location (e.g., J. Liu et al., 2018; Balestrini et al., 2020; J. Liu, Draganov, & Ghose, 2022). Since the estimated matched filter may not completely correct the erroneous virtual-shot records, we define a new weighted misfit function specifically designed for FWI applied to the merged data of the virtual shot records and the real shot records. This chapter aims to examine on field data how our approach is effective in performing an aliasing-free subsurface imaging through FWI.

3.2. METHODOLOGY

In this section, we first explore the associated challenges and the possible benefits/merits of using virtual shot records simultaneously with real shot records in FWI. The detailed procedure of our proposed approach is then provided.

3.2.1. BUILDING ALIASING-FREE SEISMIC DATA FROM SI

SI provides a virtual seismic wavefield propagating between two receivers as if a seismic signal were generated at one of the receiver positions. The retrieved virtual seismic records are merged with the real records, which is equivalent to acquiring many shot-gathers where the sources are located densely in space. To illustrate the possible benefits of using SI in terms of spatial aliasing, we suppose (i.e., synthesize) a near-surface seismic survey with a sparse distribution of seismic sources ($\Delta s_R > \lambda_{\min}/2$) and densely spaced receivers ($\Delta r \leq \lambda_{\min}/2$) (Fig. 3.1(a)). Here, we consider a 2D survey, i.e., sources and receivers along one line. We consider seismic sources to be located at the middle of two adjacent receivers, preventing receivers from interfering with the generation of seismic vibrations. Such source-receiver configurations (i.e., $\Delta s_R > \Delta r$) are typically used in a near-surface seismic survey to save time. We first apply SI to the shot records acquired in the field (D_R) in order to retrieve virtual seismic records (D_V) associated with each receiver position. D_V is then merged with D_R, providing a large seismic dataset with $\Delta s_{RV}^{\max} = \Delta r \leq \lambda_{\min}/2$ (see Fig. 3.1(b)). We perform FWI using this aliasing-free seismic data (D_{RV}) instead of using the real data only (D_R), in an attempt to facilitate high-resolution imaging. Note that this technique does not need any a priori velocity or structural information of the subsurface.

When the sources and the receivers in a seismic survey are distributed on the free surface only (Fig. 3.1(a)), a seismic response recorded at a receiver B due to a virtual source at a receiver A, which is denoted by $u(x_B, x_A)$, is calculated in the frequency domain as follows (Wapenaar & Fokkema, 2006; D. Halliday et al., 2007):

$$u(x_B, x_A) + u^*(x_B, x_A) \approx \sum_{n=1}^{N} u(x_B, x_n) u^*(x_A, x_n), \tag{3.3}$$

where the symbol * represents the complex conjugate and N is the number of sources. In case only the surface sources are used as in a typical near-surface seismic survey, SI

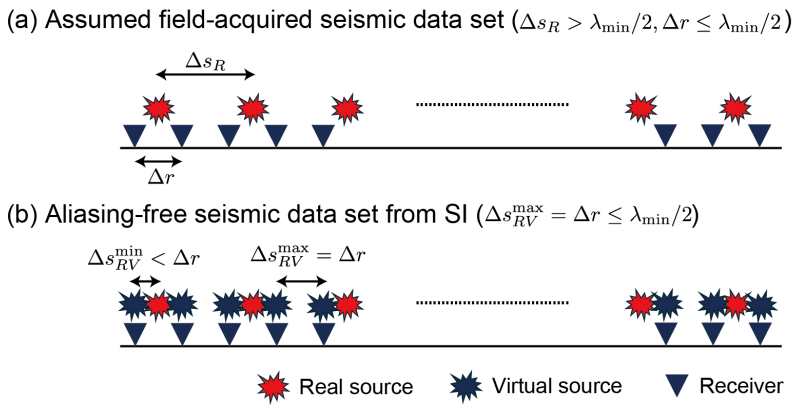

Figure 3.1: Concept of the proposed approach for creating aliasing-free seismic data using SI.

preferentially retrieves the surface waves over the body waves. This is mainly because any sources on the free surface on one side of the receiver pair fall into the so-called stationary-phase region for the surface waves, thereby facilitating preferential retrieval of the surface waves over the body waves through SI (D. Halliday et al., 2007, 2008). In shallow seismic datasets, the surface waves are generally much more energetic than the body waves, which also contributes to retrieving well the surface waves through SI. Our proposed approach is, therefore, anticipated to be effective for surface-wave dominated near-surface seismic data. Because the FWI at the near-surface scale also makes a greater use of the surface-wave information, which generally dominate the observed data (e.g., Wittkamp et al., 2018; J. Liu, Draganov, & Ghose, 2022; Y. Pan & Gao, 2023), the results of FWI are likely to be benefited when the input data are more enriched with surface waves.

Retrieving accurate amplitude and phase information while using eq. 3.3 needs several assumptions to be met (Wapenaar & Fokkema, 2006). First, one must calculate the sum of cross-correlated waveforms (i.e., $u(x_B, x_n)u^*(x_A, x_n)$) over the enclosing source boundary; this boundary should surround the medium of interest and be in the form of a sphere with a large radius. Also, the medium at and outside the enclosing source boundary should be homogeneous, and the whole medium should be lossless. In the case of the retrieval of surface waves, seismic sources should exist also in the subsurface to accurately obtain the multiple modes of the surface waves by cancelling intermodal correlation (cross terms) (D. Halliday & Curtis, 2008; Kimman & Trampert, 2010; van Dalen et al., 2013). In practice, one cannot conduct a near-surface seismic survey meeting all the above requirements. As a result, amplitude and phase errors arise in the retrieved data, deviating from the seismic wave equation. These errors are subsequently mapped onto an inverted (FWI) subsurface image as artifacts, because FWI assumes that the observed seismograms respect the wave equation.

To properly incorporate the retrieved virtual shot records into FWI, we correct amplitude and phase errors using a matched filter (e.g., J. Liu et al., 2018; Balestrini et al., 2020; J. Liu, Draganov, & Ghose, 2022). A matched filter f is estimated by solving the following minimization problem between the retrieved virtual record (D_V) and the real record for a

source position which is nearest to the virtual source (D_R^{near}):

$$\min_f \| D_R^{\text{near}} - f D_V \|. \tag{3.4}$$

This provides the corrected virtual shot record ($f D_V$), which can then be used in FWI. Note that in eq. 3.4, D_V approximates D_R^{near} through the use of the matched filter f. However, in case a virtual source does not coexist in location with a real source as shown in Fig. 3.1(b) (which is also the case of our field data), the subsurface information contained in D_V would slightly differ from D_R^{near}. This slight difference in information makes it possible to avoid the severe spatial aliasing effect, finally improving the resolution in the FWI result. Since a matched filter has a 2D window in both space and time domains (e.g., D. F. Halliday et al., 2010; J. Liu et al., 2018; Balestrini et al., 2020; J. Liu, Draganov, & Ghose, 2022), $f D_V$ does not completely correspond to D_R^{near}, resulting in some residual even after solving eq. 3.4. We expect that the remaining residuals include meaningful subsurface information due to the difference in the shot positions between D_V and D_R^{near}.

In the past decades, a matched filter has been successfully applied for various purposes including adaptive multiple elimination (Dragoset, 1995; F. Liu et al., 2000; Rickett et al., 2001; Guitton & Verschuur, 2004), adaptive subtraction of surface waves (D. F. Halliday et al., 2010; J. Liu et al., 2018; Balestrini et al., 2020; Shirmohammadi, 2024), and accurate retrieval of the surface waves by super-virtual interferometry (J. Liu, Draganov, & Ghose, 2022). In this research, we concentrate on investigating how a matched filter performs in terms of offering stability to the FWI results when both real+SI-retrieved merged data are used as input to FWI. Note that the calculation of SI and the estimation of a matched filter that we discuss in this chapter follow the work of Shirmohammadi et al. (2023).

3.2.2. Designing a weighted misfit function for the merged data

We perform 2D SH-wave FWI using FDTD forward modelling and NCG, as also discussed in Chapter 2. GCN is again used to measure the difference between the observed and the synthetic seismograms (see eq. 2.1). FWI with the GCN updates a model parameter by maximizing the cross-correlation between the normalized measured and synthetic seismic waveforms, focusing on phase matching rather than amplitude matching. Such phase-focused misfit function would weaken the impact of the remaining amplitude error in the corrected virtual shot records on FWI, while the remaining phase error would possibly degrade the inverted image quality.

In order to address this problem, we introduce the following weighed misfit function that aims at reducing the contribution from the erroneous virtual shot records to the misfit function:

$$E = E_R + E_V = \sum_i^{ns_R} E_R^{(i)} + w_j \sum_j^{ns_V} E_V^{(j)}, \tag{3.5}$$

where E_R and E_V are the misfit functions for the real and the virtual records, respectively, while ns_R and ns_V are the number of real and virtual sources, respectively. w_j is weight given for each virtual shot record ($0 \leq w_j \leq 1$). To define the variable weight, we compare the misfit value for the virtual record of virtual source j ($E_V^{(j)}$) with that for the real record with the nearest real source (E_R^{near}). When the real source is located sufficiently (in the

wavelength sense) close to the virtual source, those two misfit values ($E_V^{(j)}$ and E_R^{near}) should not be significantly different. $E_V^{(j)} \gg E_R^{\text{near}}$ implies the existence of much error in the virtual shot record. In that case, we need to reduce the impact of this virtual shot record on FWI, thus mitigating possible distortion in the inversion result. We define the following condition to determine w_j for each virtual shot record:

$$w_j = \begin{cases} 0.8 & (E_V^{(j)} < 0.8E_R^{\text{near}}) \\ 0.6 & (0.8E_R^{\text{near}} < E_V^{(j)} \leq 0.6E_R^{\text{near}}) \\ 0.4 & (0.6E_R^{\text{near}} < E_V^{(j)} < 0.4E_R^{\text{near}}) \\ 0.01 & (0.4E_R^{\text{near}} \leq E_V^{(j)}) \end{cases}. \tag{3.6}$$

Here, E_R^{near} is assumed to be negative, meaning that the observed and synthetic seismograms for a given subsurface model are positively correlated (see eq. 2.1); this is the case for our field application. We have chosen the above definition (eq. 3.6) based on several test runs of FWI considering different values for w_j. w_j is calculated for an initial model at the first iteration, and then it is fixed during the subsequent iterations. To explore the potential benefit of our weighting strategy, we compare the inverted models from FWI using weighted and unweighted misfit functions (i.e., $w_j = 1$ in eq. 3.5).

3.3. Field-data application

We demonstrate here the effectiveness of our method using the 2D SH/Love-wave seismic data acquired in the field; see Subsection 2.3.1 for details of field data acquisition. In Chapter 2, we have discussed how the overall subsurface structure is constrained by FWI compared to sparse geotechnical data. In this chapter, we delve into the possibility of improving the resolution by making use of the virtual shot records.

As mentioned earlier, our proposed approach is suitable for near-surface seismic data which are typically dominated by surface waves. We, therefore, restrict our analysis to the relatively lower frequencies (< 40 Hz) in the field data where much of the recorded wavefield energy can be attributed to the Love wave (e.g., see Figs 2.2(c)-(d)). Having higher frequencies will enhance the presence of body waves, and then the proposed approach will become less effective. Additionally, limiting the frequency components in FWI makes the computation time manageable. This is helpful because, when using the merged real+virtual source dataset in FWI, one needs to perform $ns_R + ns_V$ forward simulations for each iteration in FWI, and that is computationally demanding. Therefore, we use three inversion stages only within the framework of the multi-scale inversion: 10-15 Hz, 10-25 Hz, and 10-40 Hz (see Subsection 2.3.5). Other FWI processing steps used for the results presented in this chapter are exactly same as those in Chapter 2, including data preprocessing and sequential inversion for accurate estimation of subsoil density (see Section 2.3). We use a good initial model for FWI that is derived from SCPT and the density logging (see Subsection 2.3.3).

3.3.1. Characterizing artifacts due to spatial aliasing

In this subsection, we investigate the effect of increasing the spacing of the seismic sources on the FWI results, focusing on the following two datasets: 76 real shot gathers with $\Delta s_R = 2$ m and 38 real shot gathers with $\Delta s_R = 4$ m. These two datasets correspond to relatively densely

sampled data and sparse data, respectively. Both datasets meet the requirement for avoiding severe spatial aliasing as suggested by Brenders and Pratt (2007), i.e., $\Delta s_R \leq 3\Delta_{\text{samp}} \sim 5.625$ m.

We first compare the gradients of the misfit function for different source configurations. The gradients are calculated using the following equation (e.g., Dokter et al., 2017):

$$\begin{aligned}\frac{\partial E}{\partial V_S} &= -\frac{2}{V_S^3 \rho} \sum_{i=1}^{ns} \int_0^T dt(\hat{\sigma}_{xy}\sigma_{xy} + \sigma_{yz}\hat{\sigma}_{yz}),\\ \frac{\partial E}{\partial \rho} &= -\frac{2}{V_S^2 \rho^2} \sum_{i=1}^{ns} \int_0^T dt(\sigma_{xy}\hat{\sigma}_{xy} + \sigma_{yz}\hat{\sigma}_{yz} + V_S^2 \rho^2 \frac{\partial v_y}{\partial t}\hat{u}_y),\end{aligned} \tag{3.7}$$

where σ_{xy}, σ_{yz} and v_y represent the shear stresses and particle velocities of the forward wavefield for all ns shot positions, while $\hat{\sigma}_{xy}$, $\hat{\sigma}_{yz}$, and $\hat{u}_y$ are stresses and displacements of the adjoint wavefield. We first perform FWI at the lowest frequency stage (10-15 Hz) independently for the two source-configuration datasets, and then calculate the gradients at the second frequency stage (10-25 Hz) using each updated model at the end of the first stage. We do not investigate the gradients at the first stage, because the inversion results for the two datasets are almost the same due to the very long wavelength at that stage (~ 13 m). The comparison of the gradients at the first iteration of the second stage for the two datasets is presented in Fig. 3.2. When using the shot records with $\Delta s_R = 2$ m, the gradient with respect to V_S smoothly varies in both vertical and lateral directions (Fig. 3.2(a)), while the gradient for ρ is characterized by vertical stripes at some locations (see red arrows in Fig. 3.2(b)). With increasing the spacing of sources ($\Delta s_R = 4$ m), the overall structure of the gradient for ρ is comparable to the situation when $\Delta s_R = 2$ m; however, much more striped patterns are visible over the whole area when $\Delta s_R = 4$ m (Fig. 3.2(d)). There are a few vertical stripes also in the gradient for V_S when $\Delta s_R = 4$ m (see the red arrow in Fig. 3.2(c)). As noted earlier, the subsurface models used for the calculation of the gradients are nearly identical for the two cases. Therefore, it is the different source configurations that are responsible for producing different extents of the striped patterns in the gradients. This is clearly a consequence of spatial aliasing that we discuss here.

We next investigate how these vertical stripes are produced in the gradients of the misfit function. To achieve that, we calculate the gradients using a pair made of a single source and a single receiver using eq. 3.7 with ns=1 (see Figs 3.2(e)-(f)). In the gradient for V_S, one can clearly recognize the yellow region appearing in between the source and the receiver (Fig. 3.2(e)), where V_S needs to be updated to reduce the misfit. On the contrary, the oscillatory side bands are visible outside that region for both V_S and ρ (white arrows in Figs 3.2(e)-(f)). These are artifacts reflecting the shape of the sensitivity kernel for a point force (for example, see Fig. 5(b) in Virieux and Operto (2009)). We notice that the width of the side bands varies with depth; a narrower band is observed at the shallow part rather than at the deep part (see white arrows in Figs 3.2(e)-(f)). This reflects the effect of the difference in the wavenumber component of the sensitivity kernel depending on the scattering angle (Virieux & Operto, 2009). In this regard, the gradient for ρ is dominated by high wavenumber components due to the fact that the wavefields are scattered due to a perturbation of ρ predominantly propagating in the backward direction (Virieux & Operto, 2009; W. Pan, Geng, & Innanen, 2018; Kawasaki et al., 2024). This results in the dominance of the oscillatory side bands in the gradient for ρ rather than that for V_S (compare between

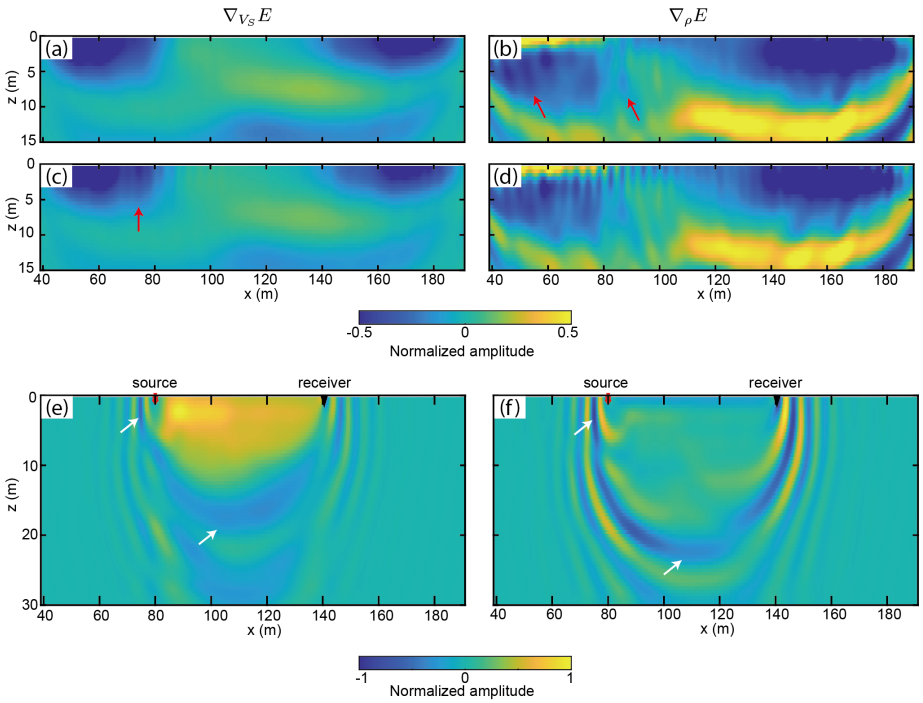

Figure 3.2: Comparison of the gradients calculated for different source configurations, (a)-(b) Δs_R = 2 m and (c)-(d) Δs_R = 4 m. (e)-(f) The gradients are calculated for a pair made of a single source and a single receiver. The red arrows mark the artefacts (appearance of stripes) created by the use of aliased surface waves in FWI. The white arrows indicate the side bands (artifacts) whose width varies with depth.

Fig. 3.2(e) and Fig. 3.2(f)). The summation of all gradients for densely distributed source-receiver pairs can suppress the oscillatory artifacts; otherwise, the acquisition footprint occurring in the gradient distorts the lateral resolution of an inverted image (Guasch et al., 2019). Our investigations suggest that the source spacing tested (especially when Δs_R = 4 m) is not sufficiently small for mitigating the oscillatory artifacts. In the framework of the gradient-based inversion as adopted in this research (see Subsection 2.2.1 for details), the model is updated in the direction along the gradient shown in Figs 3.2(a)-(d). The inverted model also includes artifacts appearing as vertical stripes in the gradients (e.g., Fig. 3.2(d)), definitely in the first iteration.

Next, we compare the estimated models using the two different source configurations after all frequency stages in the inversion. Since the inversion finally uses high-frequency components up to 40 Hz, the effect of spatial aliasing should be visualized more clearly in the estimated models rather than in the gradients (Fig. 3.2). This is illustrated in Fig. 3.3. When Δs_R = 2 m, there are a few vertical stripes in the estimated V_S (see red arrow in Fig. 3.3(a)), while stripes are slightly visible above 5 m depth in the estimated ρ (Fig. 3.3(b)). Such shallow artifacts for ρ are caused by the narrow side bands at the shallow depth due to the high wavenumber component of the sensitivity kernel, which is demonstrated while

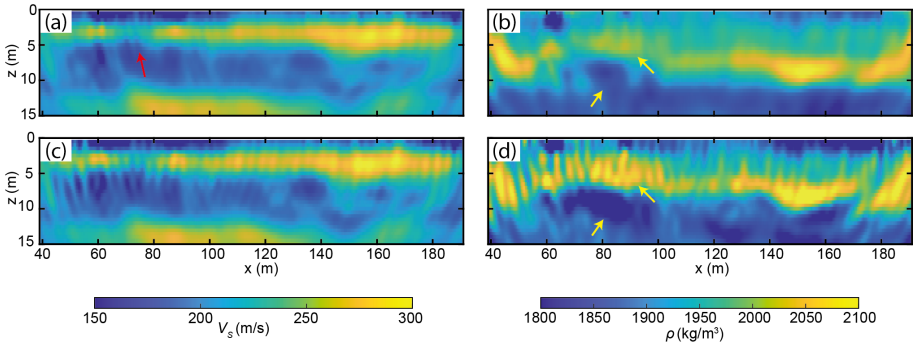

Figure 3.3: Comparison of FWI results for the different source configurations, (a)-(b) Δs_R = 2 m and (c)-(d) Δs_R = 4 m. The red arrow marks the artefacts (appearance of stripes) created by the use of aliased surface waves in FWI. The yellow arrows mark the difference in ρ estimates due to different source configurations.

investigating the gradients (white arrows in Fig. 3.2(f)). In comparison, FWI of data when Δs_R = 4 m (Figs 3.3(c)-(d)) exhibits two clear differences. Firstly, more artifacts having striped patterns are visible in both V_S and ρ images, disturbing the lateral continuity of the subsurface structure. This is demonstrated earlier too while looking at the gradients. Another difference is that the estimated ρ values slightly differ due to different source spacing (compare yellow arrows between Figs 3.3(b) and (d)). The estimated ρ using many sources located at a short spacing is, in general, more accurate. Our results demonstrate that spatial aliasing deteriorates not only the lateral continuity of the subsurface structure, but also negatively affects the absolute value of ρ obtained by FWI.

To evaluate quantitatively the extent of spatial aliasing in the estimated model, we define model roughness by the Laplacian operator Δ applied to the estimated model as follows (Köhn et al., 2016; Köhn et al., 2019):

$$\Delta m = \frac{1}{4}\left(\frac{\partial^2 m}{\partial x^2} + \frac{\partial^2 m}{\partial z^2}\right). \tag{3.8}$$

The vertical stripes produced by spatial aliasing cause an abrupt change of the estimated properties in the lateral direction, resulting in large Δm values. Fig. 3.4 shows the comparison of the spatial distribution of Δm between the cases of Δs_R = 2 m and Δs_R = 4 m. The quantification using eq. 3.8 helps visualizing many vertical stripes for both V_S and ρ when Δs_R = 4 m (see Figs 3.4(c)-(d)). One can also recognize the laterally continuous structure having high Δm, for example, around 4 m depth in Fig. 3.4(a). This possibly reflects the true subsurface structure. Besides, the magnitude of $\Delta\rho$ over the whole model space differs due to using the different source configurations (compare between Figs 3.4(b) and (d)), suggesting possible distortion of the absolute ρ values with increasing source spacing. We also calculate the square of l_2 norm of Δm, $\|\Delta m\|^2$, to quantify the overall model roughness; these values are marked in Fig. 3.4. The model roughness drastically increases with increasing source spacing. Especially for ρ, the effect of a sharp change in the estimated ρ on the model roughness is clear.

The degradation in the inverted image due to spatial aliasing as illustrated in this subsection invites misinterpretation and/or misunderstanding of the subsoil structure.

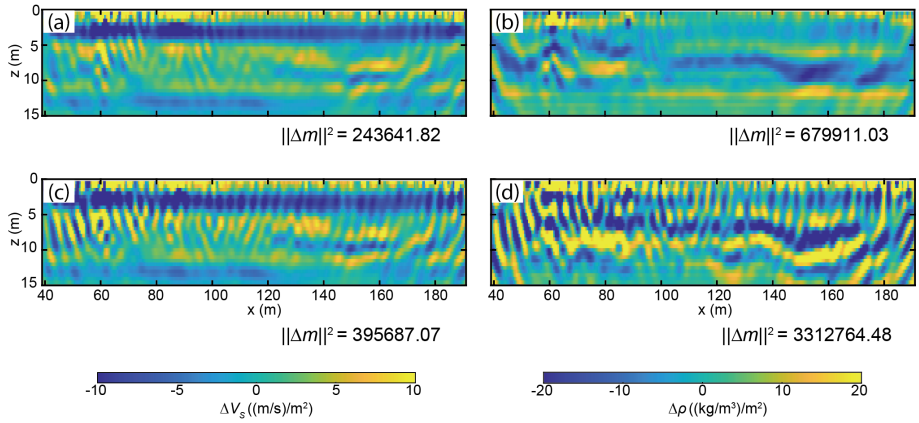

Figure 3.4: Same comparison as in Fig. 3.3, but for model roughness (Δm) of the inverted subsurface images (Fig. 3.3) calculated using eq. 3.8. The striped pattern in Δm is a consequence of using the sparse distribution of seismic sources.

3.3.2. RESULTS: RETRIEVED VIRTUAL LOVE WAVE DATA

To mitigate the effect of spatial aliasing, we make use of the virtual Love wave records that are retrieved at each receiver position using SI in combination with the use of a matched filter. This subsection shows the characteristics of the virtual shot gathers with (fD_V in eq. 3.4) and without the matched-filter correction (D_V in eq. 3.4), compared with the real shot gather (D_R^{near} in eq. 3.4). We use all available real sources (76 shots with $\Delta s_R = 2$ m) to obtain an inversion result as good as possible for our experiment site. Our proposed approach, presented in Section 3.2 above, provides an aliasing-free merged dataset with $\Delta_{RV}^{\max} = \Delta r = 1$ m $< \Delta_{\text{samp}} = 1.875$ m.

Fig. 3.5 shows a comparison of the raw virtual shot gather (D_V) with the real shot gather (D_R^{near}) at a source location which is nearest to the location of the virtual source. Both shot gathers are similarly dominated by the dispersive Love waves. However, there are a few differences visible between them (see red arrows and rectangles in Figs 3.5(a)-(b)). The undesired noise from SI applied to the data of surface seismic survey is responsible for such differences (see Section 3.2.1). The difference in subsurface information from these two shot gathers is due to their slightly different source location (0.5 m). This has possibly contributed to the slight differences in the waveforms. We investigate the difference in the dispersive characteristics in the phase velocity-frequency domain (Figs 3.5(c)-(d)). A significant difference between the two dispersion images exists at the fundamental mode below 15 Hz. We notice much less energy in the virtual record than in the real record (see red arrows in Figs 3.5(c) and (d)). Considering the corresponding wavelength ($\lambda \sim$ 13 m), it is unlikely that the slightly different source location has any such effect. This difference suggests that the retrieval of the low-frequency fundamental mode by SI is not successful in this case. In general, intermodal correlation makes it difficult to retrieve accurately the higher modes having lower energy than the fundamental mode (Kimman & Trampert, 2010; van Dalen et al., 2013). In this field application, however, we face difficulty in retrieving the fundamental mode, for which the cause is not obvious. One possible

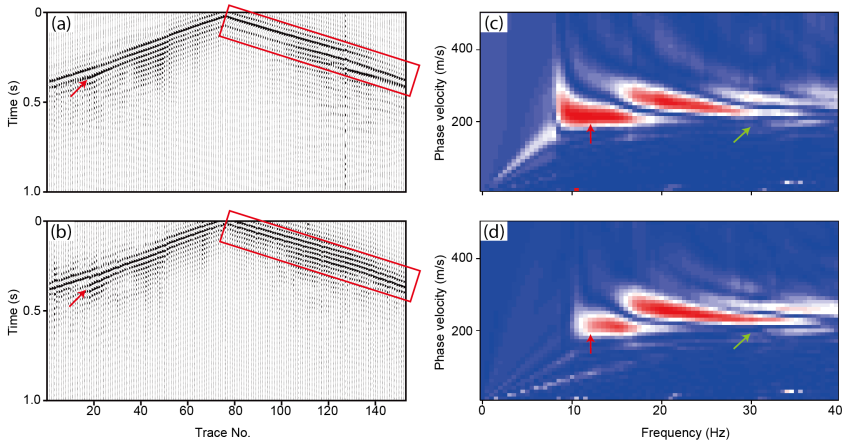

Figure 3.5: (a) Real shot gather. (b) Virtual shot gather retrieved from SI. (c) Dispersion image calculated from the real shot gather shown in (a). (d) Dispersion image calculated from the virtual shot gather shown in (b). Arrows and red boxes point out some differences between these two shot gathers.

explanation is the balance of modal energy in the observed data. The subsurface structure at this test site might have generated energetic high-frequency higher modes, thus impacting negatively the retrieval of the fundamental mode through cross-correlation and summation in SI. There is also a slight difference in the relative energy of the high-frequency higher mode between D_V and D_R^{near} (see green arrows in Figs 3.5(c) and (d)). This difference might be significant because the corresponding wavelength is relatively short ($\lambda \sim 6.67$ m), indicating the potential for successfully retrieving subsurface information through SI.

We next correct the errors in the retrieved surface waves using a matched filter following the approach described in Subsection 3.2.1. In the case of our field data, however, we could not design a matched filter using eq. 3.4 to properly correct for the erroneous fundamental mode at the low frequencies (< 20 Hz). This failure could be caused by the insufficient retrieval of the fundamental mode, as mentioned above. To tackle this problem, we extract the low-frequency components (< 20 Hz) from D_R^{near}, and then add them into the virtual-shot record. After Shirmohammadi et al. (2023), we outline the procedure:

(1) The low-frequency components (< 20 Hz) in the virtual record with a matched filter (fD_V in eq. 3.4) are erroneous, and therefore these components are removed by applying the low-cut filter.

(2) We extract the low-frequency components from the nearest real shot gather (D_R^{near}). This is achieved by first applying the same low-cut filter to D_R^{near}, and then subtracting the filtered D_R^{near} from the raw D_R^{near}.

(3) The extracted data (output from step (2)) are added to the filtered virtual shot record (output from step (1)).

Once these steps are implemented, the virtual shot record is finally composed of fD_V above 20 Hz, and D_R^{near} below 20 Hz. We anticipate that this procedure will be effective, because the low-frequency components (corresponding to wavelength > 10 m) should be nearly

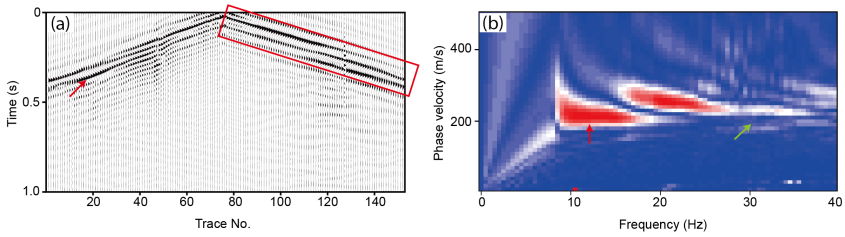

Figure 3.6: (a) Virtual shot gather with amplitude/phase corrections. (b) Dispersion image calculated from the virtual shot gather shown in (a). The red symbols mark the improvements compared to the uncorrected virtual data (Figs 3.5(b) and (d)), while the green arrow marks some difference in characteristics with respect to real seismic data (Figs 3.5(a) and (c)).

identical between the virtual and the nearest real records. The finally retrieved surface waves are shown in Fig. 3.6. The very similar waveforms are clear (compare red arrows and rectangles between Fig. 3.6(a) and Fig. 3.5(a)), while there is the slight remaining difference for the higher modes at high frequencies (≥ 20 Hz) compared with the nearest real shot gather (see green arrows in Fig. 3.5(c) and Fig. 3.6(b)). This difference suggests that additional information from the virtual shot gather may contribute to the improved resolution in the results of FWI. Further investigation into the characteristics of the retrieved Love waves will be carried out in Subsection 3.4.2.

3.3.3. RESULTS: FWI APPLIED TO THE MERGED REAL+VIRTUAL SEISMIC SOURCE DATA

We perform FWI for the aliasing-free dataset obtained by merging the corrected virtual shot gathers with the real shot gathers acquired in the field. We find that the virtual shot gathers are relatively noisy at the near offsets. Balestrini et al. (2020) earlier demonstrated that applying a matched filter produces artifacts at the earlier times, depending on the filter length. Thus, the minimum source-receiver offset used for FWI is limited to 5 m. In this subsection, we investigate how our proposed steps, namely the correction of the retrieved surface waves and the weighting strategy (eqs 3.5 and 3.6), are useful in order to avoid the severe spatial aliasing effect as discussed in Subsection 3.3.1.

POTENTIAL BENEFITS OF CORRECTING ERRORS IN VIRTUAL RECORDS

We investigate the benefit of correcting the SI-retrieved surface waves in the context of FWI. For that purpose, we compare the results of FWI using corrected and uncorrected virtual shot gathers. The merged real+virtual shot gathers are used in both cases. As demonstrated in Subsection 3.3.2, for our dataset, SI fails to retrieve successfully the low-frequency components (< 20 Hz), making it impossible to execute the first inversion stage of FWI using the uncorrected virtual records. The comparison therefore focuses on the inversion results at the second stage (10-25 Hz) using the input model from the first stage (10-15 Hz). This comparison is possible because severe spatial aliasing does not occur with the corresponding long wavelength at the lowest frequency stage, which is also pointed out in Subsection 3.3.1. Here, the real and virtual records are equally treated during the FWI by assigning $w_j = 1$ in eq. 3.5. Fig. 3.7 summarizes the investigation workflow.

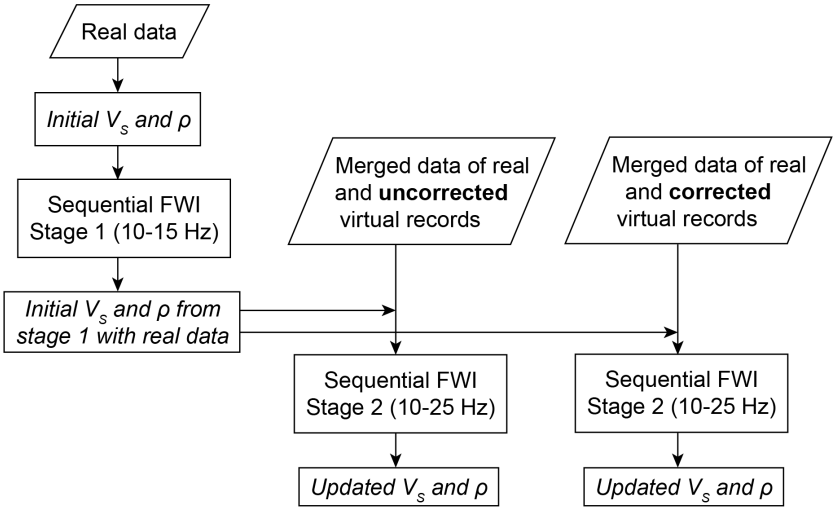

Figure 3.7: Workflow for investigating the impact of correcting the errors in the virtual shot records on the FWI results. Note that sequential FWI is composed of two simultaneous inversions for V_S and ρ, and designed for accurate density inversion (see Fig. 2.1).

A comparison of the inversion results using the above two datasets is illustrated in Fig. 3.8. When the uncorrected virtual records are used, the vertical stripes are more clearly visible in both V_S and ρ images produced by FWI (see red arrows in Figs 3.8(a)-(b)) than when using the real data alone (see Figs 3.3(a)-(b)). The erroneously retrieved surface waves do not properly respect the seismic wave equation, resulting in such unrealistic heterogeneous structure. The striped patterns are also partly caused by the significant difference in the spectral components between the real and the uncorrected virtual shot gathers, especially at the low frequencies (see Subsection 3.3.2). As low-frequency components are essential for updating the low-wavenumber structures, FWI using the uncorrected virtual records fails to update properly the low-wavenumber components. Furthermore, as shown in Fig. 3.1(b), the virtual sources are located in between the neighbouring real sources. The use of datasets with different frequency contents can, therefore, produce periodic perturbations in the gradient, and finally result in the striped-pattern artifacts in the inverted model. On the contrary, the corrected virtual records contain frequency components similar to those of the real records due to the additional low-frequency correction (see Subsection 3.3.2). This results in significantly less striped patterns, which in turn leads to more laterally continuous V_S and ρ images derived from FWI (Figs 3.8(c)-(d)). Our proposed approach for correcting the errors due to SI enhances the stability of FWI results when using virtual shot records.

POTENTIAL BENEFITS OF THE WEIGHTED FWI

So far, we have equally used real seismic and virtual seismic data during the inversion. Next, we look into the benefit of using the weighted misfit function (eqs 3.5 and 3.6) to merged real+virtual seismic data. The merged data is input to FWI. At first, we compare the inversion results between weighted and unweighted FWI. Both FWIs involve multi-scale inversion up to 40 Hz, starting with the same initial model. The workflow is summarized in

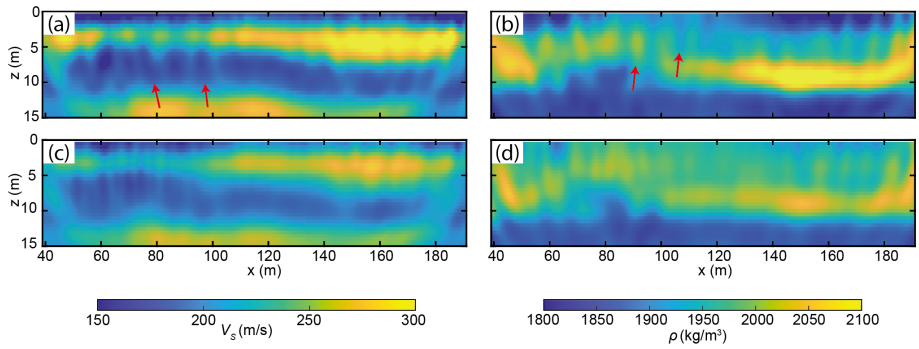

Figure 3.8: Comparison of FWI results for the merged data between (a)-(b) using the uncorrected virtual records and (c)-(d) using the corrected virtual records. The red arrows mark artifacts appearing as striped patterns due to errors contained in the virtual data.

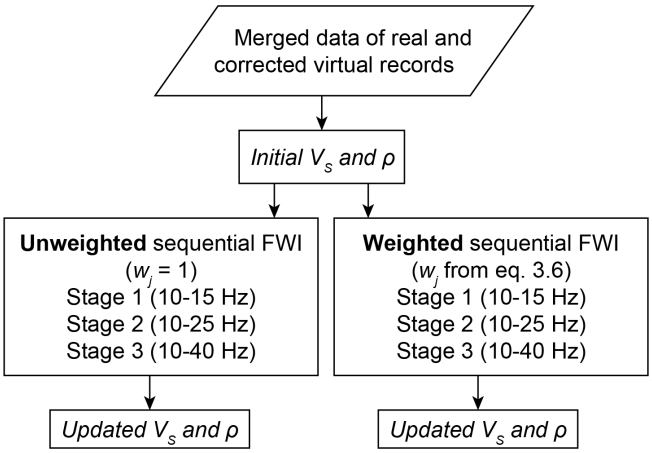

Figure 3.9: Workflow for investigating the impact of the weighted misfit function on FWI applied to the merged data of real and corrected virtual shot gathers. Note that sequential FWI is composed of two simultaneous inversions for V_S and ρ, and is designed for accurate density inversion (see Fig. 2.1).

Fig. 3.9.

We first calculate the weight for each virtual shot record at the first frequency stage (10-15 Hz) following eq. 3.6. Fig. 3.10(a) shows the misfit values for real and virtual records calculated using the initial model (Figs 2.4(a) and (c)). Note the very oscillatory distribution of the misfit values for the virtual shot records (red line in Fig. 3.10(a)) than for the real shot records (black line in Fig. 3.10(a)). Such abrupt changes in the misfit value are not expected between two neighbouring shot locations, considering the minimum wavelength at the current frequency stage (~ 13.3 m). The oscillatory nature likely represents the difference in the extent of errors contained in each virtual seismic gather. Therefore, one needs to assign a variable weight to different virtual shot gathers. Fig. 3.10(b) shows the calculated weight. There are virtual shot records at both edges of the survey line, i.e., 40

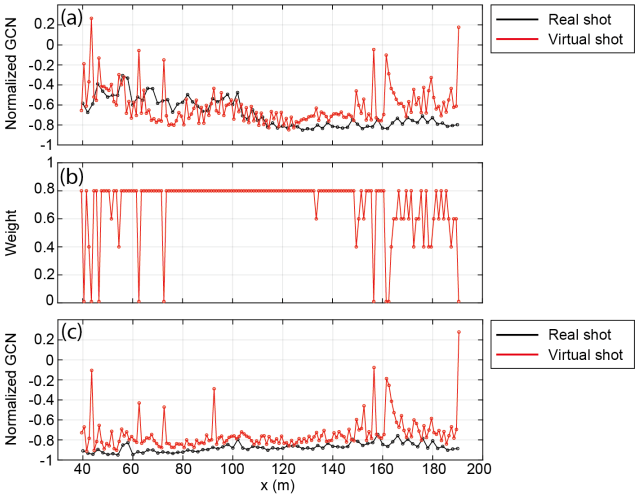

Figure 3.10: (a) Normalized GCN for real and virtual shot gathers at stage 1 (10-15 Hz) using the same initial model. (b) Calculated weight for each virtual shot gather from eq. 3.6, for which the misfit distribution is shown in (a). (c) Normalized GCN for the real and virtual shot gathers at stage 1 (10-15 Hz) for the final model.

m $< x <$ 80 m and 150 m $< x <$ 190 m, that show low weights. A possible reason is that, at the edges of the survey line, the summation of the cross-correlation waveforms cannot be performed for a homogeneous source distribution, resulting in errors in the wavefield retrieval through SI. The misfit distribution after the convergence is shown in Fig. 3.10(c). The inversion provides a good fit between the observed and the synthetic seismograms for both real and virtual seismic records, excluding the less weighted virtual shot records (see Figs 3.10(b)-(c)). In the subsequent stages, we also calculate the variable weights using the estimated model from the previous stage (Fig. 3.11). At high-frequency stages, the misfit values for the virtual records vary a lot with the source position compared to the real records, even after the convergence (see Figs 3.11(a), (c), (d) and (f)). This shows the difficulty in accurate retrieval of the higher modes at the high frequencies through SI. Nevertheless, after the weighted inversion, the misfit values for both the real and the virtual shot records are greatly reduced (Figs 3.11(c) and (f)).

We compare in Fig. 3.12 the subsurface images obtained from unweighted and weighted FWI. In contrast to FWI applied to real shot gathers only, the use of the merged data reduces the striped patterns produced by spatial aliasing, regardless of the used misfit functions. This leads to lateral continuity of structures in the FWI-derived image (compare Figs 3.3(a)-(b) and Fig. 3.12). For instance, the anomaly appearing as vertical stripes when using the real records only (red arrows in Fig. 3.3(a)) disappears by incorporating the virtual records (notice at (x, z) = (80 m, 5 m) in Figs 3.12(a) and 3.12(c)). One can also notice in Fig. 3.12 the benefits of the proposed weighting strategy. The unweighted FWI partially distorts the lateral continuity in both V_S and ρ images, which is visible in the inversion result from the real shot data only (see black rectangle and red arrow in Figs 3.12(a)-(b) compared with Figs 3.3(a)-(b)). The missing lateral continuity is restored by the weighted FWI. Clearly, introducing the variable weights is necessary in order to use beneficially the

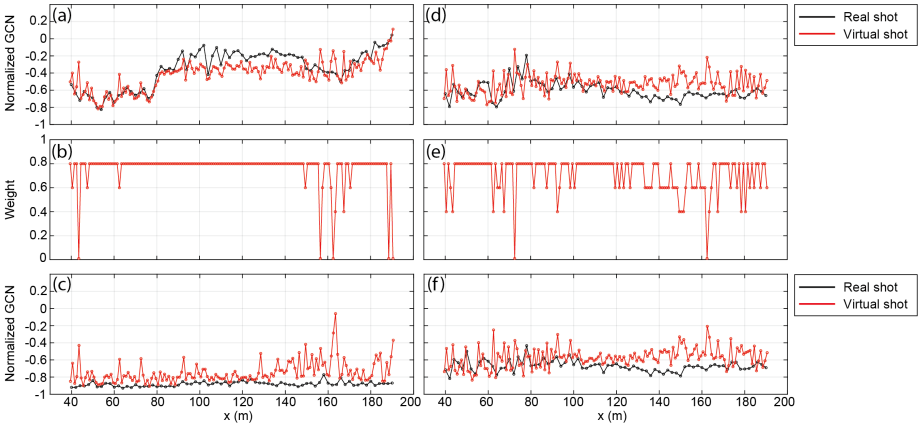

Figure 3.11: Same as Fig. 3.10, but for (a)-(c) stage 2 (10-25 Hz) and (d)-(f) stage 3 (10-40 Hz).

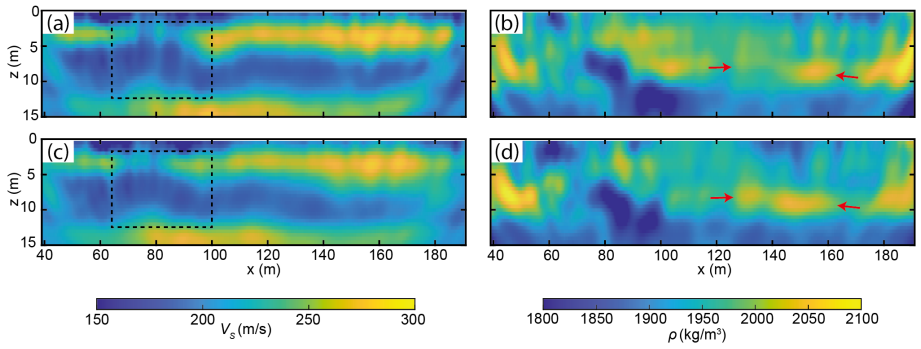

Figure 3.12: Comparison of inversion results between (a)-(b) unweighted FWI and (c)-(d) weighted FWI with weight shown in Figs 3.10 and 3.11, both applied to the merged data. The black rectangles and the red arrows show improvements in the lateral resolution due to assigning a suitable weight to each virtual shot gather.

merged real+virtual source data in FWI.

Finally, we calculate the model roughness Δm using eq. 3.8 to evaluate how the spatial aliasing effect can be reduced by making use of the virtual data (Fig. 3.13). The use of the merged data results in a laterally smooth model with very small $\|\Delta m\|^2$ compared to using the real data only in the FWI (compare between Figs 3.4(a)-(b) and Fig. 3.13). This happens due to reduction of the vertical stripes, as demonstrated also in the comparison of the derived models in Fig. 3.12. We then explore the impact of our weighting strategy on the model roughness. In FWI applied to the real data only, there is an anomaly with high Δm at (x, z) = (90 m, 3 m), shown in Figs 3.4(a)-(b). The same structure is not clear when using the merged data without weight (purple arrows in Figs 3.13(a)-(b)), while the high Δm anomaly exists when applying the weighted FWI (purple arrows in Figs 3.13(c)-(d)). This anomaly likely represents a true subsurface structure, because its shape is completely different from the artifacts due to spatial aliasing, that appear as striped patterns. This suggests that using

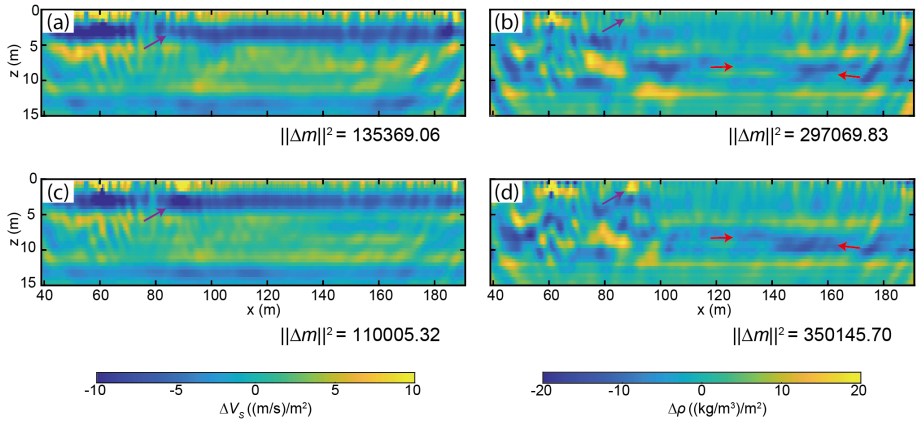

Figure 3.13: Same comparison as Fig. 3.12, but for model roughness (Δm) of the inverted images (Fig. 3.12) calculated using eq. 3.8. Note that there are fewer striped patterns compared to using the real shot records only. The red and the purple arrows mark the improvements of resolution due to using suitable weight for each virtual shot gather.

the virtual shot records in FWI without any constraints can cause a risk of deteriorating the achievable resolution. In this regard, our weighting strategy is beneficial for avoiding such risk, in turn enabling an increase of the imaging capability of the retrieved surface waves through FWI. We notice that $\|\Delta\rho\|^2$ for the weighted FWI is slightly larger than that for the unweighted FWI (see values shown in Figs 3.13(b) and (d)). This could have resulted from the successful reconstruction of the laterally continuous structure with a high value for ρ (see red arrows in Fig. 3.13(d) and in Fig. 3.12 (d)) due to adopting the weighting strategy.

Our investigation demonstrates that a weighted misfit function in FWI is of great importance to avoid losing information on subsurface due to the error in the virtual shot data.

3.4. Discussion

3.4.1. Improved subsurface structure due to the use of virtual shot records

In Subsection 3.3.3, we have demonstrated that the weighted FWI applied to the merged data of real+virtual seismograms helps avoiding the spatial aliasing in the source domain. This section focuses on how the estimated subsurface structure is improved by incorporating virtual seismic data retrieved from SI into the inversion.

We first investigate the V_S estimates through the weighted FWI using the merged data compared with using the real data only (Figs 3.14(a)-(b)). Although both cases reconstruct almost the same V_S structure, the differences at some locations are clear. One such location is at $x \sim 150$ m, where some lateral variability is recognizable when using the real data only, while the use of the merged data results in a much smoother image in the lateral direction (compare red arrows in Figs 3.14(a)-(b)). It is not possible to discuss the reliability of this difference in the absence of independent measurements at this location (see Fig. 2.2(a)).

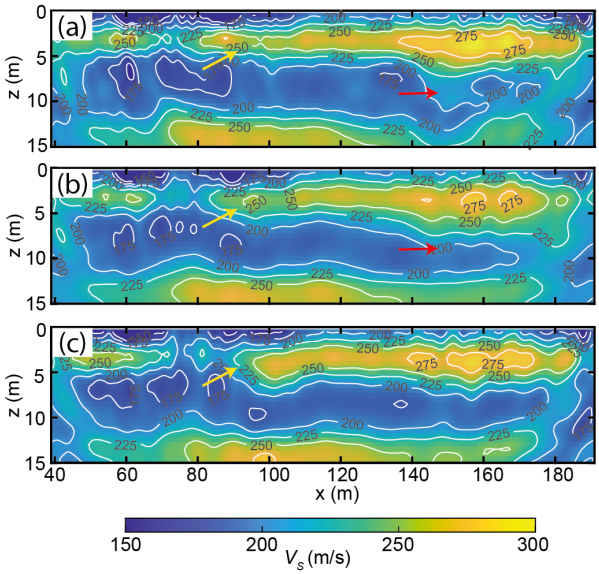

Figure 3.14: Comparison of V_S estimates: (a) FWI using the real seismic data only, (b) weighted FWI using the merged real+virtual seismic data, and (c) unweighted FWI using the merged real+virtual seismic data. The red arrows mark apparent improvements in resolution due to supplementing the virtual seismic data. The yellow arrows mark possible artifacts due to the use of the virtual seismic data, which is mitigated by using the weighted misfit function.

However, it is possible that the use of the aliasing-free seismic data does enable imaging the subsurface structure at the correct location as in conventional seismic migration (e.g., Yilmaz, 2001). Fig. 3.14 presents another difference arising from using the virtual records at $x \sim 100$ m; note the shape of V_S structure exhibiting $V_S > 225$ m/s (see yellow arrows in Fig. 3.14). The corresponding layer, when using the merged data in the FWI (Fig. 3.14(b)), is rather thick, and it dips slightly than when using the real data only in the FWI (Fig. 3.14(a)). To interpret this difference better, we show the inverted V_S from the unweighted FWI applied to the merged data in Fig. 3.14(c). We notice a much thicker high-V_S layer is with a larger dip angle than when weighted FWI is used (see yellow arrow in Fig. 3.14(c)). This suggests that the difference found in the high-V_S layer might be due to the existence of errors in the virtual shot records. These errors are mitigated by applying the weighting strategy, although some errors might still remain, resulting in the pattern observed in Fig. 3.14(b). These findings suggest that incorporating virtual seismograms may help improve the lateral resolution of the reconstructed V_S image, and reduce the artifacts associated with spatial aliasing, when combined with an appropriate weighting strategy.

Next, we investigate the possible improvement of the ρ image obtained from FWI through incorporation of the virtual shot data (Fig. 3.15). The major difference between using the merged real+virtual data and using only the real data is the presence of anomalous features showing very low ρ values below 7 m depth at $x = 80$-100 m (red arrows in Fig. 3.15(a)-(b)). The use of the merged data resolves the laterally varying structure with much smaller ρ values than when using the real data only. For a comparison, we present the spatial

distribution of CPT cone tip resistance (q_c) also in Fig. 3.15(c) (see Subsection 2.3.1 for the details of CPT surveys). At the same lateral distance, a soft clay layer having low q_c exists at much shallower part than the surrounding (see red arrow in Fig. 3.15(c)). The use of the virtual seismic shot gathers apparently helps capturing such local anomalies. To further interpret the reliability of the improvements, one needs to perform numerical investigations assuming specific models and the correct acquisition geometry.

In our field application, the lateral variability of the subsurface parameters is relatively moderate. As a result, the spatial aliasing in the source domain may not have caused severe distortions in the FWI results when using the real data alone. This may explain why the improvements due to incorporating the virtual shot gathers, although visible in certain localized areas, are somewhat limited. It is important to note that while it is true that virtual sources are created from the acquired seismic data and, in that sense, they do not introduce new independent information, yet creating virtual sources not only improves the effective source sampling and the wavefield illumination, but also it helps obtaining subsurface information that is present in the acquired wavefield but is not utilised when only actual sources were used. The impact of using additional virtual sources could be more significant in case there was much stronger lateral heterogeneity in the subsurface. Since this research is focused solely on field data, where the true subsurface structure is unknown, we have conducted only the limited evaluation for the improved resolution. Systematic synthetic reconstruction tests using heterogeneous models and realistic acquisition geometries would be required to rigorously assess the robustness and effectiveness of incorporating virtual sources into FWI.

3.4.2. Further investigation into the retrieved Love wave data

In this subsection, we explore the characteristics of the dispersive Love waves retrieved by SI compared to the dispersive Love waves observed in the field data. We compare how the dispersion characteristics vary in the space domain between real and virtual shot gathers.

In Fig. 3.16, we show the Love-wave energy at each source position for 10 Hz, 20 Hz, 30 Hz, and 40 Hz frequencies. We also mark the phase velocity that shows the maximum amplitude at each source position in Fig. 3.16, enabling us to visualize the spatial variation of the dispersive energy (see the black lines in Fig. 3.16). Note that more data samples are available for the virtual shot records (Figs 3.16(e)-(l)) than for the real shot records (Figs 3.16(a)-(d)); this is because the real and virtual sources exist at 2 m and 1 m spacing, respectively. For this reason, one can observe highly variable dispersion characteristics for the virtual Love waves (for example, compare between Figs 3.16(a) and (i)). At the lowest frequency (10 Hz), the virtual shot records do not have any coherent dispersion energy without corrections (see Fig. 3.16(e)), which is also discussed in Subsection 3.3.2. The real shot gather nearest to the virtual-source location compensates for this missing Love wave energy as shown in Fig. 3.16(i) (also see Subsection 3.3.2). At 20 Hz, their spatial distribution fluctuates highly in the uncorrected virtual data, compared to the real data (compare between Figs 3.16(b) and (f)). Considering the long wavelength corresponding to that frequency ($\sim$ 10 m), the existence of such highly fluctuating subsurface structure appears unrealistic; errors occurring during SI are partly responsible for this issue. Such errors are dampened by the matched filter in combination with the low-frequency correction, resulting in a stable distribution as we observe in Fig. 3.16(j). At further higher (30 Hz and

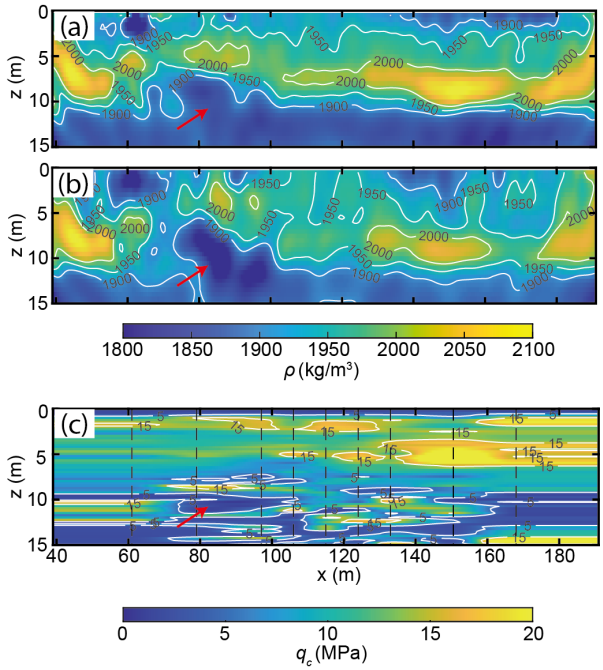

Figure 3.15: Comparison of ρ estimates: (a) FWI using the real seismic data only, (b) weighted FWI using the merged real+virtual seismic data, and (c) pseudo-2D image of the CPT cone tip resistance (q_c), also shown in Fig. 2.15(d). The red arrows mark apparent improvements due to incorporating the virtual seismic data in FWI.

40 Hz) frequencies for the Love waves, one can notice fine variations in space of the phase velocity showing maximum dispersive energy in the corrected records (compare between Figs 3.16(g) and 3.16(k) for 30 Hz, and between Figs 3.16(h) and 3.16(l) for 40 Hz). This result indicates that our approach of correcting the error caused by SI is effective, and it helps retrieving subsurface information from the virtual seismic data. The spatial variations observed in these frequencies and the corresponding wavelengths seem realistic.

In this research, we could not evaluate the accuracy of the estimated matched filter. In case a real source used for this estimation (D_R^{near} in eq. 3.4) does not coexist with a virtual source, which is the case for our field dataset, it is difficult to estimate a matched filter accurately. This problem becomes much more acute when the available seismic sources are further limited (for example, when $\Delta s_R = 4$ m). In that situation, one may not rely on a matched filter for correcting the errors in the SI-retrieved seismic data. A possible alternative approach is first to separate the multimodal dispersive data into individual modes, and then apply SI to each separated mode independently (D. Halliday & Curtis, 2008; Luo et al., 2009; Gao & Pan, 2018). This should be finally followed by the summation of the separately retrieved modes to create the fully dispersive surface wave dataset (D. Halliday & Curtis, 2008). This approach provides accurate phase information on surface waves without any cross-term spurious events. Then, the retrieved data can be directly (without matched-filter correction) used in FWI with a phase-focused misfit function as in our research (eq. 2.1).

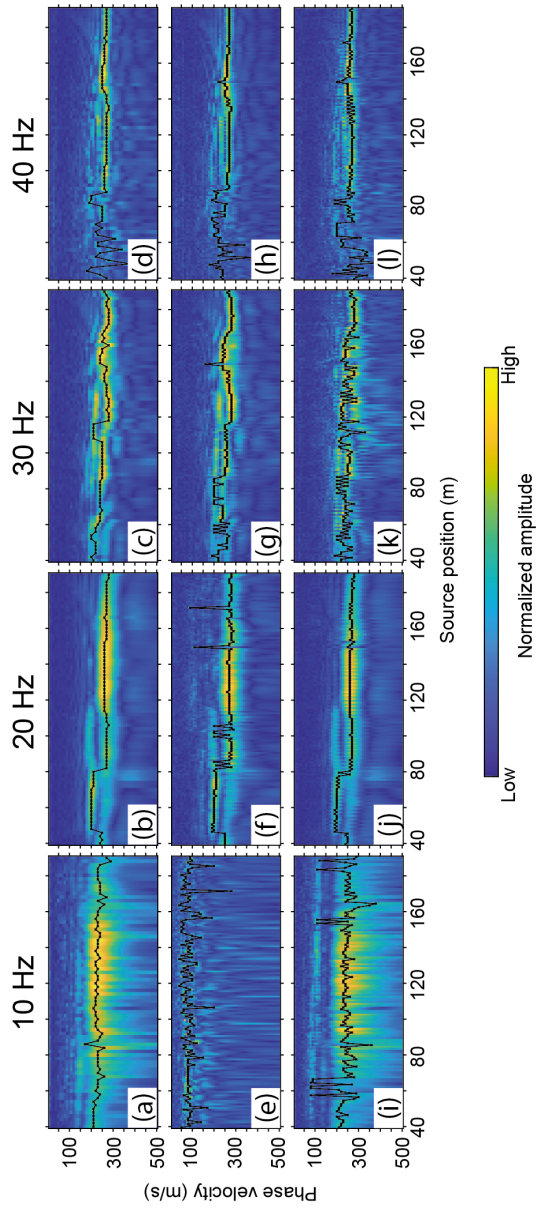

Figure 3.16: Comparison of Love-wave dispersion characteristics at monochromatic frequencies in: (a)-(d) the real (field) shot gathers, (e)-(h) the uncorrected virtual shot gathers, and (i)-(l) the corrected virtual shot gathers. The black lines indicate the phase velocities showing the maximum amplitude at each source position.

Also, one may define a new misfit function based on the forward modelling of the cross-correlation waveforms (i.e., $u(x_B, x_A) + u^*(x_B, x_A)$) (e.g., Wang et al., 2021). This will allow one to include SI-errors due to the distribution of seismic sources in the forward-modelled data.

3.5. Conclusions

In this chapter, we proposed the use of surface waves retrieved by SI in order to build aliasing-free seismic data for input to FWI. This approach enables enhancing the spatial resolution of the estimated subsurface image through FWI. We have concentrated on investigating potential challenges and benefits of the proposed approach through tests on Love-wave dominated, near-surface field-seismic data.

Through tests on field data for decimated source configurations, we illustrated that spatial aliasing in the source domain produces artifacts appearing as striped patterns in the gradient of the misfit function and in the estimated model. Additionally, the absolute value of the density becomes inaccurate with increasing spacing of the seismic source. These invite risks of misrepresentation and misinterpretation of the subsoil structure. We corrected amplitude and phase errors of the retrieved surface waves using a matched filter in combination with additional low-frequency correction. Compared with uncorrected virtual shot gathers, amplitude and phase corrected virtual shot gathers used in FWI provide greater lateral continuity and resolution in the dispersive characteristics of the Love waves. This leads to a more reliable subsurface characterization through FWI. In the inversion, we introduced a weighted misfit function to prevent worsening of the FWI results due to the remaining errors after the above-mentioned phase and amplitude corrections. The weighted FWI allows one to incorporate subsurface information from the SI-retrieved surface waves without severe distortions due to the errors in the virtual shot gathers. Tests on field data suggest that the proposed approach helps increasing the reliability of FWI results in terms of lateral resolution and estimated density value. This new technology will provide an opportunity to enhance the capability of 2D FWI without severe economic burden in seismic data acquisition, which is critical in many near-surface applications.

4

3D FWI FOR SUBSOIL DENSITY: TEST ON SYNTHETIC DATA FOR DIFFERENT FORCE DIRECTIONS OF THE SEISMIC SOURCE

Bulk density (ρ) of soil is an important indicator of soil compaction and type. A knowledge of the spatial variability of in-situ soil density is important in geotechnical engineering, hydrology and agriculture. Surface geophysical methods have so far shown limited success in providing an accurate and high-resolution image of 3D soil-density distribution. In this pursuit, 3D seismic FWI is promising, provided the robustness and accuracy of density inversion via this approach can be established in the near-surface scale. However, simultaneous reconstruction of ρ and seismic wave velocities through multi-parameter FWI remains a challenging task. Near-surface seismic data are commonly dominated by dispersive surface waves whose velocities are controlled by the value and distribution of V_S. One major difficulty in estimating reliably ρ from near-surface seismic data is due to the relatively low sensitivity of the seismic wavefield to ρ compared to seismic velocities. Additionally, the accuracy of the estimated ρ decreases due to errors in V_S, i.e., parameter coupling. Parameter coupling makes it difficult to estimate accurately ρ within the framework of conventional gradient-based FWI. More sophisticated optimization approaches (e.g., truncated Newton) can reduce the effect of parameter coupling, but these approaches are commonly not affordable in near-surface applications due to their heavy computational burden. We investigate how choosing correctly the force direction of the seismic source can contribute to a higher accuracy of ρ estimates through 3D FWI. Using scattered wavefields, the Hessian, and inversion tests, we carry out an in-depth and systematic investigation of datasets corresponding to different force directions. Using a comparison of the scattered wavefields due to

This chapter is published in Geophysical Journal International (Kawasaki et al. (2024)). For consistency with other chapters of this thesis, minor changes have been made.

a point-localized ρ perturbation for different force directions, we show the robustness of the horizontal-force dataset to noise compared to the vertical-force dataset. Furthermore, for a point-scatterer model, analysing the gradients of the misfit function using the Hessian, we show that utilizing a horizontal-force source enables one to reconstruct the high-resolution gradient with relatively small parameter coupling. Finally, performing inversion tests for two different subsoil models, we demonstrate that 3D FWI on a horizontal-force-source seismic dataset is capable of providing a more accurate 3D ρ distribution in soil compared to a vertical-force-source dataset. Our results show that the use of a horizontal-force source might allow avoiding computationally demanding, costly optimization approaches in 3D FWI.

4.1. INTRODUCTION

The distribution of density in the subsoil is generally quite heterogeneous. A knowledge of the 3D distribution of soil density is beneficial in numerous engineering and environmental applications, in urban planning and constructions, and in natural-hazard assessments. Bulk density (ρ) controls the soil's ability to provide structural support and determine water/solute movement and soil aeration. Bulk density is regarded as a key factor controlling soil compaction. Subsoil bulk density is closely linked to physical, chemical and biological properties of the soil layers. Different soil types and soil textures/structures correspond to different soil density. Density is also related to key geotechnical or hydrological parameters like porosity or void ratio, hydraulic conductivity, and small-strain shear modulus.

Soil density is conventionally measured by direct methods, e.g., excavation sampling, core and clod methods (VanRemortel & Shields, 1993) or by indirect methods, e.g., radiation and regression approaches (Lobsey & Viscarra Rossel, 2016). While the direct methods are affected by sampling disturbances, both methods are generally expensive and time-consuming. These conventional approaches are limited to a given point from where the soil sample is collected or to a 1D profile along a borehole. It is challenging to infer the 3D spatial variability of subsoil density.

Surface geophysical methods have occasionally been used to map the distribution of soil density. These methods are advantageous because they are mostly noninvasive, are generally useful for mapping large areas, and allow temporal monitoring. The microgravity method has been used for mapping variations in subsoil density related to cavities and voids and geological structures (e.g., Tuckwell et al., 2008; Arisona et al., 2018). Electrical and electromagnetic properties have been correlated to density and compaction distribution in the ground, mostly in the very shallow (< 2–3 m) soil layers which are relevant for agriculture and hydrogeology (e.g., Weihnacht & Börner, 2007; Allred et al., 2008; Franko & Grote, 2013). The bulk density inferred from these approaches is an empirical estimate, with limited spatial resolution and accuracy. Seismic wave velocities, both for P and S waves, have also been correlated to compaction and bulk density distribution in soil (Donohue et al., 2012; Anbazhagan et al., 2016; Romero-Ruiz et al., 2021).

More recently, seismic FWI has been used to obtain the 2D spatial variability of density in the near-surface (e.g., Dokter et al., 2017; Gao et al., 2020; Chen et al., 2021; Mecking et al., 2021). FWI has proven to be a powerful tool to reconstruct in high-resolution the subsurface properties by fitting the observed seismic data with synthetic data. With the increase of computation power, 3D FWI in the near-surface scale has lately been plausible

(e.g., Tran et al., 2019, 2020; Irnaka et al., 2022; Irnaka, 2022). 3D FWI can capture subsurface heterogeneities more accurately than 2D FWI because of incorporation of actual 3D wave propagation in the subsurface (Butzer et al., 2013; Irnaka et al., 2022). However, most 3D FWI studies so far concentrated on estimation of the high-resolution, near-surface seismic velocity field, and not density (e.g., Tran et al., 2019, 2020; Smith et al., 2019; Teodor et al., 2021; Irnaka et al., 2022; Irnaka, 2022).

FWI is capable of evaluating simultaneously multiple parameters viz. seismic velocities (V_P, V_S), density (ρ) and attenuation (Q_P, Q_S), across a variety of spatial scales. Herein, we will focus on 3D ρ estimation in the near-surface scale using active seismic sources. The main difficulties in resolving the ρ distribution with reasonable accuracy arise mainly from the low sensitivity of the seismic wavefield to ρ (compared to V_P and V_S) and strong coupling among multiple parameters, especially between ρ and V_S (W. Pan, Geng, & Innanen, 2018). Near-surface seismic data are typically dominated by surface waves which are most sensitive to the V_S distribution and much less sensitive to ρ. As a result, any differences in waveform due to ρ perturbations can easily be hidden by noise in real-world data.

Several approaches have so far been proposed to mitigate the parameter coupling effect in FWI (Köhn et al., 2012; Métivier et al., 2015; Wang et al., 2016; Yang et al., 2016; W. Pan, Geng, & Innanen, 2018; Gao et al., 2021). However, these approaches are mostly computationally prohibitive for near-surface applications. For instance, taking the shape of the misfit function between observed and synthetic seismic waveforms into consideration, Métivier et al. (2015) and Gao et al. (2021) applied truncated Newton method with an accurate Hessian inverse. They showed, using 2D synthetic seismic data, the superiority of this approach over gradient-based optimization approaches such as NCG and BFGS for multi-parameter FWI. However, solving the Newton's equation iteratively using the second-order adjoint-state method requires at each nonlinear iteration up to several tens of forward simulations more than the gradient-based inversion (Métivier et al., 2013). Because a typical unconsolidated and fully saturated soil column including very soft peat and clay layers can have V_S as low as 50 m/s and V_P about 1500 m/s, the forward calculation of the seismic wavefield requires very fine spatial and temporal sampling. This results in a very high computational cost. This computational burden, in addition to the low sensitivity of seismic data to ρ, have been the limiting factors for application of 3D FWI for estimating high-resolution ρ distribution in the subsoil.

The parameter-coupling effect has been conventionally evaluated by comparing the theoretical radiation pattern of the scattered wavefields between different parameter classes based on the Born approximation (e.g., Virieux & Operto, 2009; Operto et al., 2013). This theoretical approach does not take the various factors included in seismic data into account, such as the complexity of a subsurface model, the effect of finite frequency, and the acquisition geometry. This limitation can bring misunderstanding and/or misinterpretation of the parameter-coupling effect. In order to quantitatively evaluate the parameter coupling on the gradient of the misfit function in a realistic situation, W. Pan, Geng, and Innanen (2018) proposed a method that uses numerically calculated Hessian-vector products. However, this technique has not been applied to surface-wave dominated, 3D near-surface seismic data.

To mitigate the low-sensitivity and parameter-coupling issues in FWI for ρ estimation, another idea is to make a judicious choice of the force direction while generating the seismic wavefield. Previous studies have shown that, compared to a vertical-force seismic source,

using a horizontal-force source results in less parameter coupling in 2D FWI and higher resolution of the obtained V_S and ρ models (Dokter et al., 2017; Wittkamp et al., 2018). If the parameter-coupling issue is less severe in case a horizontal-force source is used, then that will lead to computational efficiency. Smith et al. (2019) and Irnaka (2022) have also shown that using a horizontal-force source has helped increasing the accuracy in the deeper part of the near-surface model obtained via 3D FWI. However, the reasons why a horizontal-force source should offer better results in FWI (greater accuracy and less parameter coupling) than a vertical-force source are not yet sufficiently understood.

In this research, we systematically investigate the effect of using different force directions on the accuracy of the 3D FWI. We first investigate the waveform differences due to a ρ perturbation, and the impact of different source-force directions on the noise robustness. To evaluate the parameter-coupling effect, we then investigate the differences in the shape of the misfit function (i.e., the gradient and Hessian). We use the numerically calculated Hessian for this purpose. The Hessian is also used to compare the resolution of the estimated density. Finally, we perform 3D FWI using synthetic data considering realistic near-surface subsoil models and different force directions.

This chapter is organized as follows. First, we briefly explain the theory of FWI that is relevant for comparing systematically the three factors mentioned above (i.e., noise robustness, parameter coupling, and resolution) for the purpose of 3D ρ estimation. We then explore in detail the effect of force directions on these three factors for a point-scatterer model. Lastly, we perform 3D FWI for a spatially uncorrelated model and a realistic subsoil model derived from field measurements, and compare the accuracy of the reconstructed ρ for different force directions.

4.2. Methodology

4.2.1. 3D FWI

FWI solves a nonlinear optimization problem to reconstruct the subsurface model by minimizing the misfit function E defined by the synthetic and the observed seismic data (e.g., Pratt et al., 1998). In this study, we use the square of l_2 norm of the waveform differences as the misfit function E:

$$E(m) = \frac{1}{2} \| u_{\text{syn}}(m) - u_{\text{obs}} \|^2, \tag{4.1}$$

where $u_{\text{syn}}(m)$ is the synthetic seismic (displacement) data calculated assuming a subsurface model m, and u_{obs} is the observed seismic data. We choose this misfit function, instead of the GCN used in Chapters 2 and 3, in order to utilize the whole waveform information contained in each force-direction dataset. Note that the misfit function does not include the explicit regularization terms. Instead, the inversion stability is ensured by applying several preconditioning filters to the gradient of the misfit function, as discussed also earlier (see Section 2.2.1). The details of the adopted filters are given below. The model parameters m are the elastic properties (V_P, V_S, and ρ) that are functions of space in 3D. We use the FDTD method to calculate the synthetic seismic data (Virieux, 1986; Levander, 1988). We generate body force in different directions (f_x, f_y, f_z) in the Cartesian coordinate system, at the same position and with the same amplitude (unit: N/m^3).

The minimization of the misfit function E in eq. 4.1 and finding an optimal solution for m over the large parameter space is a nonlinear, large-scale problem. Therefore, a local optimization approach is commonly employed to solve this problem (e.g., Mora, 1987; Pratt et al., 1998; Brossier et al., 2009). The local optimization approach iteratively updates the model parameters m using the following formula:

$$m_{n+1} = m_n + \alpha_n \Delta m_n, \tag{4.2}$$

where m_n is the model parameter at nth iteration, Δm_n is the descent direction of the misfit function E, and α_n is the step length that is estimated by a line search method (Nocedal & Wright, 2006). Among various nonlinear optimization approaches to calculate Δm_n, the gradient-based approaches, such as SD, NCG, and l-BFGS, are considered in this study, given the respective computation costs. In the case of SD, the following simple formula is used for the calculation of Δm_n:

$$\Delta m_n = -P_m \nabla_m E_n, \tag{4.3}$$

where $\nabla_m E_n$ is the gradient of the misfit function calculated by the adjoint-state method (Plessix, 2006), and P_m is the preconditioning filter. The other approaches (NCG and l-BFGS) use the same formula (eq. 4.3) at the first iteration, and after that they use Δm_n which is calculated using $\nabla_m E_n$ at the current iteration n and the previous history of $\nabla_m E_n$. Therefore, the characteristics of $P_m \nabla_m E_n$ are the key elements for effectively solving the optimization problem using these approaches (SD, NCG, l-BFGS).

To reconstruct ρ models, we apply 3D FWI to the synthetic datasets generated using different force directions for the seismic source. First, to reduce the memory requirements, we adopt the time-frequency approach (Sirgue et al., 2008; Sirgue et al., 2010): the seismic wavefield u_{syn} is simulated in the time domain, but the descent direction of the misfit function Δm_n is calculated in the frequency domain. During the nonlinear inversion, the descent direction Δm_n is calculated using the NCG method (Nocedal & Wright, 2006). Δm_n is then normalized by the maximum value of each parameter class, followed by scaling with the representative value of each model parameter. The same step length α_n is assumed for all parameter classes; α_n is estimated by a line search method in order to invert all model parameters simultaneously.

The preconditioning filter P_m in eq. 4.3 is also essential in controlling accuracy and efficiency of FWI. For P_m, we take the diagonal elements of the approximate Hessian for each parameter class (Subsection 4.7.1). In FWI, this filter is conventionally used to compensate for the effect of the limited illumination on $\nabla_m E_n$, such as geometrical spreading (e.g., Ravaut et al., 2004; Operto et al., 2004, 2006). This filter also calculates suitable scaling for each parameter class, as the diagonal elements of the approximate Hessian contain the information of the scattering radiation pattern (for details see Subsection 4.7.1). Finally, in order to reduce the computational cost to calculate the Hessian, we estimate P_m only at the first iteration, and use the same filter for the rest of the inversion. Note that this strategy can decrease the performance of FWI, e.g., convergence speed and accuracy of an estimated model, when the initial model is very far from an optimum model.

4.2.2. Approach to evaluate different force directions in 3D FWI for density

We investigate the capability of 3D FWI to estimate ρ by concentrating on three factors viz. noise robustness, parameter coupling, and resolution (Section 4.3). We then evaluate the reconstructed ρ models using different force directions (Section 4.4). In this subsection, we discuss our approach of assessing the efficacy of these different force directions, considering the above-mentioned three factors and the theory introduced in Subsection 4.2.1.

Noise robustness

For real-world applications of FWI on noisy field data, the robustness is a crucial factor. As shown in eq. 4.1, FWI finds the model parameter m that minimizes the square of the l_2 norm of the waveform residuals. Suppose the observed data with noise can be divided into data calculated using the true model and noise, i.e., $u_{\text{obs}} = u_{\text{syn}}(m_{\text{true}}) + u_{\text{noise}}$. In this case, when we consider a specific model parameter $m = m_0$ ($\neq m_{\text{true}}$), eq. 4.1 can be written as,

$$E(m_0) = \frac{1}{2} \| u_{\text{sct}}(m_0) + u_{\text{noise}} \|^2, \tag{4.4}$$

where the scattered wavefield $u_{\text{sct}}(m_0)$ due to the model perturbation $(m_{\text{true}} - m_0)$ is defined as $u_{\text{sct}}(m_0) = u_{\text{syn}}(m_{\text{true}}) - u_{\text{syn}}(m_0)$. Eq. 4.4 shows that the value of E is determined by the amplitude of noise when the amplitude of u_{noise} is larger than that of $u_{\text{sct}}(m_0)$. This makes it difficult to effectively distinguish the difference between m_{true} and m_0.

We consider a specific pair of the model (m_0, m_{true}) where the difference is only in ρ, and other properties (V_P and V_S) remain the same. Then, we calculate numerically the scattered wavefield $u_{\text{sct}}(m_0)$ and the squared norm of the amplitudes. Here, seismic sources and receivers are distributed on the free surface. We compare the noise robustness for different force directions using the squared norm of the amplitude in the scattered wavefields.

Parameter coupling

As shown in eqs 4.2 and 4.3, the preconditioned gradient $P_m \nabla_m E_n$ contains key information to obtain the accurate descent direction Δm_n close to the true model-update direction at the first iteration when using SD, NCG, and l-BFGS. The gradient $P_m \nabla_m E_n$ partly represents the shape of the misfit function E in the model domain. Generally, evaluating the shape of E is crucial in order to solve the inverse problem advantageously in terms of both accuracy and efficiency. For example, $-\nabla_m E_n$ represents the direction in which E decreases, but it is not always identical to the direction toward the true model: assuming that the misfit function E is a quadratic function, there is a possibility that the descent direction to an optimum solution of a certain parameter class (e.g., V_S) contaminates the descent direction of another parameter class (e.g., ρ). In this research, we delve into this parameter coupling contained in the gradient. As illustrated in eqs 4.2 and 4.3, the inversion at the first iteration seeks an optimum solution along the direction of $-P_m \nabla_m E_n$ using a line search method. This procedure implies that a significant parameter coupling effect in $-P_m \nabla_m E_n$ can make the model parameter fall into local minima at early iterations, and the inversion fails to converge to an optimum solution. For FWI, using datasets corresponding to different force directions implies optimizing E having different shapes in the model domain. We, therefore, investigate the shape of E and explore the parameter-coupling effect in $-P_m \nabla_m E_n$ due to the force direction.

First, we define the parameter-coupling effect in $\nabla_m E$. When the misfit function E is quasi-linear, i.e., m_n is close to the optimum solution, E can be approximated as a quadratic function of m. In this case, $\nabla_m E$ follows the Newton's equation:

$$-\nabla_m E(m_n) = H(m_n)\Delta m^N, \tag{4.5}$$

where $H(m_n)$ is the Hessian of E at $m = m_n$, and Δm^N is the model-update direction toward the optimum solution. Eq. 4.5 indicates that the update direction based on the gradient (i.e., $-\nabla_m E(m_n)/|\nabla_m E(m_n)|$) is not identical to the Newton-step direction (i.e., $\Delta m^N/|\Delta m^N|$). This difference is the parameter coupling considered in this study, which is characterized by the Hessian $H(m_n)$ in eq. 4.5. Here, the Hessian has a multi-parameter form $H_{m_i m_j}$ and is written using Jacobian ($\partial u_{\text{syn}}/\partial m$) as follows:

$$\begin{aligned} H_{m_i m_j} &= \Re\left\{\left(\frac{\partial u_{\text{syn}}}{\partial m_i}\right)^* \left(\frac{\partial u_{\text{syn}}}{\partial m_j}\right) + \left(\frac{\partial^2 u_{\text{syn}}}{\partial m_i \partial m_j}\right)^* \left(u_{\text{syn}} - u_{\text{obs}}\right)\right\} \\ &= H^a_{m_i m_j} + R_{m_i m_j}, \end{aligned} \tag{4.6}$$

where m_i and m_j are model parameters (V_P, V_S, ρ), and the symbol * denotes the complex conjugate in the frequency domain. The first term $H^a_{m_i m_j}$ on the right-hand side of eq. 4.6 is the approximate Hessian, which is the cross-correlation between Jacobians with respect to m_i and m_j. The second term $R_{m_i m_j}$ on the right-hand side of eq. 4.6 is the cross-correlation between the second-order partial-derivative wavefield and the data residual, which represents the second-order scattering (Pratt et al., 1998). In this study, assuming that the residuals are small due to small model perturbations, the second term $R_{m_i m_j}$ is neglected and only the approximate Hessian $H^a_{m_i m_j}$ is considered. Thus, eq. 4.5 can be rewritten as follows:

$$-\begin{bmatrix} \nabla_{V_P} E \\ \nabla_{V_S} E \\ \nabla_\rho E \end{bmatrix} \approx \begin{bmatrix} H^a_{V_P V_P} & H^a_{V_P V_S} & H^a_{V_P \rho} \\ H^a_{V_S V_P} & H^a_{V_S V_S} & H^a_{V_S \rho} \\ H^a_{\rho V_P} & H^a_{\rho V_S} & H^a_{\rho\rho} \end{bmatrix} \begin{bmatrix} \Delta {V_P}^N \\ \Delta {V_S}^N \\ \Delta \rho^N \end{bmatrix}. \tag{4.7}$$

The diagonal elements of the matrix on the right-hand side of eq. 4.7 (e.g., $H^a_{\rho\rho}$) represent the coefficients for the Newton step (e.g., $\Delta\rho^N$) in the gradient of the same parameter class (e.g., $\nabla_\rho E$). On the other hand, the off-diagonal elements represent how the gradient for a certain parameter class (e.g., $\nabla_\rho E$) is influenced by the Newton step of the other parameter classes (e.g., $\Delta {V_S}^N$), i.e., the parameter-coupling effect. Therefore, the effect in the gradient can be evaluated by investigating the relative strength of the off-diagonal elements with respect to the diagonal elements. Note that the diagonal elements are the auto-correlation of Jacobians for a certain model-parameter class (i.e., $m_i = m_j$), and the off-diagonal elements are the cross-correlation between Jacobians for two different model parameter classes (i.e., $m_i \neq m_j$). In this research, we calculate directly Jacobians for each parameter class using the receiver-side Green's functions and the forward-propagated wavefields, following eq. 5.6 in Butzer (2015). This is followed by the cross-correlation of Jacobians to compute the approximate Hessian (H^a) explicitly.

We evaluate eq. 4.7 using numerically calculated Hessian for a specific model in order to compare the parameter-coupling effect for different force directions (Subsection 4.3.2). Furthermore, to take into account the preconditioned gradient in the actual implementation

of FWI (eq. 4.3), we consider the preconditioning filter P_m in eq. 4.7. By multiplying both sides of eq. 4.7 with P_m, we have the following relations:

$$\begin{aligned} -P_{V_P}\nabla_{V_P}E &\approx P_{V_P}H^a_{V_PV_P}\Delta {V_P}^N + P_{V_P}H^a_{V_PV_S}\Delta {V_S}^N + P_{V_P}H^a_{V_P\rho}\Delta {\rho}^N \\ &= K_{V_P\leftarrow V_P} + K_{V_S\rightarrow V_P} + K_{\rho\rightarrow V_P}, \end{aligned} \tag{4.8}$$

$$\begin{aligned} -P_{V_S}\nabla_{V_S}E &\approx P_{V_S}H^a_{V_SV_P}\Delta {V_P}^N + P_{V_S}H^a_{V_SV_S}\Delta {V_S}^N + P_{V_S}H^a_{V_S\rho}\Delta {\rho}^N \\ &= K_{V_P\rightarrow V_S} + K_{V_S\leftarrow V_S} + K_{\rho\rightarrow V_S}, \end{aligned} \tag{4.9}$$

$$\begin{aligned} -P_{\rho}\nabla_{\rho}E &\approx P_{\rho}H^a_{\rho V_P}\Delta {V_P}^N + P_{\rho}H^a_{\rho V_S}\Delta {V_S}^N + P_{\rho}H^a_{\rho\rho}\Delta {\rho}^N \\ &= K_{V_P\rightarrow \rho} + K_{V_S\rightarrow \rho} + K_{\rho\leftarrow \rho}, \end{aligned} \tag{4.10}$$

where we call $K_{m_i\leftarrow m_i}$ and $K_{m_j\rightarrow m_i(m_i\neq m_j)}$ the update kernel and the contamination kernel, respectively (W. Pan, Geng, & Innanen, 2018). Note that W. Pan, Geng, and Innanen (2018) do not include the preconditioning filter in the definition of the kernels. Furthermore, when Δm^N is localized at a single point, the kernels are identical to the point-spread functions (PSFs, Fichtner & Trampert, 2011; Fichtner & van Leeuwen, 2015; W. Pan, Geng, & Innanen, 2018; W. Pan et al., 2019), which is used for evaluating the resolution in this study (see the next section). In this research, we numerically calculate the kernels in eqs 4.8–4.10 using a point-scatterer model considering typical near-surface seismic acquisition parameters. We then investigate how the relative strength between the update and the contamination kernels differ due to different force directions.

Resolution

Resolution is another important indicator to evaluate the performance of FWI. For instance, in near-surface engineering problems, it is sometimes important to detect the existence of a thin layer in the subsurface or to image the accurate shape of an anomaly like a void. We investigate here how the resolution of FWI in such cases might differ for the different force directions.

First, we define the resolution using kernels introduced above. Given a point-localized perturbation as Δm^N in eqs 4.8–4.10, the spatial distribution of the value of the update kernel in the model domain represents how Δm^N is smeared around a point scatterer in the preconditioned gradient. On the other hand, the distribution of the values of the contamination kernel in the model domain represents the spatial extent where the parameter coupling prevails around a point scatterer in the preconditioned gradient. We define the spreading width of the kernels as the distance between the point scatterer and the location where the value of the kernels is half of the maximum value of the update kernel. A large spreading width of the update kernel will indicate low resolution of the reconstructed model, while a large spreading width of the contamination kernel will imply occurrence of spatial parameter-coupling in a wide area around the point scatterer.

Evaluating the resolution using the kernels defined above is similar to the resolution analysis in W. Pan, Geng, and Innanen (2018), except that we use the inverse of the diagonal elements of the approximate Hessian as the generalized inverse of the Hessian in the resolution matrix (see equation 54 in W. Pan, Geng, and Innanen (2018)). As before, we numerically calculate the kernels using a point-scatterer model considering typical near-surface seismic acquisition parameters and then investigate how the spreading widths of the kernels differ for different force directions (Subsection 4.3.3).

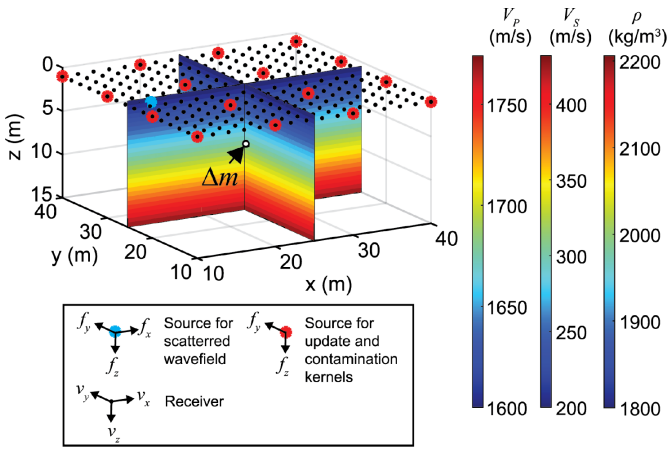

Figure 4.1: A synthetic model for investigating noise robustness, parameter coupling, and resolution.

4.3. Results of 3D FWI for different force directions: noise, parameter coupling and resolution

For these numerical tests, we consider a depth-dependent 3D model with a point scatterer at a location where V_S and ρ perturbations are allocated at a single grid ([x, y, z] = [25 m, 25 m, 7.5 m] in Fig. 4.1). The model is discretized with 100× 100× 50 grid points in x-, y-, and z-direction, respectively, with a grid spacing of 0.5 m. The background values of V_P, V_S and ρ are kept within the typical ranges found for soils, assuming fully water-saturated condition (V_P: 1600-1800 m/s, V_S: 200-450 m/s, ρ: 1800-2200 kg/m^3). Sources and receivers are distributed on the free surface as shown in Fig. 4.1. Such a setup for the numerical study allows investigating the scattered wavefields due to a point scatterer. Given a good initial model, FWI aims to reconstruct the true model using the scattered wavefield dominated by first-order scattering due to small perturbations in medium properties. The following discussion using a point scatterer can be applied to a complex wavefield in the real world, as such a wavefield can be approximated as superposition of scattered wavefields due to point scatterers distributed over the entire model space.

4.3.1. Noise robustness

We investigate for different source directions the noise robustness of ρ estimation using wavefields scattered due to a perturbation in ρ only (Subsection 4.2.2). For calculating the scattered wavefields, the background models without $\Delta\rho$ and with $\Delta\rho$ located at [x, y, z] = [25 m, 25 m, 7.5 m] are denoted as m_0 and m_{true}, respectively (Fig. 4.1). As model perturbation, a $\Delta\rho$ which is -10% of the background value is considered. We calculate three-component particle-velocity wavefields (i.e., v_x, v_y, v_z) due to a seismic source, denoted by the cyan symbol in Fig. 4.1. For a comparison between different force directions, three sources with three different force directions (i.e., f_x, f_y, f_z) are considered at the same location. Here, the directions for the two horizontal-force sources are either in the 2D plane containing both of the source and a point scatterer (x-direction) or perpendicular to it (y-direction), which

Table 4.1: Squared norm of the amplitude in the nine-component scattered wavefields shown in Fig. 4.2.

	v_x	v_y	v_z	total
f_x	10.6e-09	4.1e-09	7.9e-09	22.6e-09
f_y	7.4e-09	16.7e-09	1.2e-09	25.2e-09
f_z	5.7e-09	4.3e-09	6.5e-09	16.4e-09

enables one to take into account scattered wavefields generated by significantly different incident wavefields (i.e., SV/Rayleigh waves for an f_x source and SH/Love waves for an f_y source). We use the following Fuchs-Müller wavelet (Fuchs & Müller, 1971) with a centre frequency $f_c = 20$ Hz:

$$f(t) = \sin\left(2\pi t f_c\right) - 0.5\sin\left(4\pi t f_c\right). \tag{4.11}$$

To keep the computation time for the 3D FWI manageable, this frequency is not chosen to a higher value. Sources and receivers are located on the free surface.

In Fig. 4.2, we show the snapshots at 0.14 s, illustrating different characteristics of the wavefield due to different force directions. With horizontal-force sources, the energy of the scattered wavefields at the location of $\Delta\rho$ dominates in the backward direction (see Figs 4.2(a), (c) and (e)). These wavefields are generated by the incident SV/Rayleigh and SH/Love waves for the f_x and f_y sources, respectively; the surface waves (Rayleigh/Love waves) propagate parallel to the free surface toward the point scatterer, while the body waves (SV/SH waves) have incident angles of ~60°. When using a vertical-force source (f_z), the incoming Rayleigh wave is back-scattered with a large amplitude (see Fig. 4.2(g)), while some energy is present also in the forward direction (see Figs 4.2(g) and (i)).

To address the noise robustness, we calculate the squared norm of the amplitude in the scattered wavefields over the depth slice shown in Fig. 4.2. A comparison of the sum of the squared norm (Table 4.1) shows that the scattered wavefields due to horizontal-force sources (f_x or f_y) have more energy than those due to a vertical-force source (f_z). Additionally, Table 4.1 shows that the scattered wavefield at the same receiver component as the source (i.e., f_x-v_x, f_y-v_y and f_z-v_z) has, as expected, the largest energy. Furthermore, the scattered wavefields for the horizontal sources (f_x-v_x or f_y-v_y) have much larger energy than the vertical force (f_z-v_z). This large energy in f_x-v_x or f_y-v_y wavefields are due to the presence of backward scattering with large amplitudes (see Figs 4.2(a) and (e)). Thus, in the context of ρ estimation, 3D FWI applied to a horizontal-force dataset is more robust to noise than that applied to a vertical-force dataset (see Subsection 4.2.2), assuming same amplitude and source-time function for all sources. As the scattered wavefields generated by different incident wavefields from the two orthogonal horizontal-force sources (i.e., SV/Rayleigh waves for an f_x source and SH/Love waves for an f_y source) have larger energy than those due to a vertical-force source, the conclusion on noise robustness remains valid for the case when the source is located at any arbitrary location on the free surface.

4.3.2. PARAMETER COUPLING

Here we investigate the parameter-coupling effect in the preconditioned gradient for ρ using the update and the contamination kernels calculated for the same point-scatterer model as

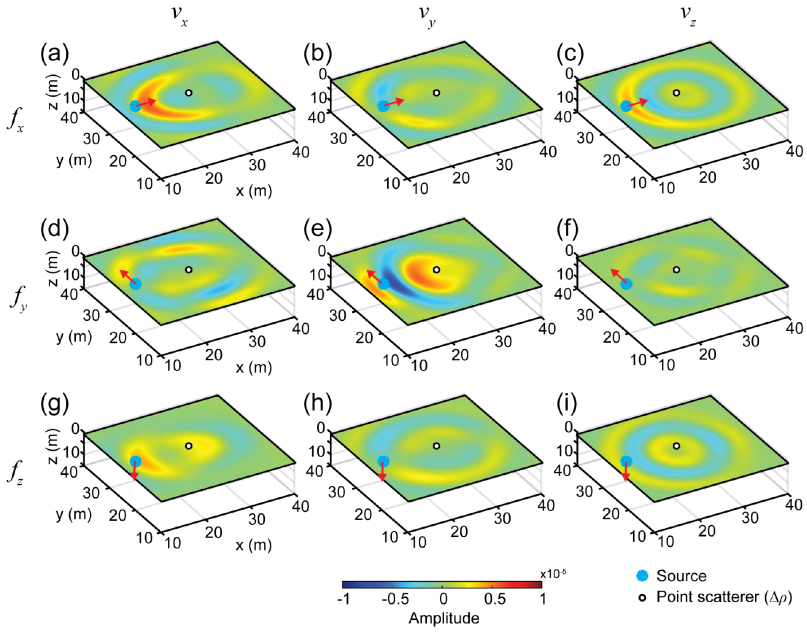

Figure 4.2: Depth slice of nine-component scattered wavefields (three-component source: f_x, f_y, f_z, three-component particle velocity: v_x, v_y, v_z) due to a point scatterer $\Delta\rho$.

in Subsection 4.3.1 (see Subsection 4.2.2). We compare the relative strength between these two kernels for different force directions.

For calculation of the kernels, 16 seismic sources located at 10 m spacing and 256 three-component receivers at 2 m spacing are used; they are respectively denoted by red and black symbols in Fig. 4.1. The vertical-force sources (i.e., f_z) and horizontal-force sources (i.e., f_y) have the same source-time function (eq. 4.11), as in Subsection 4.3.1. We consider only one horizontal-force direction (i.e., f_y) because the model and the acquisition geometry are symmetric. The kernels are calculated in the frequency domain using 8 monochromatic frequencies (i.e., 10, 14, 18, 22, 26, 30, 34, 38 Hz). This setup enables us to evaluate the impact of a typical near-surface seismic acquisition geometry on the kernels. The kernels are calculated (eqs 4.8–4.10) assuming a perturbation (-10% of the background value) as the Newton step (Δm^N) at a point scatterer.

Fig. 4.3 presents a comparison of the preconditioned gradients for ρ calculated using the adjoint-state method (i.e., $-P_\rho \nabla_\rho E$ in eq. 4.10) and the update and contamination kernels for ρ (i.e., $K_{\rho\leftrightarrow\rho}$ and $K_{V_S\rightarrow\rho}$ in eq. 4.10) between datasets corresponding to different source-force directions. The relative strength between the update and the contamination kernels is compared based on the maximum magnitude of the kernels shown in Fig. 4.3. When using the f_z dataset, $K_{V_S\rightarrow\rho}$ (Fig. 4.3(c)) has a larger relative strength than $K_{\rho\leftrightarrow\rho}$ (Fig. 4.3(b)). In other words, the effect of the perturbation of V_S (i.e., ΔV_S^N) dominates in $-P_\rho \nabla_\rho E$ (Fig. 4.3(a)); the strong parameter coupling occurs when updating the ρ model in the direction along $-P_\rho \nabla_\rho E$. On the contrary, $K_{V_S\rightarrow\rho}$ for f_y dataset (Fig. 4.3(f)) has a smaller relative strength than $K_{\rho\leftrightarrow\rho}$ (Fig. 4.3(e)). This implies that $-P_\rho \nabla_\rho E$ (Fig. 4.3(d))

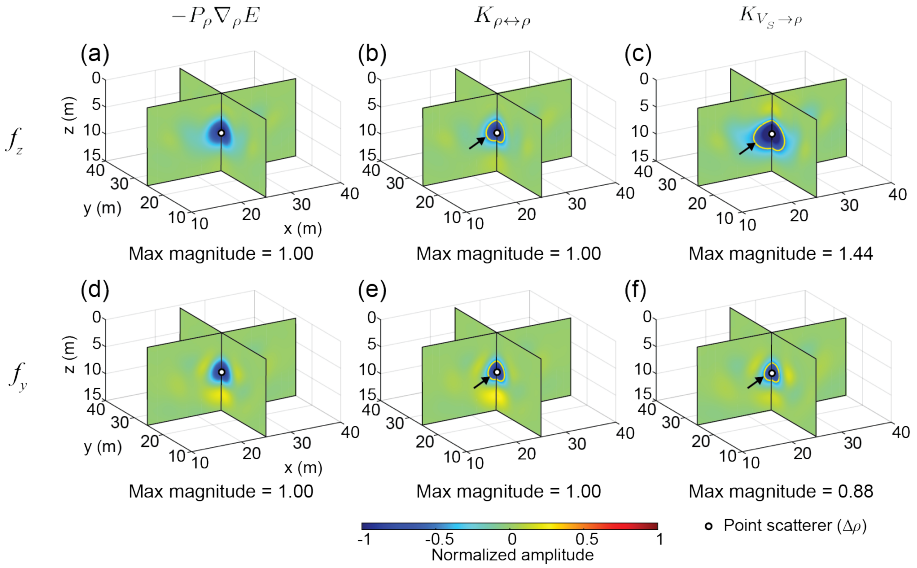

Figure 4.3: Preconditioned gradients, update kernels, and contamination kernels for ρ. Preconditioned gradients in (a) and (d) are normalized by their maximum magnitude, while the kernels in (b), (c), (e) and (f) are normalized by the maximum magnitude of update kernels. Yellow lines and black arrows in update and contamination kernels denote the spreading widths of the kernels.

is not significantly influenced by ΔV_S^N, and therefore the ρ model can be updated with a relatively weak parameter-coupling problem. From the above findings, the shape of E for the f_y dataset has more favourable characteristics for ρ estimation using 3D FWI (i.e., weak parameter coupling) than the shape of E for the f_z dataset. Choosing f_y as a force direction would result in reconstructing a more accurate ρ model within the framework of gradient-based FWI, without taking the Hessian inverse into account.

The update and the contamination kernels for V_S are also calculated (Fig. 4.4). As opposed to ρ, the relative strengths of the contamination kernels ($K_{\rho \rightarrow V_S}$) shown in Figs 4.4(c) and (f) are smaller than those of the update kernels ($K_{V_S \leftrightarrow V_S}$) shown in Figs 4.4(b) and (e), regardless of the force directions. Thus, both datasets equally allow reconstruction of an accurate V_S model without suffering from a strong parameter coupling due to $\Delta\rho^N$.

4.3.3. RESOLUTION

In this subsection, we investigate the resolution of ρ estimates using the update and contamination kernels calculated in Subsection 4.3.2. We compare the spreading widths (Subsection 4.2.2) between these two kernels for different force directions.

The spreading widths of the kernels for ρ are shown by yellow lines and black arrows in Fig. 4.3. The spreading widths of $K_{\rho \leftrightarrow \rho}$ do not significantly differ between f_z and f_y datasets (Figs 4.3(b) and (e)): the maximum widths for f_z and f_y datasets are 2.2 m and 2.1 m, respectively. This indicates that the resolution in the reconstructed ρ model would be quite similar for different force directions if the contamination kernel $K_{V_S \rightarrow \rho}$ is small. On

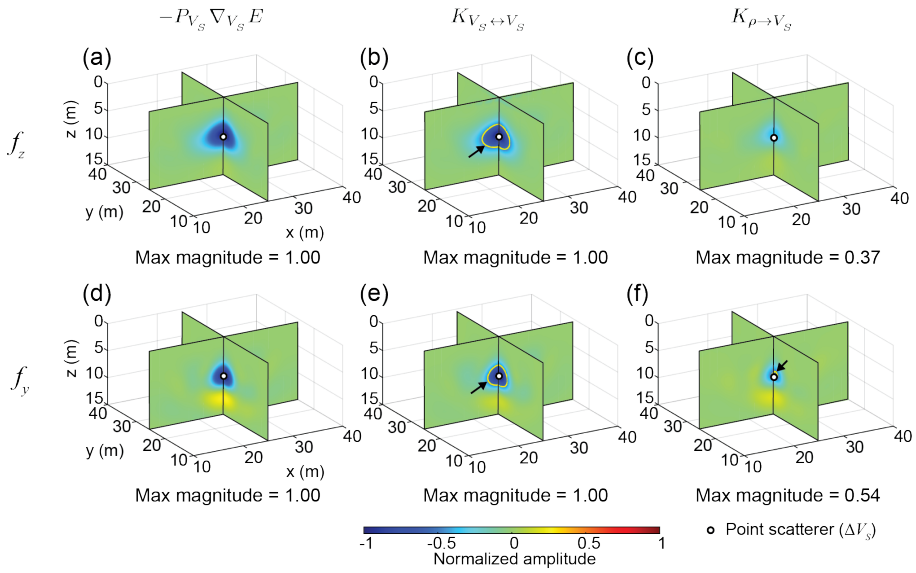

Figure 4.4: Preconditioned gradients, update kernels, and contamination kernels for V_S. Preconditioned gradients in (a) and (d) are normalized by their maximum magnitude, while the kernels in (b), (c), (e) and (f) are normalized by the maximum magnitude of update kernels. Yellow lines and black arrows in update and contamination kernels denote the spreading widths of the kernels.

the contrary, the spreading width of $K_{V_S\rightarrow\rho}$ for the f_z dataset (Fig. 4.3(c)) is much larger (3.8 m) than that for the f_y dataset (1.9 m, Fig. 4.3(f)). Therefore, use of the f_z dataset can cause artifacts due to parameter coupling (ΔV_S^N) in a wide area in the reconstructed ρ model.

Next, we examine the spreading widths of the update and the contamination kernels for V_S (yellow lines and black arrows in Fig. 4.4) to evaluate how their characteristics differ from those for ρ. The spreading width of $K_{V_S\leftrightarrow V_S}$ for the f_z dataset is larger than that for the f_y dataset (Figs 4.4(b) and (e)): the maximum width for the f_z dataset is 3.4 m, while that for the f_y dataset is 2.5 m. Therefore, the use of the f_y dataset will enable constructing a preconditioned gradient which is more focused at ΔV_S^N than using the f_z dataset. Contrary to ρ, the spreading widths of $K_{\rho\rightarrow V_S}$ for both datasets are significantly small ($<$ 0.5 m and 0.7 m, see Figs 4.4(c) and (f)), which can result in few contaminations due to $\Delta\rho^N$ in the V_S estimates for both force-direction datasets.

4.4. NEAR-SURFACE MODELS: RESULTS OF 3D FWI FOR DIFFERENT FORCE DIRECTIONS

The results in the previous section have demonstrated that FWI applied to horizontal-force datasets can reconstruct more accurate ρ and V_S models than FWI applied to vertical-force datasets, in terms of the noise robustness, weak parameter coupling, and high-resolution gradient for ρ. For ρ estimation using gradient-based FWI, the relatively weak parameter

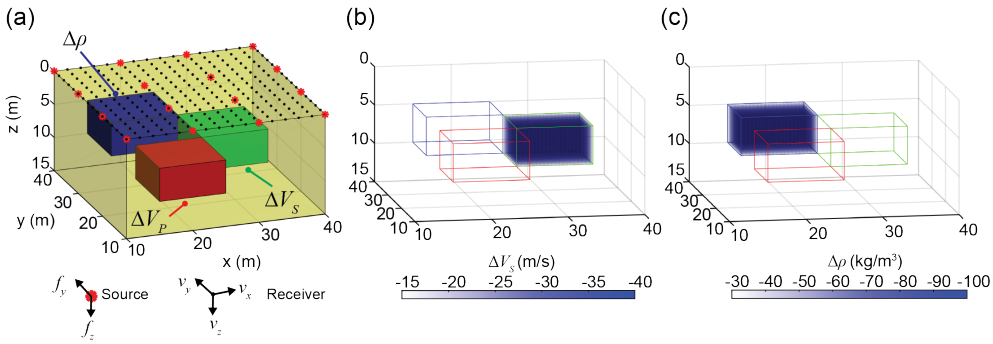

Figure 4.5: The spatially uncorrelated model for inversion tests. The red, green, and blue boxes represent the locations of the anomalies for V_P, V_S, and ρ, respectively. The models in (b) and (c) are visualized by subtracting the initial model from the true model.

4

coupling in the preconditioned gradient is the key factor which contributes to better results. In this section, we perform 3D FWI using specific near-surface models to examine this difference.

Two near-surface models are used for different purposes. First, to visualize the impact of parameter coupling on the reconstructed result, we consider a spatially uncorrelated model where the anomalous zone for each parameter class is located at a separate position (Subsection 4.4.1). Next, to approximate the field condition, we build a realistic near-surface model containing 3D heterogeneities (Subsection 4.4.2). The model is derived from actual downhole data acquired in the field. We incorporate anelastic attenuation in the synthetic data through viscoelastic forward modelling. Random noise is also added to the data.

4.4.1. FWI RESULTS FOR A SPATIALLY UNCORRELATED MODEL

MODEL BUILDING & INVERSION SETUP

Our spatially uncorrelated model represents a special case where Δm^N in eqs 4.8–4.10 is spatially decomposed into parameter classes. Data using this particular model produce the update and the contamination kernels at different locations in the preconditioned gradient. The kernels, spatially separated in the preconditioned gradient for a certain parameter class, produce the artifacts due to different parameter classes at locations that differ from the location of the correct anomaly. This helps distinguishing the parameter-coupling effect in the results.

We consider the 10 m × 5 m box-shaped anomalies for V_P, V_S and ρ located at different positions but at the same depth (Fig. 4.5). The background model varies only in depth (Fig. 4.1). Note that Figs 4.5(b) and (c) are created by subtracting the initial background model (Fig. 4.1) from the true model to clearly visualize the box-shaped anomalies. While the anomalies – ΔV_S^N and $\Delta\rho^N$ – have values which are -20% of the background, the ΔV_P^N is -10% of the background value.

We perform gradient-based 3D FWI on vertical-force (f_z) and horizontal-force (f_y) datasets. The acquisition geometry and the source wavelet are the same as those in Subsections 4.3.2 and 4.3.3. We use the background model (Fig. 4.1) as the initial model

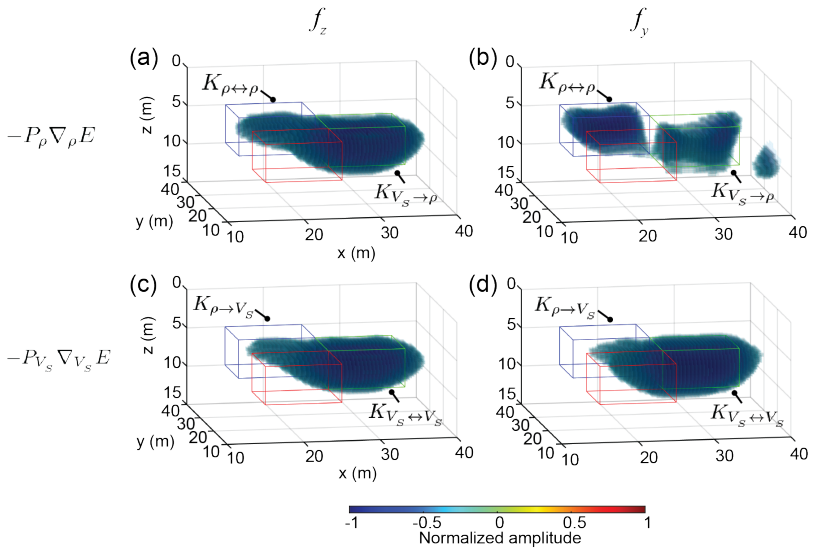

Figure 4.6: The preconditioned gradients for (a), (b) ρ and (c), (d) V_S.

in 3D FWI, and assume the source wavelet as known. During the inversion, the model parameters (V_P, V_S, ρ) are simultaneously updated. The same monochromatic frequencies as in Subsections 4.3.2 and 4.3.3 are used to calculate the preconditioned gradients. To compare the different datasets using vertical- and horizontal-force sources, we use the same stop-criterion for inversion: the iteration is stopped when the relative change between the misfit of the current iteration step and that of the second to the last iteration step is less than 1%. Since the data are not sensitive to ΔV_P because of the very long wavelength of P wave (~40 m) relative to the size of the anomaly, we discuss only about the reconstructed V_S and ρ models.

PARAMETER COUPLING: AFTER THE FIRST ITERATION

We first investigate the preconditioned gradients for ρ (i.e., $-P_\rho \nabla_\rho E$) at the first iteration using the vertical-force source (Fig. 4.6(a)) and the horizontal-force source (Fig. 4.6(b)). Because of the spatially uncorrelated anomalies, the update kernels ($K_{\rho \leftrightarrow \rho}$) are imaged around the location of the anomaly of ρ (blue boxes in Figs 4.6(a) and (b)), while the contamination kernels ($K_{V_S \rightarrow \rho}$) are distributed around the location of the anomaly of V_S (green boxes in Figs 4.6(a) and (b)). When using f_z dataset, $K_{V_S \rightarrow \rho}$ dominates significantly in $-P_\rho \nabla_\rho E$ compared to $K_{\rho \leftrightarrow \rho}$ (see Fig. 4.6(a)). On the contrary, f_y dataset produces $K_{\rho \leftrightarrow \rho}$ with larger magnitude than $K_{V_S \rightarrow \rho}$ in $-P_\rho \nabla_\rho E$ (see Fig. 4.6(b)). As a consequence, 3D FWI using f_y dataset can estimate $\Delta \rho^N$ more accurately than FWI using f_z dataset, with a weak parameter coupling due to ΔV_S^N at least at the first iteration.

As opposed to ρ, the preconditioned gradients for V_S (i.e., $-P_{V_S} \nabla_{V_S} E$) at the first iteration (Figs 4.6(c) and (d)) do not contain significant artifacts due to $K_{\rho \rightarrow V_S}$ (blue boxes in Figs 4.6(c) and (d)). This result is consistent with the results for a point-scatterer model (see Subsection 4.3.2). Besides, one can see that the amplitude distribution of $-P_\rho \nabla_\rho E$ for the f_z

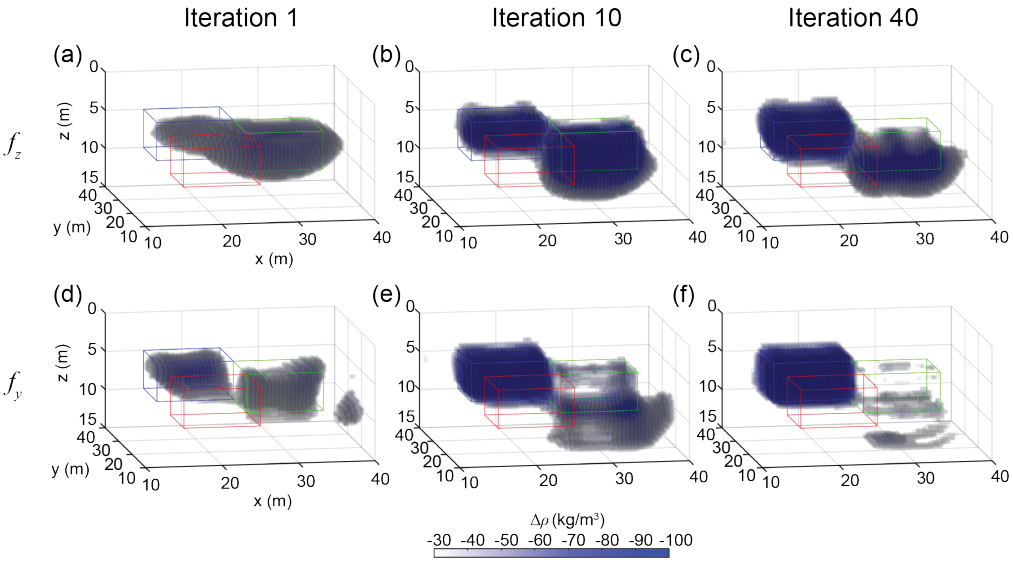

Figure 4.7: The comparison of the iteratively updated ρ models.

dataset is similar to that of $-P_{V_S}\nabla_{V_S}E$ (see Figs 4.6(a) and (c)). This suggests that $-P_\rho\nabla_\rho E$ for the f_z dataset is contaminated by ΔV_S^N.

Results after all iterations

During the inversion, the ρ models are iteratively updated (Fig. 4.7). In the first iteration, both datasets produce artifacts around the location of the anomaly of V_S associated with $K_{V_S\rightarrow\rho}$ (green boxes in Figs 4.7(a) and (d)). The artifacts are generated because the ρ models are updated in the directions along $-P_\rho\nabla_\rho E$ in the first iteration (Figs 4.6(a) and (b)) based on eqs 4.2 and 4.3. With iterations, however, the nonlinear optimization process (i.e., NCG) reduces these artifacts for both datasets, resulting in gradual reconstruction of the anomaly of ρ at the correct location (see the results after iteration 10 in Figs 4.7(b) and (e) and after iteration 40 in Figs 4.7(c) and (f)). Finally, at the convergence (i.e., after 69 iterations for the f_z dataset and after 71 iterations for the f_y dataset), the reconstructed ρ model using the f_y dataset no longer exhibits any significant artifacts that were produced at the earlier iterations (green box in Fig. 4.8(b)). On the other hand, the finally obtained result of 3D FWI using the f_z dataset shows some remaining artifacts due to parameter coupling (see the green box in Fig. 4.8(a)). Furthermore, a comparison of the 1D profiles (Fig. 4.8(c)) shows that utilizing the f_y dataset provides better ρ estimates (values closer to the true values) than the f_z dataset. The likely reason for this difference is the strong parameter-coupling effect in the f_z dataset in the preconditioned gradient (Fig. 4.6(a)). In this case, after the first iteration, the FWI estimates a ρ model which is very far from the true model (Fig. 4.7(a)), and as a consequence, at the end the final model also falls into a local minimum located in the vicinity of the solution of the first iteration.

We also examine the reconstructed V_S models after the inversion for the vertical-force dataset (Fig. 4.8(d)) and the horizontal-force dataset (Fig. 4.8(e)). Contrary to ρ, the

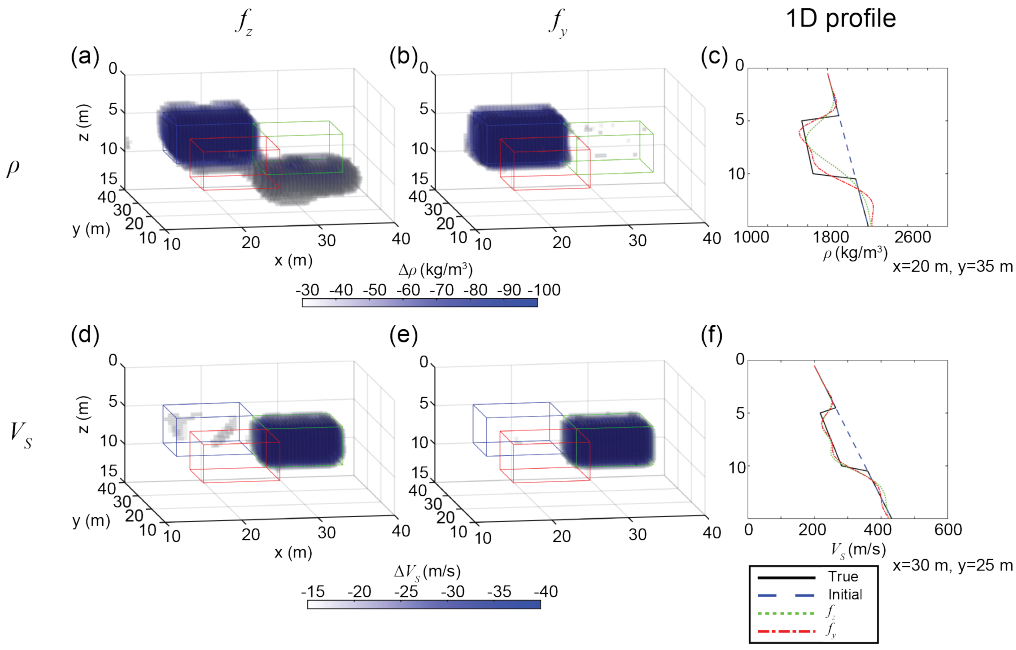

Figure 4.8: The comparison of the finally obtained (a)-(c) ρ and (d)-(f) V_S models.

anomaly of V_S is successfully reconstructed without serious artifacts regardless of the force directions (Figs 4.8(d) and (e)). Furthermore, a comparison of 1D profiles (Fig. 4.8(f)) shows that both datasets estimate almost identical V_S models.

4.4.2. FWI RESULTS FOR A REALISTIC SUBSOIL MODEL

In Subsection 4.4.1, the initial model is different from the true model at locations that differ among the parameter classes. That helped distinguishing the parameter coupling effect in the results. However, this assumption is obviously unrealistic. For FWI using field data where the accuracy of the initial model can only be controlled to a limited extent, one has to choose a suitable approach for building the initial model, considering the data quality and/or any available prior information. Besides, the inversion tests in Subsection 4.4.1 have been carried out, assuming purely elastic wavefields and noise-free data.

In this subsection, we take into consideration a more realistic situation. The subsoil model is built on downhole information obtained in the field. Unlike in Subsection 4.4.1, we work here with data having random noise and viscoelastic wavefield instead of elastic wavefield.

MODEL BUILDING & PSEUDO-SEISMIC DATA

To build the realistic 3D subsoil model, we use V_S and porosity (ϕ) data measured at a soft-soil site in the western part of the Netherlands (Fig. 4.9(a)). In this earlier study, V_S was measured at 25 cm interval in depth via SCPT (Seismic Cone Penetration Test) and the porosity from laboratory tests on soil samples collected in boreholes (Ghose, 2007;

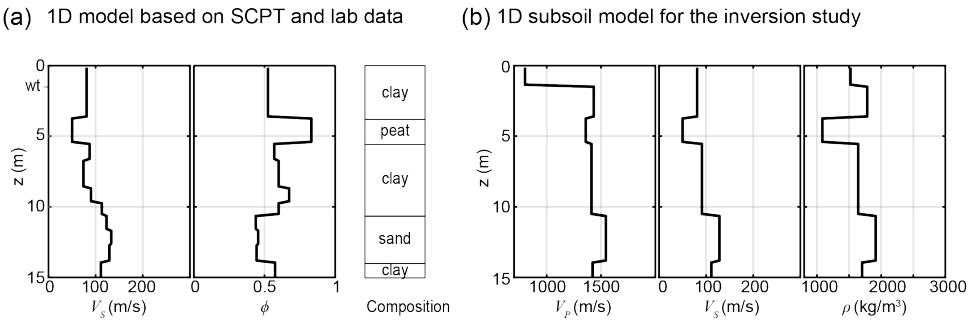

Figure 4.9: (a) The 1D layered V_S and ϕ models and soil composition (Ghose, 2007; Zhubayev & Ghose, 2012). (b) The 1D layered V_P, V_S, and ρ models for the inversion test in this research.

Zhubayev & Ghose, 2012). From continuous soil sampling performed at this site, the soil-layer composition is known (Fig. 4.9(a)). The soil column is composed of alternating layers of clay and sand. Also, a peat layer located at ~5 m depth shows a very high porosity (~0.83), indicative of low density.

Using this dataset, we have constructed a five-layered model of the near-surface (till 15 m depth) (Fig. 4.9(b)) for testing FWI. The ρ values in Fig. 4.9(b) are calculated from ϕ as follows:

$$\rho = \rho_s(1-\phi) + \phi S_f \rho_f, \tag{4.12}$$

where ρ_s is solid grain density, ρ_f is fluid density, and S_f represents the degree of water saturation. For ρ_s and ρ_f, we use the representative values for such soil types in this area (Table 4.2). Since the water table at this site is located at 1.4 m depth, we consider an unsaturated condition until 1.4 m, and a fully water-saturated condition below this depth. For the unsaturated and fully saturated conditions, we assume S_f = 50% and S_f = 100%, respectively. Since we do not have V_P data, the V_P values at the fully water-saturated condition are calculated based on Gassmann's equation (e.g., Mavko et al., 2009), while the unsaturated V_P values are assumed to be 800 m/s. For the soil properties required in the Gassmann's equation, we consider the representative values (Table 4.2) based on past research (Inci et al., 2003; Emerson & Foray, 2006; Chesworth, 2008; Kumar & Madhusudhan, 2012). Finally, extending this model (Fig. 4.9(b)), 3D heterogeneity is introduced as shown in Figs 4.10(a)-(c). The complexity of the 3D model is characterized by a peat layer (second layer in Fig. 4.9(b)) that gradually thins out in x- and y-directions and a sand layer (fourth layer in Fig. 4.9(b)) that gently dips in 3D. Note that the 1D layered model in Fig. 4.9(b) is located at the centre of the 3D model (at [x, y] = [13.5 m, 13.5 m]). In order to simulate the viscoelastic wavefields, we assume a constant value of 20 for both Q_P and Q_S, for the entire model.

For this realistic 3D subsoil model, the viscoelastic wavefields are simulated using vertical-force (f_z) and horizontal-force (f_y) sources. Since the 3D FWI applied to an f_x dataset gives almost the same results as those for 3D FWI applied to an f_y dataset for this model (see Subsection 4.8.1), we here discuss only the results for the f_y dataset. The model is discretized using 180×180×120 grid points in x-, y-, and z-direction, respectively, with

Table 4.2: Values of soil properties (Inci et al., 2003; Emerson & Foray, 2006; Chesworth, 2008; Kumar & Madhusudhan, 2012) for calculating ρ and V_P for each soil layer (ρ_s: solid density, ρ_f: fluid density, K_s: solid bulk modulus, K_f: fluid bulk modulus, ν_{sk}: Poisson's ratio of the soil skeleton).

Soil type	ρ_s (kg/m^3)	ρ_f (kg/m^3)	K_s (GPa)	K_f (GPa)	ν_{sk}
Clay	2650	1000	14	2.18	0.10
Sand	2650	1000	30	2.18	0.23
Peat	1500	1000	1.4	2.18	0.15

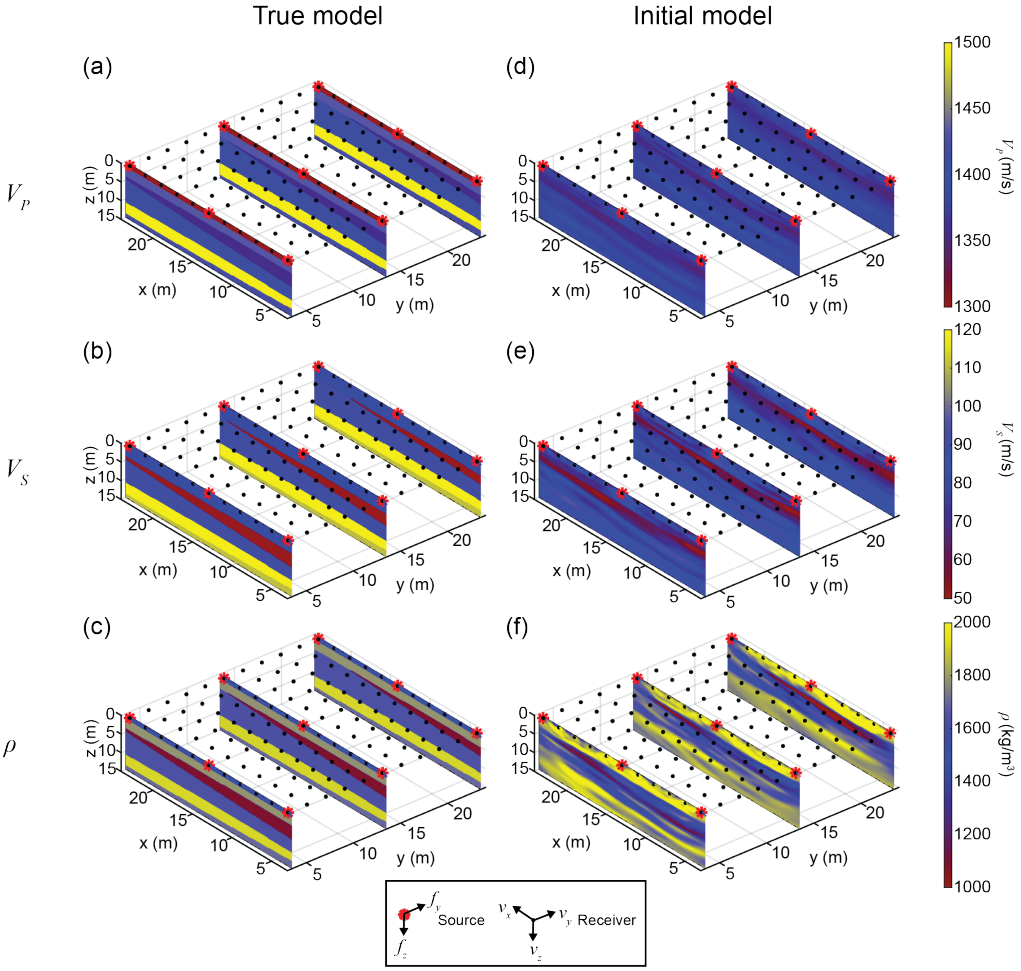

Figure 4.10: The 3D complex subsoil model for the inversion tests. The true (a) V_P, (b) V_S, and (c) ρ models. The initial (d) V_P, (e) V_S, and (f) ρ models.

a grid spacing of 0.15 m. We consider a symmetric acquisition geometry with 9 seismic sources at 10 m spacing and a fixed array of 121 three-component receivers planted at 2 m spacing, as shown in Fig. 4.10. The sources generated a Fuchs-Müller wavelet (eq. 4.11) with a centre frequency of 20 Hz. As mentioned earlier, this frequency is not chosen to a higher value only to keep the computation time for the 3D FWI manageable, while still achieving sufficiently the goals of this research. It is also the same reason why we restricted the depth to only 15 m. We finally add identical random noise to both force datasets. The S/N ratio in the y-component data (v_y) at the farthest source-receiver offset (28.3 m) due to the f_y source is ~8, while that in the z-component data (v_z) at the same offset due to the f_z source is ~60. The big difference in the S/N ratio reflects the difference in the amplitudes of the dominated wavefields in each dataset.

The example of the simulated data (particle velocity), representing field seismic data using different force directions for the seismic source, is shown in Fig. 4.11. As expected, for the f_z source, the energy is predominantly present in the vertical-component receiver (Fig. 4.11(c)), while for the same source limited amount of seismic energy present in the horizontal-component receiver (Figs 4.11(a) and (b)) is due to the Rayleigh waves. On the contrary, for the f_y source, there is more energy in the horizontal-component receivers (Figs 4.11(d) and (e)) than in the vertical-component (Fig. 4.11(f)). Additionally, the f_y data show reflected arrival from the lower boundary of the peat layer at ~0.3 s, which is less visible in the f_z data.

Initial model

We perform at first 2D SH FWI using the 2D (v_y) dataset. This dataset is derived from the f_y dataset along the three 2D lines at y = 3.5, 13.5, 23.5 m (Fig. 4.10). For an initial V_S model for the 2D SH FWI, we build a homogeneous model using the first-arrival travel times. An initial ρ model is constructed by first using an empirical relationship between V_S and V_P (Kitsunezaki et al., 1990) and then using a relationship between V_P and ρ (Ludwig, 1970).

For 2D SH FWI, we use the GCN (Choi & Alkhalifah, 2012): the model is updated to maximize the cross-correlation between the normalized observed and calculated seismograms. This misfit function does not focus on the amplitudes but on the similarities (phase matching) between the seismograms, which enables reconstructing a rough model using 2D FWI without compensating for the difference between the 3D and 2D geometrical spreading. Therefore, at this point, we apply 3D to 2D point-to-line source phase correction by convolving each trace of the 3D seismic dataset with $\sqrt{t^{-1}}$, where t is the recording time (Forbriger et al., 2014; Schäfer et al., 2014; J. Liu, Ghose, & Draganov, 2022). We assume the source-time function to be known. The V_S and ρ models are updated simultaneously during the inversion. The attenuation Q_S is assumed to be known. The estimation of Q_S is possible, for example, by using the passive-viscoelastic FWI approach (Groos et al., 2014): the optimum Q value with the minimum misfit function for an initial model is chosen through the grid search.

The V_S and ρ sections estimated by 2D SH FWI along the three 2D lines are used, followed by spline interpolation, to build the 3D initial model (Figs 4.10(e) and (f)). The V_P initial model is built using the empirical relationship between V_P and V_S (Kitsunezaki et al., 1990) (Fig. 4.10(d)). Note that the initial model in Figs 4.10(d)-(f) is used for 3D FWI

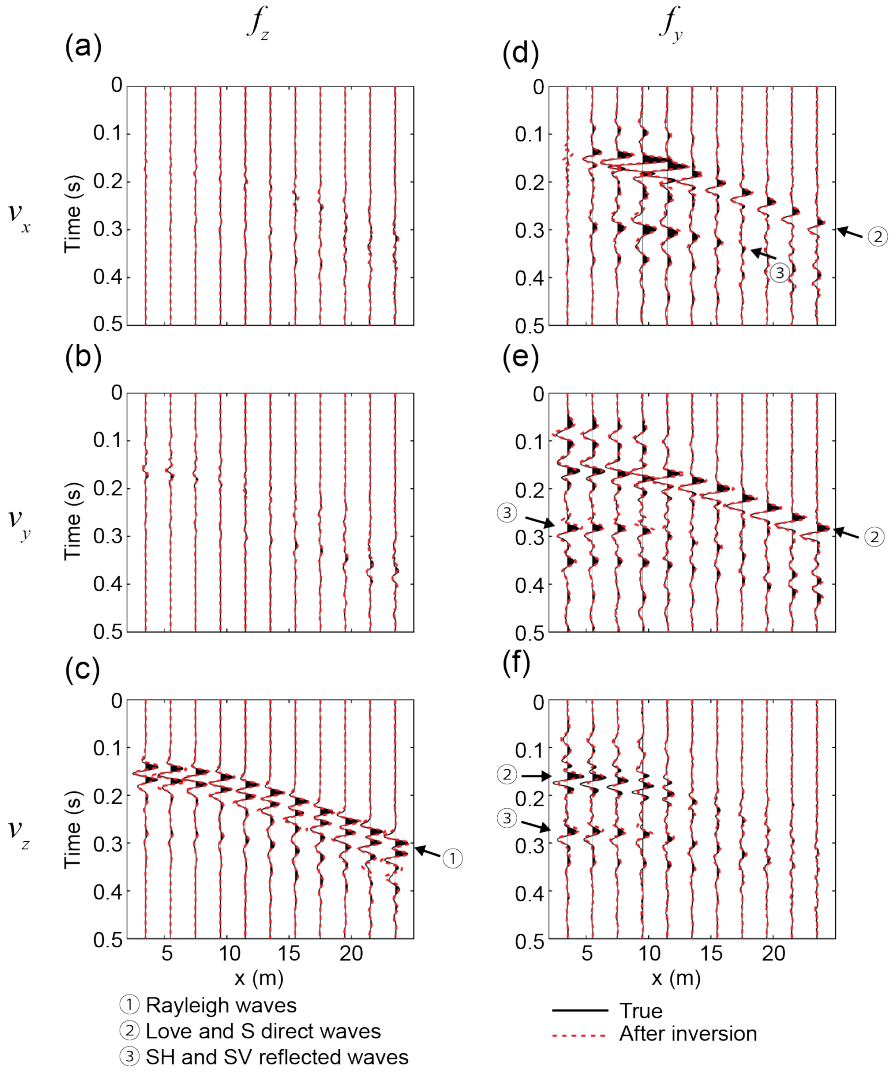

Figure 4.11: The example of the pseudo-seismic data calculated for the model shown in Fig. 4.10(a)-(c). The three-component records at y = 3.5 m (a)-(c) using an f_z source and (d)-(f) using an f_y source. The source is located at [x, y] = [3.5 m, 13.5 m]. For visualization, each trace is normalized by the maximum amplitude at a specific receiver component corresponding to a force component.

using both f_z and f_y datasets, although building an initial model using SH FWI is possible only for the f_y dataset. This allows us to investigate the sole impact of the force direction of the seismic source on the reconstructed ρ model using 3D FWI.

PARAMETER COUPLING: AFTER THE FIRST ITERATION

The preconditioned gradients for ρ ($-P_\rho \nabla_\rho E$) calculated at the first iteration for the f_z dataset (Fig. 4.12(a)) and the f_y dataset (Fig. 4.12(b)) exhibit significant differences. Contrary to Subsection 4.4.1, the update and contamination kernels are not spatially separated in the preconditioned gradient. This is because the true model perturbations (Δm^{true}) for each parameter class, i.e., the differences between the true and initial models, are distributed over the whole model, and are superimposed on each other (Figs 4.12(g) and (h)). Also, a large Δm^{true} (Figs 4.12(g) and (h)) implies that it would not be possible to assume the Newton step (Δm^N) in eqs 4.8–4.10 as we do in Subsection 4.4.1. The Newton step Δm^N could be estimated by investigating the detailed shape of the misfit function E; however, the computational cost for this analysis is prohibitively expensive. Due to these constraints, it is challenging to visualize the kernels and evaluate the parameter coupling using eqs 4.8–4.10.

In order to overcome this difficulty, we directly calculate the approximate Hessian ($H^a_{m_i m_j}$), which is a component of the kernels in eqs 4.8–4.10. The effect of the off-diagonal elements of this Hessian (i.e., the spatial cross-correlation of the Jacobians between different grids) on the preconditioned gradient varies with the spatial distribution of Δm^N. Since Δm^N is unknown, we take the relative magnitude of the coefficients of Δm^N in eqs 4.8–4.10. For this purpose, we assume a simple case where $H^a_{m_i m_j}$ is diagonally dominant. In this case, eq. 4.10 can be written as:

$$
\begin{aligned}
-\frac{1}{diag\left(H^a_{\rho\rho}\right)+\epsilon_\rho}\nabla_\rho E \approx & \frac{diag\left(H^a_{\rho V_P}\right)}{diag\left(H^a_{\rho\rho}\right)+\epsilon_\rho}\Delta V_P^N \\
& + \frac{diag\left(H^a_{\rho V_S}\right)}{diag\left(H^a_{\rho\rho}\right)+\epsilon_\rho}\Delta V_S^N \\
& + \frac{diag\left(H^a_{\rho\rho}\right)}{diag\left(H^a_{\rho\rho}\right)+\epsilon_\rho}\Delta \rho^N,
\end{aligned}
\tag{4.13}
$$

where $diag\left(H^a_{m_i m_j}\right)$ is the diagonal element of $H^a_{m_i m_j}$, and $diag\left(H^a_{\rho\rho}\right)+\epsilon_\rho$ represents the preconditioning filter for ρ (i.e., P_ρ) (see Subsection 4.7.1 for details). Evaluation of eq. 4.13 enables one to investigate the parameter coupling grid by grid, while the spatial parameter coupling between different grids is ignored.

The second term on the right-hand side of eq. 4.13 represents the parameter coupling due to V_S, and the third term represents the appropriate update direction for ρ. Because the coefficient of $\Delta\rho^N$ (the third term) is almost 1, investigating the coefficient of ΔV_S^N (the second term) allows appreciating how ΔV_S^N is amplified and how it contaminates the appropriate update direction for ρ in the preconditioned gradient. For brevity, hereafter, we call the coefficient for the second term, $diag\left(H^a_{\rho V_S}\right) / \left(diag\left(H^a_{\rho\rho}\right)+\epsilon_\rho\right)$, as the coupling coefficient of ρ.

The coupling coefficients of ρ show that their values are smaller for the f_y dataset (Fig. 4.12(e)) than for the f_z dataset (Fig. 4.12(d)). Around z = 10 m at the centre of the model,

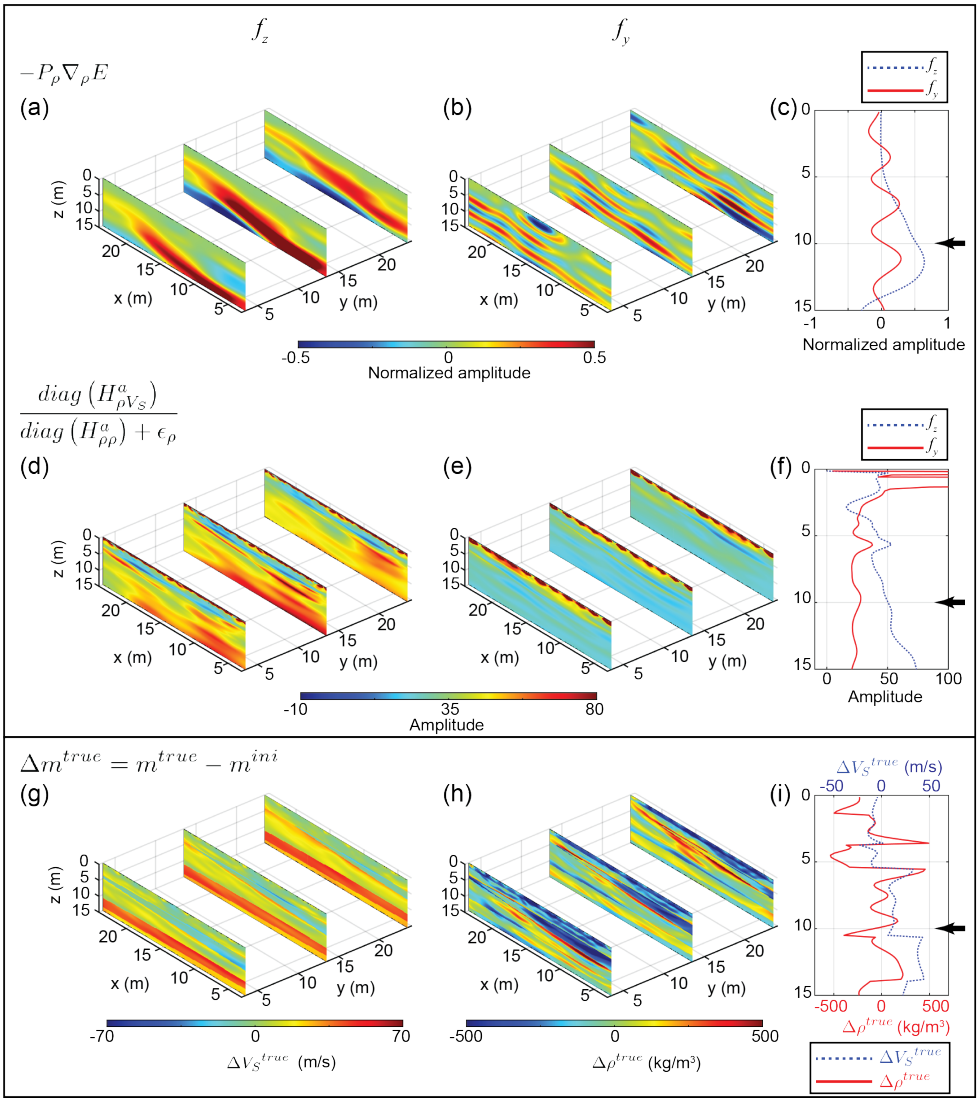

Figure 4.12: (a)-(c) The preconditioned gradients for ρ and (d)-(f) the coupling coefficients of ρ for different force datasets at the first iteration of the stage 1 shown in Table 4.3. (g)-(i) The differences between true and initial models for V_S and ρ.

for instance, the coupling coefficient of ρ for the f_y dataset is approximately 25, while that for the f_z dataset is approximately 50 (see the black arrow in Fig. 4.12(f)). Assuming that ΔV_S^N and $\Delta\rho^N$ do not significantly differ between the force directions, this difference in the amplitude of the coupling coefficients suggests that using the f_z dataset results in twice larger the parameter coupling than using the f_y dataset (see eq. 4.13). We can draw the same conclusion if the ratio of ΔV_S^N to $\Delta\rho^N$ is almost the same for the different force datasets, because the preconditioned gradient is normalized by its maximum value in the implementation of FWI here (see Subsection 4.2.1).

Next, we look more carefully into the preconditioned gradients of ρ at the centre of the model. The 1D profiles illustrate different characteristics for different force directions (e.g., Fig. 4.12(c)). Around z = 10 m, the values for the f_y dataset oscillate around zero, while almost all values for the f_z dataset are positive (see the black arrow in Fig. 4.12(c)). To investigate the possible reason, we calculate the true V_S and ρ perturbations ($\Delta {V_S}^{\text{true}}$ and $\Delta\rho^{\text{true}}$) in Fig. 4.12(i). At the same location (at the centre of the model around z = 10 m), the true model perturbations show characteristics that are similar to the preconditioned gradient: $\Delta\rho^{\text{true}}$ oscillates around zero, while $\Delta {V_S}^{\text{true}}$ is mostly on the positive side (see the black arrow in Fig. 4.12(i)). Although the true model perturbations would not accurately represent the Newton step, the similarity between $\Delta\rho^{\text{true}}$ (red line in Fig. 4.12(i)) and the preconditioned gradient for ρ for the f_y dataset (red line in Fig. 4.12(c)) permits one to anticipate that the gradient for the f_y dataset would more closely reflect $\Delta\rho^N$, compared to the gradient for the f_z dataset. On the other hand, the similarity between $\Delta {V_S}^{\text{true}}$ (blue dashed line in Fig. 4.12(i)) and the preconditioned gradient for ρ for the f_z dataset (blue dashed line in Fig. 4.12(c)) suggests that the gradient is probably heavily contaminated by ΔV_S^N. The use of the f_y dataset offers the possibility to obtain the preconditioned gradient for ρ with few artifacts due to ΔV_S^N, and hence leads to a more accurate ρ model from 3D FWI.

We also investigate the parameter coupling in the preconditioned gradient for V_S (Subsection 4.7.2). Unlike the preconditioned gradient for ρ, the different force datasets do not show significant differences in the parameter coupling. But the f_y dataset can offer higher-resolution V_S model than the f_z dataset (see Subsection 4.7.2 for more details).

Results after all iterations

During the iterations in FWI, V_S and ρ are updated simultaneously, while V_P remains fixed to the initial model (Fig. 4.10(d)); the data are not sensitive to V_P because of the very long wavelength of P wave (~40 m) relative to the heterogeneous structure. Similar to 2D SH-wave FWI, Q_P, Q_S and the source-time function are assumed to be known. To avoid cycle skipping, we perform multi-scale inversion (Bunks et al., 1995), where we gradually increase the maximum frequency for inversion (Table 4.3). We use four inversion stages; the frequencies at each stage are selected such that they continuously cover the vertical wavenumbers (Sirgue & Pratt, 2004).

When the convergence is achieved, the synthetic waveforms fit well with the observed waveforms (red dashed lines in Fig. 4.11). A comparison of the ρ models (Figs 4.13(a)-(c)) shows that use of the f_y dataset gives a better resolution of the ρ values in the clay layer than when the f_z dataset is used (see green arrows in Fig. 4.13(a)-(c)). We indeed see a sharp transition from the clay layer (third layer) to the sand layer (fourth layer) in

Table 4.3: Monochromatic frequencies for multi-scale inversion.

Stage	Monochromatic frequencies (Hz)
1	2.5, 3.8, 5.0, 6.3, 7.5, 8.8, 10.0
2	2.5, 3.8, 5.0, 6.3, 7.5, 8.8, 10.0, 11.3, 12.5, 13.8, 15.0, 16.3, 17.5, 18.8, 20.0
3	3.1, 4.3, 5.6, 6.8, 8.1, 9.3, 10.6, 11.8, 13.1, 14.3, 15.6, 16.8, 18.1, 19.3, 20.6 21.8, 23.1, 24.3, 25.6, 27.0, 28.5, 30.0
4	2.4, 3.6, 4.9, 6.1, 7.4, 8.6, 9.9, 11.1, 12.4, 13.6, 14.9, 16.1, 17.4, 18.6, 19.9, 21.1 22.4, 23.6, 24.9, 26.2, 27.7, 29.2, 30.7, 32.4, 34.2, 36.0, 37.9, 40.0

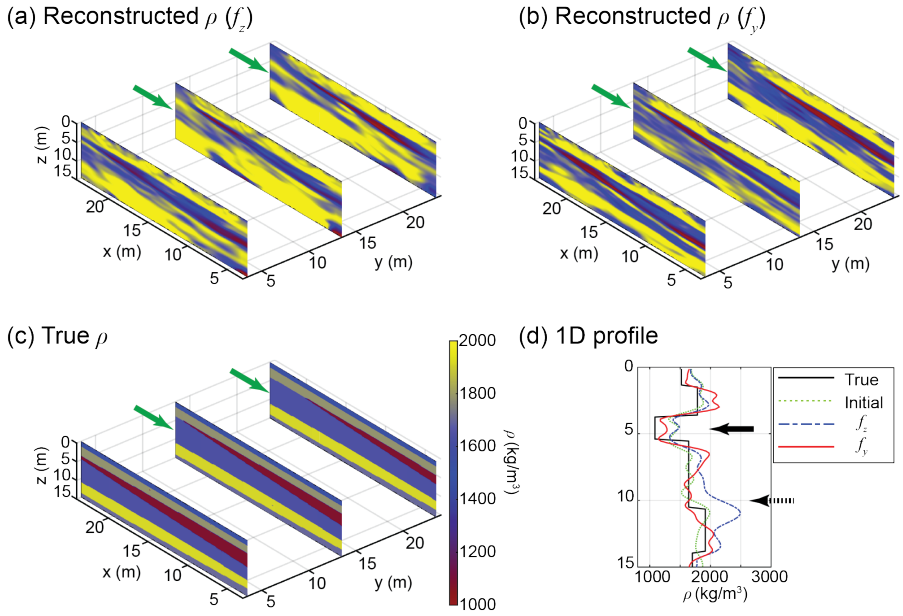

Figure 4.13: The reconstructed ρ models (a) when using an f_z dataset, and (b) when using an f_y dataset. (c) The true ρ model. The green arrow shows the clay layer. (d) The comparison of 1D profiles for the two different force-direction datasets at [x, y] = [13.5 m, 13.5 m].

case of the f_y dataset. The 1D profiles at the centre of the model also illustrate that the ρ estimates for the f_y dataset are more accurate than that for the f_z dataset, especially at ~10 m depth (see the black dashed line in Fig. 4.13(d)). This is probably because for the f_z dataset there is a relatively strong parameter coupling at around 10 m depth, while for the f_y dataset, the parameter coupling is rather weak, as demonstrated also in the previous section. Furthermore, the use of the f_y dataset in 3D FWI allows estimating the low ρ in the peat layer more accurately than the use of the f_z dataset (see the black solid arrow in Fig. 4.13(d)).

Next, in order to examine the overall accuracy of the inverted ρ models for different

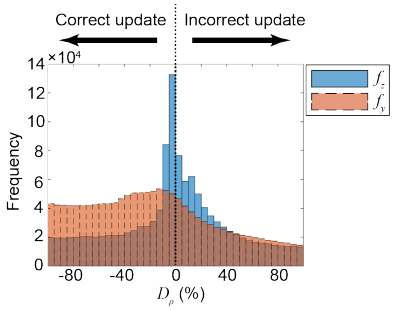

Figure 4.14: The comparison of the histograms of D_ρ for two different force-direction datasets.

force datasets, we define the rate of the model-error change as follows:

$$D_m = \frac{m_{\text{est}}^{\text{error}} - m_{\text{ini}}^{\text{error}}}{m_{\text{ini}}^{\text{error}}} \times 100, \tag{4.14}$$

where $m_{\text{ini}}^{\text{error}} = |m_{\text{true}} - m_{\text{ini}}|$ and $m_{\text{est}}^{\text{error}} = |m_{\text{true}} - m_{\text{est}}|$ represent the model errors for the initial model (m_{ini}) and for the estimated model (m_{est}), respectively. Eq. 4.14 indicates that D_m is 0 at the beginning of the inversion (i.e., $m_{\text{est}} = m_{\text{ini}}$), becomes a negative value if m_{est} approaches the true value (i.e., m_{true}), and becomes -100 if the model is perfectly reconstructed (i.e., $m_{\text{est}} = m_{\text{true}}$). On the other hand, D_m becomes a positive number if the model is updated in the opposite direction to the true value from the initial model.

To compare the overall trends of ρ estimates for f_z and f_y datasets, we calculate grid by grid D_ρ using eq. 4.14. The result is shown in histograms in Fig. 4.14. For both f_z and f_y datasets, we notice incorrect ρ updates in the opposite direction to the true model (i.e., $D_\rho > 0$). This could be due to the presence of side-lobe in the vertical section of the ρ model at the layer boundaries (note the surrounding of the peat layer in Fig. 4.13(d)), due to the limited frequency bandwidth in our data, limited acquisition geometry (e.g., Virieux & Operto, 2009; Y. E. Li & Demanet, 2016), and/or the convergence to the local minima. Such side-lobe increases the model error over the whole model during the inversion as shown in Subsection 4.8.2. Nonetheless, FWI using the horizontal-force sources provides a meaningful ρ structure. In particular, the inversion improves the delineation of the main geological structures, such as peat and sand layers, which are less clearly seen in the initial model (compare between Fig. 4.10(f) and Fig. 4.13(b)). This structural improvement is quantified using the image correlation as described in Subsection 4.8.2, which shows a significant increase in the similarity between the true and the inverted models after the convergence. This indicates that, despite localized side-lobe artifacts, the inversion resolves the overall ρ structure. The comparison of the histograms of D_ρ also illustrates that 3D FWI applied to the f_y dataset is beneficial for estimating the accurate ρ: there are correct ρ updates for the f_y dataset at many grid points (see the grids showing $D_\rho < 0$ in Fig. 4.14), while the use of the f_z dataset produces incorrect ρ updates at many points (see the grids where $0 < D_\rho < 40$ in Fig. 4.14).

For the noise-contaminated data, we note that the horizontal-force dataset has a lower S/N ratio than the vertical-force dataset. Nevertheless, using the f_y data gives much better ρ

estimates compared to using the f_z data. This suggests that horizontal-force data might be more robust to noise in the context of ρ estimation compared to vertical-force data, which is also found in Subsection 4.3.1.

Lastly, we compare the reconstructed V_S models using f_z and f_y datasets (Subsection 4.7.3). As opposed to ρ, their accuracy is not significantly different for the two force directions, except for a slight difference in resolution (see Subsection 4.7.3 for more details). The choice of the force directions of the seismic source does not significantly affect the overall accuracy of the V_S estimates; however, small changes in accuracy can still be caused by different resolution of the preconditioned gradient for V_S. The small improvement in accuracy leads to a slightly higher correlation between the true and the estimated models (see Subsection 4.8.2).

4.5. Discussion

4.5.1. Reason behind the superiority of a horizontal-force source for density reconstruction

In Section 4.4, the inversion study using two different near-surface synthetic models has demonstrated that 3D FWI applied to a horizontal-force dataset gives more accurate ρ distribution compared to that applied to a vertical-force dataset. There are two possible reasons behind the superiority of a horizontal-force source over a vertical-force source: parameter coupling between V_S and ρ is relatively weak and/or the observed data are relatively more sensitive to ρ. Based on the results shown in this chapter, we conclude that the different parameter-coupling effects contained in the preconditioned gradient can cause the difference in the accuracy of the finally estimated ρ for each force direction. Given a simple point-scatterer model, the comparison of the relative strengths between the update and the contamination kernels has shown that the contamination in the preconditioned gradient for ρ due to a V_S perturbation is less severe for a horizontal-force dataset than for a vertical-force dataset (see Subsection 4.3.2). Such a benefit of using a horizontal-force dataset has been demonstrated also for two realistic near-surface models, at least at the first iteration (see Figs 4.6 and 4.12). In the context of the gradient-based inversion, the less contaminated, preconditioned gradient at the first iteration can lead to a ρ value which is close to the global minimum. This allows one to avoid falling into a local minimum during the nonlinear inversion. This can offer finally more accurate ρ estimates after the convergence. The other possible reason, i.e., the difference in sensitivity to ρ of datasets of different-force directions, may have a rather small contribution to our results, because the spatial variability of the sensitivity is scaled for each force dataset using the diagonal elements of the approximate Hessian (see Subsection 4.7.1).

In a field application, however, the impact of different sensitivity to ρ for different source-force directions may become more significant. In particular, the SH/Love configuration exhibits stronger sensitivity to ρ perturbations than the SV/Rayleigh configuration, resulting in more energetic scattered wavefields generated by ρ contrasts (see Section 4.3.1). This enhanced sensitivity would make the SH/Love configuration more robust to noise and modelling uncertainties, such as very low signal-to-noise ratio, inaccurate attenuation parameters, and imperfect source modelling, which are generally common for field data. Therefore, in practical applications, both the reduced parameter coupling and the increased

sensitivity to ρ may contribute to the improved accuracy of ρ estimates that can be achieved using horizontal-force datasets.

4.5.2. LIMITATION OF THE ANALYSES

Our findings on parameter coupling are based on numerical investigations. Results of numerical investigations are influenced by the choice of the subsurface model, acquisition geometry, inversion method, and parameterization (e.g., Köhn et al., 2012; Métivier et al., 2015; Yang et al., 2016; W. Pan, Innanen, & Geng, 2018; W. Pan et al., 2019; Gao et al., 2021). In this regard, we have considered seismic data in the scale of near-surface exploration (i.e., several tens of meters in the horizontal direction and ~15 m in the vertical direction). Such datasets are dominated by surface waves. The impact of parameterization (e.g., seismic velocities versus impedances) on the parameter-coupling effect and the variation of this effect depending on the force direction of the source remain still an open question. This needs to be investigated in the future.

In this chapter, we have used the conventional square of l_2 norm (see eq. 4.1) for the misfit function, in order to exploit the full-waveform information, including amplitude variations. This amplitude-sensitive misfit function enables the inversion to make use of the amplitude differences between the observed and the simulated data, resulting in derivation of a more meaningful ρ structure through multi-parameter simultaneous FWI. In contrast, misfit functions that are less sensitive to the amplitude variations (e.g., the GCN, as used in Chapters 2, 3, and 5) might reduce the sensitivity to ρ, since density information is primarily contained in the amplitude variations (Płonka et al., 2016). In such cases, the inversion workflow needs to be designed carefully to stabilize the ρ reconstruction. In 2D field application, we have achieved this by introducing the sequential inversion workflow and deriving an accurate initial model from the geotechnical data (see Chapter 2). Besides, our parameter-coupling analysis shown in Section 4.3.2 is performed only when using the square of l_2 norm, since the formulation for the approximate Hessian in eq. 4.6 is derived based on this misfit function.

For inversion, we have used the NCG method with a preconditioning filter of low computational cost (Subsection 4.7.1). As mentioned in Section 4.1, other sophisticated optimization approaches, which take the accurate Hessian into consideration (e.g., truncated Newton method), can help reduce the parameter coupling (Métivier et al., 2015; Yang et al., 2016; Gao et al., 2021), but they generally increase the computational cost dramatically. Another approach, which may accurately estimate ρ, would exploit hierarchical inversion (Jeong et al., 2012; Prieux et al., 2013; Ren & Liu, 2016): seismic velocities (i.e., V_P and V_S) are updated with the fixed ρ at the first step, and then all parameters are simultaneously inverted at the second step. This hierarchical approach was earlier tested using 2D FWI in an exploration scale, and our results (Subsection 4.3.2) imply efficacy of this approach also for 3D FWI at the near-surface scale. Since the V_S estimate has a small parameter-coupling effect due to error in ρ (see, for instance, Fig. 4.4), V_S can be obtained in the first step with reasonable accuracy, which can then be used to help reducing the parameter coupling for ρ in the second step. Note, however, that the computational cost for this hierarchical approach can be much greater than the simultaneous inversion, especially for 3D FWI. Our results have demonstrated that the use of the horizontal-force datasets would enable one to obtain accurate ρ estimates at a low cost using simultaneous inversion for both ρ and V_S, without

suffering from the strong parameter-coupling problem.

Also, the difference in the parameter coupling due to different wave types is not yet well understood. Typical near-surface seismic data contain several prominent wave types – surface waves and various body waves. Each wave type is scattered due to a perturbation with different amplitude distribution, resulting in different parameter-coupling effect (e.g., W. Pan, Geng, & Innanen, 2018). In Subsection 4.3.1, for example, the scattering pattern differs due to the different incident wave types (SV/Rayleigh waves or SH/Love waves) produced by different force directions and recorded at different receiver components (see Fig. 4.2). Besides, Rayleigh wave propagation involves elliptical motion, either in retrograde or prograde sense, depending on its mode and depth. Gao et al. (2021) has shown that such different motions associated with Rayleigh waves cause different scattering patterns. Thus, the discussions in Section 4.3 are limited to the model considered in our numerical study. In this regard, a horizontal-force source generates both Rayleigh and SV waves propagating with a specific energy distribution over the whole model, which makes it difficult to evaluate the effect of the depth of a point scatterer on parameter coupling. This means that the wave type is crucial in order to estimate the extent of parameter coupling for a given subsurface model. Our numerical investigations, however, have considered the net influence on parameter coupling of all these wave types generated by a body force, and it is not possible to evaluate the contribution of one particular wave type here. Addressing this problem might help optimizing near-surface seismic acquisition. For instance, one may choose a combination of source-receiver components or an arbitrary force direction in 3D for a source such that the wave type with the smallest parameter coupling dominates the observed data. In order to evaluate the contribution from each wave type to parameter-coupling effect, the theoretical scattering pattern based on Born approximation for the surface waves as well as for the body waves would be needed (e.g., Snieder, 1986).

In the analysis of the scattered wavefields (Subsection 4.3.1), we could not separately evaluate the contributions of body waves and surface waves from the simulated wavefield snapshots. This is because, for example, in the SH/Love configuration, Love waves originate from the propagation of SH waves within the shallow, layered structure and exhibit similar polarization and comparable propagation velocities to SH body waves. As a result, their arrivals overlap significantly in both space and time, making it difficult to identify each wave mode clearly in the total wavefield snapshots. This overlap is particularly pronounced in the small-scale near-surface model and band-limited (< 40 Hz) seismic data, where the modal separation is rather incomplete. Using higher-frequency data and/or applying wavefield decomposition techniques could potentially allow clearer separation of these wave types. This remains a topic for future investigation.

Finally, the FWI result can be improved by simultaneously and/or sequentially using different force datasets during the inversion. An example can be that of a horizontal-force dataset, which is not much influenced by parameter coupling; such a dataset can be used to estimate reasonably accurate V_S and ρ at the first step, and then joint inversion of horizontal-force and vertical-force datasets may enhance the result at the second step. Furthermore, especially in the presence of significant lateral heterogeneity in the subsurface (e.g., Subsection 4.4.2), using two orthogonal horizontal-force sources (e.g., f_x and f_y) for the inversion can help improving the result: the use of the full wavefields produced by the horizontal-force sources may reduce parameter coupling further. Such simultaneous or

sequential inversion, however, increases the computation time greatly as the data volume increases. To face such challenges, more cost-effective optimization approaches, like a mini-batch method (e.g., van Leeuwen & Herrmann, 2012), might be of advantage.

4.5.3. PRACTICAL CONSIDERATIONS FOR HORIZONTAL-FORCE SOURCES

We have shown the benefit of using a seismic dataset with a horizontal-force source in 3D FWI for density. However, in the current practice of near-surface seismic investigations, use of a horizontal-force source is less common than a vertical-force source. One reason is that generating efficiently horizontally polarized seismic wave is more difficult from a practical point of view. The slipping of the friction plate is a well-known problem for traditional horizontal-force (shear-wave) sources. This makes it difficult to generate a comparably large force as a vertical-force source, which results in reduction of the investigation depth. Attenuation of shorter-wavelength S waves in the low-velocity formations is further responsible for lower S/N ratio at a given depth, compared to P waves that enrich preferentially the vertical-force data. In the recent decades, however, shear-wave vibrators with small footprints have become more accessible for subsurface investigation in the near-surface exploration scale (e.g., Ghose et al., 1996; Ghose & Goudswaard, 2004; Drijkoningen et al., 2006; Krawczyk et al., 2013; Burschil et al., 2022). Such vibrators can help generate a stable source signal with a relatively large frequency bandwidth, which should alleviate the cycle-skipping issue and increase source repeatability. Another possible effective source is an inclined impact source such as the Galperin source (Häusler et al., 2018) which has been developed for multi-component seismic data acquisition in the near-surface scale. This source can help improve the source coupling with the ground by mitigating the slipping of the friction plate. Although horizontal-component records with a high S/N ratio (produced by a strong seismic source) are crucial for the success of 3D FWI applied to a horizontal-force dataset (see e.g., Fig. 4.11), such datasets might be more noisy at high frequencies in the horizontal components than in the vertical-component records. This is due to the difficulty in achieving adequate receiver coupling with the ground over a large frequency bandwidth (Krohn, 1984). Further verification of the conclusions drawn in this chapter will be carried out in the next chapter through field studies involving three-component sources and receivers.

4.6. CONCLUSIONS

In this chapter, we looked into the performance of gradient-based 3D FWI applied to vertical-force and horizontal-force seismic datasets, in order to estimate the 3D subsoil density distribution. We investigated three important factors viz. noise robustness, parameter coupling, and resolution, through numerical tests. We simulated realistic near-surface seismic data dominated by surface waves.

Our investigations using the scattered wavefield due to a point-localized density perturbation showed that the wavefield energy for a horizontal-force source is larger than that for a vertical-force source. This contributes to robustness with respect to noise of 3D FWI using a horizontal-force dataset, for estimating the subsurface density distribution. Furthermore, our investigation on the update and the contamination kernels for a point-scatterer model indicated that the use of a horizontal-force dataset allows reconstructing the high-resolution,

preconditioned gradient for density with a relatively small parameter coupling. This is beneficial for estimating density at a low computational cost using a gradient-based FWI. Finally, inversion studies for two different near-surface models demonstrated that 3D FWI using a horizontal-force dataset can reconstruct the density distribution more accurately than that using a vertical-force dataset. A horizontal-force source is suitable for obtaining 3D subsoil density distribution through FWI, without a heavy computational burden. The subsoil density variability obtained from 3D FWI will be useful in many important applications in the near-surface scale.

4.7. Appendix

4.7.1. Preconditioning filter based on diagonal Hessian

We use the diagonal elements of the approximate Hessian (H^a_{mm} in eq. 4.6) for the preconditioning filter P_m in eq. 4.3. The diagonal Hessian is calculated by cross-correlation of the Jacobian with respect to a certain parameter class m (i.e., $\partial u_{\text{syn}}/\partial m$). Since a whole model is divided into grid points, H^a_{mm} can be written in the $N \times N$ matrix form, where N is the number of grids. Here, the diagonal elements of H^a_{mm} (i.e., $diag(H^a_{mm})$) represent the cross-correlation between the Jacobians at the same grid, while the off-diagonal elements represent the spatial cross-correlation between the Jacobians at different grids. Since H^a_{mm} is typically assumed to be diagonally dominant and banded due to the finite-frequency effect (Pratt et al., 1998), $diag(H^a_{mm})$ or its approximated form (e.g., pseudo-Hessian) has been commonly used for the preconditioning filter (e.g., Shin et al., 2001; Ravaut et al., 2004; Operto et al., 2004, 2006). In this research, we follow the approach of Butzer (2015), where the inverse of $diag(H^a_{mm})$ is used for P_m as follows:

$$P_m = (diag(H^a_{mm}) + \varepsilon_m)^{-1}, \tag{4.15}$$

where the stabilization factor (i.e., ε_m) is introduced to avoid the division by the very small values of $diag(H^a_{mm})$.

Using the preconditioning filter (eq. 4.15), one can compensate for the effect of geometrical spreading. Since the gradient ($\nabla_m E$) is calculated based on the adjoint-state method (Plessix, 2006) using the wavefield affected by geometrical spreading, $\nabla_m E$ has limited spatial distribution of the amplitudes. In the near-surface exploration scale, this indicates that the amplitudes of $\nabla_m E$ are concentrated around the free surface due to the dominance of the surface waves in the observed seismic data. Thus, without a preconditioning filter, the model around the free surface is preferentially updated during the inversion, which leads to a slow convergence (e.g., Nuber et al., 2015; Yan et al., 2020). Since $diag(H^a_{mm})$ is calculated using the Jacobian which includes the effect of geometrical spreading, its spatial amplitude distribution (energy) is concentrated near the free surface. Therefore, by using the inverse of $diag(H^a_{mm})$ as a preconditioning filter, one can compensate for the limited spatial amplitude distribution of $\nabla_m E$. This makes it possible to uniformly update the whole model from the shallow to the deep parts, resulting in a fast convergence.

There is another advantage of using the diagonal Hessian as a preconditioning filter. In multi-parameter FWI, it is necessary to estimate a suitable scaling factor for each parameter class in compensating for the amplitude distribution of $\nabla_m E$. This is because the Jacobian or the radiation pattern of the wavefield scattered due to a model perturbation differs for the

different parameter classes (e.g., Virieux & Operto, 2009; Operto et al., 2013; Gao et al., 2021). In this research, we calculate the diagonal Hessian for each parameter class. The preconditioning filter, therefore, automatically balances the spatial energy of the gradient for each parameter class.

Finally, in order to calculate the exact $diag(H^a_{mm})$, the Green's functions associated with each receiver position and each receiver component are required: we need to carry out $N_r \times N_{rc}$ simulations for each iteration, where N_r is the number of receivers and N_{rc} is the number of receiver components. Unfortunately, the computational cost for this simulation is prohibitively expensive. Therefore, to reduce the computational burden, we calculate the receiver-side Green's function only for a specific receiver component corresponding to a force component. Moreover, P_m is calculated at the first iteration and kept constant for the rest of iterations (e.g., Operto et al., 2006; Butzer, 2015), which results in the additional reduction of the computational cost.

4.7.2. PARAMETER-COUPLING ANALYSIS FOR V_S USING A REALISTIC SUBSOIL MODEL

As in Subsection 4.4.2, we investigate here the parameter coupling in the preconditioned gradient for V_S. We consider the following equation:

$$
\begin{aligned}
-\frac{1}{diag\left(H^a_{V_S V_S}\right)+\epsilon_{V_S}}\nabla_{V_S}E \approx & \frac{diag\left(H^a_{V_S V_P}\right)}{diag\left(H^a_{V_S V_S}\right)+\epsilon_{V_S}}\Delta V_P^N \\
& + \frac{diag\left(H^a_{V_S V_S}\right)}{diag\left(H^a_{V_S V_S}\right)+\epsilon_{V_S}}\Delta V_S^N \\
& + \frac{diag\left(H^a_{V_S \rho}\right)}{diag\left(H^a_{V_S V_S}\right)+\epsilon_{V_S}}\Delta \rho^N,
\end{aligned}
\tag{4.16}
$$

where $diag\left(H^a_{V_S V_S}\right)+\epsilon_{V_S}$ represents the preconditioning filter for V_S (P_{V_S} in eq. 4.9). We compare the coupling coefficients of V_S (i.e., $diag\left(H^a_{V_S \rho}\right) / \left(diag\left(H^a_{V_S V_S}\right)+\epsilon_{V_S}\right)$) for the different force datasets (Figs 4.15(d)-(f)).

The coupling coefficients of V_S show extremely small values ($\sim 10^{-2}$) below 2 m depth (Figs 4.15(d)-(f)). Note that the value is much smaller than the coefficient for ΔV_S^N (≈ 1). This indicates that the effect of $\Delta\rho^N$ on the preconditioned gradients for V_S is 10^{-2} smaller than that of ΔV_S^N: the preconditioned gradients for V_S are not significantly contaminated by the artifacts due to $\Delta\rho^N$, regardless of the force directions.

Below z = 5 m at the centre of the model, the gradient values for V_S for the f_z dataset are mostly positive (blue dashed line in Fig. 4.15(c)), which is similar to the gradient values for ρ (see the blue dashed line in Fig. 4.12(c)). Although the overall trends for the gradient for the f_y dataset is characterized by an oscillatory nature, one can recognize the large positive value around 11 m depth (see the red line and the black arrow in Fig. 4.15(c)). The true model differences ($\Delta {V_S}^{\text{true}}$ and $\Delta\rho^{\text{true}}$) show the oscillation of $\Delta\rho^{\text{true}}$ around zero and large positive values for $\Delta {V_S}^{\text{true}}$ below z = 5 m (see the black arrow in Fig.

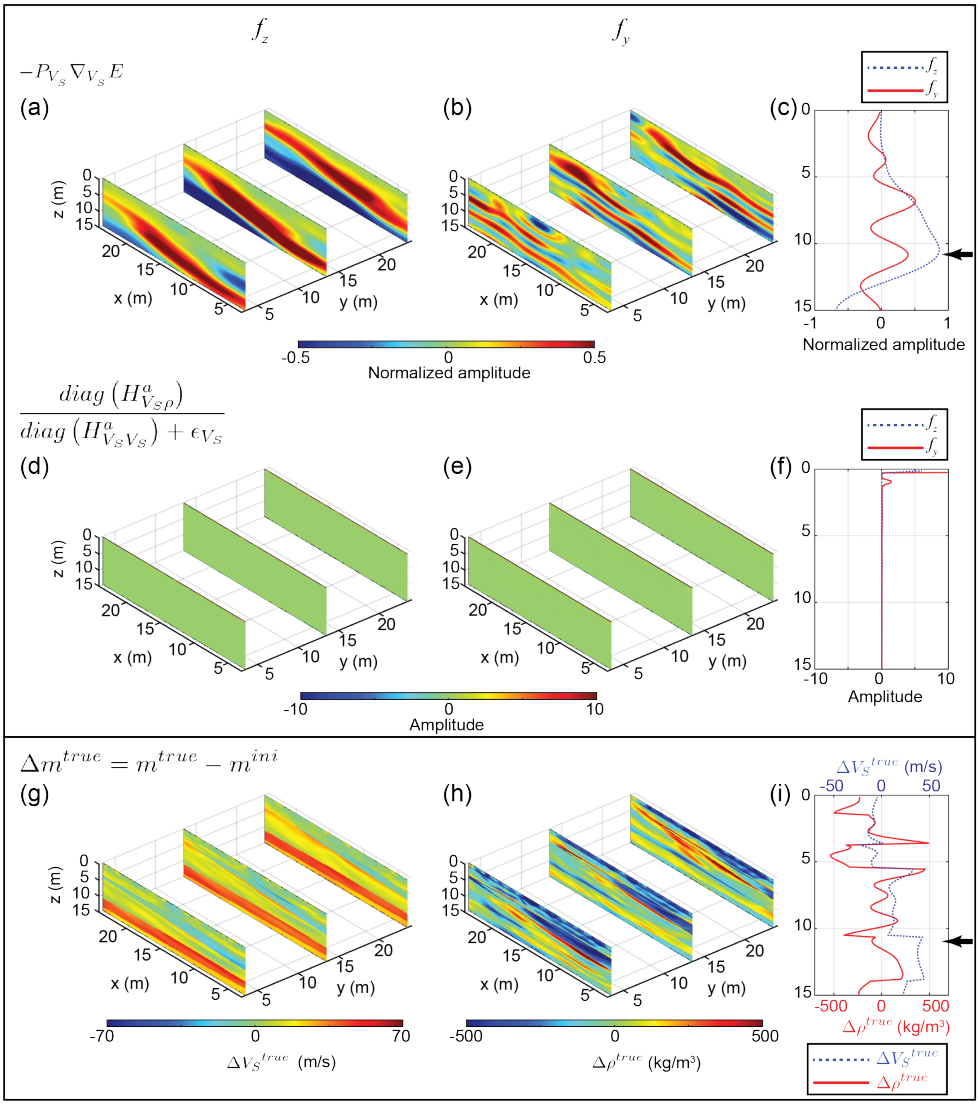

Figure 4.15: (a)-(c) The preconditioned gradients for V_S and (d)-(f) the coupling coefficients of V_S for different force datasets at the first iteration of the stage 1 shown in Table 4.3. (g)-(i) The differences between true and initial models for V_S and ρ.

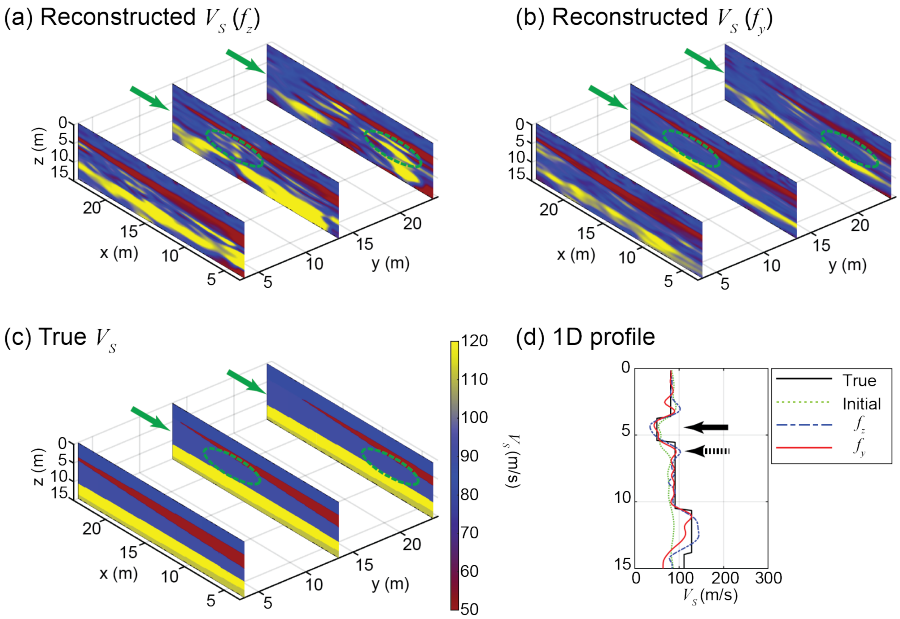

Figure 4.16: The reconstructed V_S models (a) when using an f_z dataset, and (b) when using an f_y dataset. (c) The true V_S model. The green arrow shows the clay layer. (d) The comparison of 1D profiles for the different force datasets at [x, y] = [13.5 m, 13.5 m].

4.15(i)). Thus, the large positive values of the gradient around 11 m depth for both force-direction datasets (Fig. 4.15(c)) indicate that the preconditioned gradients for V_S reflect the direction along ΔV_S^N without significant artifacts due to $\Delta\rho^N$. Besides, the oscillatory nature of the preconditioned gradient for the f_y dataset suggests the possibility of achieving higher-resolution images than with the f_z dataset (Figs 4.15(a)-(c)), which is discussed in Subsection 4.3.3.

4.7.3. INVERSION RESULTS FOR V_S USING A REALISTIC SUBSOIL MODEL

Similar to ρ (Subsection 4.4.2), we compare the reconstructed V_S models using f_z and f_y datasets (Figs 4.16(a) and (b)) with the true V_S model (Fig. 4.16(c)). Both inversions successfully reconstruct the overall V_S structure. However, the results for the f_z dataset show a few artifacts in the clay layer (see green dashed circles in Fig. 4.16(a)), while using the f_y dataset does not produce such artifacts in the same layer (see green dashed circles in Fig. 4.16(b)).

The comparison of 1D profiles illustrates better V_S estimates for the f_y dataset in the peat layer than for the f_z dataset (see the solid black arrow in Fig. 4.16(d)). Additionally, there is a larger oscillation in the clay layer when using the f_z dataset than using the f_y dataset (see the black dashed arrow in Fig. 4.16(d)). These differences reflect difference in resolution capabilities of the preconditioned gradient for the two different source directions, as discussed in Subsection 4.7.2.

We calculate the histograms of D_{V_S} (eq. 4.14) for f_z and f_y datasets (Fig. 4.17). Unlike

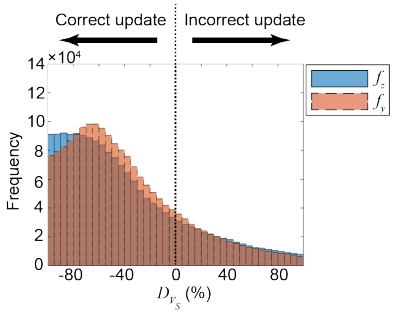

Figure 4.17: The comparison of the histograms of D_{V_S} for two different force-direction datasets.

for ρ (Fig. 4.14), one cannot recognize any significant difference among the overall trends of D_{V_S} for the different force-direction datasets. In other words, an almost identical V_S model is estimated for all different force directions of the seismic source.

These results demonstrate that the choice of the force direction does not significantly affect the overall accuracy of the V_S estimates; such a choice might cause only a small difference in the accuracy due to different resolution of the preconditioned gradient for V_S.

4.8. SUPPLEMENTARY MATERIAL

4.8.1. FWI RESULTS USING AN f_x DATASET FOR A REALISTIC SUBSOIL MODEL

The inversion test in Subsection 4.4.2 has demonstrated that 3D FWI applied to a horizontal-force dataset (f_y) can reconstruct more accurate ρ distribution than applied to a vertical-force dataset (f_z), given a subsoil model that has been built based on the actual measured data. However, use of a horizontal-force source in the different direction (i.e., f_x) may give different ρ estimates from when using an f_y source. This is because the realistic model that we have used for the inversion test contains a laterally heterogeneous structure (see Figs 4.10(a)-(c)). Furthermore, the accuracy of the initial model, which has been constructed by 2D SH FWI for the f_y dataset, differs spatially (see Figs 4.10(d)-(f)). In this section, we perform 3D FWI for an f_x dataset to compare with 3D FWI applied to an f_z dataset in terms of the accuracy of ρ estimates, as demonstrated for an f_y dataset in Subsection 4.4.2.

The example of the simulated data using the f_x source is shown in Fig. 4.18. We add random noise to the dataset as explained in Subsection 4.4.2, which results in a similar S/N ratio to the f_y dataset: the S/N ratio in the x-component data (v_x) at the farthest source-receiver offset (28.3 m) is ~8. Waveforms similar to those in case of an f_y source can be observed (see Fig. 4.18): the horizontal-component records have much more energy than the vertical-component records, and the reflected arrival from the lower boundary of the peat layer is clearly visible.

For the inversion, we use the same initial model and inversion steps as in Subsection 4.4.2. After the convergence, the simulated waveforms match well with the observed waveforms (red dashed lines in Fig. 4.18). A comparison of the ρ models shows that the use of the f_x data offers better ρ estimates than when using the f_z data (Fig. 4.19). For example, the sharp boundary between the clay (third layer denoted by the green arrows in

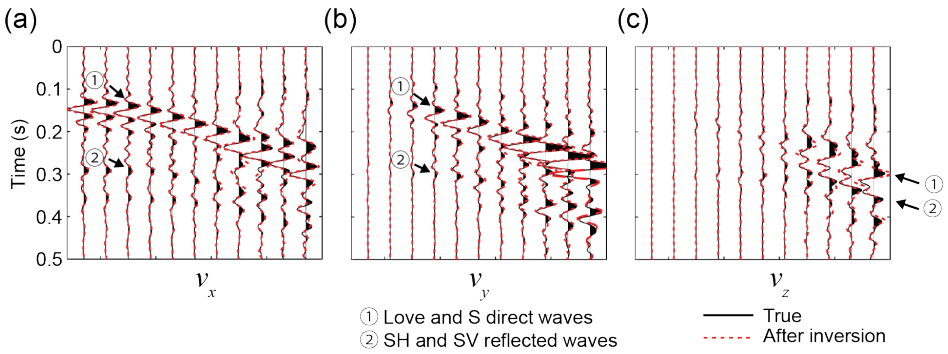

Figure 4.18: The example of the f_x pseudo-seismic data calculated for the model shown in Figs 10(a)-(c) at y = 3.5 m. The source is located at [x, y] = [3.5 m, 13.5 m]. For visualization, each trace is normalized by the maximum amplitude of v_x records.

Figs 4.19(a)-(c)) and sand (fourth layer) layers can be well-recognized in case of the f_x dataset. The 1D profiles at the centre of the model also illustrate that ρ estimates for the f_x data are much closer to the true values, for instance, at around 5 m and 10 m depths (black solid and dashed lines in Fig. 4.19(d)). Next, we calculate the histograms of D_ρ (eq. 4.14) in order to compare the overall accuracy of ρ estimates between using f_x and f_z datasets. For the f_x data, there are significantly more correct updates than for the f_z data (see the grid showing $D_\rho < 0$ in Fig. 4.20). These results show that using horizontal-force sources oriented either in x- or y-direction enables one to obtain more accurate ρ distribution than when using vertical-force sources, given a realistic subsoil model.

We also compare the reconstructed V_S estimates for the f_x and f_z datasets. Similar to the comparison between using f_y and f_z datasets (see Subsection 4.7.3), the overall V_S structure is well reconstructed for both datasets, while there are fewer artifacts in the clay layer for the f_x dataset than for the f_z dataset (see the green circles in Fig. 4.21). The comparison of 1D profiles also illustrates that using the f_x data leads to more accurate V_S values in the peat layer than using the f_z data (see the black arrow in Fig. 4.21). Lastly, we compare the histograms of D_{V_S} (eq. 4.14) for both datasets (Fig. 4.22). Reflecting the differences in the accuracy of V_S estimates as described above, one can see many more grids having D_{V_S} close to -100 (i.e., $m_{\text{est}} = m_{\text{true}}$) for the f_x data than for the f_z data (see the grids where $-100 < D_{V_S} < -60$ in Fig. 4.22).

4.8.2. In-depth evaluation of the estimated density

In this section, we investigate in detail the accuracy of ρ estimates for different force directions (i.e., f_x, f_y, and f_z). In order to evaluate the performance of 3D FWI applied to different force-direction datasets, we first calculate the model error $m_{\text{L2}}^{\text{error}} = \| m_{\text{true}} - m_{\text{est}} \|^2$, where m_{true} and m_{est} are the true and estimated models, respectively (Fig. 4.23(a)). The evolution curves of the model error with iteration show that the use of the horizontal-force sources (red and blue lines in Fig. 4.23(a)) gives less erroneous ρ than the use of the vertical-force sources (black lines in Fig. 4.23(a)). The model error $m_{\text{L2}}^{\text{error}}$, however, gets worse with

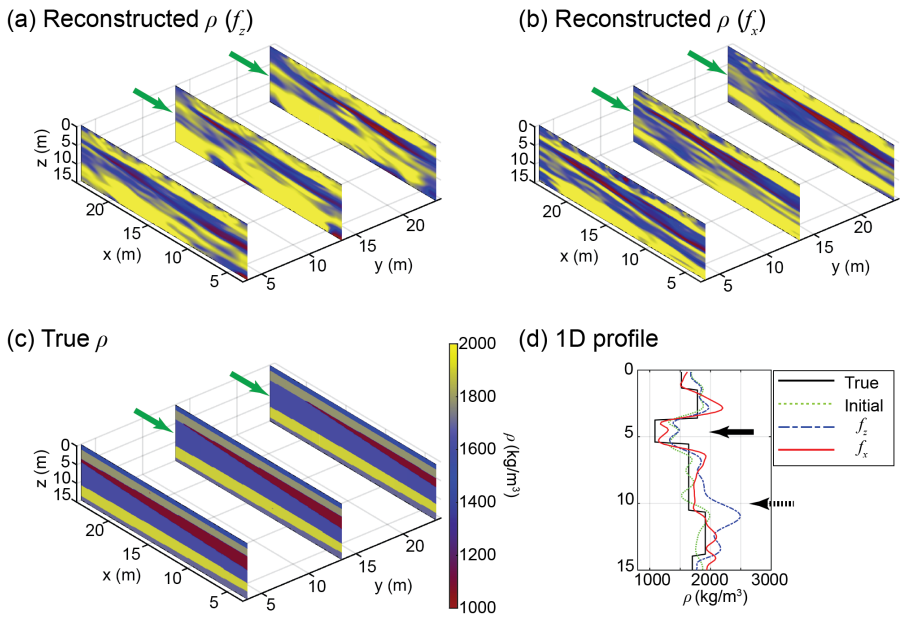

Figure 4.19: The reconstructed ρ models (a) when using an f_z dataset, and (b) when using an f_x dataset. (c) The true ρ model. The green arrows show the clay layer. (d) The comparison of 1D profiles for two different force-direction datasets at [x, y] = [13.5 m, 13.5 m].

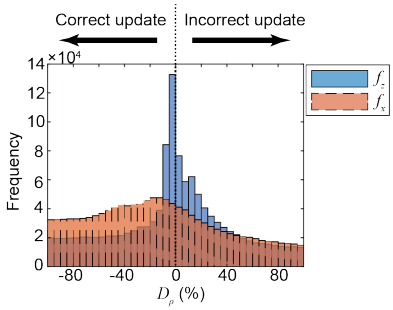

Figure 4.20: The comparison of the histograms of D_ρ for two different force-direction datasets.

iteration, even when using a horizontal-force source. In order to appreciate the reason for this, we visualize the spatial distribution of D_ρ (eq. 4.14) for the f_y data. From a comparison between the distribution and 1D profiles shown in Fig. 4.24, we notice that the grids having incorrect updates ($D_\rho > 0$) concentrate in the surrounding of the peat layer (see the black lines in Fig. 4.24), while there are many correct updates at other grids. This observation is supported by the histogram of D_ρ for the f_y dataset, illustrating many grids showing correct updates (see Fig. 4.14). The incorrect ρ updates at the layer boundary could be the side-lobe in the vertical section of the ρ model resulting from the limited frequency bandwidth in our data, and the limited acquisition geometry (e.g., Virieux & Operto, 2009; Y. E. Li &

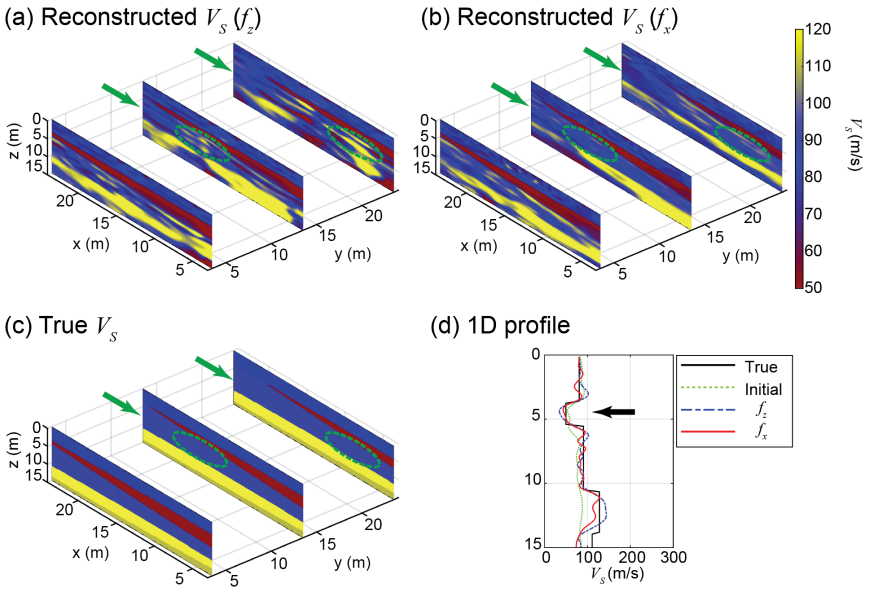

Figure 4.21: The reconstructed V_S models (a) when using an f_z dataset, and (b) when using an f_x dataset. (c) The true V_S model. The green arrows show the clay layer. (d) The comparison of 1D profiles for the different force datasets at [x, y] = [13.5 m, 13.5 m].

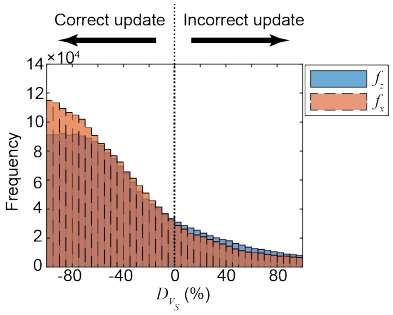

Figure 4.22: The comparison of the histograms of D_{V_S} for two different force-direction datasets.

Demanet, 2016). Such side-lobe might be caused by the drastic change in ρ values between the clay (~1700 kg/m^3) and peat (~1100 kg/m^3) layers present in our realistic model. Except the side-lobe mentioned above, 3D FWI applied to the horizontal-force data reconstructs the high-resolution layered ρ structure: the lower boundary of the pear layer and the upper boundary of the sand layer are more clearly visible compared to the initial model (see the green circles in Fig. 4.24). We quantify how the layered ρ structure is improved during the

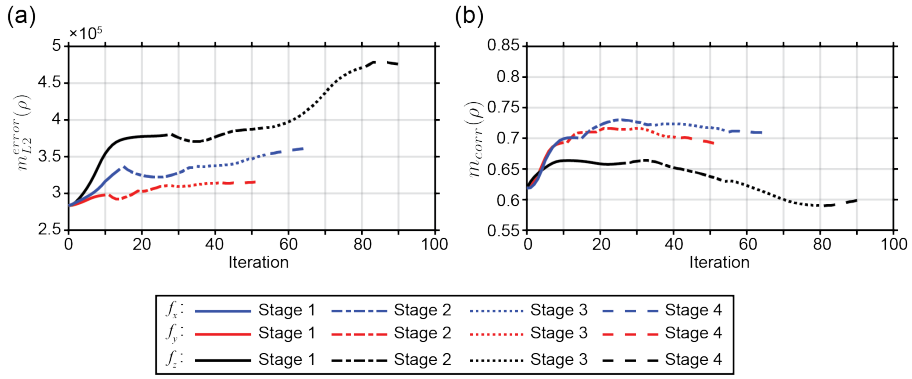

Figure 4.23: (a) The evolution curves of the model error m_{L2}^{error} for ρ estimates. (b) The evolution curves of the image correlation m_{corr} for ρ estimates.

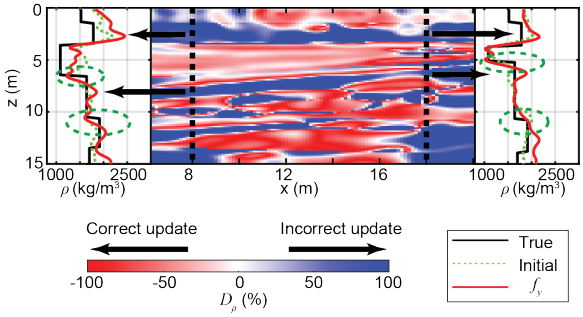

Figure 4.24: The comparison between the spatial distribution of D_ρ and the 1D profiles of ρ estimates for the f_y dataset. The 2D slice of the spatial distribution is located at y = 8.5 m.

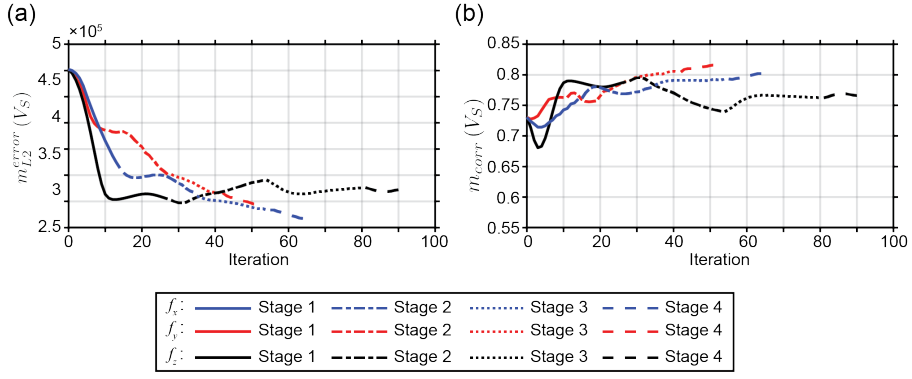

Figure 4.25: (a) The evolution curves of the model error $m_{\text{L2}}^{\text{error}}$ for V_S estimates. (b) The evolution curves of the image correlation m_{corr} for V_S estimates.

inversion by calculating the image correlation defined as follows (Dagnino et al., 2014):

$$m_{\text{corr}} = \frac{\sum \left(m_{\text{true}} - \overline{m_{\text{true}}}\right)\left(m_{\text{est}} - \overline{m_{\text{est}}}\right)}{\sqrt{\sum \left(m_{\text{true}} - \overline{m_{\text{true}}}\right)^2 \sum \left(m_{\text{est}} - \overline{m_{\text{est}}}\right)^2}}, \tag{4.17}$$

where $\overline{m_{\text{true}}}$ and $\overline{m_{\text{est}}}$ are the mean values for the true and the estimated models, respectively. A comparison of the evolution curve of the image correlation (Fig. 4.23(b)) demonstrates that 3D FWI for the horizontal-force dataset (f_x or f_y) reconstructs the ρ structure that correlates strongly with the true model (m_{corr} ~0.7), while ρ from 3D FWI for the vertical-force dataset has a lower image correlation (m_{corr} ~0.6).

Finally, we also evaluate the accuracy of the estimated V_S for different force datasets using $m_{\text{L2}}^{\text{error}}$ and m_{corr}. As opposed to ρ, the accuracy of the V_S estimates is significantly improved with iteration regardless of the force directions (Fig. 4.25(a)). Nevertheless, the use of the horizontal-force sources gives slightly higher correlation between the true and the estimated models compared to the use of the vertical-force sources (see Fig. 4.25(b)), reflecting better V_S estimates at some locations as described in Subsection 4.7.3 and Subsection 4.8.1.

5

3D FWI FOR SUBSOIL DENSITY: CONSIDERATIONS FOR THE FORCE DIRECTION OF THE SEISMIC SOURCE

FWI applied to seismic data is an effective approach for retrieving 3D spatial variability of V_P, V_S, and ρ in soil. In Chapter 4 of this thesis, we have illustrated on synthetic data that the use of horizontal-force seismic sources reduces the parameter-coupling effect between V_S and ρ, enabling relatively accurate reconstruction of ρ. In this chapter, we show on field data the benefits of using horizontal-force sources in case of 3D FWI. We examine the accuracy of the inverted V_S and ρ estimates using datasets corresponding to three different force-directions for the seismic source, namely vertical-force source and two cross-polarized horizontal-force sources. From the inversion of field data and from numerical investigations, we identify a major challenge especially when using inline horizontal-receiver data due to inline horizontal-force seismic sources: large misfit values are found between the observed and the simulated waveforms for a given initial model. This is due to the presence of the leaky wave, which is pronounced only in the simulated data and not in the field data. A reason behind the abundance of leaky wave in the simulated data was not investigated earlier. We find that 3D FWI can reconstruct the subsurface model reasonably well when we selectively use specific combinations for seismic source and receiver components that do not produce much leaky wave in the synthetic data. For horizontal-force sources, we utilize the crossline component source-receiver combination, where SH/Love wavefield is more enriched. For the vertical-force source, only vertical receiver data provide good results in FWI. A comparison of 3D FWI results for each force-direction data illustrates that the use of the horizontal-force data resolves both V_S and ρ with a better agreement with independent field and laboratory geotechnical measurements and density logging data, than using the vertical-force data. In particular for ρ, its spatial variability can be obtained only when we

make use of the horizontal-force seismic sources. This is probably due to the fact that the corresponding misfit function has a relatively higher sensitivity to ρ. Moreover, because of using selectively the SH/Love-wave-dominated data, the misfit is not much influenced by changes or uncertainties in V_P, making the inversion effectively focused on V_S and ρ estimation. Finally, we explore the possibility of further improving the FWI results by using two cross-polarized horizontal-force sources. Compared to FWI using single-component horizontal-force source data, FWI using jointly data of two cross-polarized horizontal sources enables avoiding local artifacts in both V_S and ρ images. Also, a finer ρ structure can be retrieved by such joint inversion, facilitating interpretation of subsoil structure that aligns better with the CPT data. Our research demonstrates that robust reconstruction of the 3D spatial variability of V_S and ρ in soils is possible by means of 3D FWI, if we focus on SH/Love-wave-dominated data recorded by horizontal receiver components and generated by two cross-polarized, horizontal-force seismic sources.

5.1. INTRODUCTION

V_S, ρ, and their 3D spatial variation are critically important in many geotechnical site evaluations such as soil characterization, assessing structural support, and urban planning. An accurate estimation of V_S and ρ is possible, for example, by geophysical logging performed in a borehole or by laboratory tests on soil samples collected in boreholes. However, these methods are time-consuming and expensive. It is also impractical to try to capture lateral variability in soil through geotechnical tests done at many locations in the field. Instead, one commonly relies on seismic surveys to capture lateral variability in the elastic parameters that link with many geotechnical properties of the soil. Near-surface seismic data are generally dominated by dispersive surface waves which are sensitive to V_S distribution. Dispersion-curve-inversion methods are conventionally used to estimate the spatial distribution of V_S in 2D (e.g., Park et al., 1999; Xia et al., 1999) or 3D (e.g., Y. Pan et al., 2016, 2018). However, such an inversion approach is based on 1D assumption on V_S variability. This limits the achievable lateral resolution. Also, surface wave dispersion curves are not much sensitive to ρ (Xia et al., 1999; Foti & Strobbia, 2002), leading to a difficulty in estimating the spatially varying ρ.

In recent years, a rapid increase in computation power has made 3D FWI feasible in the scale of near-surface soil investigation. 3D FWI can generate an image of the distribution of elastic properties in the unconsolidated soils in the depth range as shallow as 0–20 m, but also for greater depths (e.g., Smith et al., 2019; Tran et al., 2019; Y. Pan et al., 2021; Teodor et al., 2021; Irnaka et al., 2022; Mirzanejad et al., 2022). However, most of these earlier studies have focused on imaging seismic velocities (V_P and V_S), while the reconstruction of ρ through 3D FWI remains challenging. Also, in these previous studies, seismic vertical-receiver data due to vertical-force seismic sources are generally used in FWI. There are only a few prior attempts of FWI using horizontal-component receiver data (Y. Pan et al., 2021; Irnaka et al., 2022; Irnaka, 2022). The advantages of using horizontal-component seismic sources in 3D FWI are not yet well investigated.

In 2D FWI, SH/Love waves generated by a crossline horizontal-force source have been found to be beneficial for simultaneously resolving V_S and ρ with a high resolution (Dokter et al., 2017; Wittkamp et al., 2018, Chapter 2 of this thesis). More recently, both synthetic and field applications have shown that a horizontal-force seismic source also contributes

to accurate model building by 3D FWI. Kawasaki et al. (2024) have performed numerical investigations using a realistic, shallow subsoil model, and have investigated the difference in the accuracy of ρ estimates when vertical- and horizontal-force seismic sources are used (Chapter 4). It is found that horizontal-force seismic data have favourable characteristics for resolving relatively high-resolution distribution of ρ without severe parameter coupling. However, the advantages of horizontal-force seismic sources in 3D FWI still need to be examined on field-seismic data.

In this chapter, we explore 3D FWI results using different source-force-direction field datasets, aiming to estimate the spatial variability of V_S and ρ. The field tests focus on three-component seismic sources, namely the vertical-force source and the two cross-polarized horizontal-force sources. The accuracy of the FWI results is checked through comparison with independent V_S and ρ measurements carried out in boreholes at the same field. In the following, we first illustrate on field data a major difficulty that we recognize when horizontal-force-source data are used in FWI. In this case, it is difficult to achieve a good fit in seismic waveforms between the simulated and the observed data. We propose a practical approach to overcome this challenge. We then demonstrate how using horizontal-force sources can be beneficial for a successful imaging of V_S and ρ. Finally, we examine the potential benefits in FWI of combining data from two cross-polarized horizontal-force sources, compared to using a single horizontal-force source.

5.2. Methodology: 3D FWI using a single source component and the $f_x + f_y$ source combination

We perform 3D FWI for each force-direction source dataset using the time-frequency approach as presented in Chapter 4 (see Section 4.2.1 for details): the seismic wavefield is simulated by a finite-difference time-domain method, while the gradient of the misfit function is calculated in the frequency domain. We use the GCN to measure the difference between the observed and the simulated seismograms (see eq. 2.1). The GCN ensures that the far-offset data and the near-offset data contribute equally to the inversion by maximizing the cross-correlation between the normalized observed and synthetic seismic waveforms (see also Section 2.2.1). This characteristic is preferable to address our dataset which shows high anelastic attenuation ($Q_S \sim 5$, see Section 2.3.4). To simulate u^{syn} in eq. 2.1, we consider for the source seismic body forces – f_x, f_y, and f_z – directed respectively in x-, y-, and z-axis in the Cartesian coordinate system. Here, the horizontal axes (x and y) represent the directions in which we apply the force at the two cross-polarized, horizontal seismic sources.

In addition to the use of a single-component horizontal source, we perform a joint inversion combining in FWI data from two cross-polarized horizontal-force sources (i.e., $f_x + f_y$). In this case, the misfit function $E_{f_x+f_y}$ is calculated as follows:

$$E_{f_x+f_y} = E_{f_x} + E_{f_y}, \tag{5.1}$$

where E_{f_x} and E_{f_y} represent the misfit functions for the f_x and the f_y source datasets, respectively. In this context, note that there could be a distinct difference in energy between f_x and f_y source-generated wavefields. This difference can be present in the field data, for example, due to different ground coupling for different source-force directions. Such a

difference will manifest also in the FWI results. However, any difference in the wavefield energy between source-force directions will not necessarily mean a difference in the amount of subsurface information present in the datasets. To ensure a similar contribution from both datasets to the inversion, it is important to normalize the misfit functions for each source-type data (i.e., E_{f_x} and E_{f_y}) by their observed wavefield energy (e.g., Wittkamp et al., 2018). In our research, this is achieved by employing the GCN, in which the observed and the simulated seismograms are normalized by their energy (see eq. 2.1).

5.3. DATA ACQUISITION AND 3D FWI SETTINGS

We acquire 3D seismic data at a soft soil site in the northern part of the Netherlands to estimate the spatial distribution of V_S and ρ through FWI. To examine the accuracy of the subsurface model derived from FWI, we obtain independent geotechnical data from multiple locations covering the test site.

5.3.1. SEISMIC DATA ACQUISITION

We conduct a seismic survey using an isotropic configuration for data acquisition, employing a receiver array of 50 m×50 m (Fig. 5.1). This survey is performed in the same field as the 2D SH seismic survey; the 2D line is shown by the green line in Fig. 5.1 (see Chapters 2 and 3 for the 2D survey). Seismic signal is generated independently in x, y, and z directions (i.e., f_x, f_y, f_z) at every source point in the field. The electric linear-motor-system (LMS) vibrator of Seismic Mechatronics in vertical and horizontal modes is used as vertical- and horizontal-force sources, respectively (Noorlandt et al., 2015). 3C geophone nodes (676×3=2028 receiver channels) are used in 3D data acquisition. The parameters for seismic data acquisition are listed in Table 5.1. Although the vibroseis dataset acquired in the field corresponds to a 4–300 Hz sweep, the maximum frequency used in FWI is limited to only 25 Hz for two main reasons. Firstly and most importantly, restriction of the maximum frequency to 25 Hz is necessary to avoid acquisition footprints which occur due to spatial aliasing (of the higher frequencies) caused by the coarse (8 m) source spacing in our field acquisition (due to restricted time and resources). The acquisition footprints increase with increasing higher frequencies in the inversion (see Section 5.6.3 for details). Secondly, for 3D FWI use of relatively higher frequencies increases the computation time dramatically. This is because, while in 2D FWI the computation time increases with the square of the frequency, in 3D FWI computation time increases with the cube of the frequency. These are the two main reasons why the highest frequency used in 3D FWI of our field data is restricted to such a low value (25 Hz). This has, as expected, resulted into rather low resolution in our FWI results. Nonetheless, it is possible to make a relative evaluation of the FWI results for different source-force-direction datasets by using the same frequency band always. Independent geotechnical tests and downhole logging are performed by Fugro, and they include CPTs, V_S measurements from SCPTs, ρ measurements from gamma-gamma density logging carried out in two drilled boreholes (BH1 and BH2), and laboratory experiments on undisturbed soil samples collected in all six boreholes (BH1-BH6). We refer the reader to Fig. 2.3, where example of SCPT data and density measurements at the centre of the seismic patch (BH2) are shown.

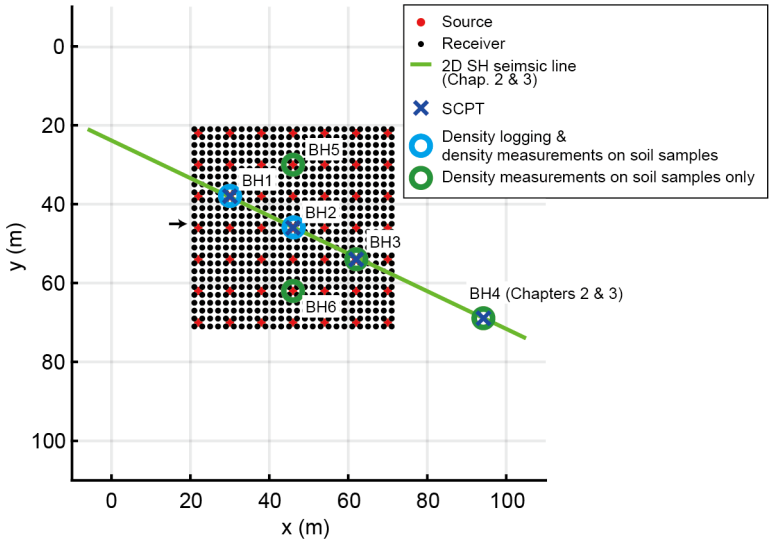

Figure 5.1: Acquisition geometry for the seismic survey. The locations of the geotechnical tests (SCPT and density measurements on soil samples in laboratory) and density logging are also shown. The black arrow marks the 2D seismic line which is used for the investigation of the leaky wave mode (see Section 5.4).

Table 5.1: Parameters for seismic data acquisition.

Parameter	Details
Source	Electrical linear-motor-driven vibrator
Source points	49 3C sources / f_x, f_y, f_z
Source signal	sweep length: 20 s / sweep frequency: 4-300 Hz / record length: 22 s
Source spacing	8 m
Source stack count	4
Receiver array	26×26=676 3C cable-free, nodal geophones / v_x, v_y, v_z
3C geophone nodes	GSX-3 (Geospace Technologies)
Receiver natural frequency	5 Hz
Receiver spacing	2 m
Time sampling interval	0.5 ms ($f_{Nyquist}$ = 1000 Hz)

5.3.2. 3D FWI settings

A good initial model is needed for a successful FWI, avoiding falling into the local minima. Following the initial model-building strategy discussed in Chapter 2, we use 1D initial models. These initial models are the highly smoothed versions of the SCPT-derived V_S and the density-log-derived ρ at BH2 (see Fig. 5.2). The goodness of these initial models is shown in Section 2.3.3 for the case of 2D SH-wave FWI. V_P is calculated from V_S using an empirical relationship between the two under the assumption of fully water-saturated soil (Kitsunezaki et al., 1990). The water table is indeed observed at our test site at only ~1.3 m depth. The dominant wavelength of S wave is ~8 m considering a frequency of 25 Hz. To account for anelastic attenuation, we perform viscoelastic simulations assuming $Q_S = 5$ over

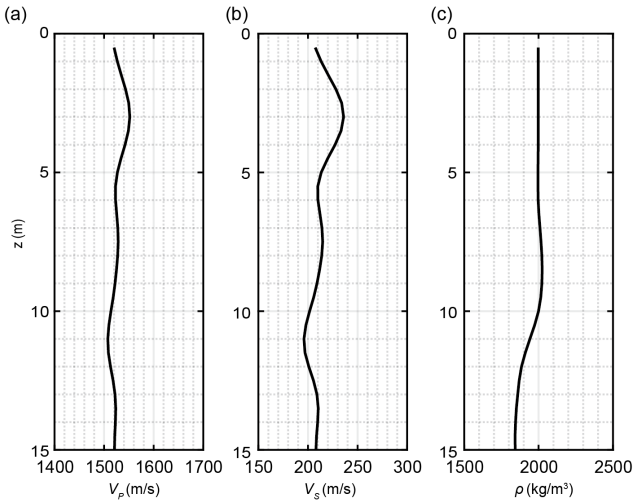

Figure 5.2: 1D initial model used for FWI.

Table 5.2: Monochromatic frequencies used for multi-scale inversion.

Stage	Monochromatic frequencies (Hz)
1	5.8, 6.8, 7.8, 8.8, 9.8, 10.8, 11.8, 12.8, 13.8, 15.0
2	6.2, 7.2, 8.2, 9.2, 10.2, 11,2, 12.2, 13.2, 14.3, 15.5, 16.8, 18.2, 19.7, 21.3, 23.1, 25.0

the whole model space; this Q_S value is estimated on 2D SH data by using a grid search and the amplitude of the observed Love wave (see Section 2.3.4). We further assume $Q_P = Q_S$ as in Mirzanejad et al. (2022).

We invert for V_S and ρ, while V_P and attenuation parameters (Q_P and Q_S) are kept fixed during the inversion. To address the cycle-skipping issue, the multi-scale inversion is performed by gradually increasing the maximum frequency used for inversion (Bunks et al., 1995). We consider two frequency stages that consist of different monochromatic-frequency combinations for the calculation of the gradient of the misfit function (Table 5.2). These frequencies are selected to cover continuously the vertical wavenumbers following the approach of Sirgue and Pratt (2004). Furthermore, we adopt a sequential inversion workflow which is built in Chapter 2. This workflow allows a relatively accurate estimation of ρ owing to the reduced coupling between V_S and ρ (see Section 2.4.1 and Fig. 2.1 for details). This workflow is applied in each frequency stage. The inversion at each stage is stopped when two consecutive iterations do not change the misfit by more than 1%. The source time function is estimated at the first iteration step using a stabilized deconvolution technique (Groos et al., 2014), and then it is fixed during the same frequency stage.

For preconditioning, we apply a circular taper to the gradient around the shot positions and balance the spatial amplitude distribution of the gradient by applying a wavefield-energy-based filter (Zhang et al., 2012). We also apply a Gaussian smoothing filter to the gradient for damping artifacts below the FWI resolution limit. We set its vertical width (i.e.,

4σ of a Gaussian function) to half the dominant wavelength (Ravaut et al., 2004). On the other hand, we also need to use a filter having horizontal width of 1.5× and 2× dominant wavelength for Stage 1 and Stage 2, respectively. This helps to avoid the deterioration of the FWI result due to acquisition footprint appearing severely in the lateral direction (see Section 5.6.3 for details), though at the expense of resolution.

For successful 3D FWI, we use only a part of the dataset acquired in the field. This will be discussed in the following section.

5.4. Challenges in 3D FWI with horizontal-force sources: influence of leaky waves

In 3D FWI, we find substantial initial misfits between the observed and the simulated seismograms, especially when inline horizontal-force sources and inline horizontal receivers are used. This issue is critical, because it can lead to cycle-skipping unless the inversion starts with very low frequency band. In our case, the inversion was initiated using the lowest frequencies available, yet the problem still occurs. This means that simply lowering the starting frequency is not a feasible solution. In this section, we investigate the cause of the problem and possible solution through numerical simulations.

5.4.1. Large initial misfits caused by leaky waves

We first perform multi-scale inversion of the inline horizontal receiver data due to the inline horizontal-force source starting with an initial model shown in Fig. 5.2. However, the inversion fails to reduce sufficiently the misfits after updating V_S and ρ. To investigate the cause of this failure, we closely examine the data. We find that a part of the seismic data has a large initial deviation between observed and simulated traces. We show an example of such large initial misfits in Fig. 5.3, focusing on a 2D seismic line at y = 45 m (see black arrow in Fig. 5.1). Fig. 5.3(a) shows the observed inline horizontal-receiver seismic traces (v_x) due to the inline horizontal-force source (f_x) at (x, y) = (22 m, 46 m). We also calculate the simulated data using the initial model (Fig. 5.2) for a comparison (Fig. 5.3(b)). Although the shot position is deviated from the receiver line 1 m in the y-direction, this deviation is much smaller than the dominant wavelength (~8 m). We anticipate that P-SV/Rayleigh mode dominates the seismic records shown here. In both observed and simulated seismograms, one can observe a seismic wave with similar propagation velocity, especially at the far offsets (see black arrows in Figs 5.3(a) and (b)). The simulated data, however, are dominated by a seismic wave mode propagating with a much higher apparent velocity (see green arrow in Fig. 5.3(b)). This fast-propagating wave is not visible in the observed data, resulting in the undesirable large misfits between observed and simulated data.

To further examine the fast-propagating seismic wave mode in the simulated data, we estimate the dispersion images in the phase-velocity-frequency domain for the observed and the simulated data (Figs 5.3(c) and (d), respectively). A comparison shows a significant difference between them. The observed seismic data are dominated by Rayleigh wave with a phase velocity of ~200 m/s over a wide frequency range, as expected (see the black arrow in Fig. 5.3(c)). On the contrary, our simulation produces a much more energetic mode with a higher phase velocity (400 m/s ~ 800 m/s) than the Rayleigh wave (see black

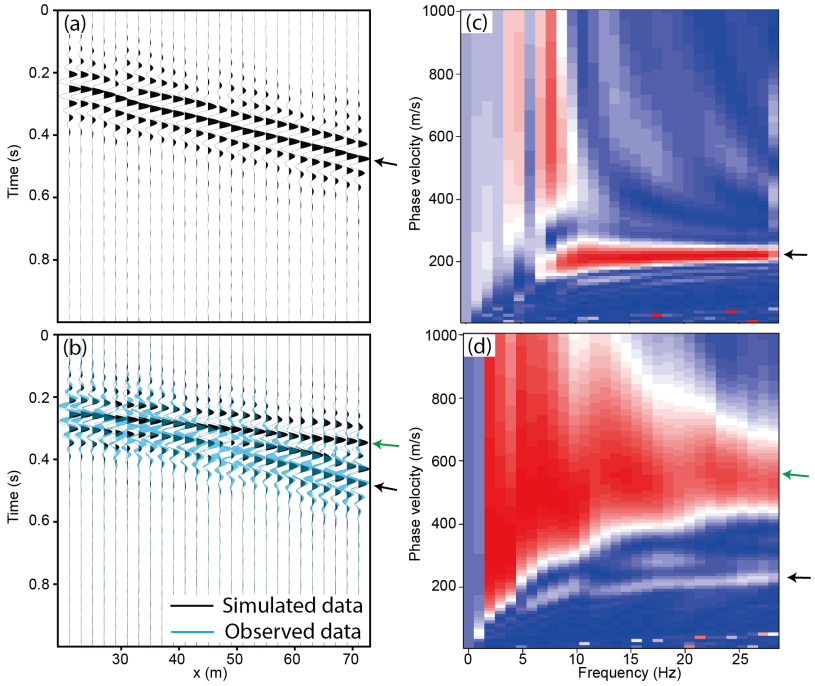

Figure 5.3: Comparison between (a) the observed and (b) the simulated inline horizontal-receiver data (common-source or shot gathers) for the inline horizontal source for our initial model of FWI (Fig. 5.2). Both common-source gathers are bandpass filtered between 6 – 25 Hz corresponding to Stage 2 of the multi-scale inversion. (c) and (d) dispersion images calculated from (a) and (b), respectively. The black arrows mark the event that is present in both the observed and the simulated shot gathers, while the green arrow indicates an event which can be observed only in the simulated data. For ease of visualization, each seismic trace is normalized by its maximum amplitude.

and green arrows in Fig. 5.3(d)). This phase velocity is larger than the given V_S (~200 m/s), while lower than the given V_P (~1500 m/s). For a comparison, we also investigate crossline horizontal-component receiver data (v_y) for the crossline horizontal-force source (f_y), considering the same 2D line (i.e., at $y = 45$ m, see Fig. 5.1). In this case, we anticipate an abundance of SH/Love mode in the seismic records. Unlike the inline horizontal receiver data for the inline horizontal source (Fig. 5.3), there is no significant difference between the observed and the simulated data (Fig. 5.4). Therefore, our detected large initial misfits occur only in the P-SV/Rayleigh-wave-dominated data.

The wave mode seen in the simulated inline horizontal receiver-component for the inline horizontal source, with a phase velocity between V_S and V_P, is known to be a leaky mode, as evidenced in the past also in synthetic and field seismic observations (Schröder & Scott, 2001; Gao et al., 2014; Lin et al., 2023). Different kinds of leaky waves can be generated in a specific situation. For example, when the V_S of an underlying half space is lower than that of the upper layer and there is a high V_S contrast between the two layers, leaky waves can be generated (Lin et al., 2023). More generally, a significant leaky mode is excited when the shallow subsurface has a high Poisson's ratio (Schröder & Scott, 2001; Gao et al.,

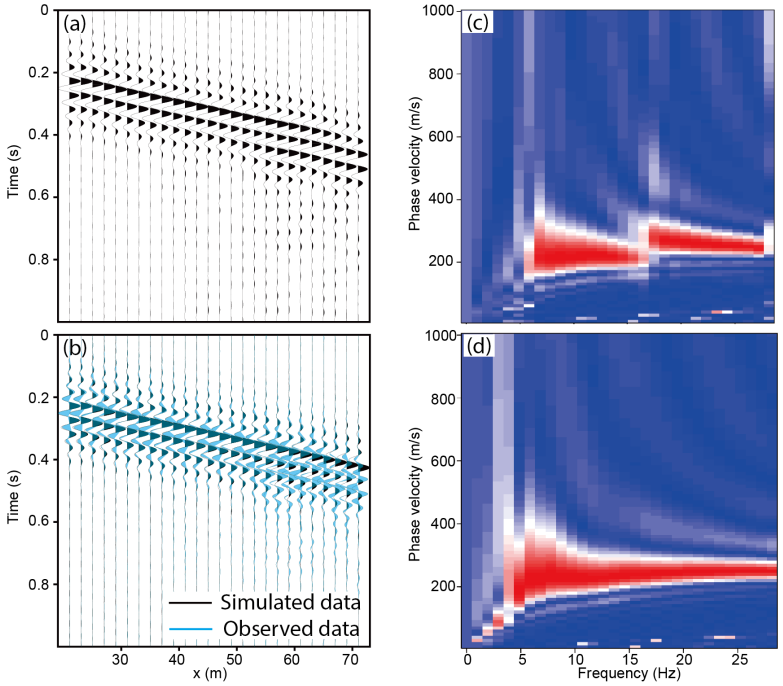

Figure 5.4: Same as in Fig. 5.3, but for the crossline horizontal-component receiver data due to a crossline horizontal-force seismic source.

2014; Lin et al., 2023). This mode is usually pronounced in the radial (inline) component of the seismic receiver. This was called intrinsic surface leaky wave by Lin et al. (2023). In our simulation, the assigned Poisson's ratio value is very high (~0.491). As a result, energetic leaky waves are seen in the simulated inline horizontal receiver data. In Fig. 5.5 we illustrate how the simulated leaky wave propagates differently than the SV-body wave and the Rayleigh wave. In our case, however, the presence of the leaky wave is not clear at all in the field data (see Figs 5.3(a) and (c)). The value of the Poisson's ratio in the topsoil layer in our field is probably not as large as the value we have assigned in our simulation. The very high value of the Poisson's ratio assigned in the simulation is due to the large V_P value estimated from the V_S using the empirical relation, even though the initial V_S derived from SCPT is probably quite accurate.

We simulate inline horizontal-component receiver data due to an inline horizontal source using three different Poisson's ratios to be constant over the whole model space. These three Poisson's ratios $\nu = 0.479$, $\nu = 0.333$, and $\nu = 0.1$ correspond to V_P values ~1000 m/s, ~400 m/s, and ~300 m/s, respectively. The V_S and ρ models are fixed in these simulations, and they are same as those determined from independent field measurements (see Fig. 5.2 and discussion in section 5.3.2). We use a Ricker wavelet with a centre frequency of 20 Hz. A simple source-time function is chosen in order to distinguish the Rayleigh wave from the leaky wave. The simulated inline horizontal receiver data (shot gathers) and the corresponding dispersion images for the three different V_P models are shown in Fig. 5.6.

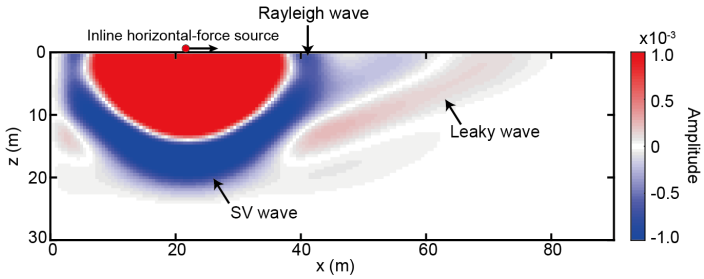

Figure 5.5: Simulated seismic snapshot showing inline horizontal-component particle velocities due to an inline horizontal-force seismic source along the 2D line indicated by black arrow in Fig. 5.1. A Ricker wavelet with a centre frequency of 20 Hz is used for the source.

With decreasing Poisson's ratio, the energy of the leaky wave decreases and reaches below the level of the Rayleigh wave (compare between black and green arrows in Fig. 5.6). Nevertheless, the leaky mode remains clear in the inline receivers when the Poisson's ratio is as low as 0.1 (see green arrows in Figs 5.6(c) and (f)). We could not justify the existence of soil layers having such a low Poisson's ratio (the corresponding V_P being ~300 m/s) below the water table at ~1.3 m in our test site. Note that, the soils here, as known from sampling in boreholes, is composed of only sand and clay.

There might also be other possible reasons for the absence of leaky waves in the observed data. Though incorporating lateral heterogeneity in the initial model is desirable, in our simulation we have assumed 1D models only. Also, large misfits might be caused by inaccurate modelling of the seismic source (e.g., Wu et al., 2025) or inaccuracy in the assumed inelastic attenuation. We could not evaluate all these effects.

5.4.2. CHOOSING SPECIFIC RECEIVER COMPONENTS FOR THE VERTICAL- AND HORIZONTAL-FORCE DATASETS

We try to mitigate falling into the local minima in inversion by excluding seismic receiver components where erroneously simulated leaky waves are present. The goal is to reduce the misfit between the observed and the simulated waveforms.

Since leaky waves are conspicuous in P-SV/Rayleigh-wave-dominated data – as seen earlier, we consider the following four source-receiver combinations: $f_x - v_x$, $f_x - v_z$, $f_z - v_x$, and $f_z - v_z$. For field data, we have shown in the previous subsection the $f_x - v_x$ data only. However, we find the leaky mode to be practically absent in all $f_x - v_x$, $f_x - v_z$, $f_z - v_x$, and $f_z - v_z$ field datasets. Next, we identify the receiver components where the leaky waves are nearly absent in the simulated data. For simulating data due to inline horizontal- and vertical-force sources, we again use a Ricker wavelet with a centre frequency of 20 Hz. Fig. 5.7 shows the simulated $f_x - v_x$, $f_x - v_z$, $f_z - v_x$, and $f_z - v_z$ shot gathers. We notice that the leaky mode has the largest relative energy in the $f_x - v_x$ data (Fig. 5.7(a)). In the $f_x - v_z$ data, the Rayleigh wave is more prominent than the leaky wave (see black and green arrows in Fig. 5.7(b)), although the leaky wave is still quite present. 3D FWI performed on the inline horizontal-force data is likely to suffer from the cycle-skipping problem, especially when the simulated data corresponding to the initial model have a leaky mode that is significantly stronger than that in the field data.

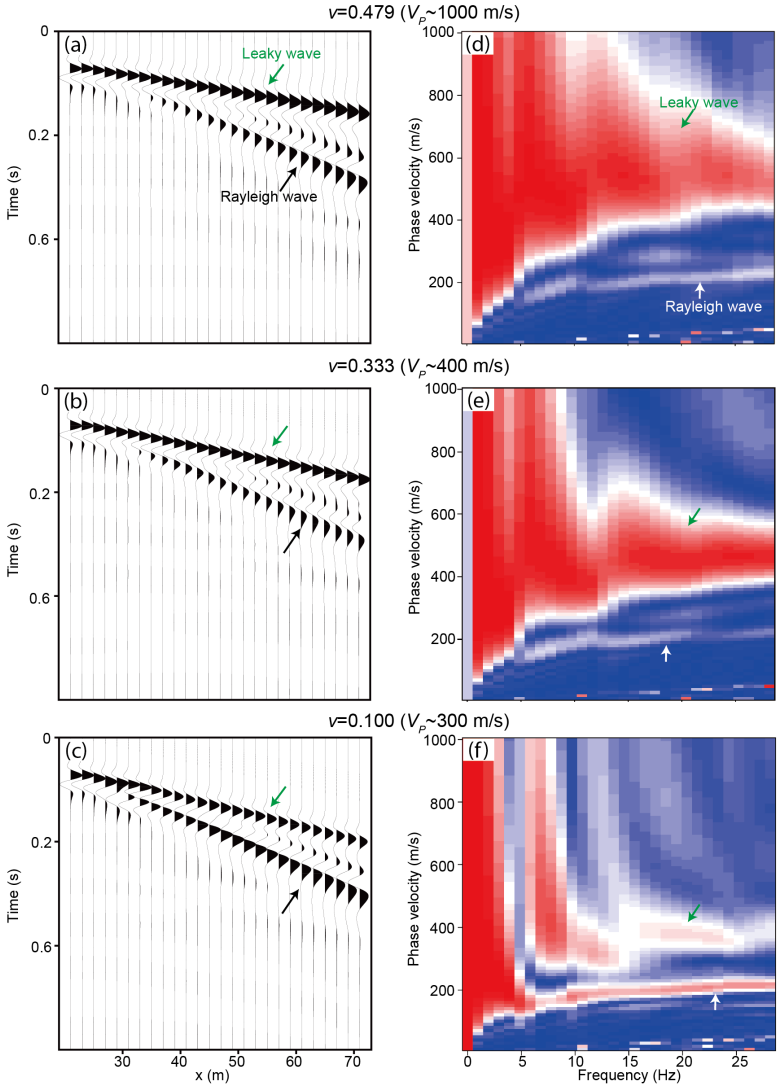

Figure 5.6: Simulated inline horizontal-component seismograms (shot gathers) for an inline horizontal-force seismic source and the corresponding dispersion images for three different V_P models. For ease of visualization, each seismic trace is normalized by its maximum amplitude.

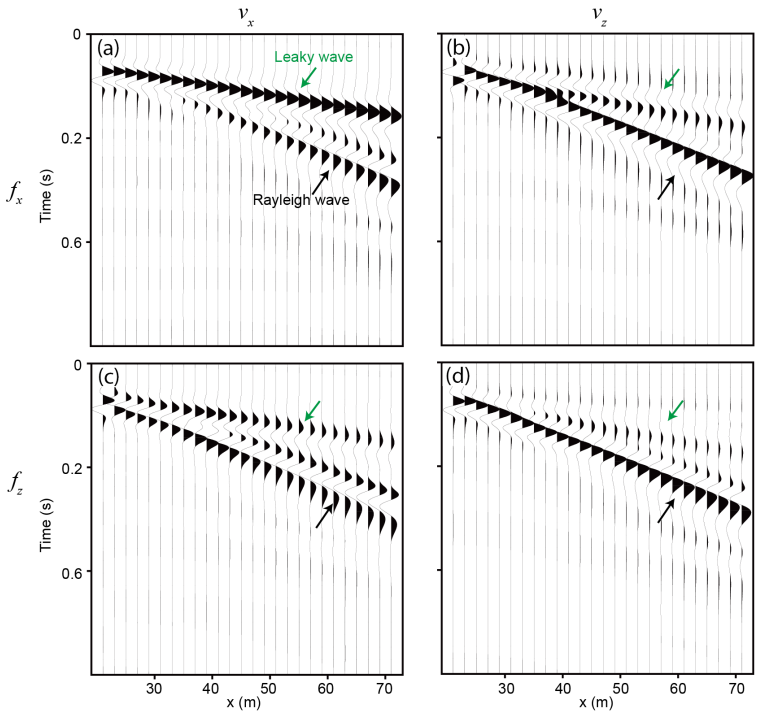

Figure 5.7: Simulated seismograms for the four source-receiver combinations: $f_x - v_x$, $f_x - v_z$, $f_z - v_x$, and $f_z - v_z$. For ease of visualization, each seismic trace is normalized by its maximum amplitude.

Therefore, for horizontal-force data, we use only data from crossline horizontal-component seismic receivers due to crossline horizontal seismic sources. In other words, we use primarily SH/Love-wave-dominated data for which leaky waves are nearly absent in the simulated data (Fig. 5.4).

Next, we look into the vertical-force source data. In the simulated data, leaky wave is present again in the inline horizontal-component seismic receiver ($f_z - v_x$) data, especially at the near offsets (see green arrow in Fig. 5.7(c)), while its energy in the $f_z - v_z$ data is relatively negligible compared to Rayleigh wave energy (see green and black arrows in Figs 5.7(d)). Therefore, we use the vertical receiver-component (v_z) data only in case of the f_z source.

Fig. 5.8 shows the source-receiver combinations which are finally used in 3D FWI involving both f_x and f_y sources. The used source-receiver combinations in FWI are indicated by rectangles in Fig. 5.8. Since the seismic sources (red dots in Fig. 5.8) are located in between two adjacent receiver lines (black dots) as explained in Fig. 5.1, we choose the nearest two receiver lines for each seismic source, and use the crossline horizontal receiver component data only (Fig. 5.8). It is possible to derive 3D image by performing at first 2D SH-wave FWI independently for each pseudo-2D seismic line, and then interpolating in between the obtained multiple 2D sections. In this research, however, we perform 3D FWI using all the crossline horizontal component data simultaneously to capture 3D subsoil

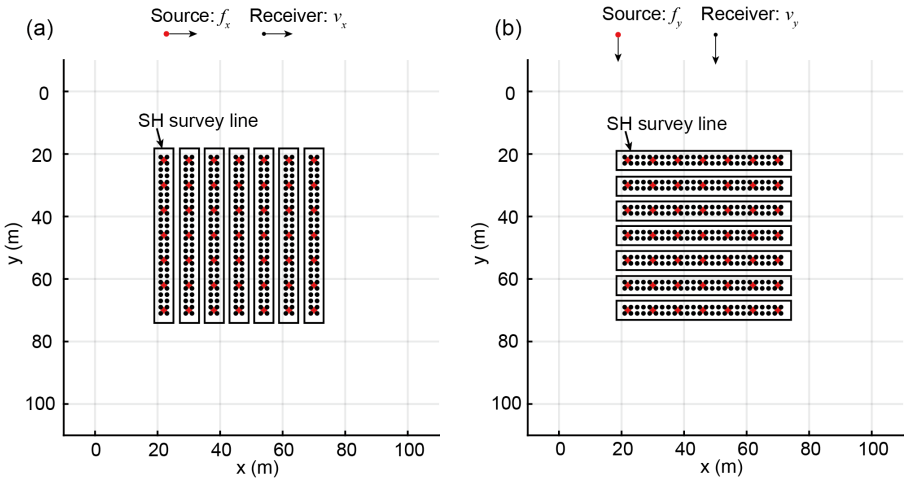

Figure 5.8: Source-receiver pairs assumed to be dominated by SH/Love waves and used in 3D FWI for horizontal-force source data. Note that seven SH survey lines are found in each horizontal-force source data (f_x and f_y).

heterogeneities. The slight offset between the source lines and the receiver lines (Fig. 5.8) impedes accurate 3D to 2D geometrical spreading correction, leading to slight error in the results of 2D FWI. We kill traces from receivers located within 10 m from each source. Since crossline source-receiver geometry does not hold at these locations, P-SV/Rayleigh dominates the seismic data at the near offsets.

To investigate the impact of our proposed data-selection strategy on 3D FWI, we calculate initial misfits using data with and without leaky-wave-contaminated simulated traces for each force-direction source data. We examine the first frequency stage (6–15 Hz) here, because it is crucial to start the lowest frequency inversion stage with low misfits in order to avoid cycle-skipping. For this calculation, we use the source time function estimated on data without the leaky wave contamination. For calculation of the misfits, since the number of traces significantly decreases after data selection, we perform a comparison of the normalized misfit between data with and without leaky-wave-contaminated traces. A normalized value of -1 indicates a perfect match between observed and synthetic data. The initial misfits are dramatically reduced by excluding the leaky-wave-contaminated traces for all source components (Fig. 5.9). This reduces the risk of falling into local minima during the inversion. The obtained FWI results will be discussed in the following section.

5.5. Results of 3D FWI

In this section, we explore how the use of the different force direction data affects the accuracy of V_S and ρ estimates. The input data used here are selected based on the strategy described in Section 5.4.2: the traces where the simulated data contain significant leaky wave mode are excluded. We compare at first the 3D FWI results between the vertical-force (f_z) source data and the horizontal-force (f_x or f_y) source data. Thereafter we investigate how the combination of cross-polarized horizontal-force ($f_x + f_y$) source datasets affect the

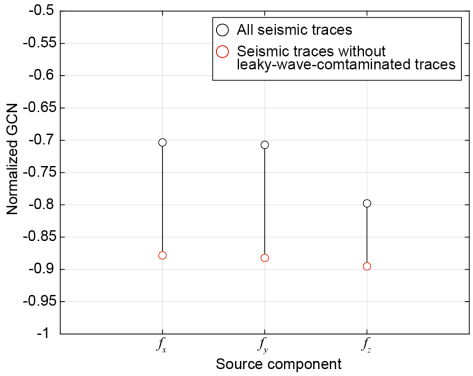

Figure 5.9: Calculated normalized misfit between observed and simulated data with and without the use of the data-selection strategy for each source component (f_x, f_y, f_z) at inversion stage 1 (6–15 Hz) shown in Table 5.2.

accuracy of the inverted 3D models.

5.5.1. FWI USING SINGLE SOURCE COMPONENT: VERTICAL-FORCE (f_z) AND HORIZONTAL-FORCE (f_x OR f_y) SOURCES

We perform 3D FWI independently on f_x, f_y, and f_z source data. The initial models of V_S and ρ are 1D. At first, we look at the 3D inverted V_S images (Fig. 5.10). A major difference in FWI results between horizontal- and vertical-force datasets can be identified at 10 m depth in the vicinity of BH2 and BH3. A low-V_S area is imaged by using data of the horizontal-force sources (f_x or f_y), while FWI using the f_z source data results in a relatively high V_S in the same area (compare Figs 5.10(b), (c), and (d) at 10 m depth). 3D FWI performed on the f_z source data provides a laterally smooth V_S distribution compared to the f_x or the f_y source data. This is in agreement with the result shown in Kawasaki et al. (2024) indicating that the vertical-force seismic data produce smoother, less-localized gradients of the misfit function than the horizontal-force data. Apart from these, another difference in the FWI result is prominent for the f_x source data: there is a high-V_S zone at around 6 m depth in the surrounding of BH2 and BH3 (red arrow in Fig. 5.10(b)). This high-V_S zone is not visible in the inverted V_S using the f_y or the f_z source data (Fig. 5.10(c) and Fig. 5.10(d)).

To check the accuracy of the FWI-derived V_S, we examine at the same location the SCPT-derived V_S and the 1D V_S profile derived from the 3D inverted result (Fig. 5.11). Admittedly, such one-to-one comparison between these two is not justified because while the FWI-derived V_S is highly smoothed in the lateral direction due to the Gaussian smoothing filter (see Section 5.3.2), SCPT provides V_S distribution at the exact location of the measurement. To address this issue, we consider the maximum and minimum values of the FWI-derived V_S at lateral locations within 2σ of the Gaussian filter (~8 m) from the SCPT location. We then compare how the ranges of these values vary with depth with the SCPT-derived 1D V_S profile (Fig. 5.11). At all three SCPT locations, 3D FWI using the horizontal-force data captures well the overall V_S trend up to 15 m depth (Figs 5.11(a)-(f)). On the contrary, the inverted V_S using the f_z source data deviates from the SCPT-derived V_S below 10 m depth at

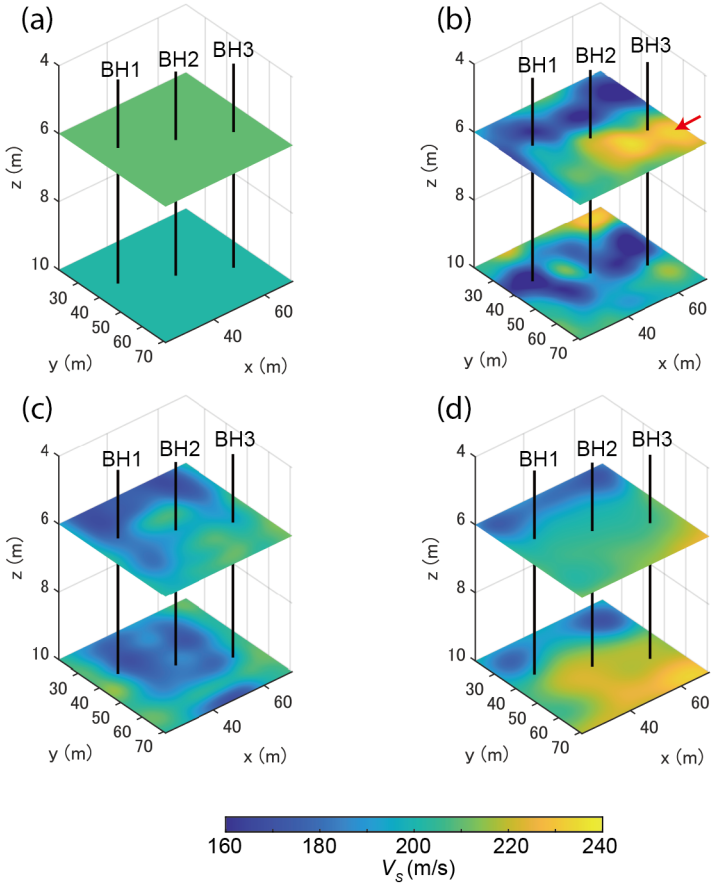

Figure 5.10: Depth slices of (a) initial V_S, (b) inverted V_S from the f_x data, (c) inverted V_S from the f_y data, and (d) inverted V_S from the f_z data. The red arrow marks a possible artifact. The source-receiver combinations used here are chosen following the strategy discussed in Section 5.4.2 (Fig. 5.8).

BH2 and BH3 (see green arrows in Figs 5.11(h) and (i)). At these locations, FWI performed on the f_z source data reveals a high-V_S zone, while the SCPTs show low V_S indicating the presence of soft sand and clay layers. We notice that at the same locations the inverted V_S using the f_z source data has few variations in the area associated with the Gaussian filter (see very narrow maximum-to-minimum ranges in Figs 5.11(h) and (i)). This indicates a low-resolution in the inverted V_S image in the lateral direction. For the f_x source data, another noted difference between the SCPT-derived V_S and the FWI-derived V_S is indicated by the red arrow in Fig. 5.11(c). This difference could be an artifact. This is endorsed by the fact that, starting from the initial V_S, the inversion updates the V_S in the opposite direction compared to the SCPT-derived V_S.

Next, we investigate how the inverted ρ estimate is influenced by the force direction of the used seismic source. The initial models of V_S and ρ are 1D. While FWI applied to the

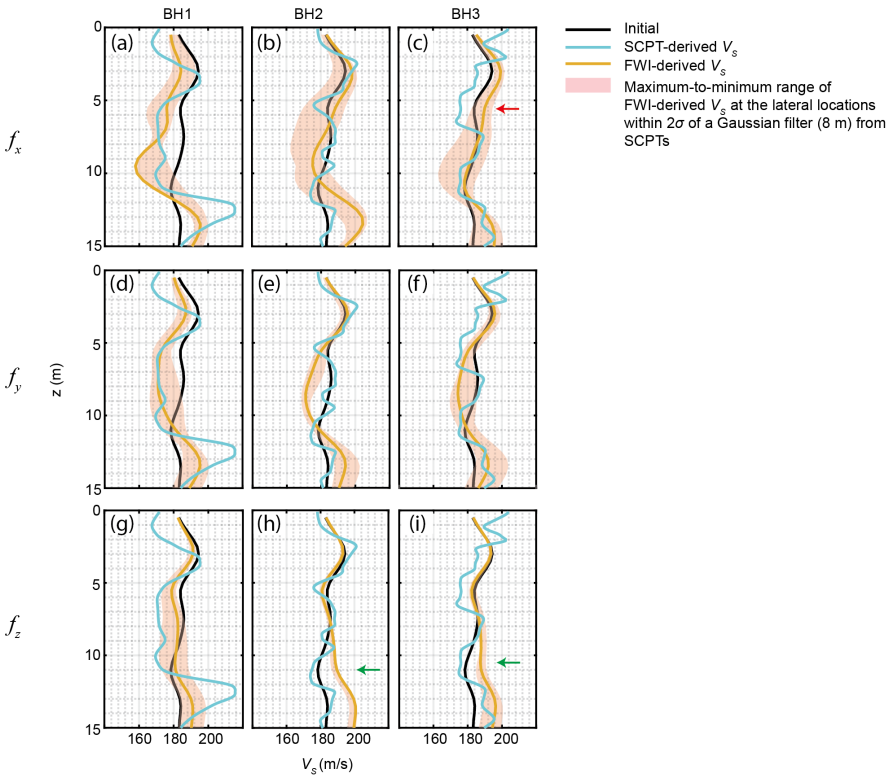

Figure 5.11: 1D profiles of the inverted V_S and the SCPT-derived V_S for (a)-(c) f_x data, (d)-(f) f_y data, and (g)-(i) f_z data. The 1D initial model is the same in all cases. The red and green arrows mark the locations where there are large differences between FWI-derived V_S and SCPT-derived V_S. The source-receiver combinations used here are chosen following the strategy discussed in Section 5.4.2 (Fig. 5.8).

horizontal-force data (f_x or f_y) reveals the laterally variable ρ structure (Figs 5.12(b) and (c)), for the vertical-force data (f_z) ρ is not much updated from the initial model (compare between Fig. 5.12(d) and Fig. 5.12(a)). There is also a difference in the inverted ρ between using f_x and f_y sources: a high-ρ anomaly appears at around 9 m depth in both inverted images, but at different lateral positions (see A1 and A2 in Fig. 5.12). Similar to V_S, we check, using ρ measured independently by density logging and through lab experiments on soil samples, the accuracy of the inverted ρ estimates using different force data for the seismic source. As earlier, we again consider the vertical trend of the maximum-to-minimum ranges of the ρ estimates at lateral locations within 2σ of the Gaussian filter from the borehole locations (Fig. 5.13). In case the f_z source data are used, the estimated ρ is almost identical with the initial ρ (see Figs 5.13(k)-(o)), which is also marked in Fig. 5.12. For the f_x and the f_y source data, however, ρ is updated in the correct direction of the measured ρ from the initial/starting value (see Figs 5.13(a)-(j)). A clear example can be seen at BH1 where the log-derived ρ is much lower than the initial ρ. At this location, 3D FWI using the horizontal-force data updates the ρ towards lower values than the initial values

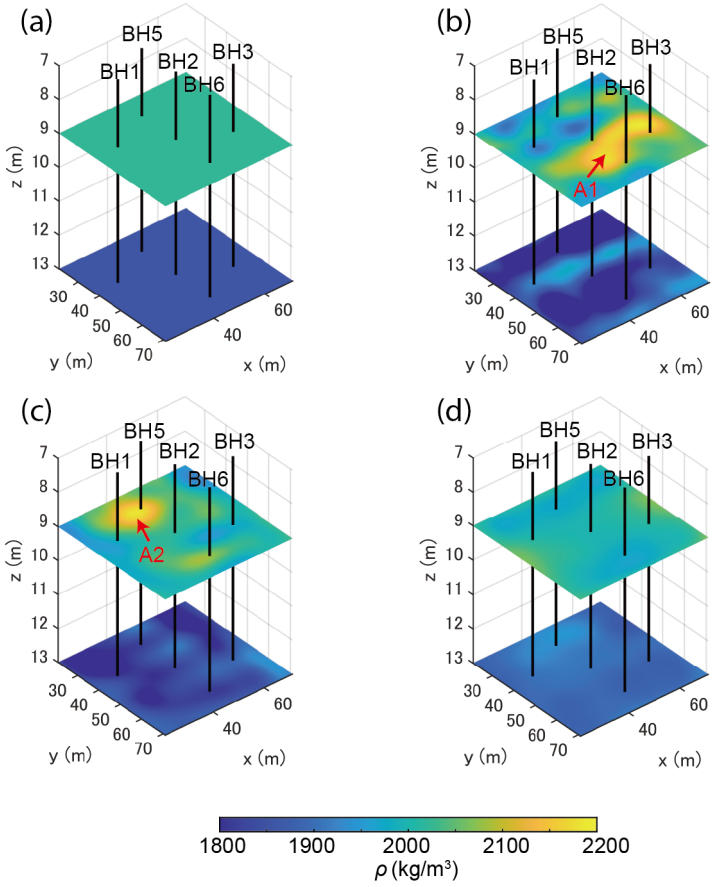

Figure 5.12: Same as in Fig. 5.10, but for ρ. The red arrows mark possible artifacts.

(see Figs 5.13(a) and (f)). These results show a good fit of the 3D FWI-derived ρ estimates with ρ obtained independently from density logging. We finally examine the locations of high-ρ anomalies A1 and A2 marked in Fig. 5.12. At these locations, the estimated high ρ is significantly different from the measured ρ values (red arrows in Fig. 5.13). Such differences are likely artifacts caused by using single component horizontal-force sources, which will be discussed in Section 5.6.2. In summary, 3D FWI using horizontal-force seismic sources is more capable of capturing the spatial variability of V_S and ρ than using vertical-force seismic sources.

5.5.2. 3D FWI COMBINING DATA FROM f_x AND f_y SEISMIC SOURCES: POTENTIAL BENEFITS OF JOINT INVERSION

In this section, we discuss the results of 3D FWI making simultaneous use of f_x and f_y source datasets. The estimated V_S from this joint inversion is shown in Fig. 5.14(a). We recognize the differences between 3D FWI using data from a single-component seismic

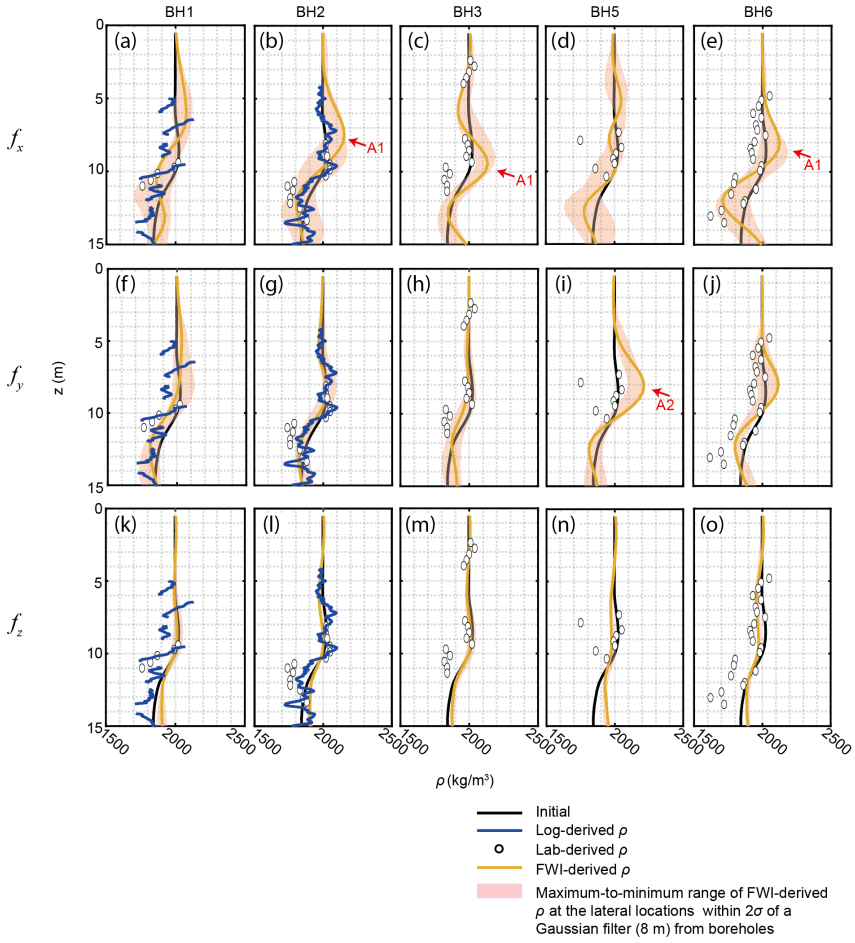

Figure 5.13: Same as in Fig. 5.11, but for ρ. The 1D initial model is the same in all cases. The red arrows mark the location where there are large differences between FWI-derived ρ, and the measured ρ by density logging and via lab experiments.

source and FWI on combined f_x and f_y source datasets. The use of $f_x + f_y$ data combination does not reveal a clear high-V_S zone at a depth of 6 m, unlike when only f_x source data are used in the 3D FWI (see the red arrow in Fig. 5.10(b) and Fig. 5.14(a)). Although compared to the FWI using the f_y sources only, the overall characteristics of V_S variations are not significantly different for the $f_x + f_y$ data combination, the joint FWI reconstructs the relatively fine structures better (compare between Fig. 5.10(c) and Fig. 5.14(a)). For ρ, there is a large difference between using single component source data and the combined $f_x + f_y$ source datasets: the high-ρ anomalies found in the result of single-component source FWI become less prominent in the result of FWI using combined $f_x + f_y$ datasets (compare between Figs 5.12(b)-(c) and Fig. 5.14(b)). Also, the joint inversion reveals much finer ρ structure than the single component source FWI. Some local anomalies are observed at 9 m

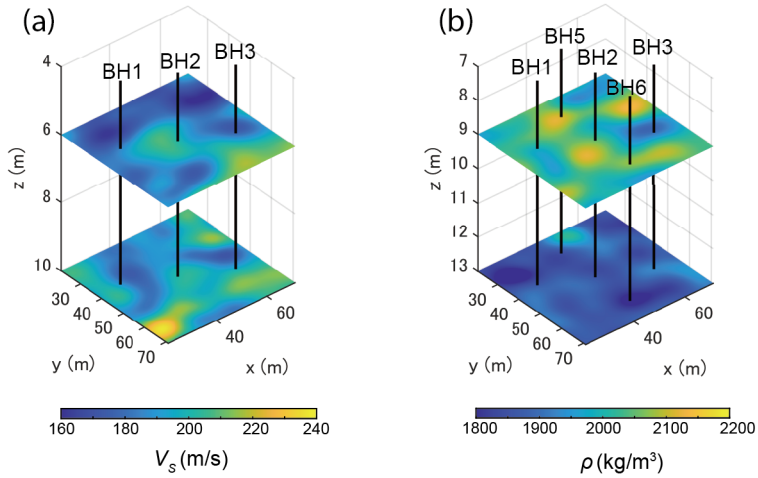

Figure 5.14: Inverted (a) V_S and (b) ρ from 3D FWI using the $f_x + f_y$ combination.

5

depth (see Fig. 5.14(b)). As in the previous section, we check the goodness of the V_S and ρ estimates from joint FWI, using the independent measurements of V_S and ρ (Figs 5.15 and 5.16). Our investigation shows that the distribution of the inverted V_S is similar between the single component source FWI and the joint $f_x + f_y$ source FWI, especially at BH1 and BH2 locations (compare Figs 5.11(a)-(b) and (d)-(e) with Figs 5.15(a)-(b)). At BH3, however, the difference with the SCPT-derived V_S as seen in the inverted result using the f_x source data is no more as clear as in the result of joint inversion of $f_x + f_y$ datasets (compare between red arrows in Fig. 5.11(c) and Fig. 5.15(c)). Regarding the estimated ρ, the vertical trend of the maximum-to-minimum ranges is similar between 3D FWI using single component source data and combined data of $f_x + f_y$ sources (compare Figs 5.13(a)-(j) and Fig. 5.16). Several improvements could be noticed at BH3 and BH6 locations. At these locations, the single component source FWI results in ρ estimates that are far from the lab-measured ρ on soil samples collected (Figs 5.13(c), (e), (h), and (j)). However, the maximum-to-minimum ranges of ρ estimates cover the ρ measurements better when the data of f_x and f_y sources are combined in 3D FWI (see green arrows in Figs 5.16(c) and (e)). We can recognize distinct improvements at the location of the artifacts (A1 and A2) appearing at 9 m depth in the result of the single-component-source FWI. These artifacts are reduced significantly in the results of joint $f_x + f_y$ FWI (compare Figs 5.13 and 5.16). These results demonstrate that the use of $f_x + f_y$ source data enhances generally the capability of the 3D FWI in terms of estimating the lateral variability of V_S and ρ in soils.

At certain restricted locations, however, the 3D FWI using single component horizontal-force data appears to perform better than the joint FWI. At BH5, for instance, the best fit between FWI-derived ρ and the ρ measurements on soil samples is found for the f_x source data (compare between Fig. 5.13(d), Fig. 5.13(i), and Fig. 5.16(d)). However, the simultaneous use of the $f_x + f_y$ source datasets does not produce severe artifacts unlike using single-component source dataset (i.e., A1 and A2 in Fig. 5.13), although these artifacts do

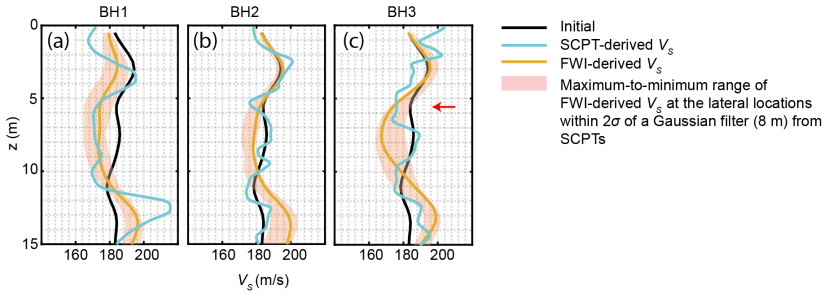

Figure 5.15: Same as in Fig. 5.11, but for the $f_x + f_y$ data. The 1D initial model is the same in all cases. The red arrow marks improvement compared to 3D FWI using the f_x data alone (Fig. 5.11(c)).

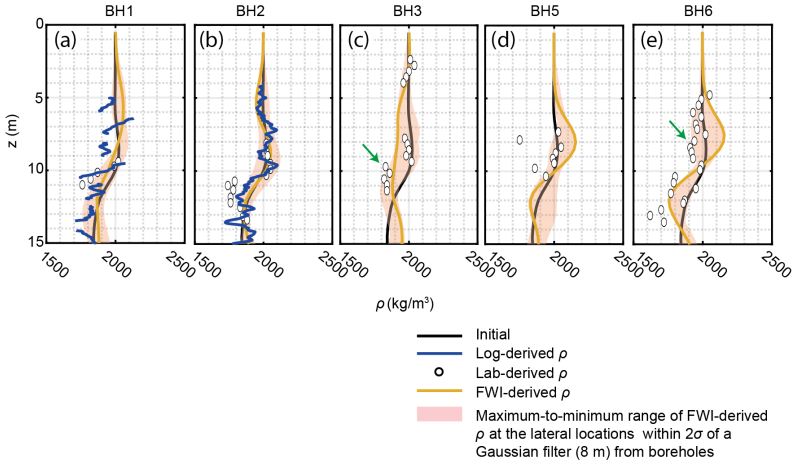

Figure 5.16: Same as in Fig. 5.15, but for ρ. The 1D initial model is the same in all cases. The green arrows mark possible improvements compared to 3D FWI applied to single-component horizontal-force seismic data as shown in Figs 5.13(a)-(j).

not vanish completely. Such improvements help in reducing misinterpretation of spatially variability based on 3D FWI results.

5.6. Discussion

5.6.1. Reason behind superiority of horizontal-force sources for successful density reconstruction

In Section 5.5.1, we have discussed that the use of data from the horizontal-force seismic sources in either x- or y-direction is beneficial for relatively accurate estimation of V_S and ρ through 3D FWI. Here we delve into the possible reasons behind the superiority of horizontal-force data.

Kawasaki et al. (2024) (Chapter 4 of this thesis) showed that horizontal-force data have the advantage of relatively less parameter coupling between V_S and ρ compared to

Table 5.3: Comparison of misfits calculated using two different ρ models.

	Normalized GCN		Rate of change (%)
	$\rho^{\mathrm{inv}(f_x+f_y)}$	ρ^{ini}	
f_x	-0.940	-0.933	0.75
f_y	-0.957	-0.950	0.65
f_z	-0.795	-0.795	0.03

vertical-force data in the context of conventional simultaneous inversion scheme. In this field application, we have suggested a sequential inversion workflow to further reduce the coupling between these two properties in 3D FWI (see Section 5.3.2).

However, a more important reason relates to the difference in the sensitivity of the misfit function to ρ for the different force-direction datasets. We investigate this possibility by looking at how the misfit values for each dataset vary due to a given change in ρ. Here, we consider two different ρ models. One is the ρ model obtained from 3D FWI using the $f_x + f_y$ source data ($\rho^{\mathrm{inv}(f_x+f_y)}$), while the initial ρ (ρ^{ini}) serves as the second model. To calculate the misfits, we use the inverted V_S obtained from joint 3D FWI, while the initial model for the other properties (V_P, Q_P, and Q_S). We quantify the difference in misfits for the two different ρ models by calculating the rate of change between the two misfit values (Table 5.3). The large rate of change means that the misfit function is highly sensitive to ρ, increasing the possibility of resolving ρ distribution by reducing the misfit changes during the inversion. As shown in Table 5.3, the rate of misfit changes for the f_x or f_y source data is larger than that for the f_z source data by a factor of more than 20. This suggests that the use of horizontal-force data is more promising for ρ estimation, whereas for the vertical-force data 3D FWI cannot update ρ effectively on the noisy field data through reducing the small difference in the waveforms due to changes in ρ. This is a possible reason why 3D FWI using the vertical-force data results in an almost identical inverted model as the initial ρ model (e.g., compare between Figs 5.12(a) and (d)).

Next, we look into how the sensitivity of the misfit function to changes in V_P depends on the force direction of the seismic source. One reason for this is to check if fixing the V_P model in 3D FWI causes a reduction in the accuracy of the inverted V_S and ρ models, for instance due to errors in V_P affecting the inversion result through parameter coupling. The sequential inversion workflow discussed earlier in this thesis is designed to reduce coupling between V_S and ρ, but it does not account for any potential coupling involving V_P (Fig. 2.1). We compare misfits for two different V_P models: V_P derived from V_S through an empirical relationship (i.e., the initial V_P model), and V_P derived from V_S assuming a specific Poisson's ratio. For the second model, we use a Poisson's ratio of 0.479 for the whole model, providing V_P values ~30% lower than the initial V_P model. For V_S and ρ, to calculate the misfits, we use the inversion result obtained on combined $f_x + f_y$ source dataset. The misfits for the two V_P models and the rate of change between them are shown in Table 5.4. The changes in the misfit due to change in V_P are very small for the horizontal-force data (f_x and f_y) than for the vertical force data (f_z). In our field application, we have chosen the SH/Love-wave-dominated receiver traces due to horizontal-force source to be used in 3D FWI, avoiding large initial misfits due to leaky waves in the simulated data. This probably reduces the impact of V_P uncertainty on the 3D FWI result using the horizontal-force source

Table 5.4: Comparison of misfits calculated using two different V_P models.

	Normalized GCN		Rate of change (%)
	V_P from an empirical relationship	V_P from an assumed Poisson's ratio (0.479)	
f_x	-0.940	-0.940	0.01
f_y	-0.957	-0.957	0.02
f_z	-0.795	-0.786	1.13

dataset. The resulting low dimensionality of the inverse problem is expected to result in a better convergence than using the vertical-force dataset.

Our investigations imply that horizontal-force source data (especially SH/Love-wave-dominated data) provide a favourable shape for the misfit function for V_S and ρ inversion.

5.6.2. FURTHER INVESTIGATION INTO POTENTIAL BENEFITS OF 3D FWI USING $f_x + f_y$ SOURCE COMBINATION

In Section 5.5.1, we have discussed the discrepancies between the 3D FWI-derived ρ and the ρ values estimated in the laboratory on soil samples (A1 and A2 in Fig. 5.13), in case a single component horizontal-force source (f_x or f_y) is used. These discrepancies become less prominent when joint inversion of both f_x and f_y datasets is performed in 3D FWI (Fig. 5.16). However, A1 and A2 may not be artifacts, but they may in fact be true subsurface structures spatially smeared due to application of strong lateral smoothing (see Section 5.3.2). We investigate this possibility here.

We first compare between the spatial variability of ρ estimates obtained from 3D FWI and the variability of CPT cone tip resistance q_c (Fig. 5.17). For this purpose, we build a pseudo-3D variability image of q_c by spatially interpolating in between measured q_c at multiple locations distributed over the whole 3D seismic acquisition patch at our test site (black crosses in Fig. 5.17(d) representing CPT locations). Next, a comparison between the spatial distributions of ρ and q_c is done at depth 9 m. The high-ρ anomalies at A1 and A2 in the 3D FWI result are marked. Around A1 and A2, q_c values are relatively low implying the presence of soft sand and clay layers (compare between Figs 5.17(a), (b), and (d)). Since both q_c and ρ are indicators of soil compaction/hardness, the different trend between these two properties appears to reflect a low reliability of the estimated ρ. We then explore the effect of the Gaussian smoothing filter on this observed differing trend. In the CPT survey, a relatively high-q_c zone is visible only in the area within 30 m < x < 40 m and 40 m < y < 50 m (Fig. 5.17(d)). Considering the given lateral width of the smoothing filter (~8 m), it is not plausible that a high-ρ zone corresponding to such a compacted soil body is smeared by spatial smoothing, and thereby A1 and A2 are produced at the different locations. We conclude that the high-ρ anomalies A1 and A2 are artifacts created due to use of single-component seismic source data, and these artifacts are reduced when we use $f_x + f_y$ source datasets in the 3D FWI (Fig. 5.17(c)). Moreover, FWI using the $f_x + f_y$ source data recovers the fine-scale anomalies having low-ρ and high-ρ values, which are denoted by solid and dashed yellow arrows in Fig. 5.17(c), respectively. Interestingly, at these anomaly positions, the spatial distribution pattern of ρ matches with that of q_c (compare solid and dashed yellow arrows in Figs 5.17(c) and 5.17(d)). The combined use of $f_x + f_y$ source

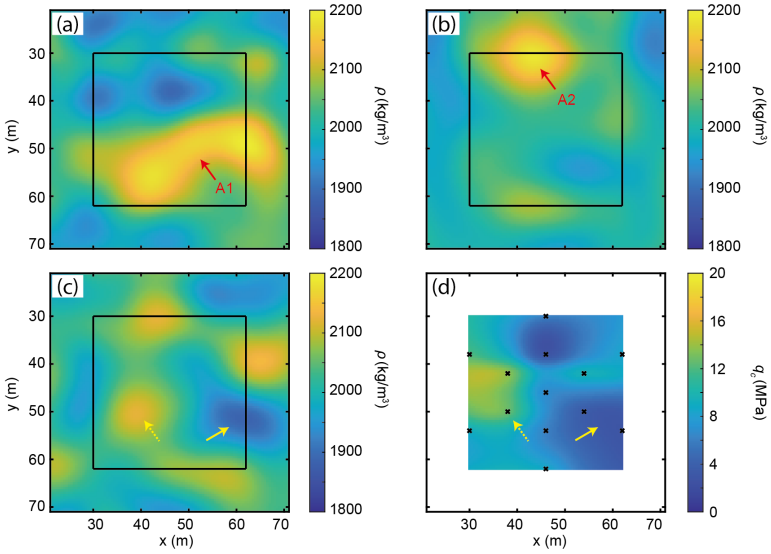

Figure 5.17: A horizontal slice showing subsoil heterogeneity at 9 m depth: (a) inverted ρ through 3D FWI using f_x data, (b) inverted ρ through 3D FWI using f_y data, (c) inverted ρ through 3D FWI using $f_x + f_y$ data, and (d) CPT cone tip resistance (q_c). The source-receiver combinations used here are chosen following the strategy discussed in Section 5.4.2 (Fig. 5.8). The red arrows indicate possible artifacts, while solid and dashed yellow arrows mark the variability in soil that match between the ρ image obtained from 3D FWI using $f_x + f_y$ data and independent data of q_c obtained at multiple locations in the field. The black crosses in (d) show the CPT locations.

dataset in the FWI is seemingly able to resolve the fine-scale ρ structure, in alignment with the soil variabilities seen in CPTs.

Next, we discuss how 3D FWI using single-component horizontal-force source data produces artifacts A1 and A2 at specific locations. To examine this, we look at how the final data misfits for each shot gather differ between the inversion results from single-component source FWI and combined $f_x + f_y$ FWI. We compute the difference between the normalized misfits obtained using the subsurface models for each FWI. For the f_x source data, for instance, we calculate the misfit difference E^{diff} as follows:

$$E^{\text{diff}} = E_{f_x}^{\text{inv}(f_x+f_y)} / n_{f_x}^{(\text{tr})} - E_{f_x}^{\text{inv}(f_x)} / n_{f_x}^{(\text{tr})}, \tag{5.2}$$

where $E_{f_x}^{\text{inv}(f_x+f_y)}$ and $E_{f_x}^{\text{inv}(f_x)}$ represent misfits for the inversion model obtained from 3D FWI using the $f_x + f_y$ source data and the f_x source data, respectively. $n_{f_x}^{(\text{tr})}$ is the total number of receiver traces for the f_x shot used in 3D FWI. If joint $f_x + f_y$ FWI improves the fit between the observed and the simulated waveforms, in comparison with single-component-source 3D FWI, E^{diff} becomes negative. In Fig. 5.18(a) we show the misfit difference for each f_x-source shot-gather, plotted at shot positions. The final misfits are reduced substantially by joint $f_x + f_y$ FWI for many shot gathers (see the red ellipse in Fig. 5.18(a)). The shot positions corresponding to greatly decreased misfit values are surprisingly close to the locations where the ρ artifact A1 is reduced through joint $f_x + f_y$ FWI (compare A1 in Fig. 5.17(a) and the red ellipse in Fig. 5.18(a)). At the same locations, the use of $f_x + f_y$ source

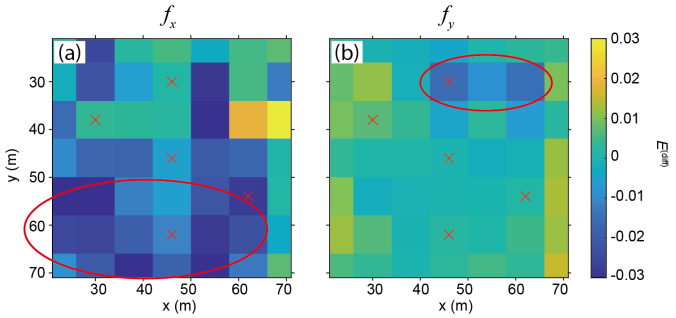

Figure 5.18: (a) Difference in the final misfit for each f_x shot gather between single-component source 3D FWI and joint $f_x + f_y$ source 3D FWI. The difference is calculated using equation: $E^{\text{diff}}_{f_x} = E^{\text{inv}(f_x+f_y)}_{f_x} / n^{(\text{tr})}_{f_x} - E^{\text{inv}(f_x)}_{f_x} / n^{(\text{tr})}_{f_x}$. (b) Same as in (a), but for each f_y shot gather. The difference is calculated in this case using equation: $E^{\text{diff}}_{f_y} = E^{\text{inv}(f_x+f_y)}_{f_y} / n^{(\text{tr})}_{f_y} - E^{\text{inv}(f_y)}_{f_y} / n^{(\text{tr})}_{f_y}$. If joint $f_x + f_y$ FWI improves the fit between the observed and the simulated waveforms, compared to single-component-source FWI, then E^{diff} becomes negative. The red ellipses mark the locations of misfit improvement due to the joint inversion. The red × marks the locations where V_S and ρ are measured independently through geotechnical and borehole measurements.

5

data combination also reduces the V_S artifact which appears when only the f_x source data are used in FWI (compare red arrow in Fig. 5.10(b) and the red ellipse in Fig. 5.18(a)). We also compute the misfit difference for the f_y-source shot gathers between the inversion result from the 3D FWI with the f_y source data and that with the $f_x + f_y$ source data (Fig. 5.18(b)). The significant misfit differences are not visible unlike the f_x source data. The final misfits are slightly improved only for a few shot gathers (see the red ellipse in Fig. 5.18(b)). Similar to the f_x source data, these shot positions are spatially correlated with the locations where we observe reduced artifact due to joint $f_x + f_y$ FWI (compare between A2 in Figs 5.17(b) and the red ellipse in Fig. 5.18(b)). These observations suggest that, compared to the single-component horizontal-force source data, the combined $f_x + f_y$ source data results in a favourable shape for the misfit function in 3D FWI, thus preventing poor inversion results due to convergence to local minima. This finally leads to a better fit between the simulated and the observed waveforms.

The above detailed discussions elucidate how the use of $f_x + f_y$ source combination in 3D FWI is beneficial for the reconstruction of both V_S and ρ, in turn offering the possibility for a better interpretation which is in agreement with the independent CPT-data-derived soil variability.

5.6.3. LIMITATIONS IN THE CURRENT 3D FWI RESULTS

We have imaged the spatial variability of V_S and ρ through 3D FWI applied to combined $f_x + f_y$ source data. However, the achieved resolution is rather limited. This is mainly due to the limiting maximum frequency value: we have used frequencies only up to 25 Hz, although the vibrator sweep range in field data acquisition is 4–300 Hz and in the raw shot gathers we do observe signals with frequency exceeding 100 Hz. We have further limited the lateral resolution by applying a Gaussian smoothing filter to the gradient of the misfit

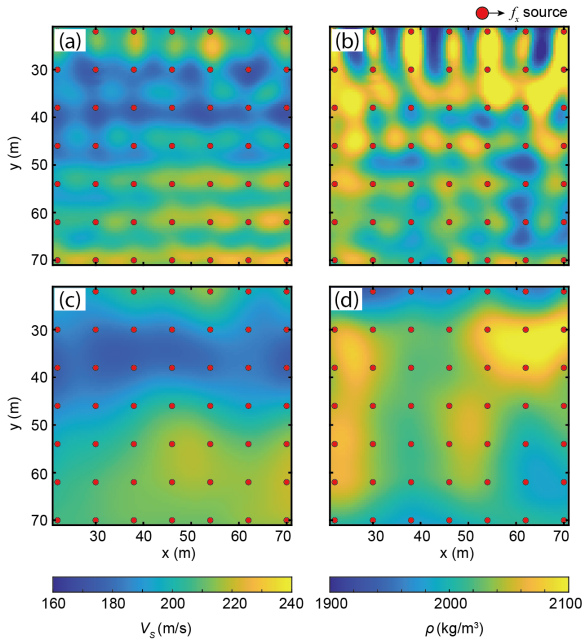

Figure 5.19: 3D FWI result after stage 1 (6–15 Hz, see Table 5.2) using the f_x-source data, (a)-(b) without any smoothing constraints and (c)-(d) with the Gaussian smoothing filter.

function (Section 5.3.2). These constraints are unfortunately unavoidable for successful FWI in order to avoid acquisition footprints due to spatial aliasing in the source domain: $\Delta s = 8$ m $> \lambda/2 = 4$ m, where Δs and λ are source spacing and the dominant seismic wavelength, respectively. We check further how a sparse source configuration can cause artifacts in the FWI result, in case the spatial smoothing is not applied to the gradient. For brevity, here we consider the inversion using the f_x source data at stage 1 (6–15 Hz) (Fig. 5.19). Clearly, many striped patterns appear, associated with the shot positions, in both V_S and ρ images. These are acquisition footprints due to spatial aliasing (Figs 5.19(a)-(b)). On the contrary, our employed Gaussian smoothing filter eliminates most of these artifacts, enabling to identify the lateral variabilities in soils (Figs 5.19(c)-(d)). We have carried out in-depth investigation, in Chapter 3, into these striped patterns using 2D SH-wave data. If the maximum frequency used in FWI is increased, the spatial aliasing effect would become very significant. This makes it difficult to incorporate much higher frequencies in the FWI. Therefore, having more seismic sources at finer spacing is required to enable using higher frequencies in the FWI and to achieve higher resolution in the obtained V_S and ρ images. In this context, one may consider building an aliasing-free seismic dataset, for instance by employing seismic interferometry (Chapter 3)

There is another limitation: we could not use in FWI all of the nine components of the acquired seismic dataset. Especially in the case of FWI applied to the horizontal-force data, we use only the SH/Love-wave-dominated data, in order to avoid large initial misfits due to leaky waves in the simulated data. Our chosen dataset contains merely 1.7% of all the

seismic traces that are acquired in the field (e.g., compare between Fig. 5.1 and Fig. 5.8). We also limit the vertical-force data to the vertical-component seismic traces only. This data-selection strategy results in a limited coverage and hence limited seismic illumination, constraining further the capability of 3D FWI in high-resolution seismic imaging. To address this issue, one needs to first understand better the reason why leaky waves are hardly generated in the field, unlike in the simulation (see Section 5.4.1). In the past decades, the characteristics of such leaky mode have been investigated focusing on seismic data involving vertical component source-receiver combination only (Schröder & Scott, 2001; Gao et al., 2014; Lin et al., 2023). Such source-receiver combination is commonly used in conventional dispersion-curve-based surface wave studies. However, our numerical investigations show that the use of an inline horizontal-force source excites more leaky waves than a vertical-force source (e.g., see Fig. 5.7). Therefore, a better understanding of the leaky wave mode, especially focusing on the effect of the seismic source type, is important in order to improve the capability of 3D FWI using horizontal-force data.

Also, building an initial model from the seismic data, such as through inversion of surface-wave dispersion curves, may help improve the matching of waveform between the observed data and the initial synthetic data. We have derived a 1D initial model from the SCPT data following the conclusion drawn in Chapter 2 about initial model building strategy. However, this choice might represent a limitation of the current study. In particular, a dispersion-based inversion using three-component seismic records could provide a suitable initial model for the field application, which might allow more consistent seismic modelling and might potentially enable the use of the full dataset acquired in the field. A systematic comparison of the initial models derived from the SCPT data and from seismic dispersion inversion would be valuable to assess their respective impact on the inversion robustness and parameter reconstruction.

Nevertheless, our proposed data-selection strategy works robustly to obtain a reliable subsurface model, avoiding the need of a special consideration for the leaky wave. One might, however, consider other solutions to reduce the effect of the leaky wave. For example, seismograms generated by an inline horizontal-force source could become usable by manually tuning the V_P model. This is because V_P controls greatly the energy of the leaky wave in the simulated data (see Fig. 5.6). Even if the chosen V_P model is off from a true one, relatively accurate V_S and ρ models might be obtained by FWI. Also, one may consider filtering out the leaky wave in the simulated data through data processing in case such leaky wave is not clearly observed in the field data, as is the situation in case of our field dataset. Since the leaky mode propagates much faster than the Rayleigh wave (Fig. 5.6), the leaky mode can be suppressed by applying a filter either in the frequency-wavenumber domain or in the phase-velocity-frequency domain (e.g., Luo et al., 2009; Gao et al., 2014). Additionally, one may use the SH/Love-wave-dominated seismic traces from the field-acquired two-component horizontal receiver traces due to two-component horizontal-force seismic sources. This is possible by performing coordinate transformation to bring the data from inline-crossline configuration to radial-transverse configuration (e.g., Burschil et al., 2022). The transverse source-receiver data should be more dominated by SH/Love waves. Such extracted SH/Love-wave data would cover a much broader range of source-receiver azimuths. This will help increasing the spatial resolution of the subsurface model obtained by 3D FWI.

5.7. Conclusions

In this chapter, we examined the effect of the force-direction of the seismic source on the 3D FWI results. We carried out a 3D seismic survey involving three-component seismic sources and three-component seismic receivers. We found that leaky waves cause large initial misfits between the observed and the simulated data. This can lead to cycle-skipping and is not easily mitigated, even when starting the inversion at the lowest available frequency. This problem is significant especially when an inline horizontal-force source is used. Through numerical investigations, we proposed 3D FWI only on SH/Love-wave-dominated receiver data due to horizontal-force seismic sources, as these data are less contaminated by leaky waves, and therefore do not suffer from inversion difficulties due to local minima. Also, for the vertical-force data, the inversion is performed using only the vertical-receiver seismic traces, as these traces are least affected by the leaky waves. We demonstrated that 3D FWI using the selected SH/Love-wave-dominated data is advantageous for relatively accurate reconstruction of V_S and ρ images, compared to using the vertical-force data. The reliability of the FWI results was validated using independent V_S and ρ measurements in the field. The superiority of the SH/Love-wave-dominated data is explained by the corresponding misfit function having relatively high sensitivity to ρ and very weak sensitivity to V_P. We finally looked into potential benefits of simultaneous use of the cross-polarized horizontal-force data. Compared to FWI using single component horizontal-force data, joint FWI allows reconstruction of both V_S and ρ without severe local artifacts. Furthermore, a much finer density structure is revealed through combining the cross-polarized horizontal-force datasets, showing good agreements with the spatial variability obtained from independent CPT cone tip resistance datasets. As a result, a better interpretation of subsoil structure is possible. In this chapter, we have proven that 3D FWI, using two cross-polarized horizontal-force sources and SH/Love-wave dominated receiver traces, is a robust approach to obtain reasonably accurate spatial distribution of V_S and ρ in 3D. This will make a positive contribution to many near-surface applications pertaining to shallow subsoil characterization.

6

Conclusions and recommendations

In this dissertation, we have looked into 2D and 3D FWI to estimate the spatial variability of ρ in soils. Towards accurate reconstruction of ρ through FWI, there are several problematic issues, which are addressed in this research, namely parameter coupling (Chapters 2 and 4), the difficulty in recovering the background distribution for ρ (Chapter 2), and the effect of spatial aliasing in the source domain (Chapter 3). Also ground truths are gathered via independent field and laboratory measurements to test our results. While looking for answers, we had in mind the need of making the economic burden of having a suitable dataset ready and performing computations for FWI manageable in the limited budget of near-surface site investigation projects. In this context, we use the gradient-based FWI throughout this research, due to its relatively low computational cost. One of the main focal points in this research is to try to understand the underlying reasons and to define the benefits of using a horizontal-force seismic source instead of a conventional, vertical-force source for successful ρ imaging through FWI. Especially for the 3D case, we have investigated, on both synthetic and field data, how FWI applied to horizontal-force source data performs for ρ estimation compared to FWI applied to vertical-force source data (Chapters 4 and 5). Our tests on 2D and 3D field data have shown that FWI is fairly capable of reconstructing the ρ distribution, with the trend agreeing with independent downhole measurements performed at multiple locations and with laboratory measurements on soil samples.

In this chapter, we summarize the main conclusions and briefly discuss the new findings reported in this thesis, followed by recommending some directions for future research.

6.1. Conclusions

Much attention has been paid towards mitigating the parameter coupling, which is a main obstacle to accurate reconstruction of ρ using FWI, in both 2D (Chapter 2) and 3D (Chapter 4). We discuss, at first, the main conclusions from these two chapters.

In Chapter 2, a sequential workflow has been proposed for FWI for ρ reconstruction.

The workflow enables weakening the coupling effect between V_S and ρ. Our new workflow is made of two stages: in the first stage, a multi-parameter inversion reduces the errors in V_S, and then in the second stage the ρ is updated in a relatively correct direction by starting with a less erroneous V_S model. We demonstrate its benefit on 2D SH/Love-wave-dominated field data. Compared to conventional simultaneous inversion, the proposed workflow improves the ρ estimates dramatically. The estimated values match well with the independent estimates of ρ obtained by density logging and from laboratory experiments on soil samples collected in boreholes. The sequential inversion, after the convergence, results in a better fit between the observed and the synthetic seismograms. We also discuss the need of a good initial model for V_S to further mitigate the parameter coupling issue. Inversion tests are conducted to compare two different initial V_S models, i.e., 1D V_S derived from SCPT data and 2D V_S derived from MALW. Our results indicate that a smoothed version of the SCPT-derived V_S profile used for input in FWI results in a less erroneous ρ variability and a better waveform matching. The proposed workflow and the SCPT-derived initial V_S model are advantageous in order to minimize the risk of falling into local minima due to parameter coupling.

In Chapter 2, we also address the difficulty in recovering the background distribution of ρ. We look into this issue using field-acquired 2D SH-wave seismic dataset. We try to incorporate sufficient low-wavenumber components of ρ into the FWI. For this purpose, a smoothed version of an 1D initial ρ model derived from the density log is used. The need and the importance of an accurate initial ρ model for successful FWI are investigated through a comparison with using a constant ρ for the initial model. Starting with the density-log-derived, smooth 1D starting ρ model, the FWI could capture the spatial variability of ρ up to 15 m depth (the 15 m depth limit, in this case, is only to keep computation time limited). The extracted spatial variability is in better agreement (compared to a constant ρ initial model) with the density logs and the density measurements on soil samples collected at multiple locations in the field. The waveform matching is also better when the initial ρ model is derived from the density log. Clearly, the accuracy of ρ estimates from FWI is greatly influenced by the goodness of the starting ρ model. The idea is that the density logging is performed only at one location in the field in order to build a good starting model, and thereafter, the lateral variability in density is estimated from the FWI of surface seismic data. Our research shows that the use of a homogeneous initial ρ, though unable to capture the correct trend of lateral ρ variability, still does provide meaningful ρ structure at many locations. Therefore, one should judiciously decide on the strategy for building the initial ρ model depending on the application goal, characteristics of the site (e.g., from available a priori information), and budget availability.

In Chapter 4, we present a systematic comparison between vertical- and horizontal-force sources on 3D synthetic data. We could disentangle the difference in parameter-coupling effect due to the different force directions. Given a point-localized perturbation model, we show that the use of horizontal-force source data can reduce the effect of errors in V_S on the gradient of the misfit function with respect to ρ, compared to using vertical-force source data. In the gradient-based inversion scheme, the less-contaminated gradient enables updating ρ in a relatively more correct direction towards the true value. Inversion tests using two different subsoil models demonstrate the benefit of horizontal-force source data to resolve ρ fairly accurately. For a spatially uncorrelated model, at the first iteration, FWI

applied to the horizontal-force source data produces fewer artifacts in the inverted ρ image due to errors in V_S than FWI applied to the vertical-force source data. The use of horizontal-force data indeed leads to a more accurate recovery of ρ without suffering from local minima. The superiority of the horizontal-force sources in FWI over vertical-force sources is also demonstrated by the inversion test performed on a more realistic subsoil model. The use of horizontal-force data provides a gradient for ρ which represents a relatively more correct update direction towards the true model, compared to using vertical-force data. This finally results in relatively more accurate estimation of ρ, where the estimated ρ variability correlates much better with the variability in the true model, while FWI applied to the vertical-force data fails to reconstruct a meaningful ρ structure.

Spatial aliasing in seismic data disturbs the high-resolution subsurface image that can be obtained by FWI. In Chapter 3, we investigate on 2D SH-wave data the impact of sparse source configuration on the FWI results (both V_S and ρ). We then present a new approach to mitigate the source sparseness issue. For our specific field site, spatial aliasing occurring due to sparse source distribution produces shot-position-related striped-pattern artifacts in the gradient and in the inversion results, causing deterioration of the lateral resolution in both V_S and ρ images derived from FWI. These artifacts are due to insufficient source spacing, failing to suppress the oscillatory side lobes in the gradient of the misfit function that appear around each shot location. In addition, the accuracy of the ρ estimates themselves is also compromised due to spatial aliasing. To address this issue, we have proposed a strategy to build aliasing-free seismic data by applying SI to the sparsely distributed shot gathers. SI is able to generate virtual surface-wave records at each receiver location from the real records that are dominated by surface waves. The retrieved dataset is then combined with the real field dataset to create densely distributed shot gathers. FWI is performed on the merged data, instead of only the real field data. To account for errors in the virtual seismic waveforms (amplitude and phase) due to SI, we use a matched filter with additional low-frequency correction. We also introduce a weighted misfit function. The inversion tests on field data demonstrate that our proposed approach improves the lateral resolution of V_S and ρ by reducing the striped patterns that occur due to spatial aliasing. The error correction approach contributes to avoiding the negative impact of using relatively low-S/N virtual records on the FWI results. The spatial distribution of ρ obtained from our newly developed method shows better correlation with the distribution of CPT cone-tip resistance, compared to when using only the aliased real (field) data in the FWI.

Throughout this thesis, we closely look into the advantages of using horizontal-force source data in FWI for the purpose of reconstructing reasonably well the ρ distribution in soils. To this end, to the best of our knowledge, this is possibly the first ever attempt to carry out 3D FWI using field-acquired horizontal-force source data. In addition to the reduced parameter-coupling effect, we recognize also other clear benefits of using horizontal-force seismic sources. Chapter 2 shows that SH-wave FWI can resolve the spatial variation of not only ρ, but also of V_S up to at least 15 m depth in soil; the obtained image gives seismic wave travel times that are in close agreement with the first-arrival travel times in the SCPT data. This result is significant for many near-surface applications, where the main target is to image the distribution of V_S. In Chapter 4, further investigation on synthetic data reveals two other merits of using horizontal-force seismic sources over vertical-force sources: robustness of FWI to noisy data and relatively high-resolution in the derived

images. The noise robustness of the FWI results (ρ image) in case of the horizontal-force data is explained by the large energy in the scattered wavefield due to the perturbation in ρ. Considering a point-localized perturbation model, we illustrate the ability of the horizontal-force data to construct a high-resolution gradient for both V_S and ρ, thereby making the model update more focused to the perturbation. Moreover, the parameter-coupling effect on the inverted ρ can be spatially limited in case of horizontal-force source data. Inversion tests using two different subsoil models demonstrate that 3D FWI applied to horizontal-force source data leads to reconstruction of higher-resolution V_S images that have fewer local artifacts, compared to vertical-force source data.

Chapter 5 presents a 3D field application to illustrate how the seismic-source component can be selected for accurate reconstruction of V_S and ρ through FWI. We encounter a major challenge when using the inline horizontal-force source dataset in FWI. 3D FWI applied to this dataset fails to extract a reasonable subsurface model and satisfactory waveform matching, even when the lowest-frequency components available in the field data are used. Detailed numerical investigation reveals that this problem is due to erroneously simulated leaky waves, which are pronounced in specific source-component data. We exclude leaky-wave-contaminated records as input to FWI. For horizontal-force source data, we use the crossline horizontal source- and receiver-component records which are dominated by SH/Love waves, while only vertical-component records are used for FWI of vertical-force source data. This selective use of data results in good waveform matching for a given initial model. We compare three source component records, namely vertical force and two cross-polarized horizontal force sources. Compared to using vertical-force source data, FWI applied to SH/Love-wave dominated horizontal-force source data captures better the 3D spatial variation of V_S and ρ. The obtained spatial variability matches with the independent measurements of V_S and ρ (ground truths). The difference in the performance of FWI for different source components can be attributed to the difference in the corresponding misfit functions. For horizontal-force source data, the effect of sensitivity of ρ on the misfit function is much greater, whereas sensitivity of V_P is very low. This selective use of source and receiver components makes the inversion more focused on the reconstruction of V_S and ρ, leading to a better reconstruction of both parameters. Importantly, this chapter also demonstrates that further improvement in the performance of FWI can be achieved by making simultaneous use of two cross-polarized horizontal-force sources. This joint FWI scheme contributes to reducing the local artifacts that appear when only single-component horizontal-force data are used in FWI, and thereby this helps in recovering a much finer ρ structure. The improved ρ estimates are better comparable to the spatial distribution of soil types, as estimated from an extensive field CPT campaign. The joint FWI also improves the misfit values at the convergence, compared to single-source-component FWI. The simultaneous use of two cross-polarized horizontal-force sources results in a more favourable shape for the misfit function, for instance, ones that have less severe local minima.

We conclude that, in 2D and 3D FWI, the use of horizontal-force seismic source data and SH/Love-wave-rich receiver component leads to more reliable imaging of ρ and V_S variability in the near-surface soils.

Next, we discuss the economic implication of the results obtained in this research. In the past, there have been attempts to improve the value of the estimated ρ from FWI by implementing advanced optimization algorithms, for example, using a truncated Newton

method (see Sections 2.1 and 4.1). The truncated Newton method modifies the shape of the misfit function to a more favourable one using the (accurately) estimated inverse of the Hessian. This reduces the local minima due to parameter coupling. But these approaches are generally computationally quite expensive because their implementation requires iteratively solving the Newton's equation using the second-order adjoint equation. This computational burden becomes quite heavy in case of 3D FWI. In contrast, the approach that we have proposed in this thesis attempts to obtain, through selective use of source and receiver components, a misfit function which is suitable for accurate reconstruction of ρ. This approach allows us to use still the gradient-based inversion which is less expensive, in order to extract reasonable and useful information about ρ variability in the subsoil. The efficacy of the data-selection approach is validated through 2D (Chapters 2 and 3) and 3D (Chapters 4 and 5) applications. Especially in 2D, SH-wave FWI is preferable from computational point of view (less computation time and lower memory requirement) than using P-SV/Rayleigh-wave data. This insight is useful for near-surface applications, because the available funding is generally much less there compared to deeper exploration-scale projects. Also, our developed approach, involving seismic interferometry, to reduce spatial aliasing effect due to sparse source distribution (Chapter 3) helps in limiting the need of many sources in the field for achieving sufficient resolution and reduced artifacts in the FWI-derived images. This should be beneficial also in near-surface temporal monitoring using FWI.

In this research, efforts have been made to collect independent ground-truthing data from the field as much as possible. For this purpose, many CPTs and SCPTs are performed to evaluate the lateral variability in soil. Also, shallow density logging, and estimation of density in the laboratory on soil samples are performed at different locations at our test site. These independent field measurements and laboratory tests are carried out by Fugro. We have tested the FWI results against these ground truths. In Chapter 2, the spatial variability of ρ derived from 2D SH-wave FWI is found to correlate with the variability of V_S and ρ deduced from independent measurements, and with that of soil types from the CPT surveys. FWI can delineate the spatial change in the attitude of the sharp boundary separating the shallow sand layer from the deep alternating layers of soft sand and stiff clay, and a laterally continuous high ρ layer. Moreover, the difference in ρ between shallow and deep sand layers, implying different porosities, is distinguishable in FWI results. In Chapter 5, FWI using simultaneously two cross-polarized horizontal-force seismic sources succeeds to capture the fine-scale changes in the soil, indicative of the laterally heterogeneous sand and clay layers. This matches with the changing soil layering seen in CPT surveys. Having independent ground truths, if feasible and affordable, is important in order to evaluate the FWI results and/or optimize the inversion so as to get reliable results.

6.2. Recommendations for future work

In this thesis, we have demonstrated the advantages of using horizontal-force source data in FWI to obtain reasonably accurate spatial variation of ρ and V_S through 2D and 3D FWI. However, our understanding of the underlying physical mechanism is still not sufficient. In the scope of this research, we could not disentangle the degree of contribution of the different wave modes, that are generated by the horizontal-force sources (e.g., SH- and SV-body waves, fundamental-mode surface waves, and higher-mode surface waves), to the reduced parameter coupling and to the reconstruction of the high-resolution gradient in

FWI. More in-depth research on this topic can be beneficial. For instance, the selective use of a specific wave mode in FWI could further improve the ρ estimates. If true, this can be useful in different scales – near-surface, deeper exploration, or global scales.

We have not checked the results of FWI using jointly vertical- and horizontal-force-source seismic records. This is because, in our research, the vertical-force data alone is found to offer relatively inferior ρ estimates (Chapters 4 and 5). Wittkamp et al. (2018) have, however, presented 2D FWI results using simultaneously vertical-force data (P-SV/Rayleigh wave) and horizontal-force data (SH/Love wave), showing improved resolution and reduced parameter coupling, in case a sufficiently accurate staring V_P model is used. Irnaka (2022) has also suggested that simultaneous use of vertical- and horizontal-force source datasets offers enhanced image resolution in FWI. In our research, we have found that using simultaneously two cross-polarized horizontal-force datasets leads to a more favourable shape for the misfit function for estimating ρ. The simultaneous use of vertical- and two horizontal-force source data might offer further improvement in this regard.

More advanced optimization approaches are likely to be more affordable in the future. They will require less computation resources than now. The computation power will also increase in the future. Much more performance enhancement for FWI is anticipated if these improvements are incorporated into the strategies and approaches that we have presented in this thesis. For instance, the truncated Newton method, which is powerful to reduce the parameter coupling and to enable more accurate model building (Gao et al., 2021, 2023), can be used with two cross-polarized horizontal-force source datasets to improve the results of FWI further. Also, the use of the Hessian inverse into the inversion have been found, mostly on vertical-force source data, to suppress artifacts caused by the limited seismic illumination and to enhance the resolution (Tran et al., 2019). It will be useful to check if further improvement is achievable if two cross-polarized horizontal-source datasets are used in this approach.

We have addressed in Chapter 3 the difficulty in 2D FWI in case the seismic sources are sparsely distributed. Spatial aliasing causes artifacts and reduces the resolution of the FWI image. The spatial aliasing issue is more severe in case of 3D FWI. The need of more seismic sources in 3D FWI dramatically increases the cost. In case of sparse source distribution, only a heavily smoothed subsoil model can be obtained from 3D FWI, as illustrated in Chapter 5. The limited resolution in the results of 3D FWI of field data, that we have illustrated in Chapter 5, is primarily due to relatively large source spacing used in the field experiment due to time- and resource-constraints. As a result, the maximum frequency that we could use (to limit the spatial aliasing effects) in FWI is only 25 Hz. This issue can be alleviated in the future if proper care is taken during data acquisition and/or spatial sampling is enhanced by extending techniques like seismic interferometry (Chapter 3) to 3D.

In our tests, we use a global-correlation misfit function to measure the difference between observed and simulated waveforms. This phase-focused misfit function ignores the inter-trace amplitude variation, and normalizes each trace using the maximum amplitude. It is chosen so as to use the near-offset and the far-offset data equally in FWI. The signal in the far offset is strongly attenuated. Also, the effect of varying receiver coupling with the ground is reduced by this normalized misfit function. However, Płonka et al. (2016) have indicated that the subsurface ρ values are much more sensitive to seismic amplitude variation than

to travel-time variation. Therefore, effective use of the amplitude information is probably necessary in the future to enhance the accuracy and resolution of the inverted ρ by FWI. In the near-surface scale, the inversion using amplitude data would need more careful consideration of the inelastic attenuation (Q_P and Q_S), which significantly affects the amplitudes in the observed seismograms. In our research, a constant Q value is assumed over the whole model. Inverting for laterally varying Q in the framework of multi-parameter inversion should be possible, though a more careful consideration of the parameter coupling involving Q is still required (e.g., Gao et al., 2020, 2021, 2023). Moreover, the source/receiver coupling with the ground should be taken into consideration to increase the robustness of inversion (e.g., Maurer et al., 2012; Hu et al., 2021).

The limited resolution in some of our results on field data (Chapters 3 and 5) is mainly due to the limited maximum frequency used in FWI (40 Hz for 2D FWI discussed in Chapter 3, and only 25 Hz for 3D FWI in Chapter 5), although our field data contain much higher frequencies. The practical reason for this is that limiting the higher frequencies makes the computation time of FWI more manageable for us, while still providing important insights - as presented in this thesis. Limiting the computation burden helps particularly in case of 3D FWI. However, there are also important technical reasons. At low frequencies much of the recorded energy in the field data is that of surface waves. The reason of limiting the maximum frequency to 40 Hz in Chapter 3 (2D FWI) is two-fold. Firstly, through seismic interferometry of near-surface seismic data we preferentially retrieve the surface waves over the body waves. This is mainly because the sources on the free surface fall into the so-called stationary-phase region of the surface waves (D. Halliday et al., 2007, 2008). Surface waves dominate the near-surface seismic data. Therefore, having higher frequencies (above 40 Hz) will enhance the presence of body waves, and the proposed approach involving merging of retrieved virtual source (surface wave) data with the real field data will be less effective. Secondly, for a maximum frequency of 40 Hz, spatial aliasing still occurs, particularly for the lowest-velocity surface waves, when the source spacing is 2 m (which is the case in our 2D field dataset, see Chapter 3). This results into artifacts (striped pattern) in the FWI result. Spatial aliasing is especially problematic for FWI of seismic data from soft soil sites, because of the very low surface- and shear-wave velocities in soft soils. When the virtual shot gathers containing surface waves are merged with the actual field shot gathers, the source spacing decreases to 1 m in the merged dataset (Chapter 3). We do see that the aliasing-related artifacts are significantly reduced and the ρ estimates are more accurate in the results of FWI performed on the merged dataset (see Section 3.3.3). The reasons for the low resolution in our 3D FWI results on field data are, firstly the used maximum frequency of only 25 Hz, and secondly the Gaussian smoothing filter applied to the gradient of the misfit function to reduce artifacts due to spatial aliasing in the data. The spatial aliasing occurs because of the source spacing of 8 m in our 3D field data (due to time and resource constraint). These reasons are discussed in detail in Section 5.6.3. In case the source spacing was very fine and/or aliasing-free seismic dataset could be successfully retrieved using techniques like seismic interferometry, and if the computation time/cost was not of concern, then one could use much higher frequencies that are present in the data and, thereby, achieve significantly higher resolution in the FWI results, while also benefiting from both surface- and body-wave information. This should be the target in the future, if technically possible and economically affordable. With increasing availability of large computation

power, many receiver channels in near-surface seismic data acquisition, distributed acoustic sensing (DAS) technology with high spatial sampling rate (e.g., Y. Pan & Gao, 2023), and new algorithms enabling near-surface FWI successful even when the source and/or receiver spacing is not sufficiently fine (e.g., Nuber et al., 2017; J. Li et al., 2024), the findings in our research will be more useful in the future to achieve very high-resolution, accurate imaging of V_S and ρ distribution in the shallow subsoil.

In recent years, to mitigate the well-known cycle-skipping issue, several misfit functions based on the optimal transport theory have been proposed and applied to seismic data in different scales (Métivier et al., 2016; Métivier et al., 2018; Borisov et al., 2025). H. Liu et al. (2024) have proposed a Wasserstein distance-based misfit function, also based on the optimal transport theory, to improve the ability of FWI to reconstruct ρ. They have shown that this misfit function is more sensitive to the low-frequency components, compared to the conventional least squares of l_2 norm. They have tried to achieve through data processing an appropriate shape of the misfit function that leads to successful inversion results. In this research, we have also targeted to obtain an appropriate shape of the misfit function for ρ inversion, by making selective use of a specific source-component dataset. We anticipate that the combination of our proposed data-selection approach with the data-processing techniques (e.g., H. Liu et al., 2024) will contribute to achieving an even better shape of the misfit function for the purpose of ρ imaging.

References

Aleardi, M., Salusti, A., & Pierini, S. (2020). Transdimensional and Hamiltonian Monte Carlo inversions of Rayleigh-wave dispersion curves: a comparison on synthetic datasets. *Near Surface Geophysics*, *18*(5), 515–543. https://doi.org/10.1002/nsg.12100

Al-Homadhi, E., & Hamada, G. (2001). Determination of petrophysical and mechanical property interrelationships for simulated sandstone rocks. *NERP (Nordic Energy Research Programme)(ed) Proceeding of the 6th Nordic Symposium Petrophysics, Trondheim, Norway*, *18*.

Allred, B., Ehsani, R., & Daniels, J. (2008). *Handbook of agricultural geophysics*. CRC Press.

Anbazhagan, P., Uday, A., Moustafa, S. S. R., & Al-Arifi, N. S. N. (2016). Correlation of densities with shear wave velocities and SPT N values. *Journal of Geophysics and Engineering*, *13*(3), 320–341. https://doi.org/10.1088/1742-2132/13/3/320

Arisona, A., Nawawi, M., Khalil, A. E., & Abdulrahman, A. (2018). Assessment of microgravity anomalies of soil structure for geotechnical 2D models. *Journal of Geoscience, Engineering, Environment, and Technology*, *3*(3), 151–154. https://doi.org/10.24273/jgeet.2018.3.3.2058

Atapour, H., & Mortazavi, A. (2018). The effect of grain size and cement content on index properties of weakly solidified artificial sandstones. *Journal of Geophysics and Engineering*, *15*(2), 613–619. https://doi.org/10.1088/1742-2140/aaa14a

Baccani, G., Bonechi, L., Bongi, M., Casagli, N., Ciaranfi, R., Ciulli, V., D'Alessandro, R., Gonzi, S., Lombardi, L., Morelli, S., Nocentini, M., Pazzi, V., Tacconi Stefanelli, C., & Viliani, L. (2021). The reliability of muography applied in the detection of the animal burrows within River Levees validated by means of geophysical techniques. *Journal of Applied Geophysics*, *191*, 104376. https://doi.org/https://doi.org/10.1016/j.jappgeo.2021.104376

Balestrini, F., Draganov, D., Malehmir, A., Marsden, P., & Ghose, R. (2020). Improved target illumination at Ludvika mines of Sweden through seismic-interferometric surface-wave suppression. *Geophysical Prospecting*, *68*(1 - Cost-Effective and Innovative Mineral Exploration Solutions), 200–213. https://doi.org/https://doi.org/10.1111/1365-2478.12890

Bell, F. G. (2016). *Fundamentals of engineering geology*. Elsevier.

Bohlen, T. (2002). Parallel 3-D viscoelastic finite difference seismic modelling. *Computers & Geosciences*, *28*(8), 887–899. https://doi.org/https://doi.org/10.1016/S0098-3004(02)00006-7

Borisov, D., Miller, R. D., & Sloan, S. D. (2025). Optimal transport-based full-waveform inversion for shallow seismic data. *Geophysics*, *90*(3), R101–R112. https://doi.org/10.1190/geo2024-0165.1

Brahim, N., Bernoux, M., & Gallali, T. (2012). Pedotransfer functions to estimate soil bulk density for Northern Africa: Tunisia case. *Journal of Arid Environments*, *81*, 77–83. https://doi.org/10.1016/j.jaridenv.2012.01.012

Brenders, A. J., & Pratt, R. G. (2007). Efficient waveform tomography for lithospheric imaging: implications for realistic, two-dimensional acquisition geometries and low-frequency data. *Geophysical Journal International*, *168*(1), 152–170. https://doi.org/10.1111/j.1365-246X.2006.03096.x

Brodic, B., Ras, P., de Kunder, R., Drijkoningen, G., & Malehmir, A. (2021). Seismic imaging using an e-vib — A case study analyzing the signal properties of a seismic vibrator driven by electric linear synchronous motors. *Geophysics*, *86*(3), B223–B235. https://doi.org/10.1190/geo2020-0181.1

Brossier, R., Operto, S., & Virieux, J. (2009). Seismic imaging of complex onshore structures by 2D elastic frequency-domain full-waveform inversion. *Geophysics*, *74*(6), WCC105–WCC118. https://doi.org/10.1190/1.3215771

Bunks, C., Saleck, F. M., Zaleski, S., & Chavent, G. (1995). Multiscale seismic waveform inversion. *Geophysics*, *60*(5), 1457–1473. https://doi.org/10.1190/1.1443880

Burschil, T., Buness, H., & Schmelzbach, C. (2022). Near-surface three-dimensional multicomponent source and receiver S-wave survey in the Tannwald Basin, Germany: Acquisition and data processing. *Near Surface Geophysics*, *20*(4), 331–348. https://doi.org/10.1002/nsg.12214

Butzer, S., Kurzmann, A., & Bohlen, T. (2013). 3D elastic full-waveform inversion of small-scale heterogeneities in transmission geometry. *Geophysical Prospecting*, *61*(6 - Challenges of Seismic Imaging and Inversion Devoted to Goldin), 1238–1251. https://doi.org/10.1111/1365-2478.12065

Butzer, S. (2015). *3D elastic time-frequency full-waveform inversion* [Doctoral dissertation, Karlsruhe Institute of Technology, Germany].

Campanella, R. G., & Stewart, W. P. (1992). Seismic cone analysis using digital signal processing for dynamic site characterization. *Canadian Geotechnical Journal*, *29*(3), 477–486. https://doi.org/10.1139/t92-052

Chen, R., & Tran, K. T. (2021). 2D Gauss-Newton full waveform inversion of SH- and Love-waves in the time domain. *Journal of Applied Geophysics*, *191*, 104363. https://doi.org/10.1016/j.jappgeo.2021.104363

Chen, R., Tran, K. T., & Wang, Y. (2021). 2D time-domain full-waveform inversion of SH- and Love-waves for geotechnical site characterization. *Near Surface Geophysics*, *19*(3), 283–295. https://doi.org/10.1002/nsg.12137

Chesworth, W. (2008). *Encyclopedia of soil science*. Springer Dordrecht.

Choi, Y., & Alkhalifah, T. (2012). Application of multi–source waveform inversion to marine streamer data using the global correlation norm. *Geophysical Prospecting*, *60*(4 - Simultaneous Source Methods for Seismic Data), 748–758. https://doi.org/10.1111/j.1365-2478.2012.01079.x

Dagnino, D., Sallarès, V., & Ranero, C. R. (2014). Scale- and parameter-adaptive model-based gradient pre-conditioner for elastic full-waveform inversion. *Geophysical Journal International*, *198*(2), 1130–1142. https://doi.org/10.1093/gji/ggu175

Dokter, E., Köhn, D., Wilken, D., De Nil, D., & Rabbel, W. (2017). Full waveform inversion of SH- and Love-wave data in near-surface prospecting. *Geophysical Prospecting*, *65*(S1), 216–236. https://doi.org/10.1111/1365-2478.12549

Donohue, S., Long, M., O-Connor, P., Eide Helle, T., Aspmo Pfaffhuber, A., & Rømoen, M. (2012). Multi-method geophysical mapping of quick clay. *Near Surface Geophysics*, *10*(3), 207–219. https://doi.org/10.3997/1873-0604.2012003

Dragoset, B. (1995). Geophysical applications of adaptive-noise cancellation. In *SEG Technical Program Expanded Abstracts 1995* (pp. 1389–1392). https://doi.org/10.1190/1.1887226

Drijkoningen, G. G., Veltman, A., Hendrix, W., Faber, K., Brouwer, J., & Hemstede, G. A. (2006). A linear motor as seismic horizontal vibrator. *68th EAGE Conference and Exhibition incorporating SPE EUROPEC 2006*, Article cp-2-00315. https://doi.org/10.3997/2214-4609.201402307

Emerson, M., & Foray, P. (2006). Laboratory P-wave measurements in dry and saturated sand. *Acta Geotechnica*, *1*(3), 167–177. https://doi.org/10.1007/s11440-006-0015-7

Eppinger, B. J., Holbrook, W. S., Liu, Z., Flinchum, B. A., & Tromp, J. (2024). 2D Near-Surface Full-Waveform Tomography Reveals Bedrock Controls on Critical Zone Architecture [e2023EA003248 2023EA003248]. *Earth and Space Science*, *11*(2), e2023EA003248. https://doi.org/10.1029/2023EA003248

Fichtner, A., & Trampert, J. (2011). Resolution analysis in full waveform inversion. *Geophysical Journal International*, *187*(3), 1604–1624. https://doi.org/10.1111/j.1365-246X.2011.05218.x

Fichtner, A., & van Leeuwen, T. (2015). Resolution analysis by random probing. *Journal of Geophysical Research: Solid Earth*, *120*(8), 5549–5573. https://doi.org/10.1002/2015JB012106

Forbriger, T., Groos, L., & Schäfer, M. (2014). Line-source simulation for shallow-seismic data. Part 1: theoretical background. *Geophysical Journal International*, *198*(3), 1387–1404. https://doi.org/10.1093/gji/ggu199

Foti, S., Hollender, F., Garofalo, F., Albarello, D., Asten, M., Bard, P.-Y., Comina, C., Cornou, C., Cox, B., Di Giulio, G., et al. (2018). Guidelines for the good practice of surface wave analysis: a product of the InterPACIFIC project. *Bulletin of Earthquake Engineering*, *16*(6), 2367–2420. https://doi.org/10.1007/s10518-017-0206-7

Foti, S., & Strobbia, C. (2002). Some notes on model parameters for surface wave data inversion. *15th EEGS Symposium on the Application of Geophysics to Engineering and Environmental Problems*, Article cp-191-00064. https://doi.org/https://doi.org/10.3997/2214-4609-pdb.191.12SEI6

Franko, K. M., & Grote, K. R. (2013). Estimation of near-surface soil density using electrical and electromagnetic geophysical techniques. *125th Anniversary Annual Meeting & Expo*, 553.

Fu, L., Liu, Z., & Schuster, G. (2018). Superresolution near-field imaging with surface waves. *Geophysical Journal International*, *212*(2), 1111–1122. https://doi.org/10.1093/gji/ggx466

Fuchs, K., & Müller, G. (1971). Computation of synthetic seismograms with the reflectivity method and comparison with observations. *Geophysical Journal International*, *23*(4), 417–433. https://doi.org/10.1111/j.1365-246X.1971.tb01834.x

Gao, L., & Pan, Y. (2018). Source signature estimation from multimode surface waves via mode-separated virtual real source method. *Geophysical Journal International*, *213*(2), 1177–1186. https://doi.org/10.1093/gji/ggy063

Gao, L., Pan, Y., & Bohlen, T. (2020). 2-D multiparameter viscoelastic shallow-seismic full-waveform inversion: reconstruction tests and first field-data application. *Geophysical Journal International*, *222*(1), 560–571. https://doi.org/10.1093/gji/ggaa198

Gao, L., Pan, Y., Rieder, A., & Bohlen, T. (2021). Multiparameter viscoelastic full-waveform inversion of shallow-seismic surface waves with a pre-conditioned truncated Newton method. *Geophysical Journal International*, *227*(3), 2044–2057. https://doi.org/10.1093/gji/ggab311

Gao, L., Pan, Y., Rieder, A., Bohlen, T., & Mao, W. (2023). Multiparameter 2-D viscoelastic full-waveform inversion of Rayleigh waves: a field experiment at Krauthausen test site. *Geophysical Journal International*, *234*(1), 297–312. https://doi.org/10.1093/gji/ggad072

Gao, L., Xia, J., & Pan, Y. (2014). Misidentification caused by leaky surface wave in high-frequency surface wave method. *Geophysical Journal International*, *199*(3), 1452–1462. https://doi.org/10.1093/gji/ggu337

Gardner, G. H. F., Gardner, L. W., & Gregory, A. R. (1974). Formation velocity and density—The diagnostic basics for stratigraphic traps. *Geophysics*, *39*(6), 770–780. https://doi.org/10.1190/1.1440465

Ghose, R., Brouwer, J., & Nijhof, V. (1996). A portable S-wave vibrator for high-resolution imaging of the shallow subsurface. *58th EAGE Conference and Exhibition*, Article cp-48-00132. https://doi.org/10.3997/2214-4609.201408721

Ghose, R. (2007). Integrating shear-wave seismic and Cone Penetration Testing to derive laterally varying geotechnical information. *STW project report DAR.5761*, 85.

Ghose, R., & Goudswaard, J. (2004). Integrating S-wave seismic-reflection data and cone penetration test data using a multiangle multiscale approach. *Geophysics*, *69*(2), 440–459. https://doi.org/10.1190/1.1707064

Gray, S. H. (1992). Frequency-selective design of the Kirchhoff migration oerator. *Geophysical Prospecting*, *40*(5), 565–571. https://doi.org/https://doi.org/10.1111/j.1365-2478.1992.tb00541.x

Groos, L., Schäfer, M., Forbriger, T., & Bohlen, T. (2014). The role of attenuation in 2D full-waveform inversion of shallow-seismic body and Rayleigh waves. *Geophysics*, *79*(6), R247–R261. https://doi.org/10.1190/geo2013-0462.1

Groos, L., Schäfer, M., Forbriger, T., & Bohlen, T. (2017). Application of a complete workflow for 2D elastic full-waveform inversion to recorded shallow-seismic Rayleigh waves. *Geophysics*, *82*(2), R109–R117. https://doi.org/10.1190/geo2016-0284.1

Guasch, L., Warner, M., & Ravaut, C. (2019). Adaptive waveform inversion: Practice. *Geophysics*, *84*(3), R447–R461. https://doi.org/10.1190/geo2018-0377.1

Guitton, A., & Verschuur, D. J. (2004). Adaptive subtraction of multiples using the L1-norm. *Geophysical Prospecting*, *52*(1), 27–38. https://doi.org/https://doi.org/10.1046/j.1365-2478.2004.00401.x

Halliday, D., & Curtis, A. (2008). Seismic interferometry, surface waves and source distribution. *Geophysical Journal International*, *175*(3), 1067–1087. https://doi.org/10.1111/j.1365-246X.2008.03918.x

Halliday, D., Curtis, A., & Kragh, E. (2008). Seismic surface waves in a suburban environment: Active and passive interferometric methods. *The Leading Edge*, *27*(2), 210–218. https://doi.org/10.1190/1.2840369

Halliday, D., Curtis, A., Robertsson, J. O. A., & van Manen, D.-J. (2007). Interferometric surface-wave isolation and removal. *Geophysics*, *72*(5), A69–A73. https://doi.org/10.1190/1.2761967

Halliday, D. F., Curtis, A., Vermeer, P., Strobbia, C., Glushchenko, A., van Manen, D.-J., & Robertsson, J. O. (2010). Interferometric ground-roll removal: Attenuation of scattered surface waves in single-sensor data. *Geophysics*, *75*(2), SA15–SA25. https://doi.org/10.1190/1.3360948

Häusler, M., Schmelzbach, C., & Sollberger, D. (2018). The Galperin source: A novel efficient multicomponent seismic source. *Geophysics*, *83*(6), P19–P27. https://doi.org/10.1190/geo2018-0020.1

Hayashi, K. (2012). Analysis of surface-wave data including higher modes using the genetic algorithm. In *Geocongress 2012* (pp. 2776–2785). https://doi.org/10.1061/9780784412121.284

Hayashi, K. (2008). *Development of surface-wave methods and its application to site investigations* [Doctoral dissertation, Kyoto University, Japan].

Hayashi, K., Matsuoka, T., & Hatakeyama, H. (2005). Joint analysis of a surface-wave method and micro-gravity survey. *Journal of Environmental and Engineering Geophysics*, *10*(2), 175–184. https://doi.org/10.2113/JEEG10.2.175

Hayashi, K., & Suzuki, H. (2004). CMP cross-correlation analysis of multi-channel surface-wave data. *Exploration geophysics*, *35*(1), 7–13. https://doi.org/10.1071/EG04007

Hu, X., Wei, G., Song, J., Yang, Z., Lu, M., & Gao, L. (2021). Full-waveform inversion with source and receiver coupling effects correction. *Geophysics*, *86*(4), R463–R470. https://doi.org/10.1190/geo2020-0331.1

Inci, G., Yesiller, N., & Kagawa, T. (2003). Experimental investigation of dynamic response of compacted clayey soils. *Geotechnical Testing Journal*, *26*(2), 125–141. https://doi.org/10.1520/GTJ11328J

Irnaka, T. M. (2022). *3D elastic full waveform inversion for subsurface characterization: study of a shallow seismic multicomponent field data* [Doctoral dissertation, Université Grenoble Alpes, France].

Irnaka, T. M., Brossier, R., Métivier, L., Bohlen, T., & Pan, Y. (2022). 3-D multicomponent full waveform inversion for shallow-seismic target: Ettlingen Line case study. *Geophysical Journal International*, *229*(2), 1017–1040. https://doi.org/10.1093/gji/ggab512

Jeong, W., Lee, H.-Y., & Min, D.-J. (2012). Full waveform inversion strategy for density in the frequency domain. *Geophysical Journal International*, *188*(3), 1221–1242. https://doi.org/10.1111/j.1365-246X.2011.05314.x

Johnston, D. H., & Toksöz, M. (1981). Seismic wave attenuation. Society of Exploration Geophysicists.

Kallivokas, L., Fathi, A., Kucukcoban, S., Stokoe, K., Bielak, J., & Ghattas, O. (2013). Site characterization using full waveform inversion [SI: José Manuel Roësset]. *Soil Dynamics and Earthquake Engineering*, *47*, 62–82. https://doi.org/10.1016/j.soildyn.2012.12.012

Karthikeyan, M., Tan, T. S., Mimura, M., Yoshimura, M., & Tee, C. P. (2007). Improvements in nuclear-density cone penetrometer for non-homogeneous soils. *Soils and Foundations*, *47*(1), 109–117. https://doi.org/10.3208/sandf.47.109

Kawasaki, Y., Minato, S., & Ghose, R. (2022). Reducing parameter coupling effect for subsoil density estimation using 3D seismic full-waveform inversion with horizontal-force source. In *Second International Meeting for Applied Geoscience & Energy* (pp. 2138–2142). https://doi.org/10.1190/image2022-3750995.1

Kawasaki, Y., Minato, S., & Ghose, R. (2025). Full-waveform inversion for imaging density variability in the near-surface soils. In *Fifth International Meeting for Applied Geoscience & Energy*.

Kawasaki, Y., Minato, S., & Ghose, R. (2024). Subsoil density field reconstruction through 3-D FWI: a systematic comparison between vertical- and horizontal-force seismic sources. *Geophysical Journal International*, *236*(2), 727–747. https://doi.org/10.1093/gji/ggad445

Kimman, W. P., & Trampert, J. (2010). Approximations in seismic interferometry and their effects on surface waves. *Geophysical Journal International*, *182*(1), 461–476. https://doi.org/10.1111/j.1365-246X.2010.04632.x

Kitsunezaki, C., Goto, N., Kobayashi, Y., Ikawa, T., Horike, M., Saito, T., Kurota, T., Yamane, K., & Okuzumi, K. (1990). Estimation of P- and S-wave velocities in deep soil deposits for evaluating ground vibrations in earthquakes. *Sizen-Saigai-Kagaku (in Japanese)*, *9*(3), 1–17.

Köhn, D., De Nil, D., Kurzmann, A., Przebindowska, A., & Bohlen, T. (2012). On the influence of model parametrization in elastic full waveform tomography. *Geophysical Journal International*, *191*(1), 325–345. https://doi.org/10.1111/j.1365-246X.2012.05633.x

Köhn, D., Meier, T., Fehr, M., De Nil, D., & Auras, M. (2016). Application of 2D elastic Rayleigh waveform inversion to ultrasonic laboratory and field data. *Near Surface Geophysics*, *14*(5), 461–467. https://doi.org/10.3997/1873-0604.2016027

Köhn, D., Wilken, D., De Nil, D., Wunderlich, T., Rabbel, W., Werther, L., Schmidt, J., Zielhofer, C., & Linzen, S. (2019). Comparison of time-domain SH waveform inversion strategies based on sequential low and bandpass filtered data for improved resolution in near-surface prospecting. *Journal of Applied Geophysics*, *160*, 69–83. https://doi.org/10.1016/j.jappgeo.2018.11.001

Krawczyk, C. M., Polom, U., & Beilecke, T. (2013). Shear-wave reflection seismics as a valuable tool for near-surface urban applications. *The Leading Edge*, *32*(3), 256–263. https://doi.org/10.1190/tle32030256.1

Krohn, C. E. (1984). Geophone ground coupling. *Geophysics*, *49*(6), 722–731. https://doi.org/10.1190/1.1441700

Kudo, K., & Shima, E. (1970). Attenuation of shear waves in soil. *Bulletin of the Earthquake Research Institute, University of Tokyo*, *48*(2), 145–158.

Kumar, J., & Madhusudhan, B. (2012). Dynamic properties of sand from dry to fully saturated states. *Géotechnique*, *62*(1), 45–54. https://doi.org/10.1680/geot.10.P.042

Levander, A. R. (1988). Fourth-order finite–difference P-SV seismograms. *Geophysics*, *53*(11), 1425–1436. https://doi.org/10.1190/1.1442422

Li, J., Mikada, H., & Takekawa, J. (2024). Improving full-waveform inversion based on sparse regularization for geophysical data. *Journal of Geophysics and Engineering*, *21*(3), 810–832. https://doi.org/10.1093/jge/gxae036

Li, Y. E., & Demanet, L. (2016). Full-waveform inversion with extrapolated low-frequency data. *Geophysics*, *81*(6), R339–R348. https://doi.org/10.1190/geo2016-0038.1

Lin, C.-P., Pan, E., Tran, Q. K., & Wu, T.-J. (2023). A unified approach for relationships among Green's function, normal modes and dispersion spectrum in layered elastic half-space, with corrected misconceptions on surface wave dispersion and testing. *Geophysical Journal International*, *232*(2), 1357–1375. https://doi.org/10.1093/gji/ggac396

Liu, F., Sen, M. K., & Stoffa, P. L. (2000). Dip selective 2-D multiple attenuation in the plane-wave domain. *Geophysics*, *65*(1), 264–274. https://doi.org/10.1190/1.1444717

Liu, H., Wu, G., Jia, Z., Li, Q., Shan, J., & Yang, S. (2024). Wasserstein distance-based full waveform inversion method for density reconstruction. *Journal of Applied Geophysics*, *223*, 105358. https://doi.org/10.1016/j.jappgeo.2024.105358

Liu, J., Draganov, D., & Ghose, R. (2018). Seismic interferometry facilitating the imaging of shallow shear-wave reflections hidden beneath surface waves. *Near Surface Geophysics*, *16*(3), 372–382. https://doi.org/10.3997/1873-0604.2018013

Liu, J., Draganov, D., & Ghose, R. (2022). Reducing near-surface artifacts from the crossline direction by full-waveform inversion of interferometric surface waves. *Geophysics*, *87*(6), R443–R452. https://doi.org/10.1190/geo2021-0613.1

Liu, J., Ghose, R., & Draganov, D. (2022). Characterizing near-surface structures at the Ostia archaeological site based on instantaneous-phase coherency inversion. *Geophysics*, *87*(4), R337–R348. https://doi.org/10.1190/geo2021-0467.1

Lobsey, C. R., & Viscarra Rossel, R. A. (2016). Sensing of soil bulk density for more accurate carbon accounting. *European Journal of Soil Science*, *67*(4), 504–513. https://doi.org/10.1111/ejss.12355

Ludwig, W. J. (1970). Seismic refraction. *The Sea*, *4*, 53–84. https://cir.nii.ac.jp/crid/1574231874743904384

Luo, Y., Xia, J., Miller, R. D., Xu, Y., Liu, J., & Liu, Q. (2009). Rayleigh-wave mode separation by high-resolution linear Radon transform. *Geophysical Journal International*, *179*(1), 254–264. https://doi.org/10.1111/j.1365-246X.2009.04277.x

Mao, J., Sheng, J., Hart, M., & Kim, T. (2016). High-resolution model building with multistage full-waveform inversion for narrow-azimuth acquisition data. *The Leading Edge*, *35*(12), 1031–1036. https://doi.org/10.1190/tle35121031.1

Masoni, I., Zhou, W., Brossier, R., Métivier, L., Operto, S., & Virieux, J. (2014). Near-surface Full Waveform Inversion Using Surface Waves and Reflected Waves. *76th EAGE Conference and Exhibition - Workshops,* Article cp-401-00042. https://doi.org/10.3997/2214-4609.20140531

Maurer, H., Greenhalgh, S. A., Manukyan, E., Marelli, S., & Green, A. G. (2012). Receiver-coupling effects in seismic waveform inversions. *Geophysics*, *77*(1), R57–R63. https://doi.org/10.1190/geo2010-0402.1

Mavko, G., Mukerji, T., & Dvorkin, J. (2009). *The Rock Physics Handbook: Tools for Seismic Analysis of Porous Media* (2nd ed.). Cambridge University Press. https://doi.org/10.1017/CBO9780511626753

Mecking, R., Köhn, D., Meinecke, M., & Rabbel, W. (2021). Cavity detection by SH-wave full-waveform inversion — A reflection-focused approach. *Geophysics*, *86*(3), WA123–WA137. https://doi.org/10.1190/geo2020-0349.1

Métivier, L., Brossier, R., Mérigot, Q., Oudet, E., & Virieux, J. (2016). An optimal transport approach for seismic tomography: application to 3D full waveform inversion. *Inverse Problems*, *32*(11), 115008. https://doi.org/10.1088/0266-5611/32/11/115008

Métivier, L., Brossier, R., Operto, S., & Virieux, J. (2015). Acoustic multi-parameter FWI for the reconstruction of P-wave velocity, density and attenuation: preconditioned truncated Newton approach. In *SEG Technical Program Expanded Abstracts 2015* (pp. 1198–1203). https://doi.org/10.1190/segam2015-5875643.1

Métivier, L., Brossier, R., Virieux, J., & Operto, S. (2013). Full waveform inversion and the truncated Newton method. *SIAM Journal on Scientific Computing*, *35*(2), B401–B437. https://doi.org/10.1137/120877854

Métivier, L., Allain, A., Brossier, R., Mérigot, Q., Oudet, E., & Virieux, J. (2018). Optimal transport for mitigating cycle skipping in full-waveform inversion: A graph-space transform approach. *Geophysics*, *83*(5), R515–R540. https://doi.org/10.1190/geo2017-0807.1

Mirzanejad, M., Tran, K. T., & Wang, Y. (2022). Three-dimensional Gauss–Newton constant-Q viscoelastic full-waveform inversion of near-surface seismic wavefields. *Geophysical Journal International*, *231*(3), 1767–1785. https://doi.org/10.1093/gji/ggac287

Mora, P. (1987). Nonlinear two-dimensional elastic inversion of multioffset seismic data. *Geophysics*, *52*(9), 1211–1228. https://doi.org/10.1190/1.1442384

Nocedal, J., & Wright, S. J. (2006). *Numerical Optimization* (2e). Springer New York, NY.

Noorlandt, R., Drijkoningen, G., Dams, J., & Jenneskens, R. (2015). A seismic vertical vibrator driven by linear synchronous motors. *Geophysics*, *80*(2), EN57–EN67. https://doi.org/10.1190/geo2014-0295.1

Nuber, A., Manukyan, E., & Maurer, H. (2015). Enhancement of near-surface elastic full waveform inversion results in regions of low sensitivities. *Journal of Applied Geophysics*, *122*, 192–201. https://doi.org/10.1016/j.jappgeo.2015.09.020

Nuber, A., Manukyan, E., & Maurer, H. (2017). Optimizing measurement geometry for seismic near-surface full waveform inversion. *Geophysical Journal International*, *210*(3), 1909–1921. https://doi.org/10.1093/gji/ggx267

Ogolo, N. A., Akinboro, O. G., Inam, J. E., Akpokere, F. E., & Onyekonwu, M. O. (2015). Effect of grain size on porosity revisited. *SPE Nigeria Annual International Conference and Exhibition*, SPE-178296–MS. https://doi.org/10.2118/178296-MS

Operto, S., Gholami, Y., Prieux, V., Ribodetti, A., Brossier, R., Metivier, L., & Virieux, J. (2013). A guided tour of multiparameter full-waveform inversion with multi-

component data: From theory to practice. *The Leading Edge*, *32*(9), 1040–1054. https://doi.org/10.1190/tle32091040.1

Operto, S., Ravaut, C., Improta, L., Virieux, J., Herrero, A., & Dell'Aversana, P. (2004). Quantitative imaging of complex structures from dense wide-aperture seismic data by multiscale traveltime and waveform inversions: a case study. *Geophysical Prospecting*, *52*(6), 625–651. https://doi.org/10.1111/j.1365-2478.2004.00452.x

Operto, S., Virieux, J., Dessa, J.-X., & Pascal, G. (2006). Crustal seismic imaging from multifold ocean bottom seismometer data by frequency domain full waveform tomography: Application to the eastern Nankai trough. *Journal of Geophysical Research: Solid Earth*, *111*(B9). https://doi.org/10.1029/2005JB003835

Pan, L., Chen, X., Wang, J., Yang, Z., & Zhang, D. (2019). Sensitivity analysis of dispersion curves of rayleigh waves with fundamental and higher modes. *Geophysical Journal International*, *216*(2), 1276–1303. https://doi.org/10.1093/gji/ggy479

Pan, W., Geng, Y., & Innanen, K. A. (2018). Interparameter trade-off quantification and reduction in isotropic-elastic full-waveform inversion: synthetic experiments and Hussar land data set application. *Geophysical Journal International*, *213*(2), 1305–1333. https://doi.org/10.1093/gji/ggy037

Pan, W., Innanen, K. A., & Geng, Y. (2018). Elastic full-waveform inversion and parametrization analysis applied to walk-away vertical seismic profile data for unconventional (heavy oil) reservoir characterization. *Geophysical Journal International*, *213*(3), 1934–1968. https://doi.org/10.1093/gji/ggy087

Pan, W., Innanen, K. A., Geng, Y., & Li, J. (2019). Interparameter trade-off quantification for isotropic-elastic full-waveform inversion with various model parameterizations. *Geophysics*, *84*(2), R185–R206. https://doi.org/10.1190/geo2017-0832.1

Pan, Y., & Gao, L. (2023). Individual and joint inversions of shallow-seismic Rayleigh and Love waves: full-waveform inversion versus random-objective waveform inversion. *Surveys in Geophysics*, *44*(4), 983–1008. https://doi.org/10.1007/s10712-023-09775-y

Pan, Y., Gao, L., & Bohlen, T. (2019). High-resolution characterization of near-surface structures by surface-wave inversions: from dispersion curve to full waveform. *Surveys in Geophysics*, *40*, 167–195. https://doi.org/10.1007/s10712-019-09508-0

Pan, Y., Gao, L., & Bohlen, T. (2021). Random-Objective Waveform Inversion of 3D-9C Shallow-Seismic Field Data [e2021JB022036 2021JB022036]. *Journal of Geophysical Research: Solid Earth*, *126*(9), e2021JB022036. https://doi.org/10.1029/2021JB022036

Pan, Y., Schaneng, S., Steinweg, T., & Bohlen, T. (2018). Estimating S-wave velocities from 3D 9-component shallow seismic data using local Rayleigh-wave dispersion curves – A field study. *Journal of Applied Geophysics*, *159*, 532–539. https://doi.org/10.1016/j.jappgeo.2018.09.037

Pan, Y., Xia, J., Xu, Y., & Gao, L. (2016). Multichannel analysis of Love waves in a 3D seismic acquisition system. *Geophysics*, *81*(5), EN67–EN74. https://doi.org/10.1190/geo2015-0261.1

Park, C. B., Miller, R. D., & Xia, J. (1999). Multichannel analysis of surface waves. *Geophysics*, *64*(3), 800–808. https://doi.org/10.1190/1.1444590

Patra, C., Sivakugan, N., & Das, B. (2010). Relative density and median grain-size correlation from laboratory compaction tests on granular soil. *International Journal of Geotechnical Engineering*, *4*(1), 55–62. https://doi.org/10.3328/IJGE.2010.04.01.55-62

Plessix, R.-E. (2006). A review of the adjoint-state method for computing the gradient of a functional with geophysical applications. *Geophysical Journal International*, *167*(2), 495–503. https://doi.org/10.1111/j.1365-246X.2006.02978.x

Płonka, A., Blom, N., & Fichtner, A. (2016). The imprint of crustal density heterogeneities on regional seismic wave propagation. *Solid Earth*, *7*(6), 1591–1608. https://doi.org/10.5194/se-7-1591-2016

Pratt, R. G., Shin, C., & Hick, G. J. (1998). Gauss–Newton and full Newton methods in frequency-space seismic waveform inversion. *Geophysical Journal International*, *133*(2), 341–362. https://doi.org/10.1046/j.1365-246X.1998.00498.x

Prieux, V., Brossier, R., Operto, S., & Virieux, J. (2013). Multiparameter full waveform inversion of multicomponent ocean-bottom-cable data from the Valhall field. Part 1: imaging compressional wave speed, density and attenuation. *Geophysical Journal International*, *194*(3), 1640–1664. https://doi.org/10.1093/gji/ggt177

Pryor, W. A. (1973). Permeability-porosity patterns and variations in some Holocene sand bodies. *AAPG Bulletin*, *57*(1), 162–189. https://doi.org/10.1306/819A4252-16C5-11D7-8645000102C1865D

Rahimi Dalkhani, A. (2024). *Transdimensional surface wave inversion: 1D, 2D and 3D applications* [Dissertation (TU Delft)]. Delft University of Technology. https://doi.org/10.4233/uuid:a4ff648f-7de1-43b1-a418-844344942c89

Ravaut, C., Operto, S., Improta, L., Virieux, J., Herrero, A., & Dell'Aversana, P. (2004). Multiscale imaging of complex structures from multifold wide-aperture seismic data by frequency-domain full-waveform tomography: application to a thrust belt. *Geophysical Journal International*, *159*(3), 1032–1056. https://doi.org/10.1111/j.1365-246X.2004.02442.x

Ren, Z., & Liu, Y. (2016). A hierarchical elastic full-waveform inversion scheme based on wavefield separation and the multistep-length approach. *Geophysics*, *81*(3), R99–R123. https://doi.org/10.1190/geo2015-0431.1

Rice-Birchall, E., Faulkner, D., & Bedford, J. (2022). The effect of grain size and porosity on the nature of compaction localisation in high-porosity sandstone. *Journal of Structural Geology*, *164*, 104740. https://doi.org/10.1016/j.jsg.2022.104740

Rickett, J., Guitton, A., & Gratwick, D. (2001). Adaptive multiple subtraction with non-stationary helical shaping filters. *63rd EAGE Conference & Exhibition*, Article cp-15-00129. https://doi.org/10.3997/2214-4609-pdb.15.P167

Robertson, P. K. (1990). Soil classification using the cone penetration test. *Canadian Geotechnical Journal*, *27*(1), 151–158. https://doi.org/10.1139/t90-014

Romdhane, A., Grandjean, G., Brossier, R., Rejiba, F., Operto, S., & Virieux, J. (2011). Shallow-structure characterization by 2D elastic full-waveform inversion. *Geophysics*, *76*(3), R81–R93. https://doi.org/10.1190/1.3569798

Romero-Ruiz, A., Linde, N., Baron, L., Solazzi, S. G., Keller, T., & Or, D. (2021). Seismic signatures reveal persistence of soil compaction. *Vadose Zone Journal*, *20*(4), e20140. https://doi.org/10.1002/vzj2.20140

Schäfer, M., Groos, L., Forbriger, T., & Bohlen, T. (2014). Line-source simulation for shallow-seismic data. Part 2: full-waveform inversion—a synthetic 2-D case study. *Geophysical Journal International*, *198*(3), 1405–1418. https://doi.org/10.1093/gji/ggu171

Schröder, C. T., & Scott, J., Waymond R. (2001). On the complex conjugate roots of the Rayleigh equation: The leaky surface wave. *The Journal of the Acoustical Society of America*, *110*(6), 2867–2877. https://doi.org/10.1121/1.1419085

Shibata, T., Mimura, M., Shrivastava, A. K., & Nobuyama, M. (1992). Moisture measurement by neutron moisture cone penetrometer: design and application. *Soils and Foundations*, *32*(4), 58–67. https://doi.org/10.3208/sandf1972.32.4_58

Shin, C., Jang, S., & Min, D.-J. (2001). Improved amplitude preservation for prestack depth migration by inverse scattering theory. *Geophysical Prospecting*, *49*(5), 592–606. https://doi.org/10.1046/j.1365-2478.2001.00279.x

Shirmohammadi, F. (2024). *Layer-specific imaging and monitoring using seismic interferometry and the Marchenko method* [Doctoral dissertation, Delft University of Technology, the Netherlands].

Shirmohammadi, F., Draganov, D., van IJsseldijk, J., Ghose, R., Thorbecke, J., Verschuur, E., & Wapenaar, K. (2023). Application of Marchenko-based isolation to a land S-wave seismic dataset. https://arxiv.org/abs/2304.09956v2

Sirgue, L., T. Etgen, J., & Albertin, U. (2008). 3D frequency domain waveform inversion using time domain finite difference methods. *70th EAGE Conference and Exhibition incorporating SPE EUROPEC 2008*, Article cp-40-00143. https://doi.org/10.3997/2214-4609.20147683

Sirgue, L., Etgen, J. T., Albertin, U., & Brandsberg-Dahl, S. (2010). System and method for 3D frequency domain waveform inversion based on 3D time-domain forward modeling. United States Patent. US 7,725,266 B2.

Sirgue, L., & Pratt, R. G. (2004). Efficient waveform inversion and imaging: A strategy for selecting temporal frequencies. *Geophysics*, *69*(1), 231–248. https://doi.org/10.1190/1.1649391

Smith, J. A., Borisov, D., Cudney, H., Miller, R. D., Modrak, R., Moran, M., Peterie, S. L., Sloan, S. D., Tromp, J., & Wang, Y. (2019). Tunnel detection at Yuma Proving Ground, Arizona, USA — Part 2: 3D full-waveform inversion experiments. *Geophysics*, *84*(1), B107–B120. https://doi.org/10.1190/geo2018-0599.1

Snieder, R. (1986). 3-D linearized scattering of surface waves and a formalism for surface wave holography. *Geophysical Journal International*, *84*(3), 581–605. https://doi.org/10.1111/j.1365-246X.1986.tb04372.x

Spitz, S. (1991). Seismic trace interpolation in the F-X domain. *Geophysics*, *56*(6), 785–794. https://doi.org/10.1190/1.1443096

Sun, M., Yang, J., Dong, L., Liu, Y., & Huang, C. (2017). Density reconstruction in multiparameter elastic full-waveform inversion. *Journal of Geophysics and Engineering*, *14*(6), 1445–1462. https://doi.org/10.1088/1742-2140/aa93b0

Tarantola, A. (1986). A strategy for nonlinear elastic inversion of seismic reflection data. *Geophysics*, *51*(10), 1893–1903. https://doi.org/10.1190/1.1442046

Teodor, D., Comina, C., Anjom, F. K., Brossier, R., Socco, L. V., & Virieux, J. (2021). Challenges in shallow target reconstruction by 3D elastic full-waveform inversion

— Which initial model? *Geophysics*, *86*(4), R433–R446. https://doi.org/10.1190/geo2019-0523.1

Tittman, J., & Wahl, J. S. (1965). The physical foundataions of formation density logging (gamma-gamma). *Geophysics*, *30*(2), 284–294. https://doi.org/10.1190/1.1439574

Tjelta, T., Tieges, A., Smits, F., Geise, J., & Lunne, T. (1985). In-situ density measurements by nuclear backscatter for an offshore soil investigation. *OTC Offshore Technology Conference*, *All Days*, OTC-4917–MS. https://doi.org/10.4043/4917-MS

Tran, K. T., & McVay, M. (2012). Site characterization using Gauss–Newton inversion of 2-D full seismic waveform in the time domain. *Soil Dynamics and Earthquake Engineering*, *43*, 16–24. https://doi.org/10.1016/j.soildyn.2012.07.004

Tran, K. T., McVay, M., Faraone, M., & Horhota, D. (2013). Sinkhole detection using 2D full seismic waveform tomography. *Geophysics*, *78*(5), R175–R183. https://doi.org/10.1190/geo2013-0063.1

Tran, K. T., Mirzanejad, M., McVay, M., & Horhota, D. (2019). 3-D time-domain Gauss–Newton full waveform inversion for near-surface site characterization. *Geophysical Journal International*, *217*(1), 206–218. https://doi.org/10.1093/gji/ggz020

Tran, K. T., Nguyen, T. D., Hiltunen, D. R., Stokoe, K., & Menq, F. (2020). 3D full-waveform inversion in time-frequency domain: Field data application. *Journal of Applied Geophysics*, *178*, 104078. https://doi.org/10.1016/j.jappgeo.2020.104078

Tran, K. T., & Sperry, J. (2018). Application of 2D full-waveform tomography on land-streamer data for assessment of roadway subsidence. *Geophysics*, *83*(3), EN1–EN11. https://doi.org/10.1190/geo2016-0550.1

Tuckwell, G., Grossey, T., Owen, S., & Stearns, P. (2008). The use of microgravity to detect small distributed voids and low-density ground. *Quarterly Journal of Engineering Geology and Hydrogeology*, *41*(3), 371–380. https://doi.org/10.1144/1470-9236/07-224

van Dalen, K. N., Wapenaar, K., & Halliday, D. F. (2013). Surface wave retrieval in layered media using seismic interferometry by multidimensional deconvolution. *Geophysical Journal International*, *196*(1), 230–242. https://doi.org/10.1093/gji/ggt389

van Leeuwen, T., & Herrmann, F. J. (2012). Fast waveform inversion without source-encoding. *Geophysical Prospecting*, 10–19. https://doi.org/10.1111/j.1365-2478.2012.01096.x

VanRemortel, R. D., & Shields, D. A. (1993). Comparison of clod and core methods for determination of soil bulk density. *Communications in Soil Science and Plant Analysis*, *24*(17-18), 2517–2528. https://doi.org/10.1080/00103629309368972

Virieux, J., & Operto, S. (2009). An overview of full-waveform inversion in exploration geophysics. *Geophysics*, *74*(6), WCC1–WCC26. https://doi.org/10.1190/1.3238367

Virieux, J. (1984). SH-wave propagation in heterogeneous media: Velocity-stress finite-difference method. *Geophysics*, *49*(11), 1933–1942. https://doi.org/10.1190/1.1441605

Virieux, J. (1986). P-SV wave propagation in heterogeneous media: Velocity-stress finite-difference method. *Geophysics*, *51*(4), 889–901. https://doi.org/10.1190/1.1442147

Wang, Y., Miller, R. D., Peterie, S. L., Sloan, S. D., Moran, M. L., Cudney, H. H., Smith, J. A., Borisov, D., Modrak, R., & Tromp, J. (2019). Tunnel detection at Yuma

Proving Ground, Arizona, USA — Part 1: 2D full-waveform inversion experiment. *Geophysics*, *84*(1), B95–B105. https://doi.org/10.1190/geo2018-0598.1

Wang, Y., Tran, K. T., & Horhota, D. (2021). Road sinkhole detection with 2D ambient noise tomography. *Geophysics*, *86*(6), KS123–KS135. https://doi.org/10.1190/geo2020-0739.1

Wang, Y., Xue, Z., Bradford, J., & Gase, A. (2025). Improving Resolution of Near Surface Structure Imaging Based on Elastic Full Waveform Inversion. *Geophysical Prospecting*, *73*(4), 1141–1153. https://doi.org/https://doi.org/10.1111/1365-2478.70000

Wang, Y., Dong, L., Liu, Y., & Yang, J. (2016). 2D frequency-domain elastic full-waveform inversion using the block-diagonal pseudo-Hessian approximation. *Geophysics*, *81*(5), R247–R259. https://doi.org/10.1190/geo2015-0678.1

Wapenaar, K., & Fokkema, J. (2006). Green's function representations for seismic interferometry. *Geophysics*, *71*(4), SI33–SI46. https://doi.org/10.1190/1.2213955

Weihnacht, B., & Börner, F. (2007). Multi-method geophysical measurements for soil science investigations in the vadose zone. *Hydrology and Earth System Sciences Discussions*, *4*(4), 2659–2681. https://hal.science/hal-00298872

Wittkamp, F., Athanasopoulos, N., & Bohlen, T. (2018). Individual and joint 2-D elastic full-waveform inversion of Rayleigh and Love waves. *Geophysical Journal International*, *216*(1), 350–364. https://doi.org/10.1093/gji/ggy432

Wu, B., Shi, C., Chen, X., & Zhang, Q. (2025). Theoretical investigation of the excitation of leaky modes for multilayered models. *Geophysical Journal International*, *240*(1), 31–45. https://doi.org/10.1093/gji/ggae367

Xia, J., Miller, R. D., & Park, C. B. (1999). Estimation of near-surface shear-wave velocity by inversion of Rayleigh waves. *Geophysics*, *64*(3), 691–700. https://doi.org/10.1190/1.1444578

Xia, J., Xu, Y., Luo, Y., Miller, R. D., Cakir, R., & Zeng, C. (2012). Advantages of using multichannel analysis of Love waves (MALW) to estimate near-surface shear-wave velocity. *Surveys in Geophysics*, *33*, 841–860. https://doi.org/10.1007/s10712-012-9174-2

Xia, J., Yin, X., & Xu, Y. (2013). Feasibility of determining Q of near-surface materials from Love waves. *Journal of Applied Geophysics*, *95*, 47–52. https://doi.org/10.1016/j.jappgeo.2013.05.007

Yan, Y., Chen, X., Huai, N., & Guan, J. (2022). Modern inversion workflow of the multimodal surface wave dispersion curves: staging strategy and Pattern search with embedded Kuhn–Munkres algorithm. *Geophysical Journal International*, *231*(1), 47–71. https://doi.org/10.1093/gji/ggac178

Yan, Y., Wang, Z., Li, J., Huai, N., Liang, Y., Song, S., Zhang, J., & Zhang, L. (2020). Elastic SH- and Love-wave Full-Waveform Inversion for shallow shear wave velocity with a preconditioned technique. *Journal of Applied Geophysics*, *173*, 103947. https://doi.org/10.1016/j.jappgeo.2020.103947

Yang, J., Liu, Y., & Dong, L. (2016). Simultaneous estimation of velocity and density in acoustic multiparameter full-waveform inversion using an improved scattering-integral approach. *Geophysics*, *81*(6), R399–R415. https://doi.org/10.1190/geo2015-0707.1

Yilmaz, Ö. (2001). *Seismic Data Analysis*. Society of Exploration Geophysicists. https://doi.org/10.1190/1.9781560801580

Yule, D. E., Sharp, M. K., & Butler, D. K. (1998). Microgravity investigations of foundation conditions. *Geophysics*, *63*(1), 95–103. https://doi.org/10.1190/1.1444331

Zhang, Z., Huang, L., & Lin, Y. (2012). A wave-energy-based precondition approach to full-waveform inversion in the time domain. In *SEG Technical Program Expanded Abstracts 2012* (pp. 1–5). https://doi.org/10.1190/segam2012-1555.1

Zhou, W., Brossier, R., Operto, S., & Virieux, J. (2015). Full waveform inversion of diving & reflected waves for velocity model building with impedance inversion based on scale separation. *Geophysical Journal International*, *202*(3), 1535–1554. https://doi.org/10.1093/gji/ggv228

Zhubayev, A., & Ghose, R. (2012). Physics of shear-wave intrinsic dispersion and estimation of in situ soil properties: a synthetic VSP appraisal. *Near Surface Geophysics*, *10*(6), 613–629. https://doi.org/10.3997/1873-0604.2012016

Acknowledgements

First and foremost, I would like to express my sincere gratitude to my promotor and daily supervisor, Dr. Ranajit Ghose, for his invaluable support and clear guidance throughout my PhD journey. He was consistently patient and supportive, even when my research did not progress as expected. He generously devoted his time to encourage me to continue my work, teaching me how to present research findings at academic conferences, and carefully reviewing my journal manuscripts and this thesis sentence by sentence. His critical and logical feedback always guided me in the right direction.

I would also like to express my deep appreciation to my daily supervisor, Dr. Shohei Minato, for his continuous support since I began my PhD at TU Delft. He supported me not only in addressing research challenges but also in adapting to life in the Netherlands. His outstanding knowledge and insightful ideas have made significant contributions to this thesis and greatly enhanced the quality of my research. We shared a lot of moments, including conversations in his office and dinners with his family, which always made me feel comfortable.

My sincere thanks also go to my copromotor, Dr. Deyan Draganov, for his constructive comments during the annual progress meetings. His unparalleled expertise in seismic interferometry was invaluable, and Chapter 3 of this thesis would not have been possible without his guidance.

This research at TU Delft would not have been possible without the financial support from OYO Corporation. I am especially grateful to Mr. Masaru Narita (former President), Dr. Hideki Saito, and Dr. Hiromasa Shima for providing me with the valuable opportunity to participate in the TUD-OYO research project and for approving the one-year extension of my stay at TU Delft. I would also like to thank my former colleagues in the Energy Division, especially Mr. Masahiro Oshima, Mr. Masanori Ebato, and Mr. Dai Nobuoka, for kindly allowing me to pursue my PhD research in the Netherlands. I am also grateful to Dr. Koichi Hayashi, currently a professor at Kyoto University, for his support with the analysis of MALW using field data and for his critical feedback, which helped deepen my understanding of the subject. I would also like to acknowledge my current colleagues in the R&D section for creating a supportive and comfortable environment that allowed me to continue working on my PhD research at OYO.

Warm thanks go to all my colleagues and friends at TU Delft for their companionship and the memorable moments we shared. In particular, the fieldwork conducted in Scheemda in the summer of 2022 for three PhD projects remains one of the most enjoyable experiences of my time at TU Delft, despite the challenging heatwave conditions. I am sincerely grateful to everyone who shared this experience: Ranajit, Deyan, Shohei, Jingming, Faezeh, Eddy, Jens, and Yuan.

Finally, I would like to express my deepest gratitude to my parents and my older sister for their unwavering support throughout my life. I am quite sure that I would not be where I am today without them.

Curriculum Vitæ

Yusuke KAWASAKI

15-11-1990 Born in Ehime, Japan.

Education

2020–2025 Ph.D. in Applied Geophysics
Delft University of Technology, the Netherlands
Thesis: Full-waveform inversion for imaging spatially varying subsoil density
Promotors: Dr. R. Ghose
Dr. ir. D.S. Draganov

2013–2015 M.Sc. in Earth and Environmental Sciences
Nagoya University, Japan

2009–2013 B.Sc. in Earth and Planetary Sciences
Nagoya University, Japan

Experience

2020–2025 PhD Candidate
Delft University of Technology, the Netherlands

2015–Present Geophysicist
OYO Corporation, Japan

List of Publications

(5) **Y. Kawasaki**, S. Minato, R. Ghose, *Full-waveform inversion for imaging density variability in the near-surface soils*, in Fifth International Meeting for Applied Geoscience & Energy, (2025).

(4) **Y. Kawasaki**, S. Minato, R. Ghose, *Subsoil density field reconstruction through 3-D FWI: a systematic comparison between vertical-and horizontal-force seismic sources*, Geophysical Journal International **236(2)**, 727-747 (2024).

(3) **Y. Kawasaki**, S. Minato, R. Ghose, *Reducing parameter coupling effect for subsoil density estimation using 3D seismic full-waveform inversion with horizontal-force source*, in Second International Meeting for Applied Geoscience & Energy, 2138-2142 (2022).

(2) **Y. Kawasaki**, R. Ghose, S. Minato, *Porosity of near-surface soil layers From 3D elastic full-waveform inversion: tests on synthetic data*, in NSG2021 27th European Meeting of Environmental and Engineering Geophysics (Vol. 2021, No. 1, pp. 1-5). European Association of Geoscientists & Engineers (2021).

(1) **Y. Kawasaki**, K. Koshika, O. Pradhan, H. Kurosawa, K. Abe, M. Yamamoto, D. Nobuoka, Y. Matsubara, M. Jha, C. Timsina, S. Shrestha, P. Pokhrel, D. Nepali, M. Bhattarai, S.N. Sapkota, H. Matsuyama, H. Miyake, K. Koketsu *Subsurface structure of the Kathmandu Valley revealed by seismic reflection and gravity surveys*, in AGU Fall Meeting Abstracts (Vol. 2019, pp. T33E-0370) (2019).